Stony Brook University

Interface Mediated Deformation Behavior in Metallic Nanostructures

A Dissertation Presented

by

Bin Cheng

to

The Graduate School

in Partial Fulfillment of the

Requirements

for the Degree of

Doctor of Philosophy

in

Materials Science and Engineering

Stony Brook University

December 2017

Stony Brook University

The Graduate School

Bin Cheng

We, the dissertation committee for the above candidate for the

Doctor of Philosophy degree, hereby recommend

acceptance of this dissertation.

Jason Trelewicz – Dissertation Advisor
Assistant Professor of Materials Science and Chemical Engineering

Dilip Gersappe – Chairperson of Defense
Professor of Materials Science and Chemical Engineering

T. Venkatesh – Committee Member
Associate Professor of Materials Science and Chemical Engineering

Garritt Tucker – External Committee Member
Assistant Professor of Mechanical Engineering at Colorado School of Mines

This dissertation is accepted by the Graduate School

Charles Taber

Dean of the Graduate School

Abstract of the Dissertation

Interface Mediated Deformation Behavior in Metallic Nanostructures

by

Bin Cheng

Doctor of Philosophy

in

Materials Science and Engineering

Stony Brook University

2017

The unique mechanical behaviors of metallic crystalline-amorphous nanolaminates and nanoglasses have attracted great interests in recent years because of their remarkable strength and excellent plasticity. The presence of amorphous-crystalline interfaces(ACIs) or glass-glass interfaces(GGIs) significantly affected the deformation behaviors of these metallic nanostructures demonstrated by a number of experimental and computational studies. However, due to limitations in the experimental characterization and simulation methods, the underlying deformation mechanisms remain elusive. In this thesis, molecular dynamics simulations and instrumental nanoindentation were employed to probe the intriguing interface mediated deformation mechanisms. Starting with the simulated deformation of a novel columnar crystalline-amorphous nanolaminate model, the mechanistic coupling of dislocation and shear transformation zone(STZ) plasticity were captured at the ACI using the continuum deformation metrics, which provides an effective pathway for accommodating strain while circumventing the formation of deleterious grain boundary voids and primary shear bands. Then, through systematically varying the layer thickness and nanocrystalline grain size of nanolaminates, illustrative compound mechanics maps together with a properties map were constructed to unveil the relationship between microstructural length scales and mechanical behaviors and establish the mechanics-driven design principles for optimizing the performance of nanolaminates. These simulation results motivated the experimental study of electrodeposition synthesized Ni-W grain size modulated nanolaminates consisting of glass-like and nanocrystalline layers characterized by electron microscopy. Nanoindentation testing was performed to evaluate the mechanical behaviors of Ni-W nanolaminates with different layer thickness ratio emphasizing on the hardness and strain rate sensitivity. The interface mediated deformation mechanisms in the nanoglasses also greatly improves their mechanical performance. In the second half of this thesis, an original method was developed to identify the interface region of the nanoglass models generated by the simulated consolidation of glassy spheres and disclosed the unique interface properties, which were used to understand the deformation behaviors of nanoglasses with different annealing states and grain sizes. It was found out that the strain was evenly distributed to the interface in the nanoglasses inhibiting severe shear localization and it is thermal annealing instead of grain size that was more effective to tune the mechanical performance of nanoglasses.

Dedication

To my grandfather, Liangyin Cheng

Table of Contents

List of Figures

Figure 1.6 Bright field transmission electron microscopy (TEM) images (a-c) of Ni-W nanocrystalline alloys as the grain size refinement. The insets of TEM images of (a-c) are the selected diffraction patterns of their corresponding TEM images showing the structural refinement as the reduction of grain size. The black circles in the high-resolution image (c) outline two grains where lattice fringes are observed. (d) The grain size-solute composition relationship of the Ni-W nanocrystalline produced by reverse pulsing (RP) and cathodic (C) electrodeposition together with a set of results from Ni-P system of Ref. [33]. (Reproduced from reference [34])

Figure 1.7 Composition of tungsten solute and grain size of Ni-W alloys as a function of current density of the periodic reverse (anodic) pulses added to the electrodeposition. The inset is the schematic current waveform of a 20ms duration forward pulse (cathodic) with a 0.2 $A \cdot cm^{-2}$ intensity, trailed by a reverse pulse of 3ms with an intensity spanning from 0 to 0.3 $A \cdot cm^{-2}$.(Reproduced from reference [34])

Figure 1.8 Nanocrystalline Ni-W alloys with patterned layer structures synthesized by reverse pulsing electrodeposition. The top rows of (a) and (b) are backscatter scanning electron microscopy (SEM) images of patterned structures with gradient tungsten composition layers and alternating high and low tungsten composition layers, respectively. The red curves map the tungsten composition as a function of distance from substrate in both SEM images. The bottom rows of (a) and (b) show the grain size and hardness of corresponding patterned structures as a function of distance from substrate. (Reproduced from reference [34])

Figure 1.9 Nanoindentation hardness (a) and activation volume (b) of Ni-W nanocrystalline alloys as a function of grain size on double logarithmic scales. The hardness values of four strain rates are presented in (a). The activation volume values in the (b) are normalized by the cubed Burgers vector b^3. (Reproduced from reference [35])

Figure 1.10 Scanning electron microscopy (SEM) images of the residual impressions of Ni-W alloys with a grain size of (a) 20nm, (b) 12nm, (c) 6nm, and (d) 3nm (Reproduced from reference [35]).

Figure 1.11 (a)Typical load-displacement curves of Ni-W alloys with grain sizes of 3, 6 and 12nm acquired by nanoindentation using a cubed corner indenter and a strain rate of 0.15^{-1}. Arrows in (a) highlight the discrete ripples or discontinuities in the loading section of 3nm sample's load-displacement curve. (b) Strain rate variation is mapped as a function of depth for the loading sections of the load-displacement curves in (a). Several arrows point out sudden increases of strain rate, which correlate to the discontinuities in the load-displacement curve of 3nm samples. (Reproduced from reference [35])

Figure 1.12 Experimental shear stress $\tau_Y = \sigma_Y/2$ at yielding plotted against shear modulus G at room temperature for 30 different bulk metallic glasses (Reproduced from reference [36]).

Figure 1.13 In situ TEM bright-field image of shear band forming during the edge deformation of metallic glasses. (a) and (b) show the same portion of the sample from different tilt angles. The arrow in the image point directly to the shear bands. (Reproduced from reference [37]) (c) shows a typical shear transformation zone (STZ) before and after shear transformation. (Reproduced from reference [38])

Figure 1.14 Cross-sectional (a) and planar (b) TEM images of as-fabricated 5/35 Cu/Zr nanolaminates. (c) Room-temperature uniaxial tensile stress-strain curves of 5/35 Cu/Zr nanolaminates, Cu/304 stainless steel nanolaminates, and pure nanocrystalline copper. (d) A HRTEM image of 5/35 Cu/Zr nanolaminate after tensile failure. Deformation twins are found in several nanograins (green arrows). Arrows indicate that dislocations tend to terminate at the ACIs (green arrows) or at the grain boundaries (red arrows), implying that ACIs might become the dislocation sources or sinks in nanolaminates structure. Stacking faults are also revealed in HRTEM images. (Reproduced from reference [39])

Figure 1.15 Molecular dynamic simulation of 5/10 Cu/Zr nanolaminate (10×15×10 nm in dimension) with periodic boundary condition. (a) A dislocation is nucleated at the lower ACI, where atoms are colored by central symmetry parameter and FCC atoms are not shown. (b) The dislocation nucleated from lower ACI is being absorbed by upper ACI and another dislocation nucleated from lower ACI is intersecting with former nucleated dislocation. (c) Activations of STZs near the ACI triggered by the

incoming partial dislocations. The atoms are colored by inelastic shear strain and atoms with shear strain less than 0.06 are not shown. (d) Distribution of inelastic shear strain after absorption of partial dislocations. The ACI sliding is shown on the lower right and upper left corners of lower ACI. (Reproduced from reference [39])

Figure 1.16 Comparison of nanocrystalline materials and nanoglasses' defect and chemical microstructures. (a) Melt of pure element. (b) single crystal. Analogy between the planar defects (a) and chemical (d) microstructures of nanocrystalline materials and their counterparts of nanoglasses depicted in (g) and (h), respectively. The amorphous structure displayed in (f) is generated by quenching the melt depicted in (e). (Reproduced from the reference [40])

Figure 1.17 Bright-field TEM images of Au-based nanograined metallic glasses sample 1 with an average grain size of 21nm (a) and sample 2 with a mean grain size of 29nm (b); Selected area electron diffraction patterns of sample 1 (b) and sample 2 (c); 3 nm probe size nanobeam diffraction patterns of sample 1 (c) and sample 2 (h); High-resolution TEM image of the glass-glass interface between particles in the sample 1 (d) and sample 2 (i). (Reproduced from reference [41])

Figure 1.18 (a) Uniaxial tensile stress-strain curves of a scandium-based nanoglass and monolithic metallic glass; (b) The fracture surface of deformed metallic glass after failure. (c) The deformation snapshots during in situ tensile testing of the nanoglass from 0% to 15.6% strain. (d) Tensile deformed nanoglass sample; (e) Enlarged view of the gauge region of deformed nanoglass sample at the plastic strain of 17%, where tensile necking is evident. Inset of (e) is the corresponding selected-area diffraction pattern. (Reproduced from reference [42])

Figure 1.19 Schematic procedures of introducing glass-glass interfaces into the amorphous matrix by (a) either consolidation of glassy powders or (b) pre-plastic deformation of bulk metallic glass. In both cases, the glass-glass interfaces are characterized by (c) an increase in Voronoi volume, defective short-range

order (low fraction of Cu-centered full icosahedra), and (d) an enhancement in the potential energy. (Reproduced from reference [43])

Figure 1.20 (a) Core-hell model of a Pd-Si glassy sphere with a grain size of 7nm after simulated annealing above the glass transition temperature. Atoms colored by green and yellow are located in the shell region with a width of ~0.5nm. Red and blue atoms are Pd and Si atoms, respectively, which are located in the core region. The compositions of Cu (b) and Zr (c) atoms in the core and shell regions are plotted as a function of Cu-Zr amorphous sphere's diameter. The dashed line is the center of (b) and (c) is the global composition of the amorphous spheres. (Reproduce from reference [44])

Figure 1.21 Deformation snapshots of a $Cu_{64}Zr_{36}$ bulk metallic glass and nanoglasses with grain sizes of 4, 10, and 16nm, respectively. Atoms are colored by local atomic shear strain. (Reproduced from reference [45])

Figure 2.1 Initial nanolaminate structures consisting of 5 nm-thick $Cu_{64}Zr_{36}$ amorphous layers combined with (a) 10 nm-thick single crystal Cu layers with the $[11\bar{2}]$, [110] and [111] directions along the x, y and z directions, respectively, and (b) 10 nm-thick columnar nanocrystalline Cu layers containing equiaxed grains in the x-y plane as shown in the inset with an average size of 10 nm. (c) The equiaxed nanocrystalline structure containing 25 grains with a volume-averaged mean grain size of 11.4 nm to match the CN-NL structure. All the atoms are colored by CNA value.

Figure 2.2 Structural characteristics of the CN-NL sample including the (a) grain size and (b) misorientation distributions for both the initial and optimized configurations. The optimized structures were achieved through a Monte Carlo procedure to sharpen the grain size distribution and maximize the average misorientation angle.

Figure 2.3 Flow curves for the single crystal-amorphous nanolaminate (SC-NL), columnar nanocrystal-amorphous nanolaminate (CN-NL) and equiaxed nanocrystalline Cu (NC-Cu) structures. Mechanical properties determined from these data can be found in Table 2.1.

Figure 2.4 Deformation snapshots of the SC-NL structure viewed along the [110] direction at 6.6%, 7.2% and 11% strain colored by the CNA value (upper) and slip vector (lower). Partial and full dislocations emitted from the ACI traverse the plane (111) and are absorbed in the adjacent ACI.

Figure 2.5 Deformation snapshots of the CN-NL structure viewed in the x-z plane at 3.2%, 7.2% and 10.8% strain colored by the CNA value (upper) and slip vector (lower). Dislocation activity is mediated by both the ACIs and grain boundaries and results in slip emerging along multiple slip planes.

Figure 2.6 Strain accommodation maps for the (a) SC-NL, (b) NC-NL, and (c) NC-Cu structures that delineate the contribution of the amorphous layer, FCC atoms, grain boundaries, and dislocations to deformation. The order of the trend titles in the legend aligns with the bar order at each strain from left-to-right.

Figure 2.7 Deformation snapshots viewed in the x-y plane (i.e. top-down view) of the (a) amorphous layer and (b) crystalline layer at strains of 4%, 8% and 12% with atoms colored according to the slip vector value. The alignment of shear bands with dislocation slip bands indicates that a coupling exists between the two disparate deformation mechanisms.

Figure 2.8 Orientation and location of the average slip vector slices for the (a) SC-NL and (b) CN-NL structures; snapshots are colored according to CNA value and rotated 90º relative to Figure 2.4 and 2.5. The average slip vector determined for each slice as a function of the applied strain for the (c) SC-NL and (b) CN-NL.

Figure 2.9 Deformation snapshots illustrating the evolution of a dislocation on the $(1\bar{1}\bar{1})$ slip plane colored via CNA value (upper) and slip vector (lower) between 4.0 and 4.26% strain. The dislocation is emitted from the intersection of a grain boundary with the upper ACI, traverses the grain along the slip and, and is absorbed into the amorphous layer across the lower ACI.

Figure 2.10 Normalized average slip vector as a function of strain for the $(1\bar{1}\bar{1})$ slip event depicted in Figure 2.9. Trends are presented for amorphous and crystalline slices immediately adjacent to (a) the upper (UACI) for slices S11 and S10, and (b) the lower ACI (LACI) for slices S2 and S3.

Figure 2.11 (a) Overall void volume fraction (in percentage) for each structure as a function of the applied strain. (b) Formation of a grain boundary nanovoid at 7% strain in the CN-NL structure upon intersection of a leading partial dislocation with the grain boundary as highlighted by the yellow arrow; atoms are colored according to their CNA value. (c) The fraction of surface atoms located in the grain interior, ACI, and grain boundaries in the CN-NL as a function of strain. (d) Void fractions (in percentage) for the CN-NL structure in part (a) delineated for slices directly adjacent to the ACIs in the crystalline layer (i.e. S3 & S10 in Figure. 2.8(b)) and the interior crystalline slices (i.e. S4 – S9 in Figure. 2.8(b)).

Figure 3.1 (a) Initial structure of columnar nanocrystal-amorphous nanolaminate (CN-NL), where the layer thickness of amorphous and crystalline layers are labeled as t_A and t_C, respectively (b) x-y plane cross-sectional view of columnar nanocrystal-amorphous nanolaminate, in which the grain size of nanocrystalline layer is denoted as d. The atoms are colored by the CNA value.

Figure 3.2 (a) Stress-strain curves of columnar nanocrystal-amorphous nanolaminates with different layer thickness ratio (t_A/t_C). Stress at the onset of plasticity (b) and flow stress (c) as a function of layer thickness ratio.

Figure 3.3 (a) The stress-strain curve of the columnar nanocrystal-amorphous nanolaminates with a layer thickness ratio (t_A/t_C) of 0.5 and nanocrystalline layer grain size of 10nm. The red dash line is the fitting line of the linear part of stress-strain curve with a 0.002 strain offset relative to the origin of the axes to determine the onset of plasticity strain and stress. (b) The atomic volume distributions of amorphous layer atoms at the initial state (black) and the onset of plasticity state (red), respectively. (c) The variance χ^2 as a function of shear strain cutoff. (d) The comparison of the atomic volume distributions of elastic (red)

and plastic (blue) deformed amorphous layer atoms to the initial amorphous layer atoms' distribution (Black).

Figure 3.4 Contour maps of (a) grain boundary, (b) dislocation, and (c) shear transformation zone (STZ) plasticity carriers in the columnar nanocrystal-amorphous nanolaminates sample set 1 as function of layer thickness (t_A/t_C) and strain.

Figure 3.5 Compound mechanisms map of the columnar nanocrystal-amorphous nanolaminates sample set 1. The area of different mechanism zone varies as function of layer thickness ratio (t_A/t_C) and strain. The 20% atom percent dotted line delineates different mechanisms mixing zone whereas the 60% atom percent solid line differentiates the single mechanism dominating zone.

Figure 3.6 Amorphous and crystalline layers' deformation snapshots of the set 1 columnar nanocrystal-amorphous nanolaminate sample with a layer thickness ratio (t_A/t_C) of 0.25 at strain 0.05 (a) and 0.15 (b) and the sample with a layer thickness ratio of 1.5 at the strain of 0.15 (c). Atoms are colored by the shear strain.

Figure 3.7 Compound mechanisms maps of the columnar nanocrystal-amorphous nanolaminates sample set 2 (a), set 3 (b), set 4 (c), set 5 (d). Area of different mechanism zone varies as the function of grain size and strain. The 20% atom percent dotted line delineates different mechanisms mixing zone whereas the 60% atom percent solid line differentiates the single mechanism dominating zone.

Figure 3.8 Stress at the onset of plasticity (a), flow stress (b), void volume fraction (c), and shear strain atom fraction (d) as a function of nanocrystalline layer grain size for the columnar nanocrystal-amorphous nanolaminates with a layer thickness ratio (t_A/t_C) from 0.25 to 1.00.

Figure 3.9 Property map for all sets of columnar nanocrystal-amorphous nanolaminates that includes one strength indicator (flow strength) and two plasticity indicators (void localization factor and shear band localization factor). The sample data points are denoted by (t_A/t_C, d), where d (nm) is the grain size of

nanocrystalline layer and t_A and t_C (nm) are the layer thickness of amorphous and nanocrystalline layers, respectively. The x position of sample data points is determined by the flow stress whereas the sample's y position, shape, and color are determined by the higher value between the void localization and shear band localization factors. The dashed line is the average line for both void localization and shear band localization factors. Four zones with different properties are outlined and labeled as I, II, III, and IV.

Figure 3.10 Amorphous and crystalline layers' deformation snapshots at the end of deformation (0.2 strain) of typical samples in Zone I (a), Zone II (b), Zone III (c), and Zone IV(d). Atoms are colored by the shear strain.

Figure 4.1 Schematic of the current waveform employed in the deposition of grain size modulated Ni-W nanolaminates, where J_{fwd} and J_{rev} are the forward and reverse current density, respectively; T_{fwd} and T_{rev} are the forward and reverse pulse duration, respectively; T_C and T_A are the deposition time of nanocrystalline layer and glass-like layer, respectively. Details are disclosed in Table 4.2 and 4.3.

Figure 4.2 Electrodeposition rates of a glass-like layer with a grain size of 5nm and a nanocrystalline layer with a grain size of 55m. The red and blue lines are the linear fits to the data points of glass-like and nanocrystalline layers, respectively, and the fitting equations are displayed close to their corresponding fitting lines. The slope of each equation is the deposition rate with a unit of $nm \cdot s^{-1}$.

Figure 4.3 X-ray Diffraction (XRD) for the monolithic glass-like and nanocrystalline samples, whose tungsten compositions are measured by energy dispersive spectroscopy (EDS) shown on the right side of the figure. The grain size of the sample displayed near the corresponding spectrum is calculated using the Williamson-Hall method [46].

Figure 4.4 Bright-field TEM images and selected area diffraction patterns for the grain size modulated Ni-W nanolaminates with t_A/t_C ratios of (a) 57nm/69nm, (c) 40nm/46nm, and (e) 17nm/17nm and their corresponding SEM images (b), (d) and (f) acquired by backscattered electron signals.

Figure 4.5 (a) Hardness plotted as a function of layer thickness ratio t_A/t_C for the grain size modulated Ni-W nanolaminates. The red and blue dash lines are the hardness values of monolithic glass-like and nanocrystalline samples, respectively, which are also used to calculate the hardness predicted by the rule of mixtures. The predicted hardness trend is displayed as green dash line. Specific t_A/t_C of each sample is listed on the right side of the (a) in the form of (sample, t_A/t_C), where t_A and t_C are in units of nanometer. (b) Hardness enhancement as a function of t_A/t_C, which are calculated based on the difference between the actual hardness of samples and their rule of mixtures predicted hardness. The t_A/t_C axes in (a) and (b) are formatted in a logarithm scale.

Figure 4.6 Hardness as a function of strain rate for five representative samples, including monolithic glass-like and nanocrystalline samples and grain size modulated Ni-W nanolaminates with t_A/t_C of 81nm/20nm, 41nm/46nm, and 19nm/76nm. The strain rate axis is formatted in a logarithm scale. The error bars of some samples are too small to be visualized in this plot.

Figure 4.7 Activation volume for the deformation of grain size modulated Ni-W nanolaminates as a function of t_A/t_C ratio (a) or glass-like layer thickness (b). The activation volume is normalized by the cubed Burger vector (b^3) of nickel lattice. The red and blue dash lines are the activation volume values of monolithic glass-like and nanocrystalline samples, respectively. The specific t_A/t_C of each sample is listed on the right side of figure (a) in the form of (sample, t_A/t_C), where t_A and t_C are in units of nanometer. The strain rate axis is formatted in a logarithm scale in figure (a).

Figure 5.1 (a) Initial FCC stacking of $Cu_{64}Zr_{36}$ glassy spheres. Cu and Zr atoms are colored red and blue, respectively. (b) y-z plane cross-sectional view of 1nm slice cut from initial structure. (c) Atomic volume distribution of bulk metallic glass (BMG) and unconsolidated nanoglass (NG). Inset is the enlarged view of BMG and unconsolidated NG's atomic volume distributions between 14 to 16 $Å^3$. (d) Consolidated nanoglass model. (e) y-z plane cross-sectional view of a 1nm slice cut from consolidated nanoglass colored by volumetric strain. (f) Atomic volume distributions of bulk metallic glass (BMG) and consolidated nanoglass. The inset is the enlarged view of BMG and unconsolidated NG's atomic volume distributions between 14 to 16 $Å^3$.

Figure 5.2 (a) Void volume fraction as a function of consolidation pressure. (b) System temperature profiles as a function of consolidation time for five different pressure ramp rates. (c) Void volume fraction as a function of pressure ramp rate. NPR is the abbreviation of no pressure ramp.

Figure 5.3 Atomic volume distributions of BMG atoms and a subset of consolidated nanoglass atoms with volumetric strain range of (a) 0~0.01, (b) 0~0.1, and (c) 0~0.2. For clarity, only copper peaks are shown in the distributions comparisons. The inset of each figure is the snapshot of nanoglass slice where atoms within certain volumetric strain range are colored green.

Figure 5.4 (a) Variance χ^2 as a function of volumetric strain cutoff. (b) Comparison of the atomic volume distributions of interface (red) and grain (blue) to the BMG's distribution (black).

Figure 5.5 (a) 5nm thick y-z and close-packed plane slices of consolidated nanoglass colored by the volumetric strain. The volumetric strain profile, normalized atomic volume and full icosahedra (FI) fraction as a function of distance along the red dash line (b) and blue dash line (c) in the y-z plane slice.

Figure 6.1 FCC stacked initial structures of $Cu_{64}Zr_{36}$ nanoglass with grain size of (a)2.5nm, (b)5.0nm, (c)10nm, and (d) 15nm. Cu and Zr atoms were colored red and blue, respectively.

Figure 6.2 Evolution of void volume fraction as a function of consolidation pressure for initial nanoglass structures with grain sizes ranging from 2.5 to 17.5 nm.

Figure 6.3 (a) Initial FCC stacked $Cu_{64}Zr_{36}$ amorphous spheres and consolidated nanoglass, where the Cu and Zr atoms were colored red and blue, respectively. Atoms in the inset window of consolidated nanoglass were colored by volumetric strain to highlight the significant volume change in the interface region. (b) Volumetric strain colored cross-sectional views of as-prepared nanoglass with a grain size of 10nm at 50K and its annealed states at 300K, 550K, and 800K. (c) Volumetric strain colored cross-sectional views of the nanoglasses with grain sizes of 2.5, 5, 10, and 15nm.

Figure 6.4 A single interface in the as-prepared (a) and 800K annealed (b) nanoglasses with a grain size of 10nm. Few interfaces in the nanoglasses with grains size of 5nm (c) and 15nm (d). Atoms are colored by normalized volumetric strain.

Figure 6.5 (a) Interface volume fraction and width as a function of annealing temperature. (b) Atomic volume and full icosahedra (FI) fraction of interface and grain Cu atoms as a function of annealing temperature. (c) Interface volume fraction and width as a function of grain size. (d) Atomic volume and full icosahedra fraction of interface and grain Cu atoms as a function of grain size.

Figure 6.6 (a) Stress-strain curves of 10nm grain size nanoglasses with different annealing states and a bulk metallic glass (BMG) sample. (b) Stress-strain curves of nanoglasses with different grain sizes ranging from 2.5 to 17.5nm. Insets of both figures are the average flow stress of corresponding nanoglasses.

Figure 6.7 (a) Deformation snapshots of nanoglasses with different annealing states and a bulk metallic glass at a strain of 0.06 and 0.18. Atoms are colored by the Von Mises shear strain. (b) Average shear strain of interface and grain atoms for different annealing state nanoglasses at 0.06, 0.12, and 0.18 strain. (c) Shear localization factor as a function of strain for nanoglasses with different annealing states and a bulk metallic glass.

Figure 6.8 (a) Deformation snapshots of nanoglasses with different grain sizes at strains of 0.06 and 0.18. Atoms are colored by the Von Mises shear strain. (b) Average shear strain of interface and grain atoms for different grain size nanoglasses at 0.06, 0.12, and 0.18 strain. (c) Shear localization factor as a function of strain for nanoglasses with grain sizes.

List of Tables

Acknowledgments

In the beginning of this thesis, I would like to express the greatest gratitude to my advisor Professor Jason Trelewicz for everything over these five years. Professor Trelewicz introduced me to the fascinating world of metallic nanostructures, taught me the nature of performing good research, guided me through the difficulties, and provided me with endless support both in my study and life. It is Professor Trelewicz that makes me believe that I can perform world-class research and influence my field of study. I will bear the spirit of Professor Trelewicz in mind and continue to pursue the truth of science and engineering. I would like to thank my thesis committee members, Professor Dilip Gersappe, Professor T. Venkatesh and Professor Garritt Tucker, for their guidance in the past five years. I truly learned a lot from your expertise.

I would like to thank my wife, Wenjuan Song particularly. It is you that accompanied me through these incredible five years in U.S. and shared the happiness, sadness, frustration, and success with me. I cannot imagine how hard it would be if not for your support. Thank you for always being there for me. I would like to offer my enormous appreciation to my parents, Yubao Cheng and Junhua Liu for all the support that got me through the hardness in these years. You encouraged me to achieve the best in every aspect of my life and overcome any difficulty I encountered. I am so lucky to have you as my parents and my greatest role model. I would like to thank my unborn child. The joy you brought to me at the end of my doctoral career is tremendous. You will encourage me to be the best father ever and continue to thrive. I would like to thank all my family for the support and understanding and help me to achieve the goals of my life.

I would like to thank all the members in the Engineering Metallic Nanostructures Laboratory, including Oliva Donaldson, Yang Zhang, Jonathan Gentile, Wenbo Wang, W. Streit Cunningham, Jian Dong, David Wang, and Lacey Schwab. I would like to thank Jonathan Gentile and David Wang for the training on the metallographic and nanoindentation techniques, Yang Zhang and Wenbo Wang for the insightful discussions on the atomistic simulations, W. Streit Cunningham for the electron microscopy image processing. It is a great honor for me to work with you in my doctoral career and have you as my best friends at Stony Brook. I would like to especially thank Olivia Donaldson not only for all the experiment guidance and transmission electron microscopy characterization but also for the help of getting used to life in America. It is your patience and kindness that help me got through several critical points in my doctoral career and familiar with the language, culture, and lifestyle in U.S. I will cherish all the good memories of co-founding the Engineering Metallic Nanostructures Laboratory and you as my lifelong friend.

I would also like to thank Debby Michienzi, Shauntae Smith, Chandrani Roy and Rosa Diliberto from our department office for all the help with paperwork. I would like to also thank our department laboratory director Jim Quinn for all the help with experiments and hazardous wastes. I would also like to thank Kim Kisslinger and Fernando Camino from Center for Functional Nanomaterials at Brookhaven National Laboratory for the training and help on the electron microscopes.

Chapter 1: Introduction

1.1 Mechanical Behaviors of Nanocrystalline Metals and Amorphous Solids

1.1.1 Strength scaling in nanocrystalline metals

Extraordinary high strength can be realized by refining the grain size of a metal to the nanocrystalline regime [31, 32, 48-51]. This well-known engineering practice to strengthen metals and alloys is extrapolated from the empirical Hall-Petch (H-P) relationship [52, 53]:

$$\sigma_y = \sigma_0 + K_d d^{-1/2} \quad (1.1)$$

where d is the grain size, σ_y is the yield strength, and σ_0 and K_d are the material dependent constants. As the Hall-Petch equation describes, with the reduction of grain, the yield strength will exhibit an increase that scales with the inverse square root of the grain size. The underlying mechanics of this behavior involve grain boundaries impeding the motion of dislocations, which ultimately results in dislocation pile-ups that further hinders dislocation motion and in turn, an increase in strength [54]. This empirical equation is well established in coarsened grain materials. Therefore, it is reasonable to postulate that when the grain size is reduced to nanoscale, extremely high strength will be observed, especially in well-prepared, high quality nanocrystalline samples. Experimental data from the uniaxial tension/compression tests and micro- or nano- indentation have validated this prediction [2, 3, 16]. As shown in Fig. 1.1(a), nanocrystalline copper with a grain size of 10 nm approaches a hardness as high as 3GPa and a yield strength of 1GPa, which is significantly greater than its coarsen-grained counterparts (50MPa yield strength). The yield strength vs $d^{-1/2}$ plot in Fig. 1.1(b) shows a similar trend as in Fig. 1.1(a), which follows the Hall-Petch relationship into the nanocrystalline regime.

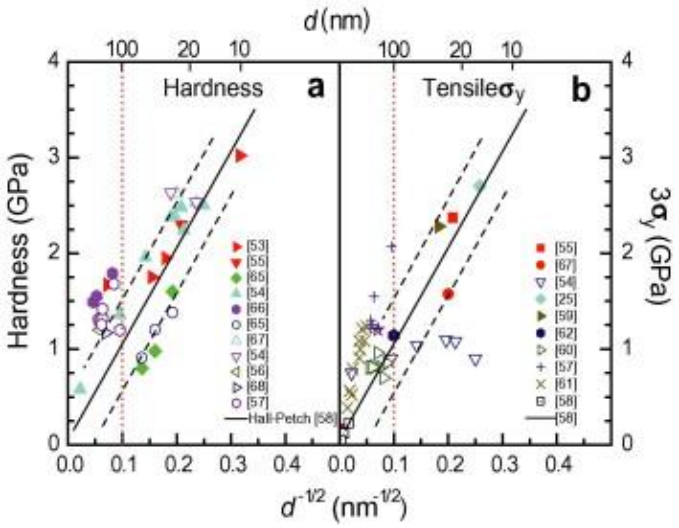

Figure 1.1 Experimental data summary on the strength scaling from the literature of Cu samples. Strength (or hardness) is plotted as a function of $d^{-1/2}$. (a) includes experiment data from literature on hardness[1-5] (solid symbols) and yield strength[2, 4, 6-9] (empty symbols). (b) includes literature data of tensile yield strength[2, 3, 6, 7, 10-15]. Straight lines represent the Hall-Petch relation extrapolated from mc Cu[11]. (Reproduced from reference [16])

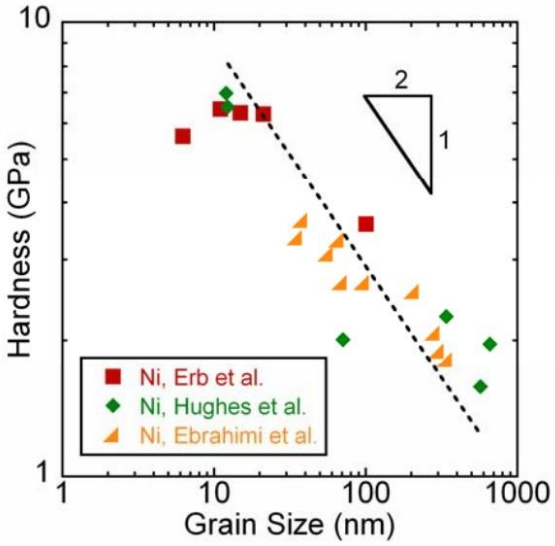

Figure 1.2 Hardness experiment data from the studies of Erb et al. [17], Hughes et al. [18] and Ebrahimi et al. [19]. Hall-Petch relationship breakdown can be observed at nc Nickel samples grain sizes ranging from 10 to 20 nm. (The figure was prepared by J.R. Trelewicz)

However, further experimental [35, 55-57] and molecular dynamics simulation [20, 48, 58, 59] evidence indicates that when grain size is reduced below about 10-20nm, the strength and hardness plateau and even exhibit an inflection where a decrease in strength is observed at the finest nanocrystalline grain sizes; this phenomenon is known as the "Hall-Petch Breakdown" [32]. Experimental data for nanocrystalline Ni in Fig. 1.2 shows that with the refinement of grain size, the increase in

hardness deviates from the Hall-Petch relation below about 10-20 nm. A similar trend was found in molecular dynamic deformation simulations of nanocrystalline Cu. These results indicate a shift in the underlying deformation mechanisms below this breakdown grain size, where dislocation-dominated plasticity succumbs to grain boundary-mediated deformation processes such as atomic shuffling, sliding, and migration [48, 58, 60-63]. As a result of this transition in the deformation physics, a peak strength can now be expected to occur at a finite grain size in the range of 10-20 nm, which has been confirmed for a number of nanocrystalline metals and alloys [17, 20, 35, 55].

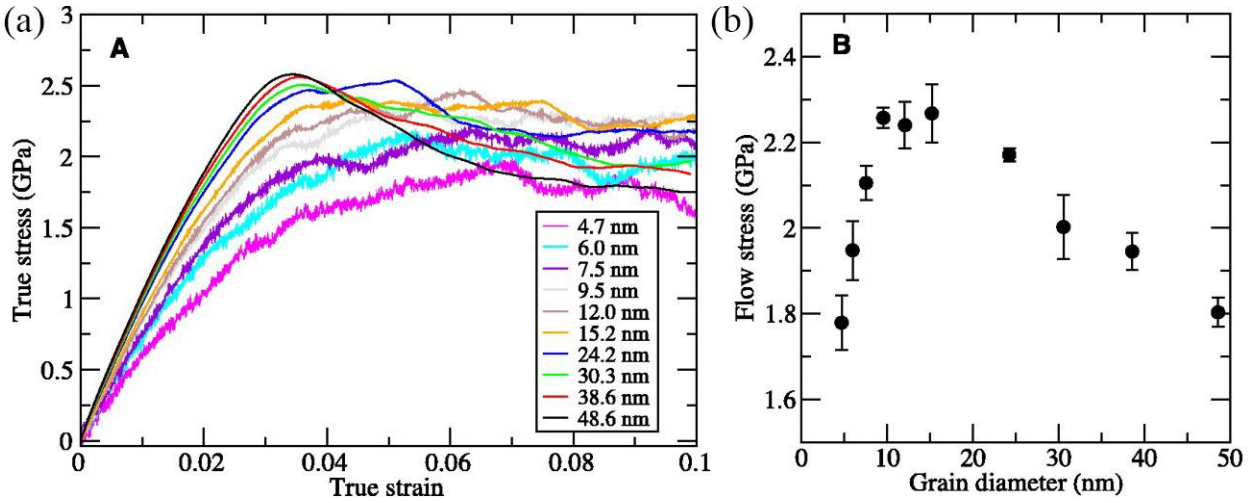

Figure 1.3 Molecular dynamics simulation results[20] of nc-Cu uniaxial tensile deformation. (a) Stress-strain curves for 10 simulations with varying grain sizes. (b) The flow stress, defined as the average stress in the strain interval from 7 to 10% deformation. The error bars indicate the fluctuations in this strain interval (1 standard deviation). A maximum in the flow stress is seen for grain sizes of 10 to 15 nm, caused by a shift from grain boundary–mediated to dislocation-mediated plasticity. (Reproduced from reference [20])

1.1.2 Ductility and fracture of nanocrystalline metals

While significant improvements in strength are realized through nanostructuring a metal, it also has negative implications for ductility and fracture. The ductility of a metal characterizes its ability to plastically deform prior to fracture under tensile stresses [31]. Considerable elongation (usually 10% percent or above) of high strength nanocrystalline metals is desired in order to increase their technological utility as a new structural material. However, accumulated data from the literature suggest that nanocrystalline metals cannot withstand tensile elongation even up to few percent. Fig. 1.4 shows the tensile elongation for a variety of nanocrystalline metals plotted against the yield strength. Clearly, the

ductility of high strength nanocrystalline metals is worse than its coarse-grained counterparts. For example, nanocrystalline Cu only exhibits a tensile elongation of 10%, contrary to the 60% elongation of microcrystalline Cu [24]. Three mechanisms have been proposed to explain the poor ductility of nanocrystalline metals [64]: 1) lack of available strain accommodation processes such as dislocation slip or grain boundary sliding, 2) premature flow instability from preexisting processing introduced flaws, and 3) low strain hardening capability.

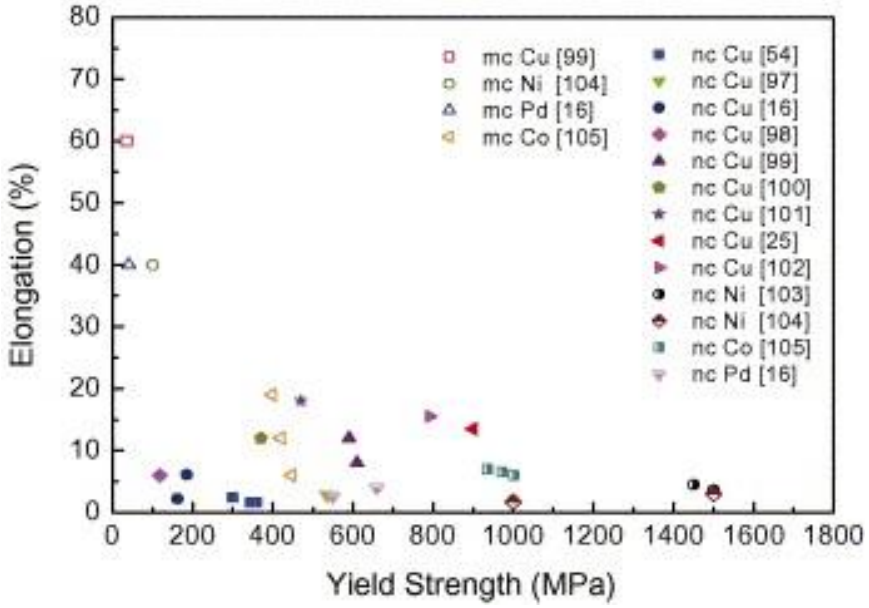

Figure 1.4 Summary of literature reported tensile elongation to failure plotted as a function of yield strength of different nanocrystalline metals with grain sizes less than 100nm[2, 10, 21-30]. Generally speaking, most of the nc-metals' tensile ductility is rather low, usually below 10%. (Reproduced from reference [31])

Due to the plastic instability of nanocrystalline metals, fracture occurs with limited accumulation of plastic strain through the initiation, propagation, and coalescence of nanovoids or nanocracks. During early stages of plasticity, inelastic strain presents a strong trend to localize and form regions of high plastic shear, which results in the eventual formation of a crack. Most reported fracture morphologies for nanocrystalline metals consist of mixed nanovoids, microvoids, and shear regions. In Kumar's study of electroplated nanocrystalline nickel, they report that the spacing and size of these voids are on the order of 1 micron, which is considerably larger than the grain size. Several other studies confirmed this finding [65, 66]. Hasnaoui [66] and Farkas [67] performed MD simulations to study the fracture mechanics of

nanocrystalline metals. They suggest that nanovoids are found at grain boundaries and triple junctions ahead of a propagating crack. The primary crack front grew through the linking of these voids, ultimately succumbing to intergranular fracture.

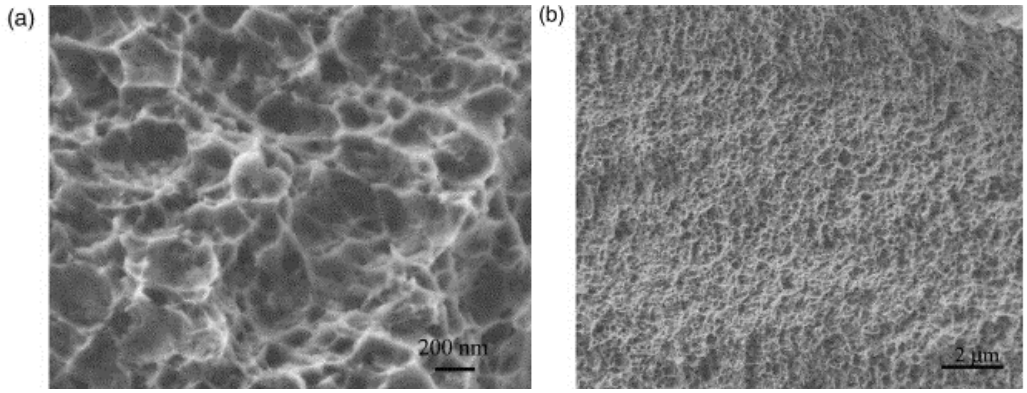

Figure 1.5 Fracture surface morphology of a 30 nm grain size electroplated Ni tensile sample. (a) dimple rupture with dimples that are significantly larger in diameter(200-400nm) than grain size, and (b) a lower magnification image showing the prevalence of fracture mode. (Reproduced from reference [32])

1.1.3 Grain size tunable Ni-W nanocrystalline alloys synthesized by reverse pulsing electrodeposition technique

Nanocrystalline metals can be synthesized from a variety of techniques, such as inert gas condensation [49], severe plastic deformation [68], mechanical alloying [69] and electrodeposition [17] etc. However, the revelation of size-dependent properties of nanostructured metals is hindered by the difficulty of acquiring high-quality samples, the pre-existing processing faults, and the lack of control over the grain size in most of the methods, which fuel the controversy of the intriguing deformation mechanisms exhibited by nanocrystalline metals. In addition, even at room temperature, a number of pure nanocrystalline metals demonstrate a thermal instability against grain coarsening, which mainly results from a large fraction of high energy interfaces struggling against the equilibrium tendency [70-72]. The thermal instability makes it rather difficult to obtain nanocrystalline metals with the finest grain size and unveil the transition of deformation mechanisms across the "Hall-Petch Breakdown" regime.

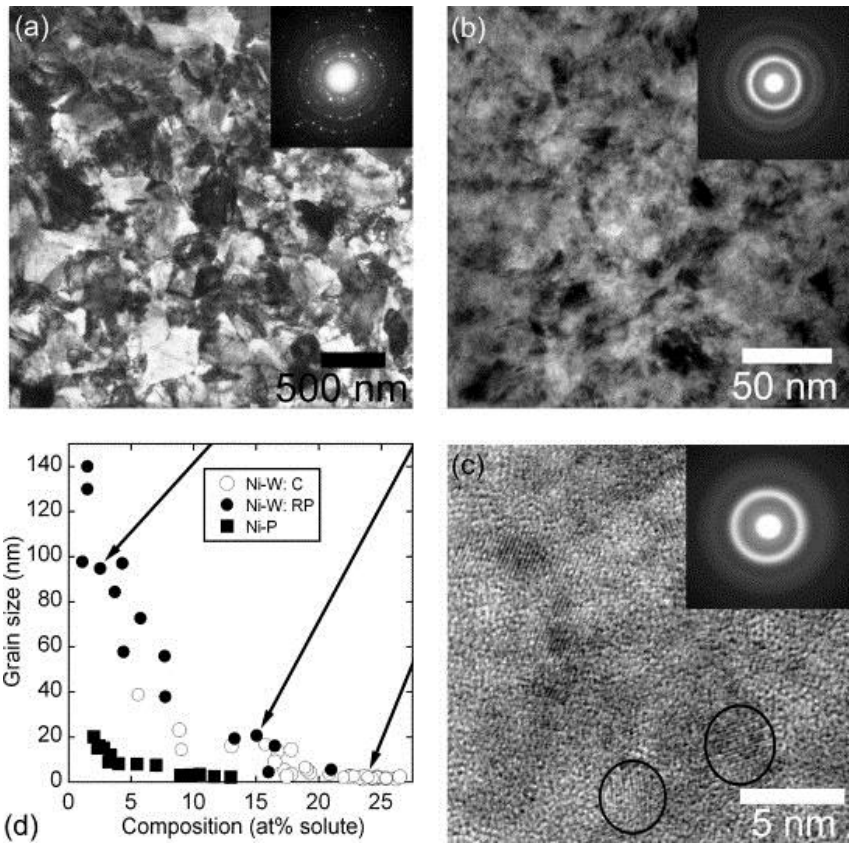

Figure 1.6 Bright field transmission electron microscopy (TEM) images (a-c) of Ni-W nanocrystalline alloys as the grain size refinement. The insets of TEM images of (a-c) are the selected diffraction patterns of their corresponding TEM images showing the structural refinement as the reduction of grain size. The black circles in the high-resolution image (c) outline two grains where lattice fringes are observed. (d) The grain size-solute composition relationship of the Ni-W nanocrystalline produced by reverse pulsing (RP) and cathodic (C) electrodeposition together with a set of results from Ni-P system of Ref. [33]. (Reproduced from reference [34])

Alloying of additional elements to the pure nanocrystalline metals has emerged as an alternative method of producing the nanostructured metals that could reach the finest grain size approaching the amorphous limit. The addition of solute elements not only thermodynamically stabilizes the nanocrystalline alloys by segregating solute atoms to the grain boundaries and settling the high interface energy but also enables access to a variety of grain sizes via controlling the amount of solute present in the nanocrystalline alloys [73-75]. An excellent example of grain size controllable binary alloys is given by Deter and Schuh et al [34] as shown in Fig. 1.6, where the Ni-W nanocrystalline alloys with a variety of grain sizes were synthesized using electrodeposition. The variance of Ni-W alloy's grain size as a function of the tungsten solute concentration is plotted in Fig. 1.6(d). It is evident that the grain size

confirmed collectively by transmission electron microscopy (TEM) images in Fig. 1.6 (a), (b), (c) and X-ray diffraction (not shown here), is closely linked to the concentration of solute tungsten atoms measured by energy dispersive X-ray spectroscopy (EDS). The strong dependence of grain size on the tungsten solute concentration is rationalized by theoretical calculation [75], Monte Carlo simulation [76], and atom probe tomography[77] that the tungsten solute's relatively weak segregation tendency to the grain boundaries led to this grain size-solute concentration correlation.

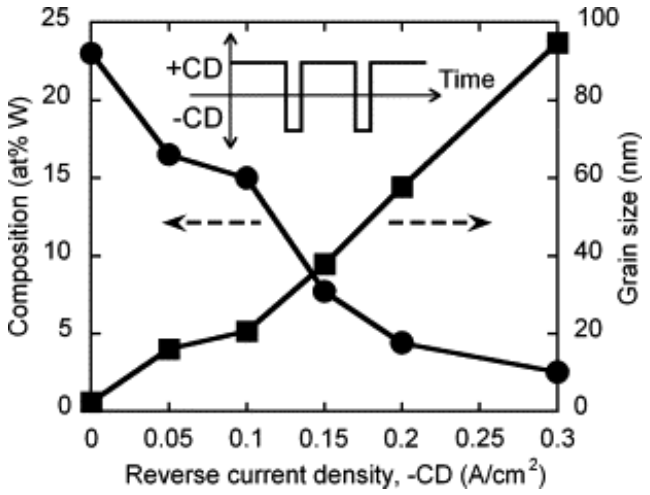

Figure 1.7 Composition of tungsten solute and grain size of Ni-W alloys as a function of current density of the periodic reverse (anodic) pulses added to the electrodeposition. The inset is the schematic current waveform of a 20ms duration forward pulse (cathodic) with a 0.2 A▪cm^{-2} intensity, trailed by a reverse pulse of 3ms with an intensity spanning from 0 to 0.3 A▪cm^{-2}.(Reproduced from reference [34])

The key strength of Detor and Schuh's Ni-W nanocrystalline alloys work [34] is the precise control of grain size over a broad range of grain sizes, which is realized via adding periodic reverse pulses during the electrodeposition of Ni-W alloys. The tungsten atoms indicate a high tendency to be removed in the periodic short reverse pulse during the long forward pulse of co-depositing nickel and tungsten atoms. Therefore, as shown in Fig. 1.7(d), the composition of tungsten in the deposited Ni-W alloy scales with the reverse current density, which enables the dynamic control of the tungsten concentration and in turns grain size via simply adjusting the reverse current density. The reverse pulse electrodeposition technique demonstrates a capability of obtaining high quality nanocrystalline alloys with the grain size spanning from above 100nm (~140nm) to almost the amorphous limit (~2nm) whereas the Ni-W and NiP

nanocrystalline alloys [33] deposited using the conventional cathodic electrodeposition are limited within 40nm as depicted in Fig. 1.6 (d) and usually degraded by the significant defects, such as pits, pores and cracks. In addition, by manipulating the current waveform, the patterned nanocrystalline electrodeposits can be prepared as illustrated in Fig. 1.8 (a) and (b), in which the grain size gradient structure and grain size modulated laminate are displayed, respectively. The tungsten solute concentration in these patterned structures is customized by designing a different working function at different stages of deposition. As a result, the grain size and mechanical performance are deliberately varied in different layers of the electrodeposits as demonstrated in Fig. 1.8. The ability of patterning nanostructure using the reverse pulsing electrodeposition facilitates the design of hierarchical metallic composites that can combine the strength of different grain sizes and optimize the mechanical performance of Ni-W nanocrystalline alloys.

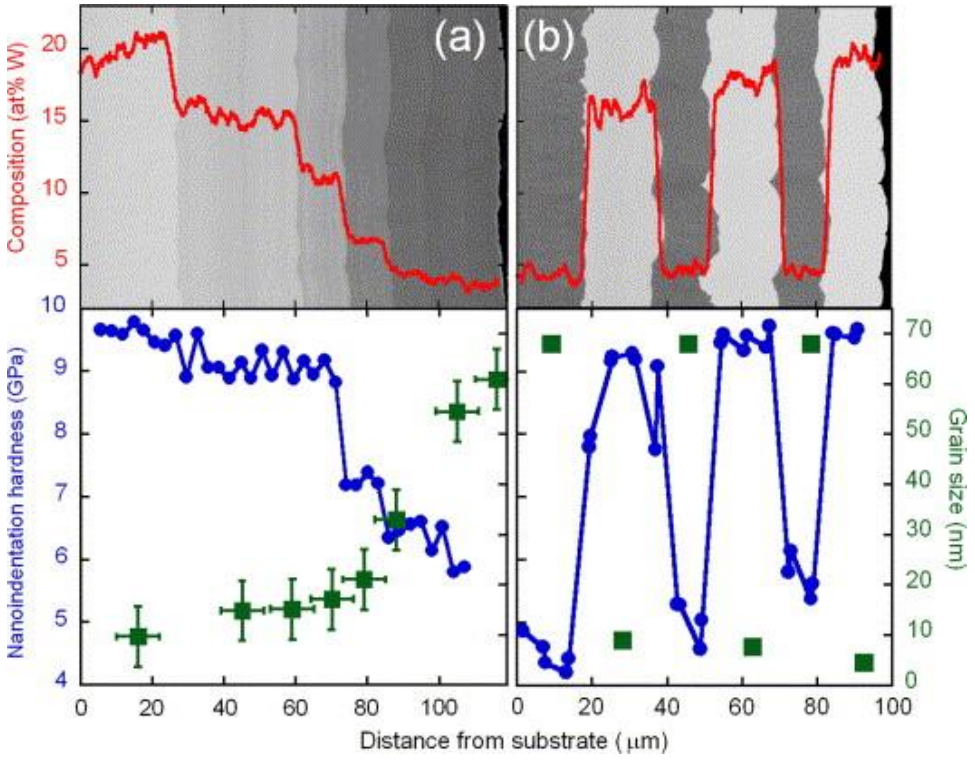

Figure 1.8 Nanocrystalline Ni-W alloys with patterned layer structures synthesized by reverse pulsing electrodeposition. The top rows of (a) and (b) are backscatter scanning electron microscopy (SEM) images of patterned structures with gradient tungsten composition layers and alternating high and low tungsten composition layers, respectively. The red curves map the tungsten composition as a function of distance from substrate in both SEM images. The bottom rows of (a) and (b) show the grain size and hardness of corresponding patterned structures as a function of distance from substrate. (Reproduced from reference [34])

1.1.4 Hall-Petch breakdown in nanocrystalline alloys and crossover to glass-like deformation behavior at the finest grain size

The novel reverse pulsing electrodeposition technique enables access to the majority of grain sizes within the nanometer scale (<100nm), which paves the way for mapping out the grain size-dependent properties of nanocrystalline alloys across the entire Hall-Petch breakdown regime. Trelewicz and Schuh [35] carried out the nanoindentation testing of the reverse pulsing electrodeposited nanocrystalline Ni-W alloys with a grain size ranging from 3~150nm. Fig. 1.9 shows the nanoindentation hardness values of nanocrystalline Ni-W alloys as a function of grain size over four strain rates. It is evident that the hardness results follow the classical Hall-Petch strength scaling down to 20nm grain size. However, as the further refinement of grain size down to 10-20nm, the hardness exhibits a plateau breakdown regime and even in the higher strain rate data set, a slight strength weakening trend is observed. Thus, the Hall-Petch breakdown is experimentally validated to the 10~20nm regime, which agrees with most of the atomistic simulation studies [20, 59, 78] and existing experimental data [17-19].

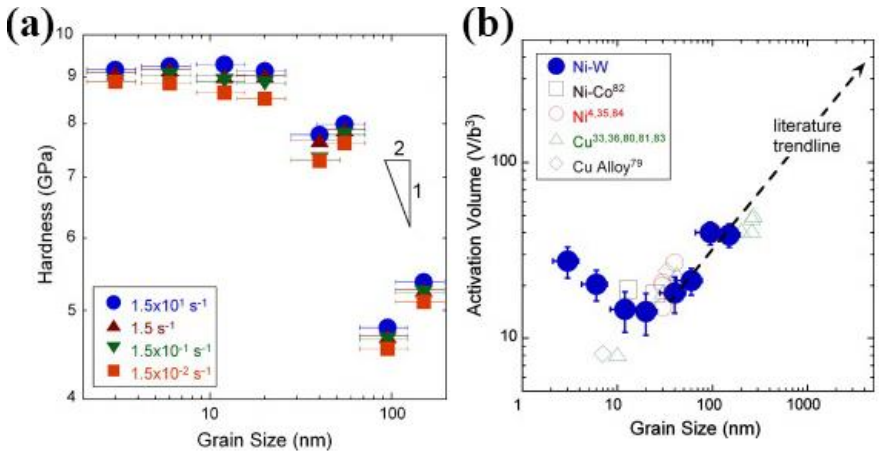

Figure 1.9 Nanoindentation hardness (a) and activation volume (b) of Ni-W nanocrystalline alloys as a function of grain size on double logarithmic scales. The hardness values of four strain rates are presented in (a). The activation volume values in the (b) are normalized by the cubed Burgers vector b^3. (Reproduced from reference [35])

To capture the transition of deformation mechanisms, the activation volume for this set of samples was calculated based on the strain rates sensitivity testing and plotted in Fig. 1.9 (b), where the activation volume was found to decrease along with the grain size down to 10-20nm suggesting the

increasing strain rate sensitivity as the grain size refinement. Nevertheless, the activation volume started to rise with the further reduction of the grain size and the materials became increasingly strain rate insensitive. Therefore, a minimum value around 10-20nm was identified as the transition regime, where the deformation shifted from a strain rate sensitive manner of nanocrystalline metals to the rate-independent glassy-like inhomogeneous flow mode like the classic amorphous solids' response.

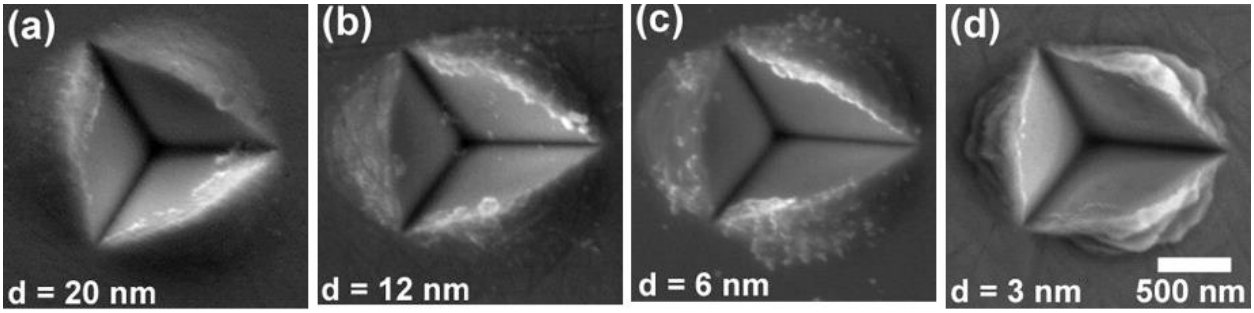

Figure 1.10 Scanning electron microscopy (SEM) images of the residual impressions of Ni-W alloys with a grain size of (a) 20nm, (b) 12nm, (c) 6nm, and (d) 3nm (Reproduced from reference [35]).

The glassy-like deformation behavior indicated by the elevating activation volume at the finest grain size of nanocrystalline Ni-W alloys unveils the intriguing deformation mechanism of this crossover grain size regime that bridges typical nanocrystalline metals responses to the severe localization deformation behaviors of amorphous solids. Qualitative and quantitative evidence are provided by Trelewicz and Schuh [35] using the scanning electron microscopy (SEM) and the strain rate variation of the loading section of typical load-displacement curves. As shown in Fig. 1.10 (a), (b), and (c), the SEM images of nanoindentation residual impressions of grain size 20, 12, and 6 nm are characterized by a smooth and homogenous pile-up surrounding the impression site like the typical characteristic of conventional polycrystalline materials. The residual impression of the 3nm grain size sample shows the inhomogeneous pileup with obvious shear offsets as depicted in Fig. 1.10(d), which is characteristic of the unstable plastic flow of amorphous solids. By examining the load-displacement curves of Ni-W alloys as shown in Fig. 1.11(a), the discrete ripples or discontinuities are observed in the curve of 3nm whereas the other grain size samples' curves are smooth and continuous. The strain rate variation during the loading section of curves as shown in Fig. 1.11(b), where the constant strain rate is observed in the grain

size 6 and 12 nm sample. The several sudden increases of strain rate or evident peaks in the plot of the 3nm sample are presented and correlated to the discrete ripples in the load-displacement curve, which quantitatively identified the unstable plastic flow via shear banding.

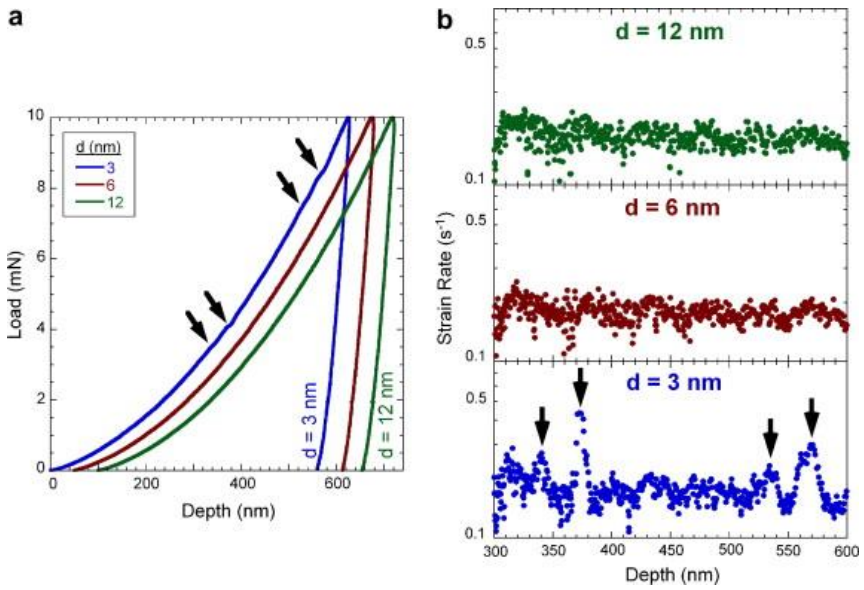

Figure 1.11 (a)Typical load-displacement curves of Ni-W alloys with grain sizes of 3, 6 and 12nm acquired by nanoindentation using a cubed corner indenter and a strain rate of 0.15^{-1}. Arrows in (a) highlight the discrete ripples or discontinuities in the loading section of 3nm sample's load-displacement curve. (b) Strain rate variation is mapped as a function of depth for the loading sections of the load-displacement curves in (a). Several arrows point out sudden increases of strain rate, which correlate to the discontinuities in the load-displacement curve of 3nm samples. (Reproduced from reference [35])

1.1.5 Extraordinary high strength of amorphous solids

The extreme grain size refinement in a metal or alloy is the amorphous limit where no long-range order exists in the material, which can consequently be classified as amorphous solids or metallic glass. Since first introduced in the 1960s' by Klement et al. [79], bulk metallic glasses (BMG) have been extensively studied due to their exceptional properties, such as high strength [36, 80], excellent abrasion and wear resistance, and remarkable anticorrosion attributes [81]. In tension, a metallic glass can exhibit a strength of 1.5 GPa while in compression, a strength as high as 5GPa can be achieved [80]. Even though large elastic strains of 2% can be obtained, nearly no macroscopic plastic strain has been reported during the tensile deformation of bulk metallic glasses [80, 82, 83]. The shear strength of metallic glasses has been suggested to be close to the theoretical value of ~0.1 G (G is the shear modulus) based on the

Frenkel model [84-87]. However, the highest observed shear strength determined by traditional mechanical testing is generally much smaller than this theoretical value. Through examining elastic constants and compressive yield strength of 30 metallic glasses in room temperature, Johnson and Samwer [36] concluded an average shear strength of ~0.026G, which is derived from the maximum resolved shear stress τ_y=γ_cG (γ_c= 0.0267$\pm$0.0020 is the slope shown in Fig. 1.12) at yielding of the unstressed glass limit. This experimental determined shear strength is almost 3~4 times smaller than the theoretical value. This clear difference between theoretical and experimental value is related to the fundamental unit of deformation captured by the shear localization deformation model for metallic glasses.

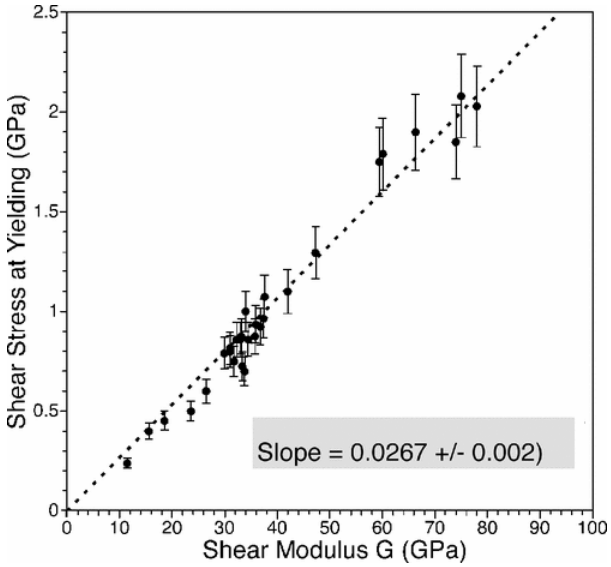

Figure 1.12 Experimental shear stress $\tau_Y = \sigma_Y/2$ at yielding plotted against shear modulus G at room temperature for 30 different bulk metallic glasses (Reproduced from reference [36]).

1.1.6 Shear banding in the amorphous solids

It is well known that the ductility of crystalline materials relies on their atomic configuration and chemical bonding. Generally, low lattice resistance for dislocation motion and multiple slip systems in a highly symmetrical crystal configuration results in good ductility. In disordered solids, such as metallic glasses, there is no well-established relationship between atomic structures and mechanical properties. Even though metallic glasses possess ultrahigh strength at room temperature, generally they exhibit poor

global ductility due to the formation and quick propagation of narrow shears bands. During the plastic deformation of metallic glasses, shear bands accommodate most of the plastic strain, which initiates strain softening and finally leads to fracture with a limited global accumulation of plastic strain. Fig. 1.13 (a) and (b) shows typical TEM images of shear offsets that formed on the surface of a metallic glass due to the propagation of dominant shear bands [37]. Formation of shear bands releases strain energy built up from elastic loading and the confinement of strains to narrow shear paths, which leads to catastrophic failure of metallic glasses.

The catastrophe failure of bulk metallic glasses via shear banding remains as the Achilles' heel for BMG to be used as structural materials [82, 83]. In past decades, the research on the deformation behavior of bulk metallic glasses was focused on improving the accommodation of plasticity and the prevention of shear localization [88-91]. Several strategies [88, 92, 93] have been proposed to improve the tensile ductility of bulk metallic glasses, among which include introducing the structural inhomogeneity, such as crystalline precipitates [94, 95], dendrites [92, 96], and pre-induced shear bands [97, 98], becomes a promising method to reflect and/or distribute shear bands. Recently, engineering glass-glass interfaces (GGIs) into the metallic glass matrix has emerged as a new approach to improve the plasticity of metallic glasses [42, 99].

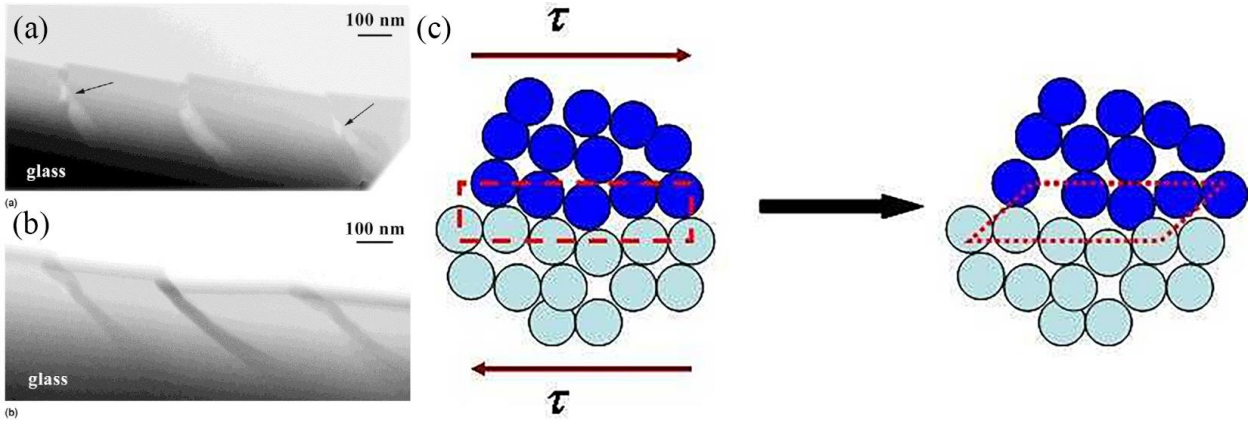

Figure 1.13 In situ TEM bright-field image of shear band forming during the edge deformation of metallic glasses. (a) and (b) show the same portion of the sample from different tilt angles. The arrow in the image point directly to the shear bands. (Reproduced from reference [37]) (c) shows a typical shear transformation zone (STZ) before and after shear transformation. (Reproduced from reference [38])

1.1.7 Shear transformation zone in metallic glasses

One widely applied concept to explain the deformation mechanism in amorphous solids is shear transformation zone (STZ) proposed by Argon [38], which states that a group of atoms cooperatively rearrange during deformation through the overcoming of a saddle point in a potential energy landscape. This coupled atomic motion is illustrated in Fig. 1.13 (c). Based on deformation simulations, STZ is composed of a few to ~100 atoms, which is frequently observed in a variety of metallic glass models simulated with different compositions and empirical interatomic potentials [83, 100-104]. Therefore, STZ is a common deformation feature in the metallic glasses. Local atomic structures strongly affect the operation of STZs during the deformation of metallic glasses. Under uniform stress, STZs in the metallic glasses is first initialized in the sites with favorable energetics, which is related to local atomic configurations [100, 104-107]. It is believed that the deformation of metallic glasses is governed by the distribution of free volume and the sites with higher free volume shows a higher tendency to accommodate local shear [38, 108, 109]. Another feature of deformation through STZs is that this mechanism is dilatational. Specifically, the atomic dilatation not only exists when atoms are overcoming the saddle point configuration but also remains as a semi-permanent increase of free-volume that accumulates locally after the operation of STZ mechanism [83].

Plastic deformation through STZs in metallic glasses involves the evolution of free-volume, which is also commonly observed in another type disordered structure—non-equilibrium grain boundaries—in nanocrystalline metals. Non-equilibrium grain boundaries are characterized by an excess free volume, high potential energy, and disordered atomic structure, etc as compared to equilibrium grain boundaries [110]. To characterize the degree of disorder, the excess free volume of non-equilibrium grain boundaries is commonly measured by summing the extra free volume with respect to the free volume of equilibrium grain boundaries. Due to high energy and extreme atomic misfit characteristics, the excess free volume is related to the most of the deformation behaviors of non-equilibrium grain boundaries, such as grain boundary sliding, atomic shuffling, migrating, and dislocations emitting events [58, 60, 111-114].

However, STZs in the metallic glasses and non-equilibrium grain boundaries deformation in the nanocrystalline metals are essentially disparate. Non-equilibrium grain boundaries are the structural defects in nanocrystalline metals, whereas STZs are not the defects in metallic glasses. Instead, STZs are actually small deformation events, which are characterized by their transient feature. Specifically, the STZs are not observed at a single instant time during the deformation. Rather, they are only captured by inspecting a deformation process from one moment to another moment, accompanied by a change in the free volume distribution [83].

1.2 Amorphous-Crystalline Interfaces in the Deformation of Crystalline-Amorphous Nanolaminates

1.2.1 Interface mediated deformation behaviors in the crystalline-amorphous nanolaminates

One promising route to improving the ductility of nanocrystalline metals is using gradient nanostructures containing, e.g., bimodal nanocrystalline grain size distributions [115] or periodically modulated crystalline-amorphous patterned structures [39]. While amorphous metals also suffer from limited plastic strain prior to fracture as a result of plastic strain localizing to form shear bands [109, 116-119], a number of observations have suggested that the synergistic interaction between dislocation and shear transformation zone (STZ) plasticity across the amorphous-crystalline interface (ACI) can fundamentally alter the mechanical behavior [39, 120-123]. These materials represent a specific subset of metallic multilayers often referred to as crystalline-amorphous nanolaminates, and have demonstrated the sought-after combination of high strength (>1.0 GPa) and improved tensile elongation to failure (>13%) that has eluded equiaxed nanocrystalline metals for over a decade [39, 120, 124-129].

The role of interfaces in fully crystalline metallic nanolaminates have been studied extensively in systems containing coherent [130-132], semi-coherent [133-135], and incoherent [136-138] interfaces, which govern the dislocation physics at the nanoscale. While slip transmission dominates plasticity in nanolaminates containing coherent interfaces [139-141], dislocation mechanisms shift to confined layer

slip in systems with incoherent interfaces [136, 142, 143]. The interfaces in crystalline-amorphous nanolaminates can be classified as a unique type of incoherent interface containing complex intrinsic dislocation structures and compositional gradients [126] that impact strain transfer characteristics [144, 145]. In light of the critical role of grain boundaries played in the deformation physics of nanocrystalline metals, the introduction of incoherent interfaces (i.e. ACIs) can be expected to open up new regimes in the mechanical behavior. In equiaxed nanocrystalline Ni-W alloys, Rupert et al. [146] demonstrated that through manipulation of the interfacial state, defect sources can be limited for enhancing strength without augmenting the fundamental mechanisms accommodating plasticity. It is in this vein that ACIs have been employed to engineer sources and sinks for defects in crystalline-amorphous nanolaminates.

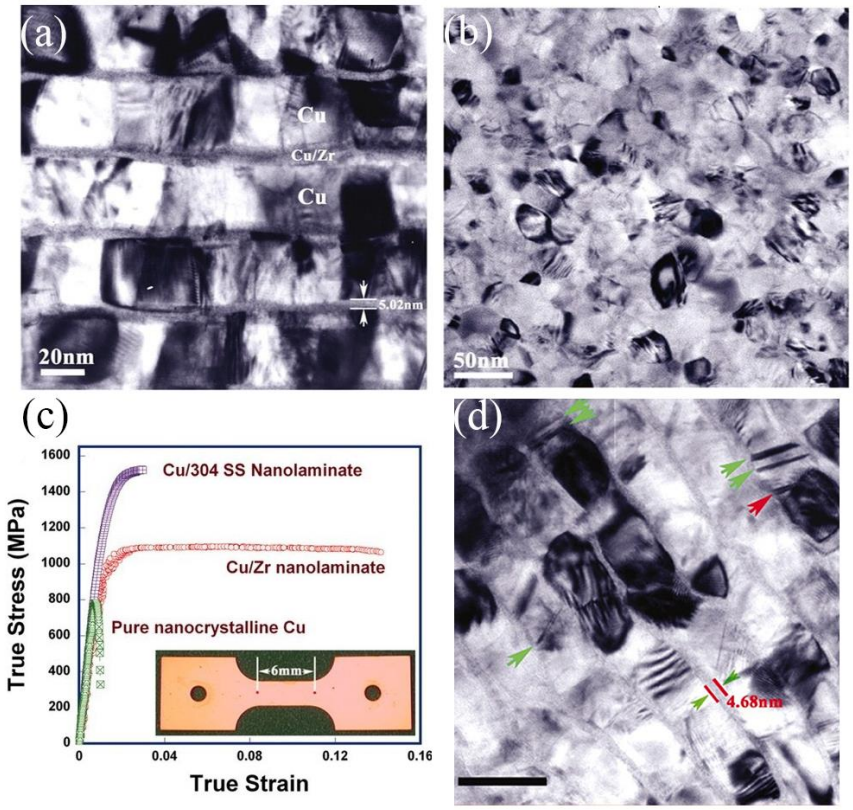

Figure 1.14 Cross-sectional (a) and planar (b) TEM images of as-fabricated 5/35 Cu/Zr nanolaminates. (c) Room-temperature uniaxial tensile stress-strain curves of 5/35 Cu/Zr nanolaminates, Cu/304 stainless steel nanolaminates, and pure nanocrystalline copper. (d) A HRTEM image of 5/35 Cu/Zr nanolaminate after tensile failure. Deformation twins are found in several nanograins (green arrows). Arrows indicate that dislocations tend to terminate at the ACIs (green arrows) or at the grain boundaries (red arrows), implying that ACIs might become the dislocation sources or sinks in nanolaminates structure. Stacking faults are also revealed in HRTEM images. (Reproduced from reference [39])

A pioneering example is found in the Cu-Cu_3Zr system studied by Wang et al.[39]. Using magnetron sputtering deposition, a crystalline-amorphous nanolaminate structure was fabricated by alternatively depositing nanocrystalline Cu layers and amorphous $Cu_{75}Zr_{25}$ layers, which were formed by solid-state amorphization reaction between Cu and Zr atoms. The cross-sectional and planar TEM micrographs, as shown in Fig. 1.19 (a) and (b), indicate that the nanocrystalline Cu layers have an average grain size of 35 nm, which is equal to the nanocrystalline layer thickness while the thickness of amorphous Cu/Zr layers is determined to be approximately 5-10nm. An out-of-plane (111) texture is found in the nanocrystalline layer while the in-plane grain orientations are random. As shown in Fig. 1.14 (c), under uniaxial tensile loading, this nanolaminate structure exhibited exceptional ductility relative to both crystalline metallic multilayers and equiaxed nanocrystalline by showing a tensile elongation up to 13% while retaining a high yield strength of ~1 GPa. The high-resolution TEM (HRTEM) image of crystalline-amorphous nanolaminate after the tensile failure is shown in Fig. 1.13(d), where no heavy dislocation storage or pileup is observed and no evidence of shear banding is presented. However, several dislocation activities are indeed captured in the TEM image, where several partial dislocations are found transecting the nanograins with both ends terminating at the ACIs. These findings suggest an interface mediated deformation mechanism in that the ACIs are involved both in the activation and annihilation of dislocations during the deformation. Further measurements of the activation volume and strain rate sensitivity were consistent with interface-mediated dislocation plasticity [125] suggested by post-mortem TEM observations.

Several additional studies have demonstrated ductility improvements in crystalline-amorphous nanolaminates citing comparisons with equiaxed nanocrystalline metals [129, 147, 148] while others have focused on understanding the implications of the hierarchical structure for limiting shear localization in the amorphous regions [120]. Introduction of the nanocrystalline layers inherently disrupts the continuity of the amorphous phase, which has been demonstrated to constrain shear band growth [149] and promote homogenous plastic flow [150]. Simultaneously, the inherent structural length scale defined by the

thickness of the amorphous layers suppresses the onset of shear instabilities. Citing the aged-rejuvenation-glue-liquid shear band model [151], Wang et al. suggested that shear localization was inhibited when the amorphous layer thickness was less than a critical incubation length scale required for STZs to evolve into a mature shear band [39]. Despite conceptual differences in the synergistic effects of yielding in each phase, a number of studies [152-154] have substantiated the embryonic shear band argument for suppressing shear instabilities in crystalline-amorphous nanolaminates.

Significant insight has been gained on the coupling between dislocation and STZ plasticity through compression and nanoindentation experiments, which facilitate plastic strain accumulation without the onset of early fracture that results from localization in tension. By analyzing the plastic zone beneath the indents via correlative atom probe tomography and TEM, Guo et al. determined that dislocation glide in the crystalline Cu layers coincided with shear banding in the CuZr amorphous layers [122, 123, 155]. Microcompression testing of Cu/CuZr nanolaminates by Zhang et al. [121, 156] revealed that dislocation-free nanocrystalline layers were accompanied by the nucleation of nanocrystallites within the amorphous layers. This deformation-induced partial devitrification was attributed to the transfer of plastic strain upon the absorption of dislocations across the ACI into the amorphous layers. Despite these compelling observations, assessment of the mechanistic coupling between dislocation and STZ plasticity has been largely based on inferences from post-mortem analysis of defects or other local structural changes.

1.2.2 Length scale effect on the mechanical performance of crystalline-amorphous nanolaminates

Even though the vast improvement was attained in Wang et al's [39] crystalline-amorphous nanolaminates, the strength of the nanolaminate was not substantially enhanced. To optimize the strength of nanolaminates, a larger volume fraction of amorphous material (i.e. thicker amorphous layers) have produced Cu-CuZr nanolaminates with strengths approaching 2.5 GPa, but at the expense of ductility as evidenced by the reduced tensile elongation to failure of 4% [154]. Therefore, the co-deformation of the crystalline and amorphous phases thus depends on the microstructural length scales of the nanolaminates

as well as the interactions between dislocation, grain boundary, and STZ plasticity across the amorphous-crystalline interfaces (ACIs). An optimal length scale combination of layer thickness and grain size of the nanocrystalline layer is desired to balance the strength and ductility of nanolaminates.

The implicit dependence of strength and toughness on the critical microstructural length scales of crystalline-amorphous nanolaminates, namely amorphous and crystalline layer thicknesses denoted t_A and t_C, respectively, and grain size, d, has been the focus of nanoindentation and micropillar compression studies [120, 123, 150, 157-160]. Employing layer thickness ratio in categorizing the results, nanolaminates with $t_A/t_C > 1$ generally exhibited fully developed shear bands in the amorphous layers [123, 157, 159-161]. In the extreme case where $t_A \approx 10 \cdot t_C$, a mature shear band propagated through the entire thickness of the nanolaminate where its path aligned with slip bands in the crystalline layers [122, 123, 155, 157]. Conversely, nanolaminates with $t_A/t_C \leq 1$ exhibited signatures of ACI-mediated dislocation plasticity without the formation of a dominant shear front [150, 153, 158-161]. Employing a constant layer thickness ratio of $t_A/t_C = 1$, Zhang et al. [120] explored the intrinsic size effects in nanolaminates containing layer thicknesses, t, of 5 – 150 nm. A critical transition length scale of t = 10 nm was identified through micropillar compression testing where deformation shifted from localized shear banding for t < 10 nm to homogenous flow at t > 10 nm. The appearance of this crossover was attributed to the onset of ACI-mediated dislocation plasticity for thicknesses greater than 10 nm and thus consistent with the physics uncovered through a number of molecular dynamics (MD) studies [39, 145, 162, 163]. In addition, shear band propagation was confined by the nanocrystalline layers at these length scales [153] albeit with a caveat relating to geometric stress concentrations under compressive loading.

While nanoindentation and microcompression testing of crystalline-amorphous nanolaminates have provided significant insight into the role of microstructural length scales on the mechanisms accommodating plastic strain, tensile testing is ultimately required to map their strength-ductility envelope and widely accomplished in the Cu-CuZr system. In nanolaminates dominated by amorphous material (i.e. $t_A/t_C > 1$), the crystalline layers have been demonstrated to suppress catastrophic shear

localization commonplace in metallic glasses albeit with little impact on ductility as evidenced by a maximum of 4% strain to failure [154, 164]. The tensile behavior of crystalline-rich nanolaminates ($t_A/t_C \leq 1$) has been explored more extensively with a range of studies consistently revealing yield strengths exceeding rule-of-mixtures predictions and no evidence of failure through shear localization [39, 129, 147, 152, 165, 166]. However, despite the microstructural similarities of the nanolaminates, only a small subset of samples have reported appreciable ductility, which was attributed to ACI-mediated dislocation activity as confirmed through post-mortem TEM observations and MD simulations [39]. The plastic strain to failure was otherwise limited to < 4%, although dimpled fracture surfaces indicative of a ductile failure mechanism was observed on a number of the samples [152, 164].

1.2.3 New insight into the mechanical behaviors of crystalline-amorphous nanolaminates from atomistic simulations.

Given the challenges in bridging measured properties to the underlying deformation mechanisms, atomistic simulations have been an essential component in understanding the unique mechanical behavior of crystalline-amorphous nanolaminates. The role of ACIs in dislocation and STZ plasticity was first uncovered through an elegant single crystal-amorphous nanolaminate model built by Wang et al [39]. As shown in Fig. 1.15 (a) and (b), the partial dislocation was indeed initiated at the lower ACI and subsequently absorbed by the opposite ACI during the simulated tensile deformation of nanolaminates. The accommodation of partial dislocations in the upper ACI triggered STZs characterized by clusters of structurally disordered atoms with high Von Mises strain as illustrated in Fig. 1.15 (c). This kind of heterogeneous initialization of STZs resulted in a chain reaction in the nearby region, where more STZs were activated and diffused deep into the amorphous layer shown in Fig. 1.15 (d). The ACI sliding was also captured in Fig. 1.15 (d) as a result of stress concentration relief due to the dislocation activation. The authors argued that the omnidirectional property of STZs in the amorphous layer is able to accommodate infinite selections of possible plastic shear strain, whereas grain boundaries and crystalline-crystalline interfaces (CCI) are limited by the crystallographic incompatibility, which is believed to promote the

formation of nanocracks and nanovoids. Based on these findings, the ACIs can be regarded as natural sources and sinks of dislocations and lead to the effective transfer of shear strain through the nanolaminate structure.

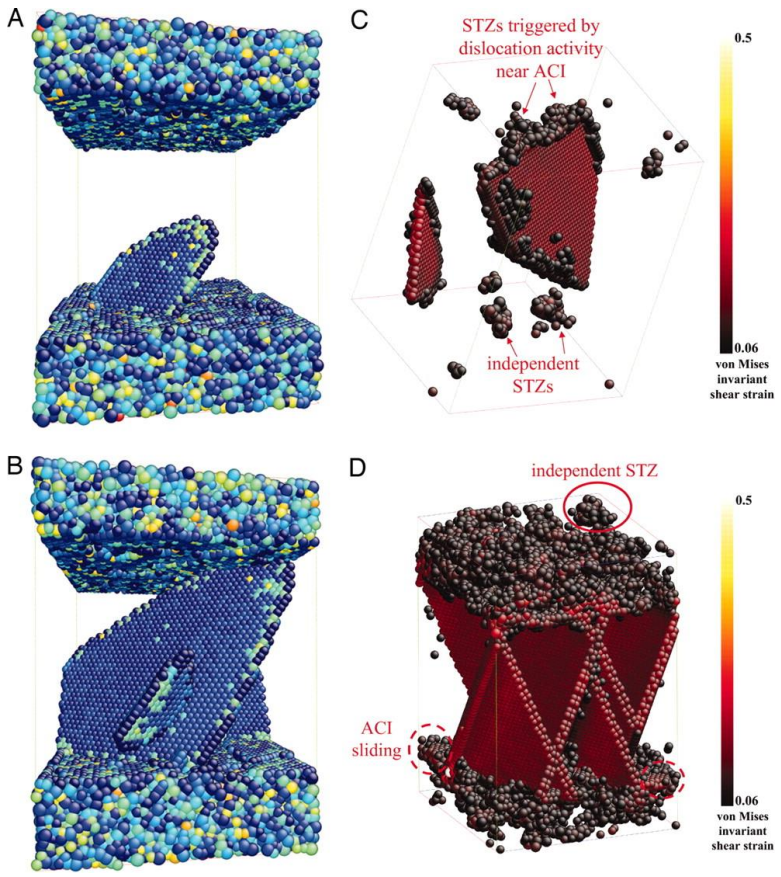

Figure 1.15 Molecular dynamic simulation of 5/10 Cu/Zr nanolaminate (10×15×10 nm in dimension) with periodic boundary condition. (a) A dislocation is nucleated at the lower ACI, where atoms are colored by central symmetry parameter and FCC atoms are not shown. (b) The dislocation nucleated from lower ACI is being absorbed by upper ACI and another dislocation nucleated from lower ACI is intersecting with former nucleated dislocation. (c) Activations of STZs near the ACI triggered by the incoming partial dislocations. The atoms are colored by inelastic shear strain and atoms with a shear strain less than 0.06 are not shown. (d) Distribution of inelastic shear strain after absorption of partial dislocations. The ACI sliding is shown on the lower right and upper left corners of lower ACI. (Reproduced from reference [39])

The interaction of dislocation and STZ across the ACI was further substantiated in the simulations by Pan and Rupert [163] on bicrystals containing amorphous intergranular films, which acted as efficient sinks for dislocations that delayed the onset of interfacial cracking relative to “clean” grain boundaries. Brandl et al. [126] explored Cu-CuZr crystalline-amorphous nanolaminates comparable to the previously described simulation structures under shear deformation boundary conditions. Interfacial shear

was accommodated by the emission and propagation of dislocations at the ACI, in turn facilitating co-deformation of the nanolaminate phases. Interfacial sliding has also been connected to localized STZ plasticity acting in cooperation with dislocation motion by Chen et al. [145]. Mechanistic transitions were also explored through systematic variations of the single crystal layer thickness, which demonstrated that the dominant deformation mode shifted from shear banding in the amorphous layer to co-deformation accommodated by STZ and dislocation plasticity with increasing crystalline layer thickness [161]. Finally, the addition of free surfaces under simulated compressive loading by Arman et al. [162] revealed that dislocations, particularly of screw orientation, nucleated from the free surfaces but were subsequently absorbed in the ACIs and shear bands in the amorphous layer were observed to align with the resulting dislocation slip bands.

1.3 Glass-glass Interfaces in the Deformation of Metallic Nanoglasses

1.3.1 Intriguing properties of glass-glass interfaces in the metallic nanoglasses

Nanostructured metallic glasses with a large fraction of glass-glass interfaces (GGI) incorporated are termed nanoglass (NG) by Gleiter [40, 167, 168], which represents a new class of non-crystalline solids. As illustrated in Fig. 1.16, in analogy to nanocrystalline materials, nanoglasses consist of nanometer-sized glassy regions connected by glass-glass interfaces with enhanced free volume [40]. Due to structural inhomogeneity at interfaces, nanoglasses present improved mechanical performance [42, 168], enhanced magnetic properties [169, 170], and structural ultrastability [99, 171] comparing to homogeneous metallic glasses. The synthesis of nanoglasses was first realized using the inert-gas condensation (IGC) by Jing et al [172], where nanometer-sized glassy clusters condensed from the evaporated materials in the inert gas environment were consolidated at a pressure of up to 5 GPa. In addition to IGC, magnetron sputtering [41, 173], pulsed electrodeposition [174], and severe plastic deformation [97, 175] have been developed for the production of nanoglasses, making it accessible for researchers to probe the unique structural and properties of nanoglasses.

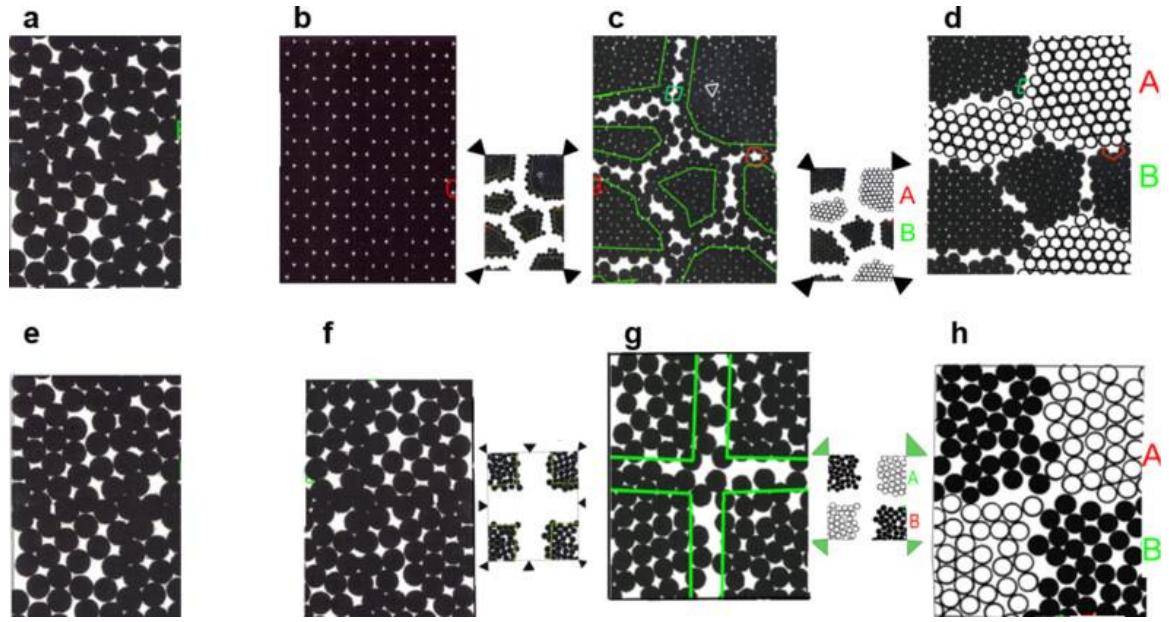

Figure 1.16 Comparison of nanocrystalline materials and nanoglasses' defect and chemical microstructures. (a) Melt of pure element. (b) single crystal. Analogy between the planar defects (a) and chemical (d) microstructures of nanocrystalline materials and their counterparts of nanoglasses depicted in (g) and (h), respectively. The amorphous structure displayed in (f) is generated by quenching the melt depicted in (e). (Reproduced from the reference [40])

The structural characterization of nanoglasses has been focused on capturing the physical presence of glass-glass interfaces, which generally exhibit a reduction in density and nearest-neighbor atoms [40]. Using positron annihilation spectroscopy and small angle X-ray diffraction, Fang et al. [99] demonstrated that as-prepared $Sc_{75}Fe_{25}$ nanoglass synthesized by IGC was composed of 65 vol% glassy and 35 vol% interface regions and the corresponding interface width was identified as 0.8nm. The annealing of as-prepared nanoglass samples can increase the interface volume up to 44 vol% and interface width up to 1.2 nm. However, an increase of density in the interface region was also observed as the sample volume augment suggesting a delocalization of the excess free volume. Chen et al. [41] performed a structural analysis on the magnetron sputtered Au-based nanoglass with grain sizes ranging from 21 to 29nm. As displayed in Fig. 1.17, TEM bright field images suggest the existence of light contrast GGIs with a typical width of 2~3nm between the high contrast amorphous grains. The authors attributed the contrast difference of interface and grain regions in TEM image to the density difference in the

nanoglasses. Synchrotron radiation of nanoglass results reported by Ghafari et al. [176] suggests a change in the short- and intermediate-range order of nanoglasses as comparing to the rapidly quenched metallic glasses and a reduction of the first-nearest neighbor coordination in nanoglasses.

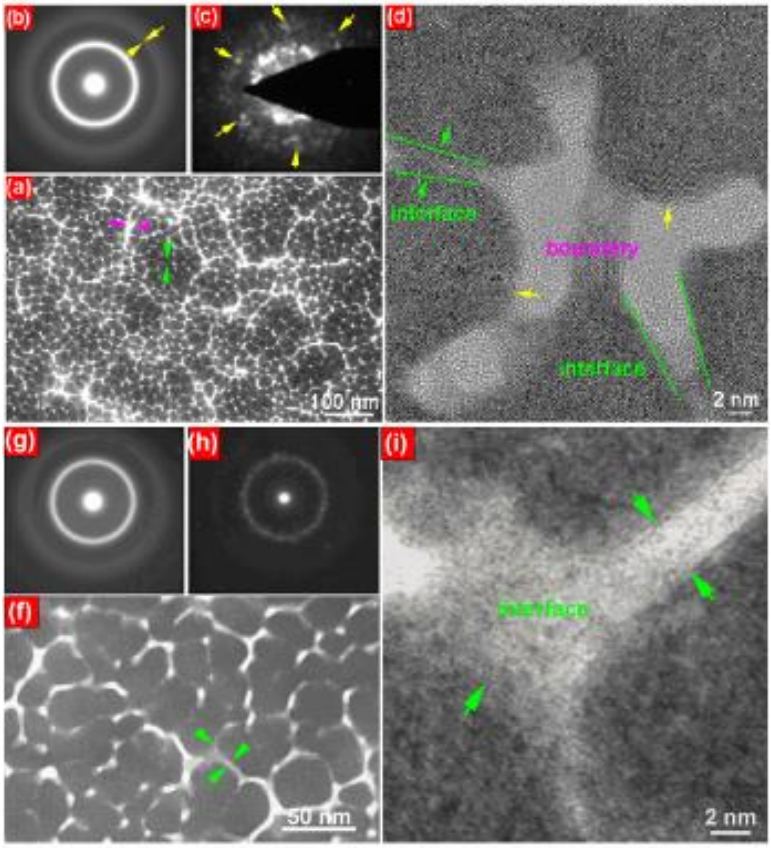

Figure 1.17 Bright-field TEM images of Au-based nanograined metallic glasses sample 1 with an average grain size of 21nm (a) and sample 2 with a mean grain size of 29nm (b); Selected area electron diffraction patterns of sample 1 (b) and sample 2 (c); 3 nm probe size nanobeam diffraction patterns of sample 1 (c) and sample 2 (h); High-resolution TEM image of the glass-glass interface between particles in the sample 1 (d) and sample 2 (i). (Reproduced from reference [41])

The ultrastability of nanoglasses has been reported by several works [41, 99, 171, 177, 178], suggesting that GGIs can stabilize nanoglasses against structural change at elevated temperatures. By applying the different heating rate to nanoglass during a differential scanning calorimetry measurement, Wang et al. [171] reported that nanoglasses show an ultrastable kinetic characteristic at a lower heating rate and similar kinetic behavior as the melt-spun ribbon at a high heating rate. Franke et al. [177] measured the thermal expansion of nanoglasses during the heating and cooling process and disclosed the partially lost and redistribution of excess free volume, which was initially dominating in the GGIs. Fang

et al. [99] observed similar results of excess free volume delocalization in annealed nanoglass and reported an increase in the interfacial volume. Annealing of nanoglass may reduce the excess free volume in the GGI but it is unable to completely remove the structural inhomogeneity introduced by GGIs, making it possible for the researcher to exam the mechanical behavior of nanoglasses after thermal relaxation. Most of the annealed nanoglasses indicate an increase in the strength [99], which can be linked to the structural homogenizing process. The reduction of excess free volume during this process could increase the difficulty for shear band initiation but is not able to inhibit the deformation of nanoglasses through multiple shear bands. However, when the annealing temperature is above the glass transition temperature, the mechanical performance of nanoglass is more like a melt-spun ribbon fashion [177].

The mechanical behaviors of nanoglasses are substantially affected by the glass-glass interface in the structure. Because of the presence of relatively low density of GGIs, the mechanical testing of nanoglasses indicates a lower strength when comparing to the monolithic metallic glasses [42, 99]. However, the enhancement of plasticity in the nanoglasses is significant. Wang et al. [42] employed nanoindentation, in situ compression tests, and tensile testing within the TEM to systematically assess the plasticity of a scandium-based nanoglass and shows a promising improvement in term of tensile ductility. The load-depth curves of nanoglass from nanoindentation testing revealed the absence of discrete bursts of rapid displacement, which is usually a signal of shear band nucleation and propagation in amorphous solids [179], compared to monolithic metallic glass. The in situ compression test demonstrated that the nanoglass can withstand plastic strain up to 43% while maintaining a substantial flow stress, whereas the metallic glass failed shortly after the elastic limit through catastrophic shear banding. An even astounding result shown in Fig. 1.18 was observed via in situ tensile testing of the nanoglass, which exhibits a total plastic strain ~15% under the tensile loading. As shown in Fig. 1.18 (e), a necking behavior of the gauge length was captured suggesting the inherent ductile feature of nanoglasses. Wang attributed the observation of excellent plasticity exhibited by the nanoglass to the formation of numerous small shear bands facilitated by GGIs, which distributed the shear strain and prevented severe shear localization. The

following work by Wang et al. [168] also discloses that the mechanical behavior of nanoglasses is sample size independent while the deformation in the metallic glasses strongly depends on sample size.

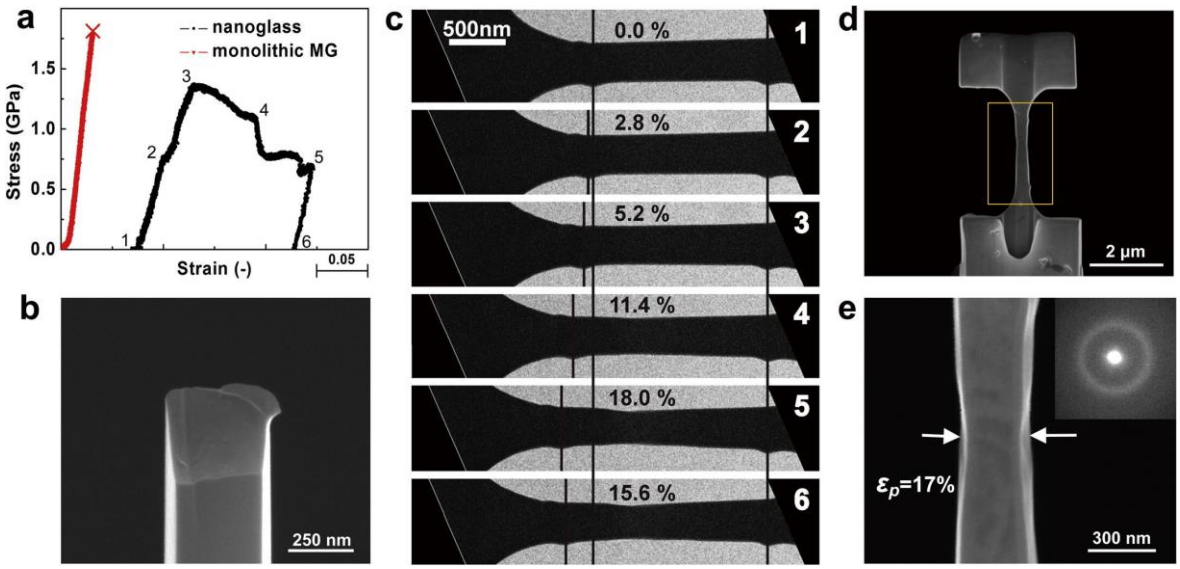

Figure 1.18 (a) Uniaxial tensile stress-strain curves of a scandium-based nanoglass and monolithic metallic glass; (b) The fracture surface of deformed metallic glass after failure. (c) The deformation snapshots during in situ tensile testing of the nanoglass from 0% to 15.6% strain. (d) Tensile deformed nanoglass sample; (e) Enlarged view of the gauge region of deformed nanoglass sample at the plastic strain of 17%, where tensile necking is evident. Inset of (e) is the corresponding selected-area diffraction pattern. (Reproduced from reference [42])

1.3.2 Unveiling the unique properties of glass-glass interfaces from an atomistic simulation perspective

With the difficulty of direct observation of GGI's characteristics via experimental methods, computational models provide a convenient way to study GGIs at an atomic resolution. Several atomistic models have been developed to unveil the unique properties of GGIs, starting with the simplest bicrystal-like nanoglasses models. By joining two planar relaxed glass-glass surfaces, as shown in Fig. 1.19, a bicrystal-like $Cu_{64}Zr_{36}$ nanoglasses set-up was generated by Ritter. et al [43]. Structural characterizations of the ~1nm thick GGI region indicate an excess free volume of 1-2% in terms of an increase of interface atomic Voronoi volume, a non-equilibrium state in terms of an enhanced potential energy, and a defective short-range order in terms of a decrease of Cu-centered full icosahedra (FI) fraction, which is the backbone polyhedra for the high strength in Cu-Zr metallic glass system. Under tensile loading, softer GGIs acted as the precursors of shear band formation, which lowered the yield stress of the whole

structure. All of the above-mentioned simulation results suggest that the GGIs in nanoglasses is essentially similar to the shear band in the deformed homogenous metallic glasses, structurally and mechanically. Structural analysis of a bicrystal-like nanoglass model built by Adibi et al. [180] discloses that the interfacial excess free volume and defective FI fraction are more prominent in the Cu-Zr nanoglasses with higher Cu fraction and the estimation of interfacial width decreased from 1.67 to 1.38 nm.

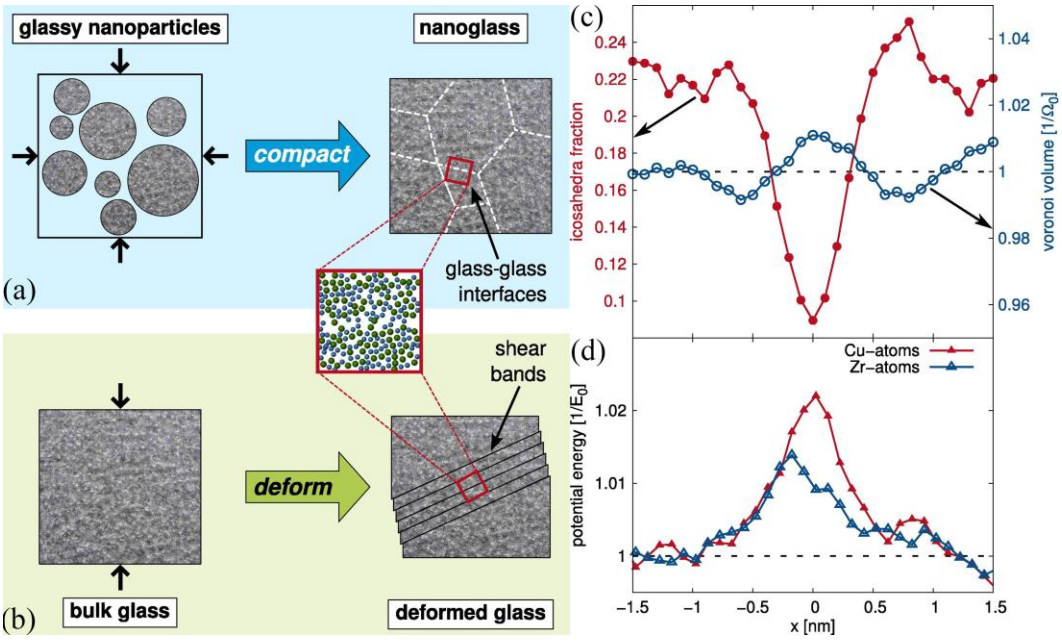

Figure 1.19 Schematic procedures of introducing glass-glass interfaces into the amorphous matrix by (a) either consolidation of glassy powders or (b) pre-plastic deformation of bulk metallic glass. In both cases, the glass-glass interfaces are characterized by (c) an increase in Voronoi volume, defective short-range order (low fraction of Cu-centered full icosahedra), and (d) an enhancement in the potential energy. (Reproduced from reference [43])

In aligning with experiments, the stability of nanoglasses has attracted a number of simulation studies for capturing the structural homogenizing process at elevated temperatures. Ritter et al. [43] carried out a simulated annealing of the bicrystal-like nanoglass model at temperatures up to 800K, which is at 85% of the transformation temperature T_g of the dense glass. Surprisingly, the GGIs can be stable at this high temperature despite a significant recovery of short-range order (FI) at the interface region, but the structural difference between interface and bulk regions still exists. To assess the density or atomic volume change during a simulated annealing, two nanoglasses generated from consolidated glassy

nanoparticles by Soqu et al. [181] were relaxed at high temperatures. The results show that the nanoglass with monolithic Ge composition was able to maintain its interfacial low-density feature up to 500K for an extended time while the binary Cu-Zr nanoglasses system lost its low-density GGIs and homogenized for a short relaxation at 300K.

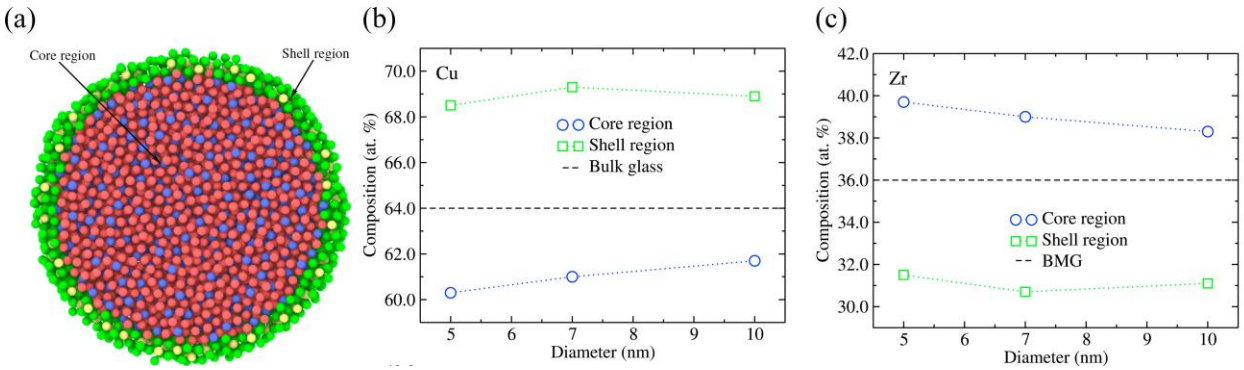

Figure 1.20 (a) Core-hell model of a Pd-Si glassy sphere with a grain size of 7nm after simulated annealing above the glass transition temperature. Atoms colored by green and yellow are located in the shell region with a width of ~0.5nm. Red and blue atoms are Pd and Si atoms, respectively, which are located in the core region. The compositions of Cu (b) and Zr (c) atoms in the core and shell regions are plotted as a function of Cu-Zr amorphous sphere's diameter. The dashed line is the center of (b) and (c) is the global composition of the amorphous spheres. (Reproduce from reference [44])

Surface segregation studies of binary nanoglasses with a core-shell structure as illustrated in Fig. 1.20 (a) by Adjaoud et al. [44] demonstrated that the core enrichment and surface depletion of high potential energy elements in the binary system after annealing can optimize the binding energy in the system. In the Cu-Zr system, the Zr atoms with higher cohesive energy were segregated to the core and Cu atoms were thus enriched in the interface region as depicted by Fig. 1.20 (b) and (c). Because of the higher population of smaller Cu atoms in the surface, the relative number density in the interface of the segregated sample is slightly higher than the bulk region, which might explain Soqu et al.'s [181] observation of a density homogenization process in the Cu-Zr system upon annealing. Another core-shell nanoglass model consolidated from nanoparticles condensed during a physical vapor deposition process by Danilov et al. [178] reveals a similar result that a different energy landscape and segregation phenomenon in interfacial regions were attained comparing to the melt-quenched metallic glass and stabilized the nanoglass structure against phase transitions during the heating process.

The interfacial defect, length scales, chemical compositions and annealing states have become pivots of nanoglass mechanical simulations, where two Cu-Zr nanoglass models were built for simulated mechanical testing of nanoglasses. One is idealized columnar grains with a hexagonal cross-section prepared by Soqu et al. [182] by consolidating glassy nanoparticles cut from a simulated quenched BMG. Another computational model generated by Adibi et al. [180] was constructed by applying Poisson-Voronoi tessellation to the quenching generated metallic glasses slab or nanopillar, where random position shifts of atoms were performed within each Voronoi cell followed by a pressure consolidation to eliminate voids. As shown in Fig. 1.21, both models demonstrated that catastrophic failure via single shear banding in the BMG under uniaxial loading can be suppressed by introducing GGIs into the metallic glasses matrix [180, 182], where the defective short-range order and excess free volume features enabled the interfaces region to accommodate most of the initial shear strain and promote multiple shear bands formation in nanoglasses [182]. However, the augment of grain size may cause nanoglasses to lose their improved plasticity, as there exists a certain grain size where the deformation transforms from homogenous plastic flow to localized shear banding. In the columnar nanoglass model, the critical grain size is 10nm, whereas in the Voronoi partitioned columnar nanoglass this grain size decreases to 5nm [45, 183]. Adibi et al [180] rationalized this observation by arguing that the estimated interface atom fraction decreases with the increase of grain size by assuming a constant interface width of 1.38nm and the single shear band cannot be avoided if there are not enough interfaces for inducing interfacial plasticity. As a consequence, the extremely fine grain size (<5nm) is necessary for achieving superior plasticity.

Interestingly, the following study by Adibi et al. [184] suggests an observation of ductile tensile deformation and failure through necking instability in Cu-Zr nanoglasses pillars with a grain size up to 20nm. The absence of shear instability in the large grain size NG nanopillars was attributed to the 3D Voronoi NG nanopillars configuration, where the fraction of interfacial materials was enhanced and shear band propagation was constrained by the excellent GGI connectivity in 3D Voronoi configuration as compared to 2D columnar structures. The influence of the chemical composition of nanoglasses has also

been probed by Adibi et al. [180] and Soqu et al. [45] in Cu-rich and Zr-rich Cu-Zr nanoglasses. The effect of GGIs on mechanical performance was found to be more prevalent in the Cu-rich nanoglasses since the topological disorder is obvious when more Cu atoms are present [45]. The strength of nanoglasses was found to scale with the fraction of Cu atoms, which is also related to the concentration of short-range order (FI) in the nanoglass samples [180]. Despite the substantially improved plasticity induced by the defective GGI in the nanoglasses, it also weakens the strength of the original metallic glasses matrix [45, 183]. To enhance the strength of nanoglasses, simulated annealing was performed to the as-consolidated nanoglasses and the enhancement of strength is evident [45, 182]. Using the bicrystal-like model, Ritter and Soqu show that it is the delocalization of excess free volume and recovery of short-range order in the interfaces that account for this strength enhancement. However, the single shear band failure during the deformation simulation is once again seen in the annealed nanoglass samples [182].

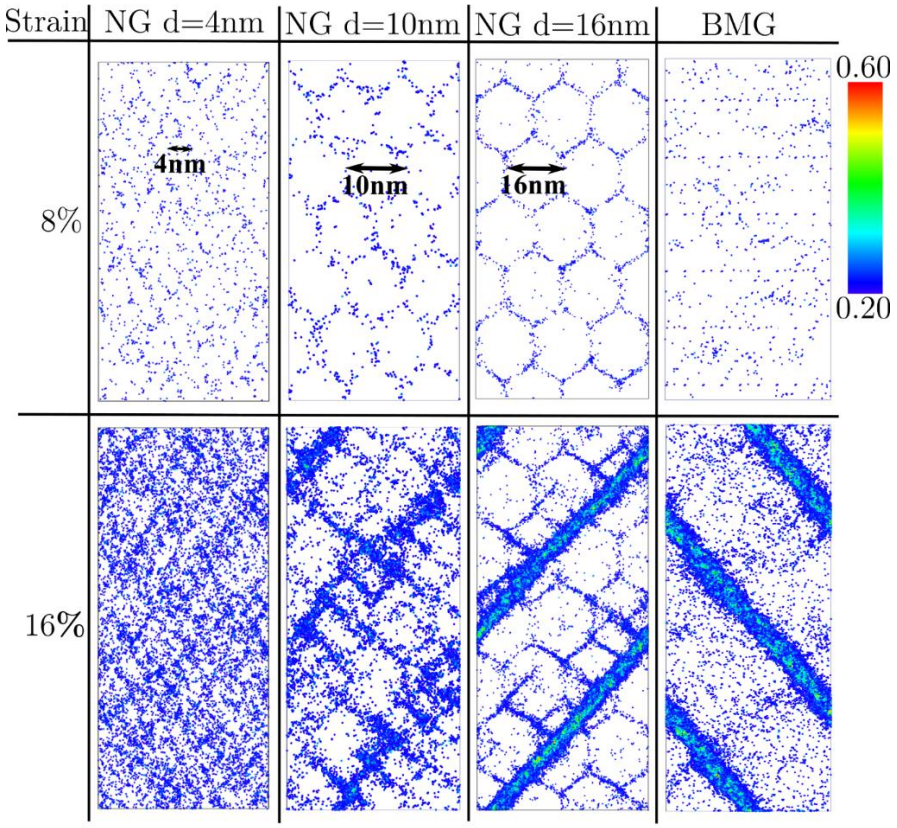

Figure 1.21 Deformation snapshots of a $Cu_{64}Zr_{36}$ bulk metallic glass and nanoglasses with grain sizes of 4, 10, and 16nm, respectively. Atoms are colored by local atomic shear strain. (Reproduced from reference [45])

1.4 Problem Statements

The coupling between dislocation and STZ plasticity at the ACIs in crystalline-amorphous nanolaminates provides a new mechanism for accommodating plastic strain during deformation. While several pioneering experiments have demonstrated the unique combination of strength and ductility afforded by the co-deformation of the crystalline and amorphous phases, mechanistic insights have largely been inferred from post-mortem deformation structures. Molecular dynamics simulations have been successful in capturing transient coupling events between the disparate deformation mechanisms operating at the ACIs. Despite these perceptive results, a number of open questions must be addressed to bridge the deformation physics from simulations with experimental mechanical behavior measurements. Perhaps one of the most important issues is that the existing computational models employ single crystal orientations completely absent of grain boundaries, which represent a critical feature in the deformation of nanostructured metals. How will grain boundaries bias the onset of dislocation and STZ plasticity in the respective regions of the nanolaminate, and what are their implications for the interfacial deformation physics? With a better understanding of the synergistic interactions between grain boundaries, ACIs, and the mechanisms accommodating plastic strain at the nanoscale, nanolaminate architectures can be designed to expand the strength-ductility envelope in nanostructured metals.

The size effect of crystalline-amorphous nanolaminate also stimulated numerous studies based on both experimental or computational approaches. However, substantial limitations are inherent in these studies. There is no denying that nanoindentation and micropillar compression provide a convenient way for comprehensively studying the strength and plasticity of nanolaminates. Nevertheless, it is not a proper method of addressing the ductility of nanolaminates, which is the key mechanical properties of materials under tensile loading; For uniaxial tensile tests, the sample preparation is considerably difficult as the processing introduced defects will fast failure the materials and hinder the revealing of nanolaminates' intrinsic ductility. Atomistic simulations enable an alternative approach to studying the defect-free nanolaminates sample, but most of the literature employed a single crystalline nanolaminate model with

no grain boundaries and only focused on the STZ-dislocation coupling mechanics. The systematic study of microstructural length scale effects to the mechanical properties of nanolaminates is lacking.

The experimental synthesis of crystalline-amorphous nanolaminates has largely relied on the magnetron sputtering. Despite the high-quality films the sputter can obtain, they are substantially limited by the relatively low deposition rate and high cost, which constrain the wide application of the nanolaminates as a practical engineering material. In addition, a strong tendency of (111) texture during magnetron sputtering deposition is frequently observed. As discussed above, the reversing pulsing electrodeposition has the capability of synthesizing the Ni-W nanocrystalline alloys with a grain size spanning from hundreds to a couple of nanometers, which is close to the amorphous limit [34]. The nanoindentation work performed by Trelewicz and Schuh [35] demonstrated the glass-like deformation behaviors of Ni-W nanocrystalline alloys at the finest grain size. Therefore, is it possible to produce the grain size modulated Ni-W nanolaminates that consist of glass-like layers with the finest grain size and nanocrystalline layers? Since the nanocrystalline Ni-W layers prepared by electrodeposition are characterized by an equiaxed grain structure, what is the mechanical behavior of grain size modulated nanolaminates with equiaxed nanocrystalline layers compared to the sputtering deposited textured nanolaminate? The excellent maneuverability of reverse pulsing electrodeposition enables the precise control of grain size and thickness of individual layers, which make it possible to explore the effect of length scales to the deformation of grain size modulated Ni-W nanolaminates. At last, the relatively low cost and fast production attributes of reversing pulsing electrodeposition may facilitate the large production of this novel metallic nanostructure, which can be used in the practical engineering applications.

While existing atomistic simulations have provided useful insight into the intriguing properties of GGIs in the nanoglass, the defective characteristics of interfaces captured in these models are primarily derived from bicrystal-like GGI models and the estimation of interfacial volume fraction was based on a constant planar interfacial width. Is the observation made from this bicrystal-like or planar GGI model an

adequate representative of real interfaces obtained via inert gas condensation or magnetron sputtering experiments? Is there a way to directly estimate the interfacial volume and width of nanoglasses consolidated from glassy metallic glasses spheres? Experimental mechanical testing of nanoglasses revealed excellent plasticity in the form of a multiple shear bands accommodation mechanism instead of a catastrophic single shear banding failure. However, controversy remains among the simulated mechanical testing nanoglasses with 2D columnar or 3D Voronoi-celled configurations regarding of the grain size effect on the mechanical performance. Existing computational models may not well resemble nanoglasses obtained through IGC process and plague the unique deformation behavior of nanoglasses. What is the mechanical response of nanoglasses that are generated via consolidation of nanoparticles with varying grain sizes? How do the interfacial characteristics relate to the mechanical behavior of consolidated 3D nanoglasses? Annealing processes were proven to be viable for enhancing the strength of as-prepared nanoglass by several experimental and computational studies. Nevertheless, the systematic study with respect to the influence of annealing on the mechanical performance of nanoglasses is still lacking. How do the interfacial factors determine the strength and plasticity of nanoglasses under different annealing states?

The knowledge gaps mentioned above exhibit a number of opportunities for fundamental scientific research of interface mediated deformation behaviors in the crystalline-amorphous nanolaminates and metallic nanoglasses, and the central goals of this dissertation study are to

(i) elucidate the STZ-dislocation coupled deformation behaviors and the mechanism for the vast ductility improvement in a novel crystalline-amorphous nanolaminate model that emulates the experimental attainable nanolaminate structures.

(ii) systematically study the microstructural length scales effect to the deformation mechanisms of the crystalline-amorphous nanolaminates with respect to the strength and plasticity and develop a mechanics driven design principle for optimizing the mechanical performance of the nanolaminates.

(iii) synthesize grain size modulated Ni-W nanolaminates with equiaxed nanocrystalline grain structure using the reverse pulsing electrodeposition method, and probe into the effect of layer thickness ratio to the deformation behaviors of nanolaminates using nanoindentation and strain rate sensitivity testing.

(iv) develop a novel method for isolating the interface region in computational nanoglass models consolidated from glassy nanoparticles and characterize the interface properties with regarding the volume fraction, width, excess free volume, and short-range order.

(v) comprehensively investigate the grain size and annealing state's effect on the deformation behaviors of 3D sphere-consolidated nanoglasses with the help of a newly developed interface characterization method.

The following five chapters of this dissertation are arranged in a way that each chapter addresses one goal of this dissertation in a sequential order.

Chapter 2 Mechanistic Coupling of Dislocation and Shear Transformation Zone Plasticity in Crystalline-Amorphous Nanolaminates

In this chapter, a new crystalline-amorphous nanolaminate model is constructed that incorporates grain boundaries through the addition of columnar nanocrystalline grains in the crystalline layers to more closely resemble experimentally accessible nanolaminate structures. Uniaxial tensile deformation is accomplished using molecular dynamics with a strain rate of 10^8 s^{-1}, and the strain distribution among competing mechanisms is quantified via continuum deformation metrics. Our results demonstrate that STZ activity at the ACI is influenced by the presence of grain boundaries and responsible for the emission of interfacial dislocations, which are absorbed collectively by grain boundaries and the amorphous layers through continued deformation. Dislocation annihilation at the ACIs combined with a reduction in grain boundary plasticity abates grain boundary microcracking, thus providing an explanation for the exceptional ductility exhibited by crystalline-amorphous nanolaminates relative to equiaxed nanocrystalline counterparts.

2.1 Simulation Procedures

Molecular dynamics (MD) simulations were carried out using the Large-scale Atomic/Molecular Massively Parallel Simulator (LAMMPS) platform [185]. The embedded-atom method (EAM) potential developed by Mendelev et al. [186] for the Cu-Zr binary system was employed, as it provides a good representation for both Cu-Zr metallic glasses [186] and pure crystalline Cu [187]. To build the various nanolaminate configurations, a $Cu_{64}Zr_{36}$ amorphous alloy was generated by heating a single crystal Cu-Zr alloy to 2000 K for 2 ns, followed by quenching to 300 K at a cooling rate of 0.01 $K \cdot ps^{-1}$. The single crystal-amorphous nanolaminate (SC-NL) was then constructed by combining a 5 nm-thick layer of the quenched $Cu_{64}Zr_{36}$ amorphous alloy with a 10 nm-thick single crystal Cu layer oriented with the $[11\bar{2}]$, $[110]$, and $[111]$ directions along the x, y and z directions, respectively. The application of periodic boundary conditions and homogenous structure effectively resulted in this configuration requiring only

11,930 atoms to model a 5/10 (i.e. a 5 nm-thick amorphous layer and 10 nm-thick crystalline layers) single crystal-amorphous nanolaminate. The SC-NL is illustrated in Fig. 2.1(a), and is comparable to the structure studied by Wang et al. [39].

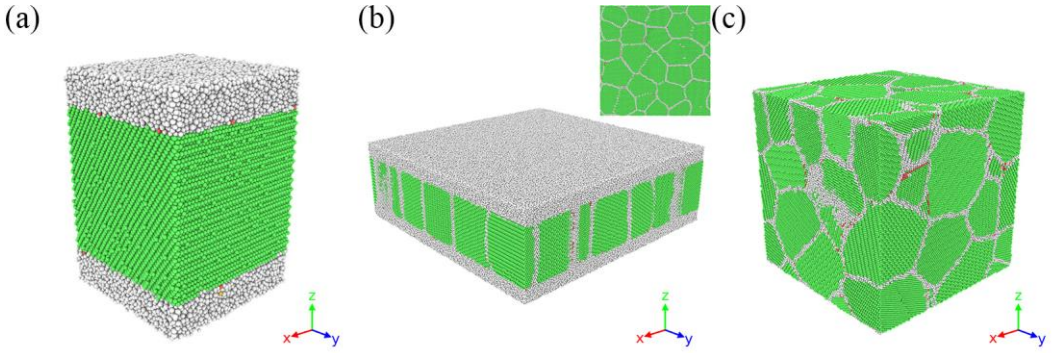

Figure 2.1 Initial nanolaminate structures consisting of 5 nm-thick $Cu_{64}Zr_{36}$ amorphous layers combined with (a) 10 nm-thick single crystal Cu layers with the $[11\bar{2}]$, [110] and [111] directions along the x, y and z directions, respectively, and (b) 10 nm-thick columnar nanocrystalline Cu layers containing equiaxed grains in the x-y plane as shown in the inset with an average size of 10 nm. (c) The equiaxed nanocrystalline structure containing 25 grains with a volume-averaged mean grain size of 11.4 nm to match the CN-NL structure. All the atoms are colored by CNA value.

A second crystalline-amorphous nanolaminate configuration was constructed for this study where columnar nanocrystalline grains were introduced into the crystalline layer, as shown in Fig. 2.1(b). This columnar nanocrystal-amorphous nanolaminate (CN-NL) structure is a better representation of experimentally attainable nanolaminates that contain grain boundaries in the crystalline layers and employed the same 5/10 configuration as the SC-NL. A plan view of the 10 nm-thick columnar nanocrystalline layer is illustrated in the inset of Fig. 2.1(b), where the 10 nm in-plane grain size was achieved by applying a Voronoi tessellation method [188] in the x-y plane only; in the z-direction, the grains were constructed to produce a 10 nm-thick columnar structure that terminates at the ACI. As demonstrated by the initial grain size distribution in Fig. 2.2(a), the Voronoi structure contained a number of both large (> 20 nm) and small (< 5 nm) grains relative to the average grain size. To sharpen the grain size distribution and eliminate outlying grain sizes, a Monte Carlo algorithm was applied to achieve a minimum grain size of 5 nm and a larger frequency of grains near the mean grain size of 10 nm; this optimized distribution is also depicted in Fig. 2.2(a), and exhibited a volume-averaged grain size of 11.4 nm.

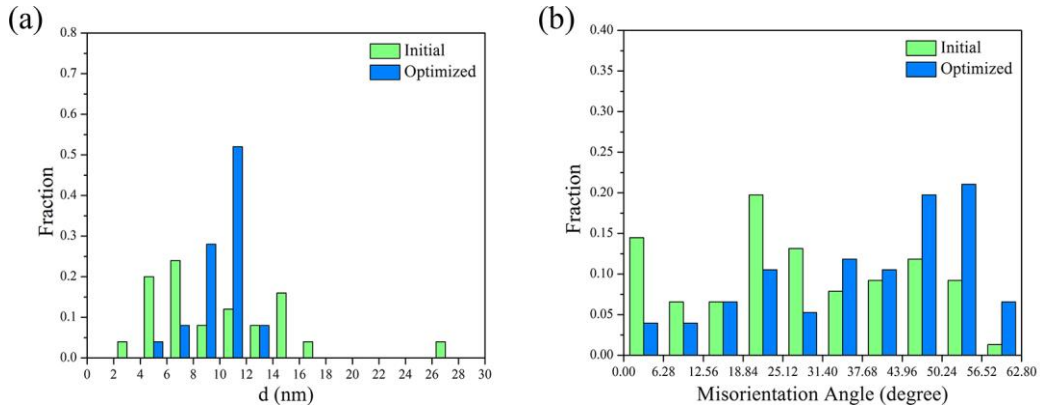

Figure 2.2 Structural characteristics of the CN-NL sample including the (a) grain size and (b) misorientation distributions for both the initial and optimized configurations. The optimized structures were achieved through a Monte Carlo procedure to sharpen the grain size distribution and maximize the average misorientation angle.

The initial misorientation distribution in the x-y plane of the CN-NL structure also contained a large number of low-angle misorientations (<14º) as depicted in Fig. 2.2(b), which will undergo grain coalescence via grain boundary migration [189] resulting in an increase in the mean grain size. To eliminate these mobile low-angle grain boundaries, a second Monte Carlo algorithm was applied to the CN-NL structure to maximize the average misorientation angle from 27.91º to 38.04º while simultaneously reducing the number of low-angle grain boundaries (cf. Fig. 2.2(b)). A total of 25 grains was used in the construction of the columnar nanocrystalline layer, and when combined with the $Cu_{64}Zr_{36}$ amorphous layer, the optimized 5/10 CN-NL structure contained a total of 2,211,972 atoms for a sample size of 44.4 nm × 44.4 nm × 14.8 nm.

A final equiaxed nanocrystalline Cu (NC-Cu) sample was constructed using a three-dimensional Voronoi tessellation method to provide a direct comparison with the two nanolaminate structures. In particular, the NC-Cu simulation cell contained 25 grains with a volume-averaged mean grain size and misorientation angle of 11.4 nm and 38.04º, respectively. These parameters were selected to match the volume-averaged mean grain size and misorientation distribution of the crystalline layer in the CN-NL sample. The resulting NC-Cu structure, which contained 1,622,110 atoms and a cell size of 27.09 nm × 27.07 nm × 27.07 nm, is illustrated in Fig. 2.1(c).

An energy minimization procedure was performed on all three structures to reach a final relative energy convergence of 10^{-12}, followed by a simulated annealing at 650 K for 1 ns to generate realistic ACIs. This temperature was carefully chosen to provide sufficient thermal energy for local relaxation of the interfaces while remaining well below the glass transition temperature of 737 K for the $Cu_{64}Zr_{36}$ amorphous alloy [190]. The structures were then cooled to a temperature of 300 K using a rate of 1 $K \cdot ps^{-1}$ and relaxed for an additional 0.4 ns to eliminate the pressure in all dimensions. The deformation simulations were conducted at 300 K using uniaxial loading in the x-direction at a constant strain rate of $10^8 \cdot s^{-1}$, and the normal stresses in the y- and z-directions were relaxed to zero to allow lateral contraction during deformation. An isobaric-isothermal (NPT) ensemble was used to control the temperature and pressure during relaxation and deformation, and all simulations employed a time-step of 2 fs.

Characterization of the structures employed multiple quantitative tools often beginning with a common neighbor analysis (CNA) method [191, 192], which indexes each atom according to its local atomic coordination. The structures in Fig. 2.1 employ the CNA scheme, where green atoms exhibit face-centered cubic (FCC) coordination, red atoms hexagonal close-packed (HCP) coordination (e.g. atoms commonly found in stacking faults), and grey atoms other coordination; the latter generally captures atoms occupying grain boundary sites in the crystalline layer and all atoms in the amorphous layer. Following deformation, local atomic slip was quantified using a slip vector analysis [193] with an atom's slip vector, $\boldsymbol{s}^{\alpha}$, defined as:

$$\boldsymbol{s}^{\alpha} = -\frac{1}{n_s}\sum_{\beta \neq \alpha}^{n}(\boldsymbol{x}^{\alpha\beta} - \boldsymbol{X}^{\alpha\beta}) \quad (2.1)$$

where n is atom α's total number of nearest neighbors and n_s is atom α's total number of slipped nearest neighbors. The variables $\boldsymbol{x}^{\alpha\beta}$ and $\boldsymbol{X}^{\alpha\beta}$ represent the interatomic distance vectors between atom α and neighbor atom β in a deformed condition and reference state, respectively.

Combined with CNA values, the slip vector can be used to estimate the Burger's vector of each atom and distinguish between competing deformation mechanisms [194]. In the subject simulations,

particular emphasis was placed on delineating partial from full dislocation slip. Partial dislocations containing HCP coordinated atoms in a stacking fault will have a slip vector approximately equal to the Burger's vector for partial slip, i.e. $\|\boldsymbol{b_p}\| = a/\sqrt{6}$ where a is the lattice constant. Full dislocation slip will instead involve FCC atoms, which exhibit a slip vector comparable to the Burger's vector for full slip, i.e. $\|\boldsymbol{b_f}\| = a/\sqrt{2}$. For Cu with a lattice constant of 3.615 Å, the slip vectors for partial and full slip will be approximately 1.47 and 2.55 Å, respectively. The slip vector was also employed to quantify local deformation for grain boundary and amorphous atoms, which enabled a quantitative comparison between competing deformation mechanisms in the crystalline and amorphous layers [193].

While the slip vector is convenient for identifying deformation mechanisms and their relative distributions, the contribution of these mechanisms to the total strain was captured using the Green strain tensor, which is defined as:

$$\boldsymbol{E} = \frac{1}{2}[\boldsymbol{F^T F} - \boldsymbol{I}] \qquad (2.2)$$

where $\boldsymbol{I}$ is the identity tensor and $\boldsymbol{F}$ is the deformation gradient calculated according to the method described by Tucker et al. [194]. The application of continuum-level kinematic metrics such as the Green strain tensor enabled a quantitative characterization of strain accommodation in the subject nanolaminate structures, thus representing an important tool for uncovering the deformation physics at the nanoscale. Finally, to study the implications of various deformation mechanisms for void formation, a surface mesh method was employed to calculate void volume fractions formed during uniaxial deformation. The open-source OVITO software [195] was used in the CNA and surface mesh techniques, whereas the slip vector and Green strain tensor were determined using custom codes designed for execution in C.

2.2 Deformation Mechanisms and Strain Accommodation

In this section, the deformation behavior of the three simulation structures are presented focusing first on the flow curves, followed by a description of the underlying mechanisms accommodating

plasticity, and concluding with the distribution of strain among these competing deformation mechanisms. The stress-strain curves for the SC-NL, CN-NL and NC-Cu structures deformed under uniaxial tensile loading at 300K with a strain rate of $10^{8} \cdot s^{-1}$ are shown in Fig. 2.3. While few disparities were apparent in the flow curves for the NC-Cu and CN-NL structures, the SC-NL sample exhibited noticeably different yielding behavior as evidenced by the abrupt stress drops with increasing strain. This was also manifested in the mechanical properties cataloged in Table 2.1, where the elastic modulus and stress at the onset of global plasticity (determined using a 0.2% offset criterion) of the SC-NL were significantly greater relative to the equiaxed nanocrystalline and columnar nanolaminate structures.

While the reduced elastic modulus of the SC-NL structure can be attributed to the anisotropy of the system and specific crystallographic orientation aligned with the tensile axis [59], additional analysis was required to understand the mechanisms responsible for the onset of global plasticity. Deformation snapshots were constructed as a function of the applied strain with emphasis herein placed on differentiating mechanisms in the SC-NL and CN-NL structures; the deformation physics in NC-Cu are addressed extensively in literature [20, 60, 194] and thus only those aspects pertinent to the discussion of toughness are presented in Section 5. Snapshots are shown at three different strains in Fig. 2.4 for the SN-NL structure with atoms colored by both the CNA value and slip vector.

Local plasticity initiated in the SC-NL at a strain of approximately 3% that derived from the activation of STZs in the amorphous layers. The onset of global plasticity corresponding to the appreciable stress drop of greater than 3.5 GPa at approximately 6% strain was attributed to the emission of a dislocation from the lower ACI as evidenced in the CNA representation of Fig. 2.4 viewed along the [110] direction; the leading partial (grey ‘other coordination’ atoms) and stacking fault (red HCP-coordinated atoms) emerged just prior to 6.6% strain. Atoms in the stacking fault have a characteristic slip vector of 1.4 – 1.6 Å [193, 194], and partial dislocation activity was thus captured by the green atoms in the slip vector snapshots.

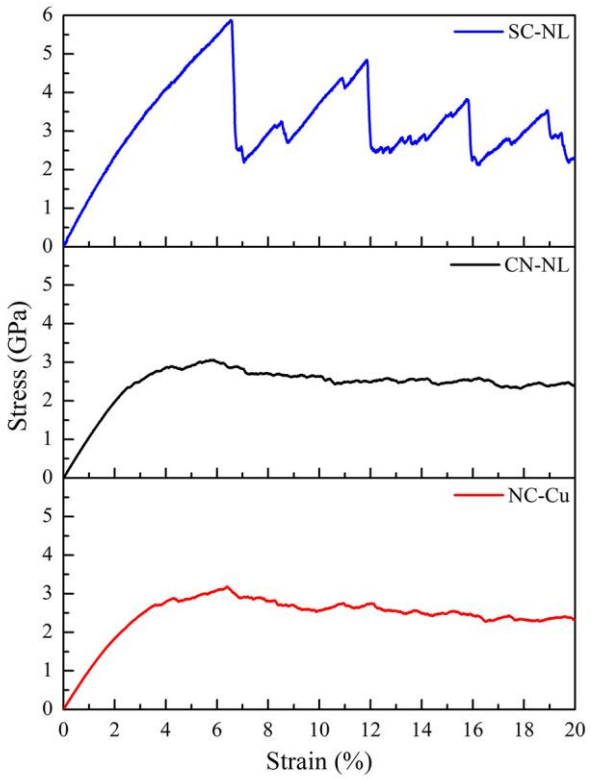

Figure 2.3 Flow curves for the single crystal-amorphous nanolaminate (SC-NL), columnar nanocrystal-amorphous nanolaminate (CN-NL) and equiaxed nanocrystalline Cu (NC-Cu) structures. Mechanical properties determined from these data can be found in Table 2.1.

A major advantage of employing the slip analysis is its ability to capture full dislocation plasticity [193, 194], which is absent in the CNA representation as fully slipped atoms return to their initial FCC configuration. For example, the leading partial dislocation emitted from the ACI at 6.6% strain was followed by a trailing partial and absorption of this full dislocation at the adjacent ACI just prior to 7.2% strain. Because the atoms experienced full slip with a slip vector magnitude of approximately 2.55 Å, full dislocation slip was evident in the slip vector representation (i.e. by the atoms colored red). This is even more prevalent at a strain of 11% where multiple slip traces resulting from the propagation of full dislocations were apparent in the slip vector analysis. By correlating dislocation activity via slip vector with the flow curve in Fig. 2.3, the sharp stress drops were attributed to the emission of partial dislocations from the ACIs.

Table 2.1 Mechanical properties of SC-NL, CN-NL and NC-Cu structures

Structure	Elastic Modulus (GPa)	Strain at the onset of plasticity (%)	Stress at the onset of plasticity (GPa)
SC-NL	115.92	3.07	3.34
CN-NL	103.46	2.38	2.26
NC-Cu	98.52	2.2	1.97

The flow curve for the CN-NL structure was free of large stress oscillations, which indicates that the transition to dislocation plasticity was fundamentally altered by the introduction of grain boundaries. From the deformation snapshots shown in Fig. 2.5, the onset of dislocation plasticity corresponded to the emission of a leading partial dislocation and stacking fault from the intersection between the upper ACI and grain boundary plane at approximately 3.2% strain. The slip vector analysis revealed a region of high slip in the amorphous layer directly above this grain boundary-ACI intersection, suggesting STZ activity triggered emission of the observed partial. The full dislocation generated upon emission of the trailing partial was absorbed across the adjacent ACI at 7.2% strain, which can only be observed in the slip vector scheme. Absorption of this dislocation triggered a series of atomic rearrangements via STZ activity in the amorphous layer to accommodate the transfer of plastic strain. From this region of locally high slip, a new partial dislocation was nucleated at 10.8% strain within the same grain, and the resultant stacking fault is indicated by the white arrow in Fig. 2.5. The neighboring grain exhibited extensive plasticity, which produced intrinsic and extrinsic stacking faults as well as deformation twins; the latter is denoted by the yellow arrow. Collectively, these deformation processes align with the defects observed through post-mortem TEM measurements on Cu-Cu_3Zr crystalline-amorphous nanolaminates [39].

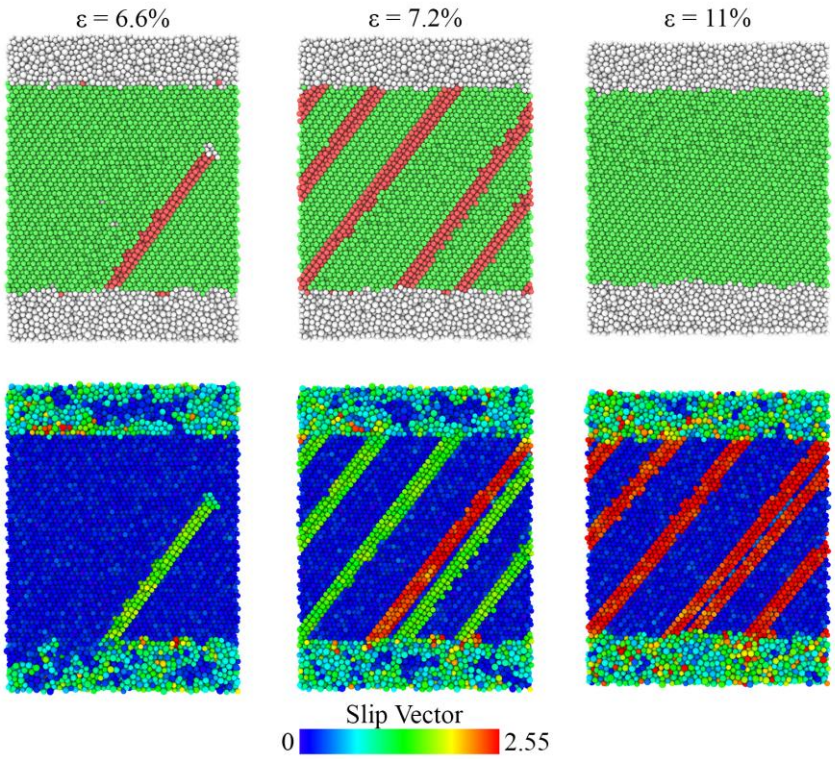

Figure 2.4 Deformation snapshots of the SC-NL structure viewed along the [110] direction at 6.6%, 7.2% and 11% strain colored by the CNA value (upper) and slip vector (lower). Partial and full dislocations emitted from the ACI traverse the plane (111) and are absorbed in the adjacent ACI.

Although deformation was accommodated by dislocations and STZs in both the SC-NL and CN-NL structures, the introduction of grain boundaries in the latter augmented the onset of global plasticity based on the coupling between these disparate mechanisms. During the early stages of deformation, localized slip was first activated in the amorphous layer and further biased to regions adjacent to the grain boundaries, which in turn triggered the emission of dislocations. Collective shearing enabled by the redistribution of free volume during the process of STZ formation [38, 196] has previously been linked to the emission of dislocations at ACIs [126]. However, the biasing of STZ activity to regions in direct vicinity of the grain boundaries indicates a reduced activation barrier resulted from the presence of these boundaries. While this likely derived from limited slip transfer between the grain boundaries and amorphous regions promoting the formation of stress concentrations near the interface, it decidedly shifted the onset of dislocation plasticity to lower strains relative to the SC-NL structure.

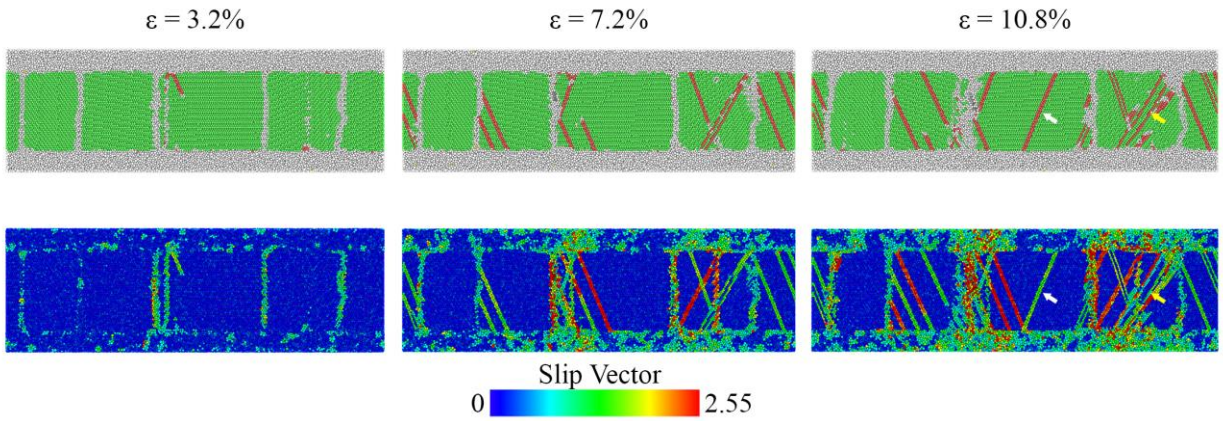

Figure 2.5 Deformation snapshots of the CN-NL structure viewed in the x-z plane at 3.2%, 7.2% and 10.8% strain colored by the CNA value (upper) and slip vector (lower). Dislocation activity is mediated by both the ACIs and grain boundaries and results in slip emerging along multiple slip planes.

As compared to NC-Cu, the flow curve for the CN-NL structure exhibited many similar features and consequently, the properties calculated from the respective stress-strain curves were nearly identical. However, the mechanisms accommodating strain at the nanoscale differed considerably. Detailed analysis of the deformation mechanisms in NC-Cu has been the subject of other pioneering works [20, 60, 112]. Here, we focus on differentiating the dominant mechanisms accommodating strain in all three structures using the Green strain tensor analysis, and the results are summarized in Fig. 2.6.

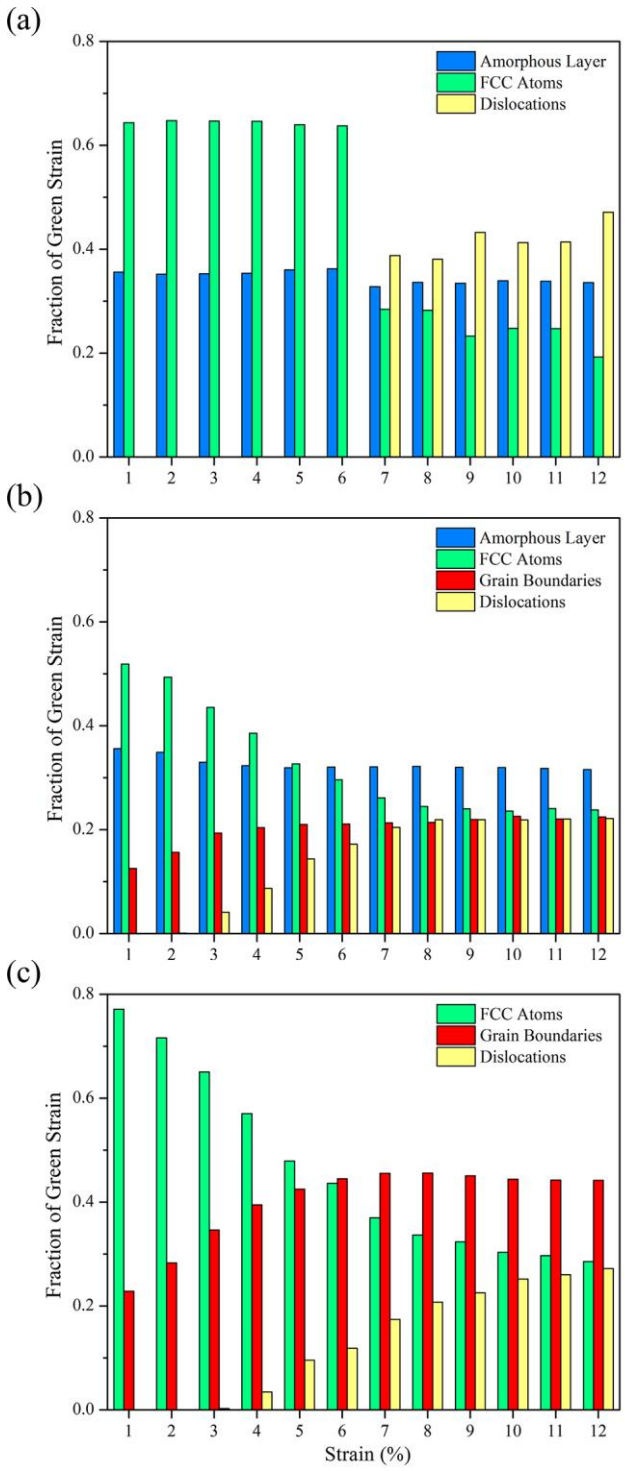

Figure 2.6 Strain accommodation maps for the (a) SC-NL, (b) NC-NL, and (c) NC-Cu structures that delineate the contribution of the amorphous layer, FCC atoms, grain boundaries, and dislocations to deformation. The order of the trend titles in the legend aligns with the bar order at each strain from left-to-right.

Deformation was accommodated in the CN-NL structure by four primary mechanisms: straining of the FCC lattice, dislocations, grain boundary mediated plasticity, and STZ activity in the amorphous

layer. In the SC-NL captured in Fig. 2.6(a), grain boundaries were not available to absorb plastic strain energy and as a result, dislocations accommodated the majority of plastic strain upon global yielding with additional contributions from STZ activity in the amorphous layer. In the absence of an amorphous layer, plastic strain largely partitioned to the grain boundaries in NC-Cu as evident in Fig 2.6(c). Conversely, the presence of the amorphous layer in the CN-NL structure suppressed grain boundary plasticity by more than 50%, which was manifested by the substantial reduction in the grain boundary Green strain in Fig. 6(b). The fraction of strain accommodated by dislocation plasticity was nearly identical for the NC-Cu and CN-NL structures; however, the Green strain analysis does not capture implicit interactions between dislocation and STZ plasticity. Such an analysis necessitates tracking of the atomic slip vector over predefined strain intervals and is the subject of the following section. Nevertheless, the results demonstrated that grain boundaries significantly altered the process of strain accommodation in crystalline-amorphous nanolaminate models, which produced conspicuous changes in their flow behavior.

2.3 Quantifying STZ-Dislocation Coupling and the Onset of Plasticity

A comprehensive analysis of the coupling between STZ and dislocation plasticity is presented in this section with a particular focus on quantitative characterization through tracking the of atomic slip vector during an isolated dislocation event. Dislocations have been demonstrated to nucleate at the ACI near regions of high atomic slip associated with STZ activity. While the formation of STZs in the SC-NL was distributed along the entire ACI and in agreement with other studies [39, 126, 145], STZ activity was biased to the grain boundary intersections with the ACI in the CN-NL structure suggesting that shear band formation will align with the grain boundary network. Plan views of the amorphous layer in the x-y plane of the CN-NL sample are illustrated in Fig. 2.7(a) at three different strains; the formation of a shear band nucleus was evident at the lowest strain of 4%. A doubling of the strain was accompanied by the appearance of large secondary shear bands, which thickened as strain was further increased to 12%. The plan view of the crystalline layer in the x-y plane shown in Fig. 2.7(b) demonstrates that shear band formation aligned with the dislocation networks, which also appeared to be mediated by the grain

boundaries. While the coupling between dislocations and STZ plasticity is implied by these observations, the sequence of the deformation events cannot be ascertained from the deformation snapshots alone.

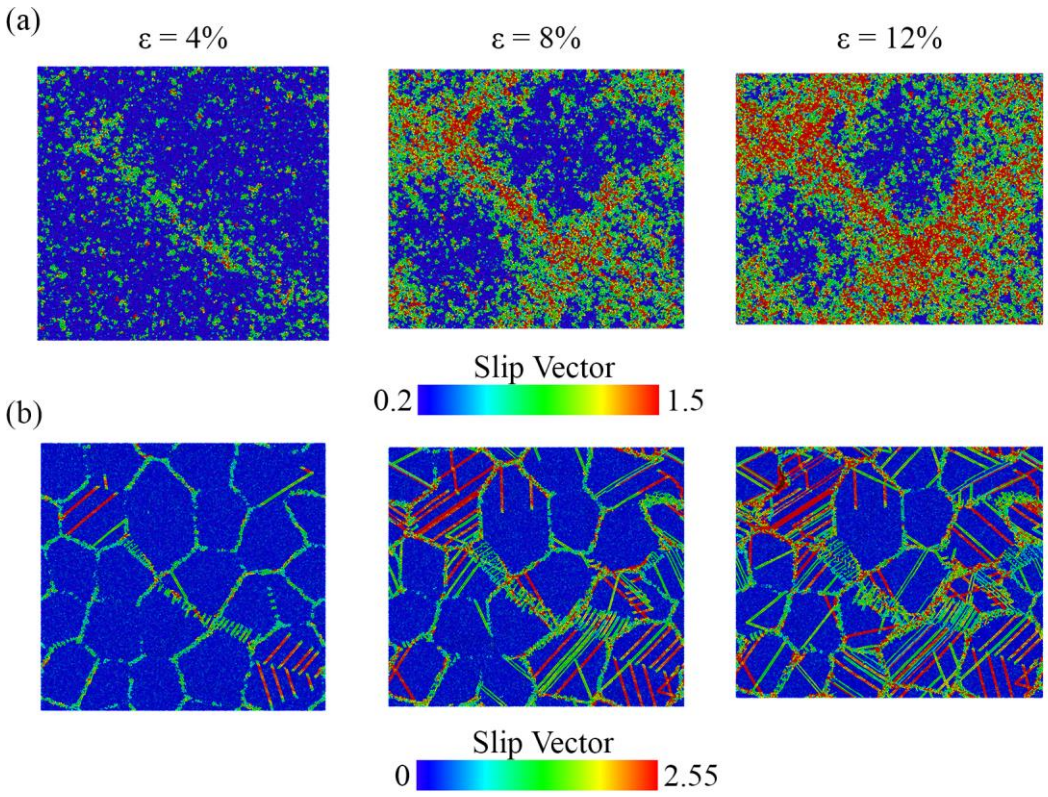

Figure 2.7 Deformation snapshots viewed in the x-y plane (i.e. top-down view) of the (a) amorphous layer and (b) crystalline layer at strains of 4%, 8% and 12% with atoms colored according to the slip vector value. The alignment of shear bands with dislocation slip bands indicates that a coupling exists between the two disparate deformation mechanisms.

To understand the onset of dislocation plasticity and its connection to shear localization at the ACI, an analysis technique was developed to map the average slip vector in discrete layers by dividing the nanolaminate structures evenly into 12 slices parallel to the plane of the ACI, as illustrated in Fig. 2.8(a) and 8b for the SC-NL and CN-NL, respectively. Each slice was assigned a number from 1 – 12 where slices S1, S2, S11, and S12 were located in the amorphous layer while slices S3 – S10 were distributed across the crystalline layer. The average slip vector was computed for each slice and mapped as a function of slice number in Fig. 2.8(c) and 2.8(d) for the SC-NL and CN-NL, respectively.

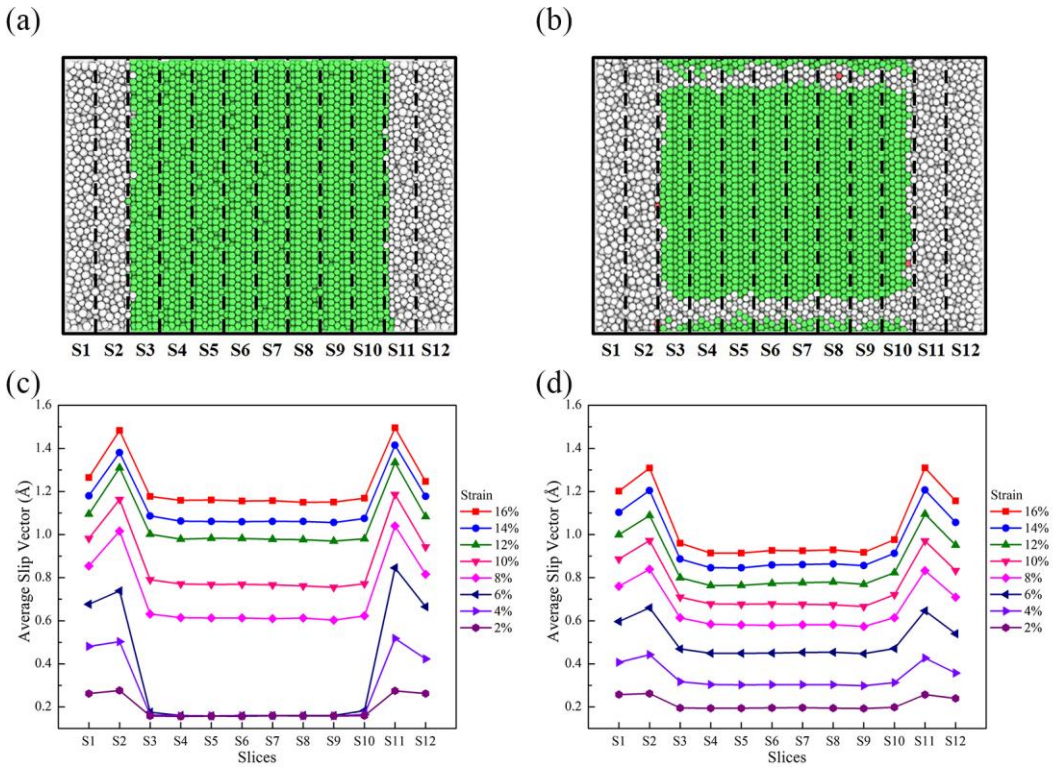

Figure 2.8 Orientation and location of the average slip vector slices for the (a) SC-NL and (b) CN-NL structures; snapshots are colored according to CNA value and rotated 90º relative to Figure 2.4 and 2.5. The average slip vector determined for each slice as a function of the applied strain for the (c) SC-NL and (b) CN-NL.

At low strains up to 6% in the SC-NL, the average slip vector trends in Fig. 2.8(c) demonstrated severe strain partitioning to the amorphous layer, which confirmed the previous observations from the Green strain analysis in Fig. 2.6(a). Between 6 and 8% strain, the precipitous jump in the average slip vectors for the crystalline slices corresponded to the initial stress drop just after 6% strain in the flow curve (cf. Fig. 2.3) and the onset of dislocation plasticity from the Green strain analysis. The next abrupt increase between 10 and 12% strain aligned with the second large stress drop in the flow curve and another burst of dislocation activity. Throughout all stages of deformation, the average slip vector was greater in the amorphous layer; however, slices located directly adjacent to the ACI (i.e. S2 and S11) exhibited a peak in the slip vector at all strains, resulting in the formation of a strain gradient across the ACI. This gradient was most severe just prior to the onset of plasticity in the crystalline layer and was subsequently relieved by dislocations accommodating a significant fraction of the plastic strain (40% from the Green strain analysis in Fig. 2.6(a)).

The sudden jumps in the slip vector trends for the crystalline region of the SC-NL were absent during deformation of the CN-NL as evident in Fig. 2.8(d), substantiating the more gradual onset of macroplasticity in the flow curve. The absence of slip vector bursts can be attributed to grain boundaries mediating plastic strain accumulation during the initial stages of deformation as quantified in the Green strain analysis shown in Fig. 2.6(b). This was manifested as a steady monotonic increase in the average slip vector across the crystalline layer, i.e. in slices S3 – S10, particularly at strains of 2, 4, and 6% in Fig. 2.8(d). Further contributing to this gradual increase was the onset of dislocation plasticity at a strain of 3%, which was delayed to 7% strain in the SC-NL. Elimination of the sharp strain gradient at the ACI suggests that the grain boundaries reduce the activation barrier for dislocation nucleation, and is commensurate with the models proposed by Asaro and Suresh [197] for nanocrystalline metals.

While tracking of the average slip vector in discretized slices demonstrated biased slip to the amorphous layers at low strain, a focused analysis of a single dislocation nucleation and propagation event was performed to quantify the different stages of microplasticity in the CN-NL structure. The deformation snapshots illustrated in Fig. 2.9 capture the lifetime of a dislocation that was emitted from a grain boundary-ACI intersection as viewed on the $(1\bar{1}\bar{1})$ slip plane. In the snapshots colored according to the CNA value, a leading partial was first nucleated at 4% strain and followed by a stacking fault as the partial traversed the grain. At 4.18% strain, a trailing partial was emitted that removed the stacking fault as it propagated across the grain, and was subsequently absorbed just after 4.26% strain at the lower grain boundary-ACI intersection resulting in full dislocation glide.

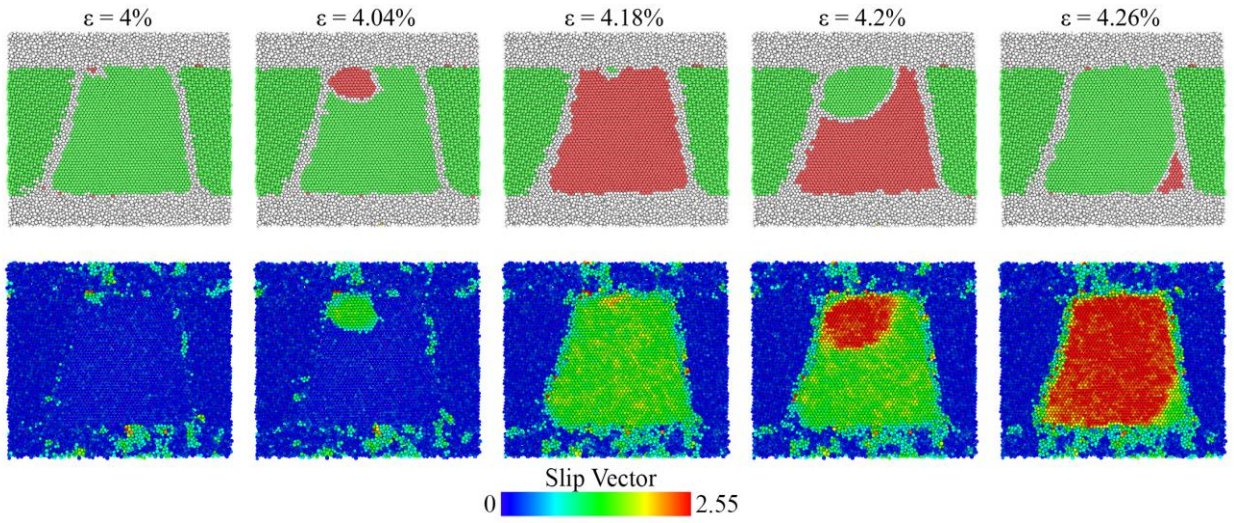

Figure 2.9 Deformation snapshots illustrating the evolution of a dislocation on the $(1\bar{1}\bar{1})$ slip plane colored via CNA value (upper) and slip vector (lower) between 4.0 and 4.26% strain. The dislocation is emitted from the intersection of a grain boundary with the upper ACI, traverses the grain along the slip and, and is absorbed into the amorphous layer across the lower ACI.

The emission of this trailing partial from a different location on the ACI indicated that grain boundary-ACI intersections are not solely responsible for the onset of dislocation plasticity. Instead, dislocation emission events directly correlated with regions of high local atomic slip at the ACI. In the snapshots indexed by slip vector in Fig. 2.9, emission of the trailing partial at 4.18% strain occurred where STZ activity impinged on the ACI, not at its intersection with the grain boundary. Thus, while grain boundaries reduce the activation barrier for dislocation nucleation as previously noted, the general emission of dislocations from regions of high local atomic slip indicates that slip transfer across the ACI governed dislocation nucleation in the CN-NLs. Slip biasing to atoms near the grain boundaries in the amorphous layers, especially at low strains, can be attributed to stress concentrations that form at the grain boundary-ACI intersection rather than deriving from mechanisms proposed for grain boundary-mediated plasticity in equiaxed nanocrystalline metals such as grain boundary sliding [197].

To capture instantaneous changes in the slip history and substantiate the proposed slip transfer mechanism in crystalline-amorphous nanolaminates, the average atomic slip vector of each slice was normalized by the average slip vector of the entire $(1\bar{1}\bar{1})$ slip plane illustrated in Fig. 2.9. Denoted the normalized average slip vector, trends are shown in Fig. 2.10(a) for slices immediately adjacent to the

upper ACI in the amorphous (S11) and crystalline (S10) layers as a function of strain; analogous results are shown in Fig. 2.10(b) for slices adjacent to the lower ACI (S2 and S3, respectively).

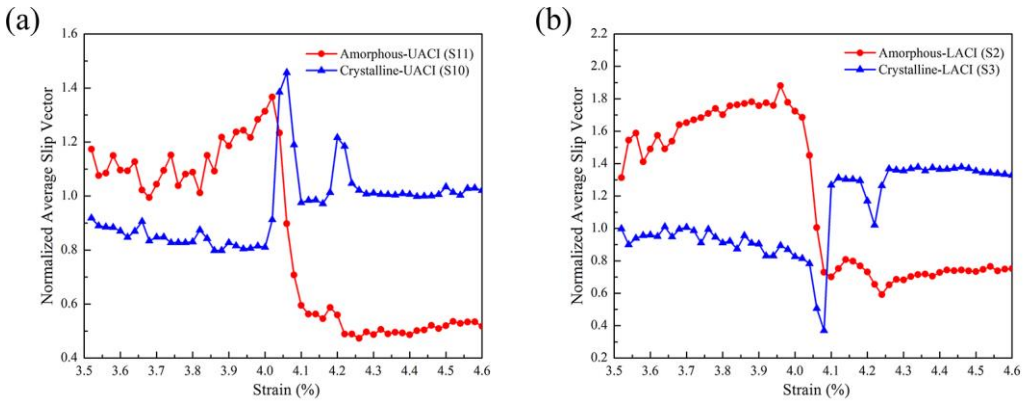

Figure 2.10 Normalized average slip vector as a function of strain for the $(1\bar{1}\bar{1})$ slip event depicted in Figure 2.9. Trends are presented for amorphous and crystalline slices immediately adjacent to (a) the upper (UACI) for slices S11 and S10, and (b) the lower ACI (LACI) for slices S2 and S3.

Prior to the emission of the leading partial, a strain gradient developed across the ACI, which is captured in Fig. 2.10(a) by the enhanced normalized average slip vector for the amorphous atoms in slice S11 relative to the crystalline atoms in slice S10. At about 4% strain, emission of the leading partial was accompanied by an abrupt drop in the normalized average slip vector of the amorphous S11 slice and immediately followed by a precipitous increase in the crystalline S10 slice. The second peak in the normalized average slip vector of the amorphous S11 slice around 4.18% strain developed just prior to emission of the trailing partial and was followed by the peak in the trend for the crystalline S10 slice as the trailing partial passed through this particular region of the nanolaminate. Emission of both the leading and trailing partials thus derived from an identical slip transfer mechanism where STZ activity impinging on the ACI produced regions of high local atomic slip, which in turn triggered the nucleation of dislocations to accommodate the high interfacial strain gradient.

Tracking of the normalized average slip vector in slices adjacent to the lower ACI revealed additional interactions between dislocations and STZ plasticity. Prior to the nucleation of the leading partial at the upper ACI, a strain gradient also developed at the lower ACI. However, emission of the leading partial manifested instead as a sharp drop in the normalized average slip vector in Fig. 2.10(b),

which was a result of the overall increase in the entire slip plane's average slip vector upon nucleation of this partial dislocation. Propagation of the leading partial through the crystalline S3 slice occurred at approximately 4.1% strain, as evidenced by the abrupt increase in the normalized average slip vector of this region. Immediately following propagation through the crystalline S3 slice, the leading partial impinged on the lower ACI producing a peak in the normalized average slip vector of the amorphous S2 slice that corresponded to the activation of new STZs. Dislocation absorption by an amorphous phase has been demonstrated to trigger STZ activity in other studies [163, 198], and the results presented herein provide quantitative evidence for this slip transfer mechanism in crystalline-amorphous nanolaminates.

Direct coupling between dislocation slip and STZ plasticity has been shown to transpire through two mechanisms: (1) the emission of dislocations from sites of high local atomic slip deriving from STZ activity impinging on the ACI, and (2) the triggering of new STZs upon absorption of dislocations across an ACI. Once dislocation slip is established, these slip transfer mechanisms collectively operate throughout all stages of deformation and provide a sustainable process for accommodating plastic strain through coupled dislocation-STZ plasticity. Grain boundaries played a critical role in strain accommodation process especially the onset of global yielding, which resulted from biased dislocation emission from grain boundary-ACI intersections. These stages of deformation and the underlying mechanisms will, therefore, be more closely representative of the deformation behavior exhibited by experimental nanolaminates that inherently contain a hierarchy of structural length scales.

2.4 Implications of Coupled Dislocation-STZ Plasticity for the Strength-Ductility Envelope

The Green strain analysis summarized in Fig. 2.6 provided quantitative evidence for plastic strain collectively partitioning to the grain boundaries and the amorphous layer prior to the onset of dislocation plasticity in the CN-NL structure. By tracking the atomic slip in discretized slices within a slip plane, a connection was established between grain boundary and STZ-mediated plasticity, which was further bridged to the process of dislocation nucleation that ultimately governed the strength of these materials. Conversely, ductility will be controlled by the ability to inhibit the formation of grain boundary microcracks while simultaneously circumventing strain localization in the amorphous regions. The role of dislocation-STZ coupling in impeding these failure mechanisms is addressed in this section, with a focus on slip transfer via dislocation absorption at the ACIs and its implications for shear localization and void formation.

Plastic strain accumulation in equiaxed nanocrystalline metals is often limited by the formation of stress concentrations that derive from dislocation-grain boundary interactions. These stress concentrations promote the initiation of grain boundary voids and cracks [32, 115], and their subsequent coalescence leads to brittle intergranular fracture [199]. To quantify the process of void formation, a surface meshing technique [195] was applied and the resulting void fractions are depicted in Fig. 2.11(a) for each structure as a function of the applied strain. In the NC-Cu and CN-NL structures, void initiation occurred at approximately 6% strain, followed by growth at a constant rate up to 11% strain. A change in slope was apparent for NC-Cu at 11% strain that captured a transition in the growth rate, which continued through the duration of the simulation. Consequently, the final void fraction in NC-Cu at 20% strain was more than double the CN-NL structure. When combined with the complete absence of voids in the SC-NL, these results indicate that void formation derived from the interaction of defects with grain boundaries.

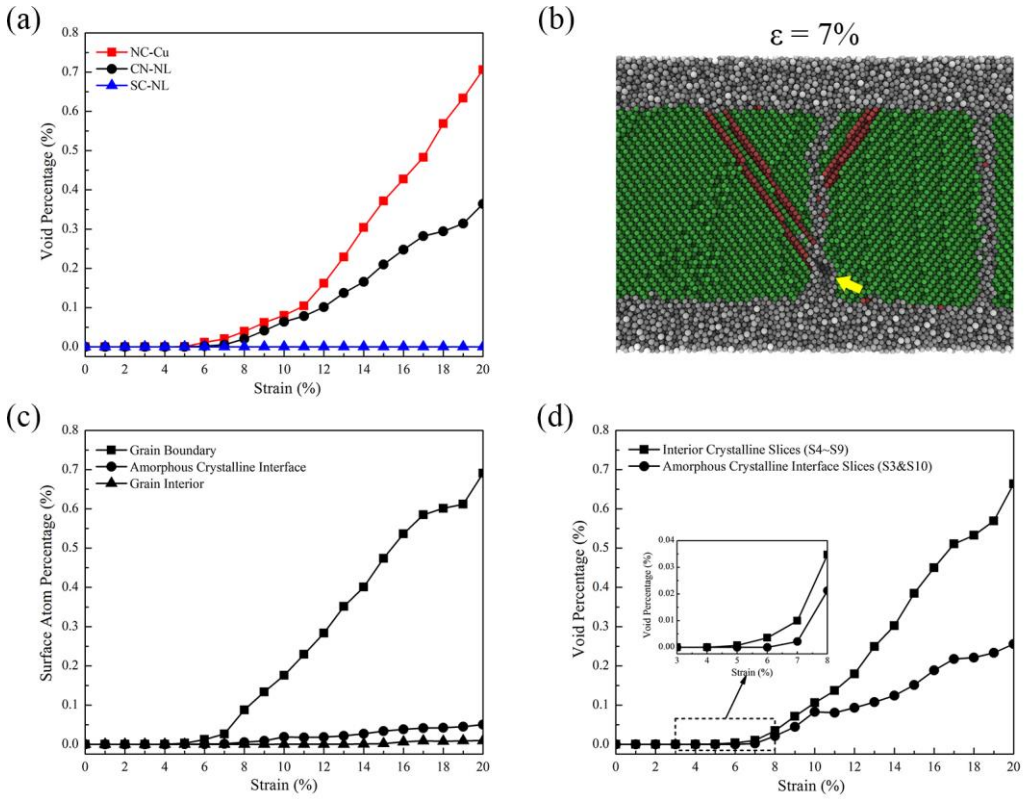

Figure 2.11 (a) Overall void volume fraction (in percentage) for each structure as a function of the applied strain. (b) Formation of a grain boundary nanovoid at 7% strain in the CN-NL structure upon intersection of a leading partial dislocation with the grain boundary as highlighted by the yellow arrow; atoms are colored according to their CNA value. (c) The fraction of surface atoms located in the grain interior, ACI, and grain boundaries in the CN-NL as a function of strain. (d) Void fractions (in percentage) for the CN-NL structure in part (a) delineated for slices directly adjacent to the ACIs in the crystalline layer (i.e. S3 & S10 in Figure. 2.8(b)) and the interior crystalline slices (i.e. S4 – S9 in Figure. 2.8(b)).

In the context of the Green strain analysis in Fig. 2.6, grain boundaries accounted for greater than 40% of the strain in NC-Cu, whereas only 20% was accommodated by grain boundaries in the CN-NL structure. However, NC-Cu contained nearly double the volume fraction of grain boundaries (16.6%) relative to the CN-NL structure (8.7%), and grain boundaries will inherently accommodate a greater amount of plastic strain. This provides one possible explanation for the improved ductility of crystalline-amorphous nanolaminates, i.e. they contain fewer grain boundary sites for the initiation of grain boundary microcracks. From a simple qualitative inspection, voids were determined to form in the CN-NL structure primarily at the grain boundaries upon impingement of a leading partial as demonstrated in Fig. 2.11(b) at 7% strain. This is in good agreement with equiaxed nanocrystalline metals where crack formation transpires preferentially at grain boundaries, [199] and is often linked to dislocation-grain

boundary interactions [32]. Despite these similarities, the underlying mechanisms responsible for void initiation could also be influenced by the hierarchical structure albeit in a more inconspicuous manner.

A surface atom technique based on the distribution of Voronoi volumes was developed to quantify the correlation between void initiation sites and grain boundaries. The Voronoi volume employs nearest neighbor atoms to provide a local measure of the space occupied by each atom and represents the volume of a Voronoi polyhedron that encompasses each atomic site [43]. The formation of a void produces a shift in some of an atom's nearest neighbors that manifests as an increase in the average Voronoi volume. Consequently, atoms located on a void or crack surface denoted herein as "surface atoms" exhibit abnormally large Voronoi volumes greater than 18.5 $Å^3$, which lies convincingly outside the range of Voronoi volumes for Cu of 9 – 16 $Å^3$. Using this technique, surface atoms were identified and their allegiance to the grain interiors, grain boundaries, and ACIs tracked during deformation. The fraction of surface atoms determined for each of these regions is shown in Fig. 2.11(c) as a function of the applied strain.

Surface atoms were detected in the grain boundary region at approximately 6% strain indicating that voids nucleated in the grain boundary regions (i.e. a 1.2 nm thick region around the grain boundaries) well after the early stages of plastic deformation involving dislocation, grain boundary, and STZ plasticity. With increasing strain, the fraction of surface atoms in the grain boundaries grew precipitously while it remained relatively insignificant in the intragranular regions. Only a small fraction of surface atoms were identified in the ACI region after about 9% strain, which suggested that the ACIs reduced the propensity for void formation. This was substantiated by separating the void fractions for the ACI regions (i.e. slices S3 and S10) from the other crystalline slices of the CN-NL structure, and the trends are shown in Fig. 2.11(d). Voids initially formed in the interior crystalline slices as evident in the inset, and their volume fraction with increasing strain was consistently greater relative to the ACI regions. Taken collectively with the biased void nucleation within the grain boundary regions from Fig. 2.11(c), it can be inferred that voids formed predominantly in the central regions of grain boundaries.

Based on the above analysis, the ability of dislocations to be absorbed across the ACIs without the onset of void nucleation represents a new fundamental mechanism for limiting damage accumulation at the nanoscale. Our results are in excellent agreement with the atomistic simulations conducted by Pan and Rupert [163] that demonstrated delayed interfacial cracking upon the absorption of dislocations in boundaries containing amorphous complexions. From the alternative perspective of shear localization in monolithic amorphous alloys, the hierarchical structure of crystalline-amorphous nanolaminates confines shear localization within the thin amorphous layers. Limiting the propagation of a dominant shear front while simultaneously nucleating new shear bands through the transfer of plastic strain upon dislocation absorption provides two additional mechanisms for enhancing plastic strain accommodation, and in turn, ductility relative to monolithic metallic glass counterparts [154]. The unique ability to circumvent grain boundary microcracking collectively with catastrophic shear localization contributes to the appreciably improved toughness of crystalline-amorphous nanolaminates relative to equiaxed nanocrystalline metals.

2.5 Concluding Remarks

In this chapter, molecular dynamics simulations were employed to quantify the plastic strain distribution among competing deformation mechanisms in crystalline-amorphous nanolaminate models containing columnar nanograins. Significant insight was gained into the coupling between disparate mechanisms at the nanoscale using continuum deformation metrics, summarized as follows:

i. The addition of grain boundaries into the crystalline layers of the nanolaminate biased STZ activity to regions near these boundaries, which reduced the activation barrier for dislocation plasticity as manifested by the reduced stress at the onset of global yielding for the CN-NL.
ii. Direct coupling between dislocation slip and STZ plasticity transpired through two mechanisms including the emission of dislocations from sites of high local atomic slip deriving from STZ activity impinging on the ACI, and the triggering of new STZs upon absorption of dislocations across an ACI that in turn promotes additional dislocation plasticity.

iii. The biasing of void formation to the central regions of the grain boundaries relative to the ACIs and its connection to dislocation plasticity indicated that the accommodation of dislocations at ACIs abated void nucleation within the CN-NL structure.

iv. The propagation of a dominant shear front was limited by shear band confinement to the amorphous layers collectively with the nucleation of new shear bands promoted by the transfer of plastic strain upon dislocation absorption across the ACIs.

Based on the above results, the improved toughness of crystalline-amorphous nanolaminates relative to equiaxed nanocrystalline metals can be understood in the context of the interplay between disparate deformation mechanisms at the nanoscale and its ability to limit grain boundary microcracking while simultaneously inhibiting catastrophic shear localization. The incorporation of grain boundaries into the nanolaminate model was essential to capturing the influence of hierarchical structural length scales on the deformation physics, which drastically affected the damage accumulation mechanisms and flow behavior. Using these structural length scales to tune the plastic strain distribution among competing mechanisms, new design strategies can be realized for expanding the strength-ductility envelope in nanostructured metals.

Chapter 3 Mechanics Driven Design of Crystalline-Amorphous Nanolaminates

In this chapter, molecular dynamics (MD) simulations are employed to map the influence of microstructural length scales on the underlying deformation mechanisms and mechanical properties in crystalline-amorphous nanolaminates. The layer thickness ratio and nanocrystalline grain size are systematically varied, and the mechanical response of the nanolaminates are characterized under uniaxial tensile loading through deformation metrics for atomistic simulations. Illustrative compound deformation mechanisms maps rooted in the contributions of the three dominant deformation mechanisms – STZ, dislocation, and grain boundary plasticity – are generated for each microstructural length scale combination. Combined with deformation snapshots, the compound mechanism maps provide new insights into the mechanistic transitions in crystalline-amorphous nanolaminates as a function of their hierarchical microstructural length scales. The implications of these transitions for the resulting mechanical properties are finally understood through flow stress-void formation-strain localization maps, from which new design strategies are outlined for expanding the strength-ductility envelope gradient nanolaminate structures.

3.1 Simulation Procedures

The nanolaminate architecture employed for exploring deformation mechanisms and property scaling were modeled after the columnar nanocrystal-amorphous nanolaminate (CN-NL) constructed in Chapter 2. As shown in Fig. 3.1, the nanolaminate structure contained a columnar nanocrystalline Cu layer of thickness, t_C, and grain size, d, produced through a Voronoi tessellation method [188] applied in the x-y plane. The nanocrystal layer was sandwiched between amorphous $Cu_{64}Zr_{36}$ layers of thickness, $t_A/2$ and application of periodic boundary conditions in the z-direction produced the final patterned nanolaminate structure. Each microstructural variable was systematically tailored over the range of 2.5 – 20nm, and the ratio of the amorphous-to-crystalline layer thickness (t_A/t_C) was used in categorizing the results. For the range of thicknesses explored, t_A/t_C varied over the range of 0.25 – 1.5 capturing both

crystalline and amorphous dominated states, respectively, and grain sizes spanned the well-known Hall-Petch breakdown regime [35]. A detailed selection of length scales is demonstrated in Table 3.1, where five sets of combinations are presented. In each set of samples, either t_A/t_C or d is kept as a constant, the other variable is subjected to change and the figure notations are exhibited in the last column to correlate each set of samples with their corresponding compound mechanisms map (CMM).

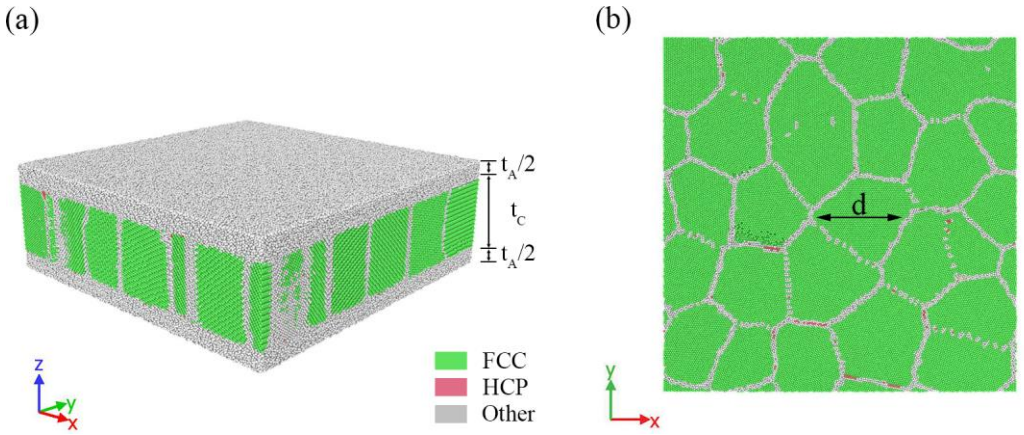

Figure 3.1 (a) Initial structure of columnar nanocrystal-amorphous nanolaminate (CN-NL), where the layer thickness of amorphous and crystalline layers are labeled as t_A and t_C, respectively (b) x-y plane cross-sectional view of columnar nanocrystal-amorphous nanolaminate, in which the grain size of nanocrystalline layer is denoted as d. The atoms are colored by the CNA value.

MD simulations were performed using the Large-scale Atomic/Molecular Massively Parallel Simulator (LAMMPS) package [185], and atomic interactions were described by the embedded-atom method (EAM) potential developed by Mendelev et al. [200] as it accurately captures the behavior of both Cu-Zr metallic glasses [200] and pure crystalline Cu [187]. Each nanolaminate configuration was subjected to an energy minimization procedure to achieve a final relative energy convergence of 10^{-12} and subsequently relaxed at 650K for 1 ns to provide sufficient thermal energy for interfacial relaxation while remaining below the glass transition temperature of 737K for the $Cu_{64}Zr_{36}$ amorphous alloy [190]. Following relaxation, structures were cooled at a rate of $1K \cdot ps^{-1}$ to 300 K and relaxed for an additional 0.4 ns to achieve a pressure-free condition in all dimensions. Uniaxial tension along the x-direction of the nanolaminate models (i.e. parallel to the layers) was conducted at a strain rate of 1×10^{8} s^{-1} and temperature of 300K with the normal stresses in the y- and z-directions relaxed to zero to facilitate lateral

contractions during deformation. A timestep of 2 fs was used in the relaxation and deformation processes with an isobaric-isothermal (NPT) ensemble applied to control the temperature and pressure.

Table 3.1 Detailed selection of length scales of columnar nanocrystal-amorphous nanolaminates and the corresponding compound mechanisms maps (CMMs)

Sample Set	t_A (nm)	t_C (nm)	t_A/t_C	d (nm)	CMM
1	2.5, 5, 10, 15	10	0.25, 0.50, 1.00, 1.50	10	Fig. 3.7
2	5	5	1.00	5, 10, 15, 20	Fig. 3.9(a)
3	5	10	0.50	5, 10, 15, 20	Fig. 3.9(b)
4	5	15	0.33	5, 10, 15, 20	Fig. 3.9(c)
5	5	20	0.25	5, 10, 15, 20	Fig. 3.9(d)

A number of quantitative methods were utilized to characterize structural reconfigurations and mechanisms accommodating plasticity during deformation. A common neighbor analysis was employed to index each atom based on its local atomic coordination as illustrated in Fig. 3.1; atoms with face-centered cubic (FCC) coordination are rendered green, atoms in stacking faults with hexagonally close-packed (HCP) coordination are rendered red, and atoms with all other coordinations are rendered grey. The 'other coordination' category captures disordered atoms found in both the grain boundaries and amorphous layers. A slip vector analysis coupled with the CNA method was used to distinguish partial from full dislocation slip following the framework described by Tucker et al. [194] and previously adopted for characterizing dislocation plasticity in crystalline-amorphous nanolaminates [201]. The Von Mises shear strain was employed to quantify grain boundary and STZ plasticity [202], which required distinguishing atoms that experienced plastic events during deformation as described in Section 3.2. The open-source OVITO software [195] was employed for rendering snapshots during deformation and calculating local atomic coordination, atomic volume, and void volume fraction through a surface mesh technique. Slip vector and Von Mises shear strain values were ascertained using custom algorithms designed for execution in C.

3.2 Compound Mechanisms Maps

In this section, the effect of layer thickness ratio to the deformation behaviors of CN-NLs is investigated beginning with the mechanical responses of the first set of samples, which have a constant grain size of 10nm and varying t_A/t_C ratio from 0.25 to 1.5. Three plasticity contour maps are generated describing the contributions of three major plasticity carriers to the total plasticity as functions of t_A/t_C and strain. A compound mechanisms map that incorporates all three carriers is developed and different mechanisms zones are identified and associated with typical deformation snapshots for confirming the deformation behaviors of CN-NLs.

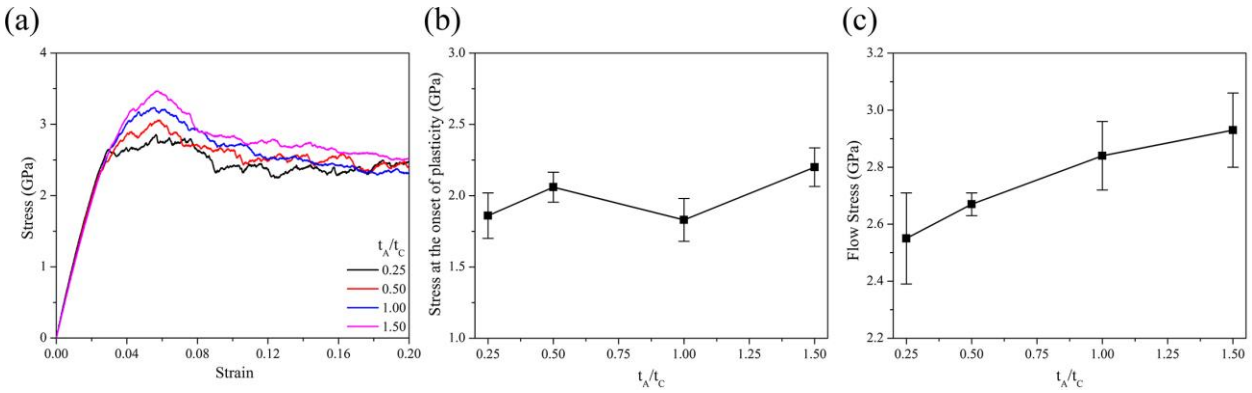

Figure 3.2 (a) Stress-strain curves of columnar nanocrystal-amorphous nanolaminates with different layer thickness ratio (t_A/t_C). Stress at the onset of plasticity (b) and flow stress (c) as a function of layer thickness ratio.

The mechanical responses of CN-NLs are usually controlled by their microstructural length scales as shown in Fig. 3.2(a), where stress-strain curves of the first set of CN-NLs are exhibited. Evidently, the elastic parts of stress-strain curves are found to be identical for all four samples, which can be understood by the constant nanocrystalline grain size and similar chemical composition. The onsets of plasticity of these samples were determined to be ~0.02 strain via traditional linear fitting of their stress-strain curves with a 0.002 strain offset and the stresses at the onset of plasticity were calculated and presented in Fig. 3.2(b). It is interesting that the stress values are fluctuating around 2.0 GPa except for the t_A/t_C = 1.5 sample, whose stress at onset of plasticity reached 2.2 GPa. This indicates that the effective yielding behaviors were determined by the constant grain size for nanolaminates with a layer thickness ratio less

than 1.5 whereas the thicker amorphous layer in the t_A/t_C = 1.5 sample altered the onset of plasticity behavior of nanolaminates. After global plasticity was triggered, the stresses of all samples kept increasing until about 0.06 strain and then committed to strain softening forming stress overshoots in stress-strain curves. The degree of stress overshoots generally scales with the layer thickness ratio, especially for the t_A/t_C = 1.5 sample, where a hump shape stress-strain curve is observed, suggesting severe strain localization. The flow stresses between 0.07 to 0.1 strain were then averaged to assess the strength during the plastic deformation and displayed in Fig. 3.2(c), where the flow stress is found to increase with the increasing t_A/t_C ratio. It is evident that the layer thickness ratio governed the flow strength during the plastic deformation stage.

Even though stress-strain curves give a good description of mechanical properties, it is not able to disclose information about the mechanisms operating as samples deforming. To study the deformation events, three plasticity carriers were isolated in the CN-NL structures: deformed grain boundary atoms, dislocations, and STZs. Lattice dislocations among crystalline Cu atoms are usually determined by the abrupt increase of the slip vector value to a specific level, in our case 1.47 and 2.55 Å for partial and full dislocations, respectively [201]. However, there is no established method for distinguishing plastic events in structurally disordered STZs and grain boundaries atoms using shear strain, which increases continuously as structures deform. Therefore, a shear strain threshold is needed for isolating plastic deformed disordered atoms.

Coupling the shear strain value and atomic volume dilatation feature of plastic deformed disordered atoms [38, 83, 203], a method for isolating plastic deformation is hereby presented. As a prerequisite, the onset of plasticity strain of the whole structure needs to be determined. Taking the CN-NL with a t_A/t_C ratio of 0.5 and a grain size of 10nm as an example, the onset of plasticity strain was determined to be 0.0216 using the abovementioned method and illustrated in Fig. 3.3(a). Then, the shear strain of amorphous atoms at 0.0216 strain was calculated using the initial structure as the reference state. Atomic volume distribution of amorphous atoms was also introduced by calculating the atomic volume of

atoms using Voronoi tessellation [43, 45, 204, 205]. Fig. 3.3(b) demonstrates the comparison of distributions of amorphous atoms at the initial and onset of plasticity states. The first peaks centered around 12.5 $Å^3$ correspond to the copper atoms whereas the second peaks centered around 22.5 $Å^3$ link to the zirconium atoms. Comparing to the initial distribution, a slight shift of deformed atoms' distribution to the right, or to a larger atomic volume, was observed revealing the augment of atomic configuration owing to the deformation.

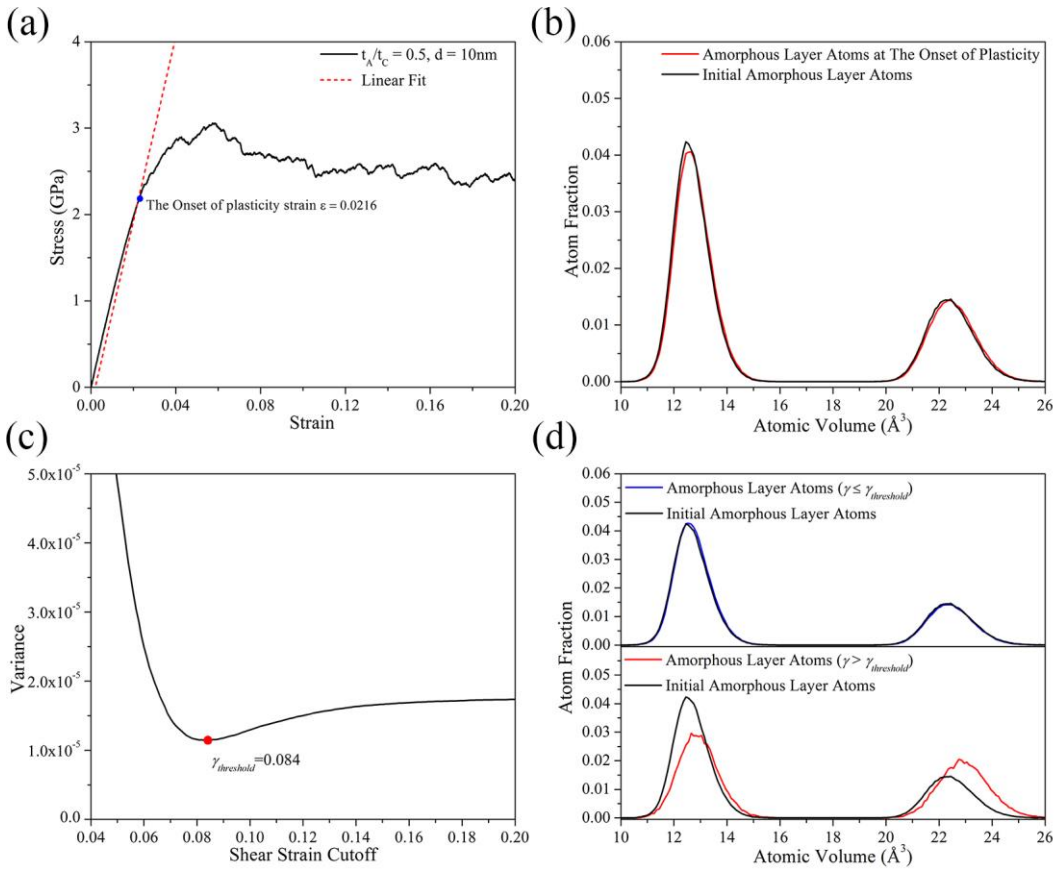

Figure 3.3 (a) The stress-strain curve of the columnar nanocrystal-amorphous nanolaminates with a layer thickness ratio (t_A/t_C) of 0.5 and nanocrystalline layer grain size of 10nm. The red dash line is the fitting line of the linear part of stress-strain curve with a 0.002 strain offset relative to the origin of the axes to determine the onset of plasticity strain and stress. (b) The atomic volume distributions of amorphous layer atoms at the initial state (black) and the onset of plasticity state (red), respectively. (c) The variance χ^2 as a function of shear strain cutoff. (d) The comparison of the atomic volume distributions of elastic (red) and plastic (blue) deformed amorphous layer atoms to the initial amorphous layer atoms' distribution (Black).

The atomic volume distribution at the onset of plasticity contains atoms that contributed to either elastic or plastic deformation. To decompose this distribution, a shear strain assorted atomic volume distribution fitting method was developed beginning with the key value of variance χ^2:

$$\chi^2 = \sum_k^N [F_C(k) - F_R(k)]^2 \qquad (3.1)$$

where *k* stands for the k^{th} bin of the discretized atomic volume in the distribution functions, N is the total number of bins used in the distribution functions, and $F_C(k)$ and $F_R(k)$ are the atom fraction values for the k^{th} bin of the current and reference state, respectively. In this case, the current state is the structure at the onset of plasticity and the reference state is the initial structure. The variance value provides a measurement of the atomic volume distribution difference between current and reference states. The larger the variance value is, the more substantial the difference of two states is.

Based on the distribution of shear strain, a temporary shear strain cutoff (γ_{cutoff}) was set, which was sampled consecutively from 0 to 0.2 with an increment of 0.001. For those atoms that have shear strain value from 0 to γ_{cutoff}, the atomic volume distribution was generated and the variance was calculated. The variance was then plotted as a function of shear strain cutoff as shown in Fig. 3.3(c), where a minimum value was achieved at the shear strain of 0.084. The atomic volume distribution of atoms that have a shear strain value less than 0.084 shows the highest resemblance or best fit to the initial distribution. Thus, this group of atoms is thought to be elastic deformed whereas the atoms that have shear strain more than 0.084 were plastic deformed. The plastic deformation shear strain threshold was therefore set as 0.084. The comparison of elastic and plastic deformed atoms' distributions to the initial distribution is shown in Fig. 3.3(d). It is evident that the distribution of elastic deformed atoms is very close to the initial distribution except for a very small shift to the right because of elastic lattice straining. On the contrary, the distribution of plastic atoms significantly deviates from undeformed distribution. Not only did peaks shift considerably to the right, but also were broadened signifying the conspicuous dilatation of local atomic configuration. Therefore, the shear strain assorted atomic volume distribution

fitting method successfully captured the plastic deformed atoms using both shear strain and free-volume increase theory of amorphous solids [38, 203].

It is well known that the plastic deformation of grain boundaries takes the form of grain boundary sliding, atom shuffling, and free-volume migration [60, 206], which also lead to an increase of dilatation of local atomic configuration proved by Tucker et al. [194]. As a consequence, the same method was applied to the grain boundary atoms and a shear strain threshold of 0.041 was attained. Due to the same relaxation and deformation conditions, the shear strain thresholds were applied to all CN-NL structures to isolate plastic events of structurally disordered atoms. Once the three plasticity carriers were identified, each carrier's atom percent out of the total number of carriers was calculated and mapped as functions of both strain and t_A/t_C ratio, resulting in plasticity contour maps shown in Fig. 3.4. Three zones are identified on these maps for a better understanding of plastic behaviors: dominating zone colored deep red with an atom percent over 60%; minority zone colored deep blue with an atom percent less than 20%; intermediate zone colored gradually from blue to red with an atom percent between 20 and 60%.

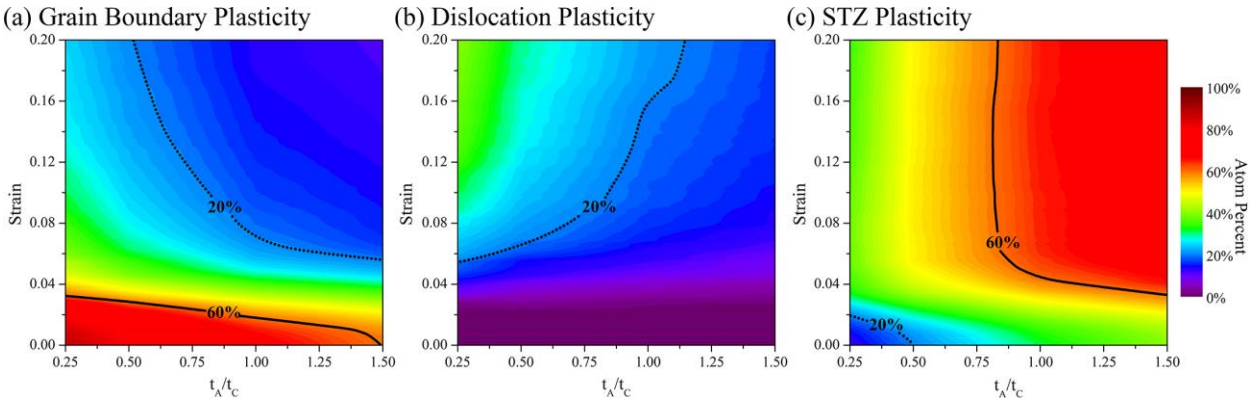

Figure 3.4 Contour maps of (a) grain boundary, (b) dislocation, and (c) shear transformation zone (STZ) plasticity carriers in the columnar nanocrystal-amorphous nanolaminates sample set 1 as function of layer thickness (t_A/t_C) and strain.

The grain boundary plasticity map in Fig. 3.4(a) indicates that grain boundary generally dominated the plasticity in the early stage of deformation (<0.04 strain) but its contribution to the total plasticity decreased as the t_A/t_C ratio and strain increased and became neglectable at higher strain and t_A/t_C ratio. In nanocrystalline metals, the grain boundary contributes significantly to deformation in the low

strain range through grain boundary sliding, migration and atom shuffling [60]. In our case, due to the constant grain size, the atom percent of plastic deformed grain boundary atoms around the onset of plasticity (~0.02) strain are very close for all samples except for the t_A/t_C =1.5 sample and dominating the amount of plasticity carriers, which explains their similar elastic behaviors and stress values at the onset of plasticity. However, the increase of the amorphous atoms fraction by enhancing the t_A/t_C ratio to 1.5 suppressed the grain boundary plasticity by activating more STZ carriers instead and in turns changed the onset of plasticity behavior of the corresponding nanolaminate.

For dislocation plasticity, there is no mechanism dominating zone as depicted in Fig. 3.4(b), where only an intermediate zone is identified located in the high strain and low t_A/t_C ratio region. In the other region, the contribution of dislocations is trivial. The grain size of this set of samples is so small (10nm) that they are located within the Hall-Petch breakdown regime, in which the classical dislocation dynamics shifts to grain boundary mediated plasticity and dislocations' contribution to total plasticity is greatly limited. On the contrary, the introduction of amorphous layers to nanocrystalline layers rendered the STZs a prominent role in the deformation process. As illustrated in Fig. 3.4(c), the STZ dominated deformation shortly after the onset of plasticity for the samples with t_A/t_C ratio greater than 0.75. The intermediate zone took the rest of the area in the contour map except for a very small minority zone in the low strain and t_A/t_C ratio region. Meanwhile, STZs atom percent increased monotonously as the t_A/t_C ratio enhanced when the deformation stabilized after 0.06 strain. This result agrees with the flow stress trend suggesting that the STZ plasticity carrier was the determining factor for the strength of CN-NLs during the plastic deformation stage.

There is no doubt that the plasticity contour maps give excellent descriptions of deformation behaviors for each mechanism individually. However, it is still difficult to correlate one mechanism contribution to the others. Therefore, we generated a compound mechanisms map that contains all mechanisms' contributions to better interpret the plasticity of CN-NLs. This compound mechanisms map originated from three contour maps, where we took the dominating zones directly from the contour maps

and completely neglected minority zones. The 60% solid lines were used to outline the dominating zone where only one mechanism was operating. The rest of the map is a mixing of operating mechanisms. However, only mechanisms in the intermediate zone were counted and we used the 20% dotted line to delineate different mechanisms mixing zones.

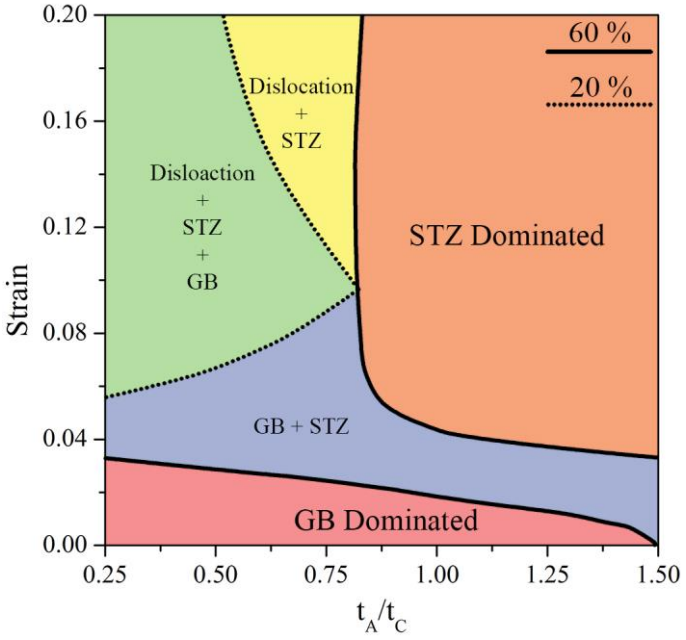

Figure 3.5 Compound mechanisms map of the columnar nanocrystal-amorphous nanolaminates sample set 1. The area of different mechanism zone varies as function of layer thickness ratio (t_A/t_C) and strain. The 20% atom percent dotted line delineates different mechanisms mixing zone whereas the 60% atom percent solid line differentiates the single mechanism dominating zone.

Fig. 3.5 shows the compound mechanisms map for the first set of samples. There are only two mechanism dominating zones: GB dominated and STZ dominated zones located in the same positions in Fig. 3.4(a) and (c) whereas for mechanism mixing zones, three regions were divided: GB + STZ, Dislocation + STZ + GB, and Dislocation + STZ zones. The GB + STZ zone mainly positioned itself after the GB dominated zone and ended at about 0.06 to 0.08 strain. The Dislocation + STZ + GB and Dislocation + STZ zones are found at higher strain (>0.08) and low t_A/t_C ratio (<0.75) after plastic deformation stabilized. In these mechanisms zones, none of the plasticity carrier atom fraction exceeded 60% or less than 20% and they contributed equally to the global plasticity.

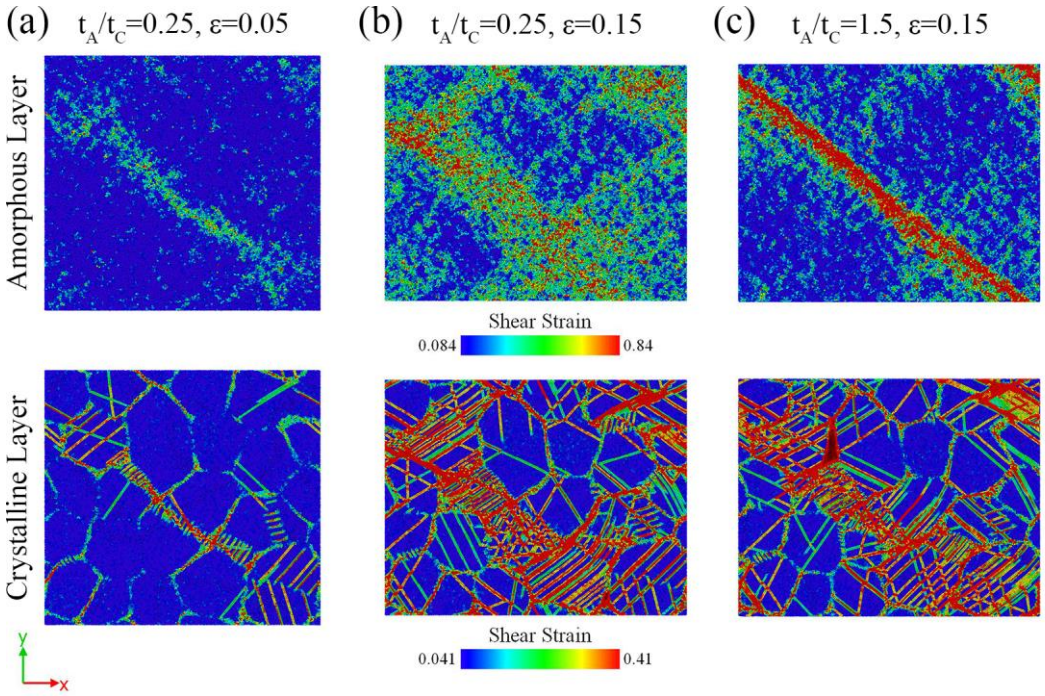

Figure 3.6 Amorphous and crystalline layers' deformation snapshots of the set 1 columnar nanocrystal-amorphous nanolaminate sample with a layer thickness ratio (t_A/t_C) of 0.25 at strain 0.05 (a) and 0.15 (b) and the sample with a layer thickness ratio of 1.5 at the strain of 0.15 (c). Atoms are colored by the shear strain.

Several typical deformation snapshots are exhibited and correlated to the different zones in the compound mechanisms maps to confirm the deformation behavior of CN-NLs. Fig. 3.6(a) shows the amorphous and nanocrystalline layers' snapshots of t_A/t_C = 0.25 sample at 0.05 strain, where atoms are colored by shear strain. This combination of t_A/t_C ratio and strain is located in the GB + STZ zone in the compound mechanisms map. The snapshot indicates that an embryonic shear band was formed and angled 45 degrees to the x-axis in the amorphous layer while the grain boundaries migrations were observed in the nanocrystalline layer that aligning with the embryonic shear band. In addition, the grain boundary sliding and slightly dislocation gliding were captured in the other region of the nanocrystalline layer. This set of snapshots confirms that the major operating mechanism of this t_A/t_C ratio and strain combination was GB + STZ.

Fig. 3.6(b) presents the snapshots for the same sample at a higher strain of 0.15 located in the Dislocation + STZ + GB zone. The amorphous snapshot suggests the embryonic shear band was

broadened and a second shear localized area that is perpendicular to the embryonic shear band was formed, which aligned with severe dislocation activities in the nanocrystalline layer. In this length scale combination, the three carriers collectively contributed to the plasticity and avoided strain being localized in any form of mechanism. Surprisingly, a mature shear band was attained at the same strain of 0.15 but for the t_A/t_C =1.5 sample shown in Fig. 3.6(c), which is located at the STZ dominated zone. Due to the increase of amorphous layer thickness, the embryonic shear band was able to develop into a mature shear band that significantly limited the plasticity. At the same time, the dislocation and grain boundary activities in the nanocrystalline layer were inevitably concentrated in the pathway that aligning with the shear band. The formation of the mature shear band also confirms that the stress hump observed in its stress-strain curve in Fig. 3.3(a) is indeed a sign for severe shear localization.

3.3 Collective Role of Microstructural Length Scales

In this section, the focus is placed on the CN-NL sample sets (Set 2~5) with t_A/t_C ratio decreasing from 1.0 to 0.25, where no single mature shear band is observed. Compound mechanisms maps were generated for these sets of samples, in which grain size was used as the x-axis to study its effect to the plasticity for each set of CN-NLs. Then, factors that control strength and ductility are presented and correlated to the compound mechanisms maps for an in-depth understanding of length scales' relationship to the overall mechanical properties of CN-NLs. The compound mechanisms maps for nanolaminates with t_A/t_C ratio of 1.0, 0.5, 0.33 and 0.25 were generated and exhibited in Fig. 3.7 (a), (b), (c), and (d), respectively. Generally, there are four mechanisms zones existing in most of the maps except for Fig. 3.7(a), where only three zones are presented. Each mechanisms region area is changing with respect to strain, grain size and t_A/t_C ratio, which will be explained sequentially in the following paragraphs.

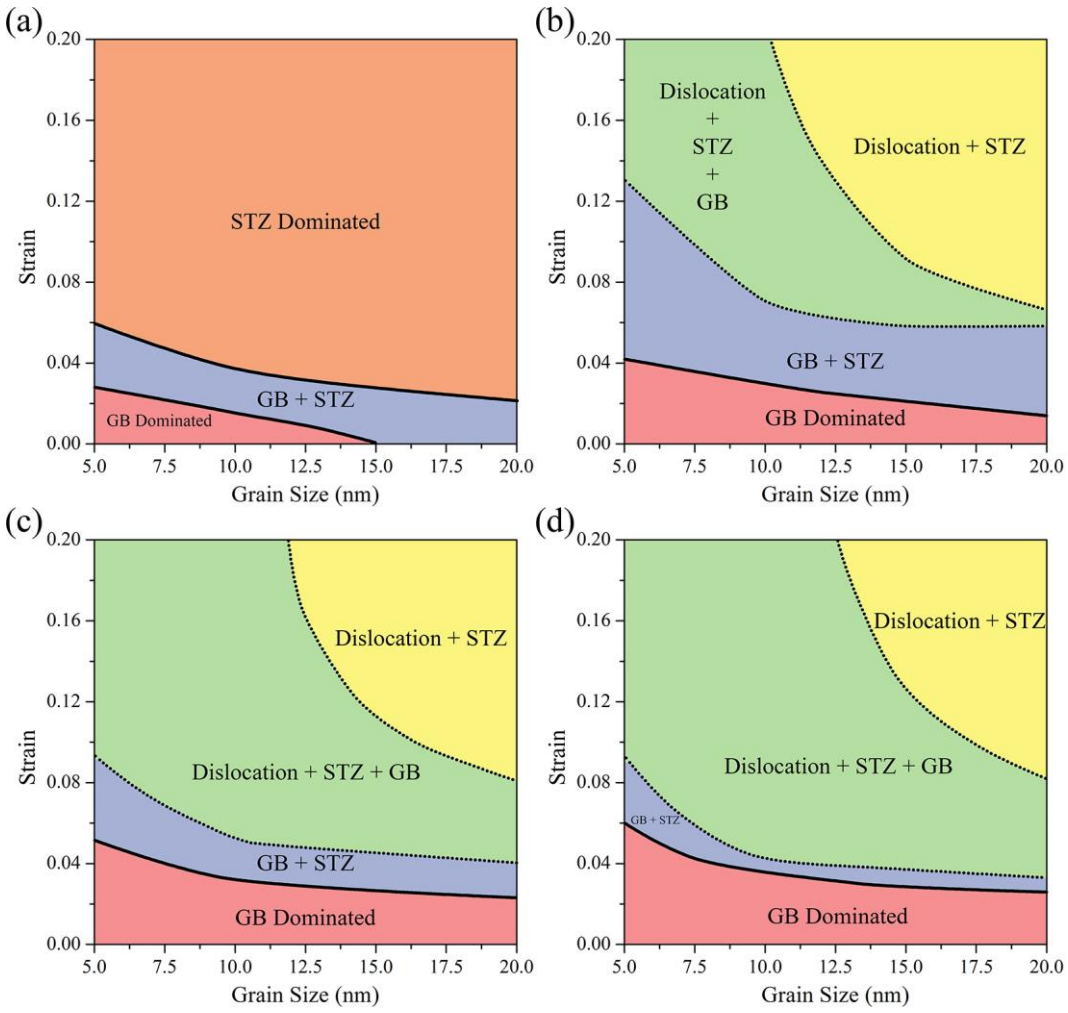

Figure 3.7 Compound mechanisms maps of the columnar nanocrystal-amorphous nanolaminates sample set 2 (a), set 3 (b), set 4 (c), set 5 (d). Area of different mechanism zone varies as the function of grain size and strain. The 20% atom percent dotted line delineates different mechanisms mixing zone whereas the 60% atom percent solid line differentiates the single mechanism dominating zone.

In Fig 3.7(a), the only STZ dominated zone among the four maps is presented for the CN-NL samples with a t_A/t_C of 1.0, indicating that for the equal amorphous and nanocrystal layer thickness samples, STZs were the major plasticity carriers during plastic deformation and became more prevalent when grain size increased. Another single mechanism majored region is the GB dominated zone, which appears in all four mechanisms maps at low strains. With the decrease of the t_A/t_C ratio from 1.0 to 0.25, the area of the GB dominated zone increased. This can be understood by the fact that with the increase of the nanocrystalline phase fraction, more grain boundary atoms were present in the samples. At the same time, the area of GB-dominated zone was decreasing with the enlargement of grain size. The lower

fraction of grain boundary and easier dislocation activation accounted for this change at the larger grain size. One interesting thing to note is that for the CN-NLs with a t_A/t_C of 1.0 and $d \geq 15$nm, the GB-dominated zone was completely eliminated and deformation at a very early stage directly entered the GB + STZ zone, signifying that the STZ plasticity was substantially promoted at low strain for larger grain sizes at this t_A/t_C ratio which might lead to shear bands.

In addition to the two single mechanism dominating zones, there are three mechanism mixing zones starting with the GB + STZ zone, which is usually located at the early stage of plastic deformation. For t_A/t_C =1.0, the GB + STZ zone even extended to the elastic deformation stage and served as the transition zone between GB-dominated and STZ dominated zones. This zone suggests that grain boundary plasticity at low strain acted as triggers for STZs in the amorphous layers. The area of GB + STZ zones in the rest of compound mechanisms maps shrank as t_A/t_C decreased and grain size increased, which can be attributed to the onset of dislocation plasticity at a higher nanocrystalline phase and larger grain size samples. With the operation of dislocation plasticity carrier, the compound mechanisms maps came into the Dislocation + STZ + GB zone for the samples with t_A/t_C less than 1.0. This triple mechanism zone prevails in the small grain size and low t_A/t_C ratio samples where grain boundaries still played a vital role in the plastic deformation. However, at higher t_A/t_C and grain size region, the triple zones gave way to the Dislocation + STZ zones, in which the fast propagation of dislocations was coupled with the aggregation of STZs.

Once the compound mechanisms maps were developed, it is easier to interpret the strength and ductility properties via correlating them to the mechanism zones in the maps. Fig. 3.8(a) presents the stress at the onset of plasticity calculated at about 0.02 strain for four sets of nanolaminates, which were determined by the grain sizes and layer thicknesses collectively. In the crystalline-rich sample sets with t_A/t_C ratios of 0.33 and 0.25, a typical Hall-Petch Breakdown behavior was observed where the stress at onset of plasticity increased at first, reached the highest stress and then decreased as the grain size kept refining. The corresponding compound mechanism maps suggest that the GB dominated mechanism was

operating in these samples at the onset of plasticity strain around 0.02 and controlling the effective yielding of CN-NLs.

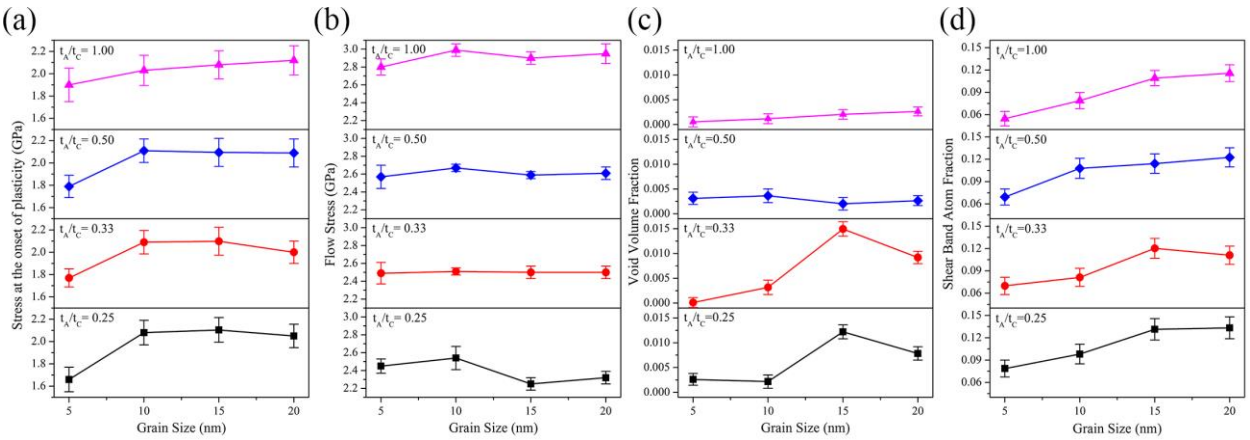

Figure 3.8 Stress at the onset of plasticity (a), flow stress (b), void volume fraction (c), and shear strain atom fraction (d) as a function of nanocrystalline layer grain size for the columnar nanocrystal-amorphous nanolaminates with a layer thickness ratio (t_A/t_C) from 0.25 to 1.00.

However, the Hall-Petch Breakdown behavior was absent in the sample set of t_A/t_C = 1.0. The stress remained increasing monotonously as the grain size enhancing indicating that the high fraction of amorphous phase presented in the CN-NLs significantly altered their deformation behaviors, which were no longer solely affected by grain size. With the help of compound mechanisms map, the operating mechanism around the onset of plasticity strain was found shifting from GB dominated when grain sizes are smaller than 10nm to GB + STZ at larger grain sizes. The coupling of grain boundary and STZ plasticity suppressed the dislocation plasticity, eliminated the stress softening due to the activation of dislocations and finally led to a completely STZ dominated zone in high strain. An interesting trend was found in the t_A/t_C = 0.5 samples set. The stress at the onset of plasticity initially increased and completely plateaued with the grain size increase. The compound mechanism map shows that the grain size of 20nm sample entered the GB + STZ zone at the onset of plasticity and thus strength weakening was inhibited. This set of samples served as the transition region between amorphous-rich and crystalline-rich sample sets.

Comparing to the stress at the onset of plasticity, the flow stress trends in Fig. 3.8(b) are straightforward. It is obvious that the flow stresses were not affected by grain sizes for all sets as they were only oscillating around certain value for each set. Nevertheless, as the t_A/t_C value increased, the flow stress level increased simultaneously. As it was demonstrated in the former section, the flow stress was strongly affected by the STZ plasticity. The increased t_A/t_C ratio coupled with the prevalence of STZs activities and in turn enhance the flow stress. Therefore, it is evident that the layer thickness ratio is the controlling factor of flow stresses during the plastic deformation of CN-NLs.

Unlike strength properties, the ductility properties of nanolaminate are rather difficult to obtain via examining stress-strain curves since simulated uniaxial tensile deformation will not commit to fracture due to the periodic boundary conditions. Therefore, an alternative method needs to be employed to gauge the ductility of nanolaminates. In this article, we propose the calculation of void volume fraction and the shear band atoms fraction as the criterions for judging nanolaminates' toughness. The calculation of void volume fraction is straightforward. The volume of voids at the end of the simulation (0.2 strain) was summed using the surface mesh method embedded in OVITO [195] and normalized by the total structure volume.

The void volume fraction values as a function of grain size for last four CN-NLs sets are exhibited in Fig. 3.8(c), where two disparate trends are observed. The samples with t_A/t_C ratios of 1.0 and 0.5 indicate low void volume fractions and were insensitive to the grain size variance whereas for the samples with t_A/t_C ratios of 0.33 and 0.25, the void volume fractions depended on the grain size, which generally increased with grain size enlargement, reached a maximum value at grain size of 15nm and decreased at the grain size of 20nm. The voids formed in the nanolaminates were usually located at grain boundaries and are the result of grain boundaries and dislocation interactions at low strain (~0.06) shortly after stress overshoot [201]. Because of the high fraction of the amorphous phase, the dislocation activities at low strain for first two sets of CN-NLs were suppressed, which can be explained by the compound mechanism maps. At low strain about 0.06, the mechanism operating in these two sets for all

grain sizes was STZ dominated or GB + STZ with no trace of dislocations, which inhibited the initialization of grain boundaries voids. However, the prevailing STZs mechanism can also limit plasticity by triggering shear banding and the fast failure of nanolaminates, which will be discussed later.

The situation is quite different in high nanocrystalline phase samples (t_A/t_C = 0.33 or 0.5) in that grain size significantly affected the void volume fraction. The low void volume fractions for small grain sizes (5nm and 10nm) can be attributed to the lack of dislocations at the strain when voids are generally initialized. However, for larger grain sizes, the early activation of dislocations enabled the CN-NLs entering the Dislocation + STZ + GB zone quickly and promoted the grain boundaries and dislocations interactions. Undoubtedly, the grain boundary voids were greatly enhanced as well. The understanding of decreasing volume fraction after 15nm grain sizes can be referred to the strongest grain size (10 - 20nm) for nanocrystalline metals [20], where deformation shifts from the dislocation dominated mechanism to the grain boundary mediated mechanism. The lack of strain accommodation processes and thus stress concentration led to a higher void fraction for this cross-over grain size. However, as grain size increased to 20nm, the higher fraction of dislocations was triggered and coupled with STZ mechanisms, which relieved the stress concentration by providing more ACI sites instead of grain boundaries for strain accommodation and thus lowering the void volume fraction. The CN-NL with extremely large grain sizes is almost the same as the single crystal nanolaminate, in which no void was formed as proved in Chapter 2.

Another plasticity limiting factor is the shear banding in the CN-NLs. As shown in Fig. 3.6(c), the formation of a single mature shear band can lead to the catastrophic failure of CN-NLs. However, the characterization of shear bands is rather difficult for there is no method that can well distinguish shear band atoms from the rest of amorphous atoms. The only difference existing between two group of atoms is that the shear band atoms have extremely high shear strain value, which is usually ten times greater than the STZ threshold value and colored deep red as shown in Fig. 3.6(c). Therefore, if amorphous atoms with high shear strain are denoted as shear band atoms, the shear band atoms fraction was obtained by

dividing shear band atoms over total STZ atoms. Fig. 3.8(d) presents the four sets of CN-NLs' shear band atom fractions at the end of deformation (0.2 strain) as a function of grain size. Similar trends were found, where shear band atoms fraction increased with the grain size augment. The increasing level of dislocation and STZ coupling behavior was responsible for these increasing trends and the shear band aligning with dislocation slip bands in the large grain size samples. Meanwhile, the shear band atoms level for all four sets of samples are very close. However, when considering the amorphous phase fraction of different t_A/t_C ratios, the shear localization levels are essentially different and the following section will address this issue.

3.4 Property Mapping for Crystalline-amorphous Nanolaminate Design

In this section, the strength and plasticity of five sets of samples with different layer thickness and grain size combinations were combined into a property map, which lays down the blueprint for CN-NL design. Four zones with different properties were identified in the properties map and typical deformation snapshots were associated with property zones to uncover the relationship between deformation behaviors and mechanical properties.

Strength and plasticity indicators can be individually plotted as functions of characteristic length scales (t_A/t_C, d) as shown in Fig. 3.8. However, for design purposes, a map that includes all key mechanical properties for all samples is needed so that the ideal length scale samples with best mechanical performance can be identified. To construct such a map, axes should be set in the first place and thus the sample points can be placed on the map. In our map, the flow strength was chosen as the x-axis to represent the nanolaminates' strength property. Comparing to the effective yield stress, the average flow stress between 0.07 to 0.1 strain is a better representative for comparing strength difference of disparate deformation behaviors [20]. Because of the two plasticity limiting factors in nanolaminates (shear bands and grain boundary voids), the implication of plasticity requires two representatives in the properties maps as the y-axes, which are void localization and shear band localization factors. These two

localization factors were derived from void volume fraction and shear band atom fraction, respectively but were not exactly the same.

The following equation gives the calculation method of localization factors:

$$Void\ /\ Shear\ Band\ Localization\ Factor = \frac{F_i * W_i}{(\sum_i^N F_i * W_i)/N} \quad (3.2)$$

where F_i is either void volume fraction or shear band atom faction at the end of simulation (0.2 strain) of sample i; W_i is the weight imposed on the F_i, which can be the fraction of deformed atoms that contributed to either crystalline layer (GB + Dislocation) or amorphous layer (STZ) plasticity out of total plasticity carriers, and N is the total number of samples in this study. The reason why we put a weight on the F_i was that the void and shear band's contributions to the total plasticity were fundamentally different in the nanolaminate samples with t_A/t_C equal to 0.25 and 1.0. As demonstrated in Fig. 3.8(d), the shear band atoms fraction of t_A/t_C=1.0 for all grain size is at the same level compared to t_A/t_C = 0.25. However, when considering their contributions to the total plasticity, the t_A/t_C=0.25 sample was determined by either Dislocation + STZ + GB or Dislocation + STZ mechanisms combinations whereas t_A/t_C =1.0 was solely dictated by STZ mechanism. Therefore, a weighting multiplier is necessary for differentiating these two kinds of localization factors. At last, to bring all factors to the same level for convenient comparing, the initial weighted localized factors were normalized by all sample's average value. Therefore, void localization and shear band localization factors can be directly compared and the localized factor of 1.0 serves as the common average value for both localization factors.

The x coordination of each sample in the property map was simply determined by its flow stress value. However, the situation with y coordination is a little bit complicated since there exist two localization factors for each sample. Therefore, the localization factor with the higher value was chosen as their representative for this sample and denoted with a certain color and shape in the property maps. After positioning all the samples, four distinct zones are identified in the property map as shown in Fig. 3.9. To better understand the mechanical properties, typical snapshots of amorphous and nanocrystalline layers of

representative samples are presented in Fig. 3.10 for all four zones. At last, a table that summarizes the length scales, mechanisms, and properties for four zones is exhibited in Table 3.2 for the purpose of identifying ideal length scale with desired mechanical properties.

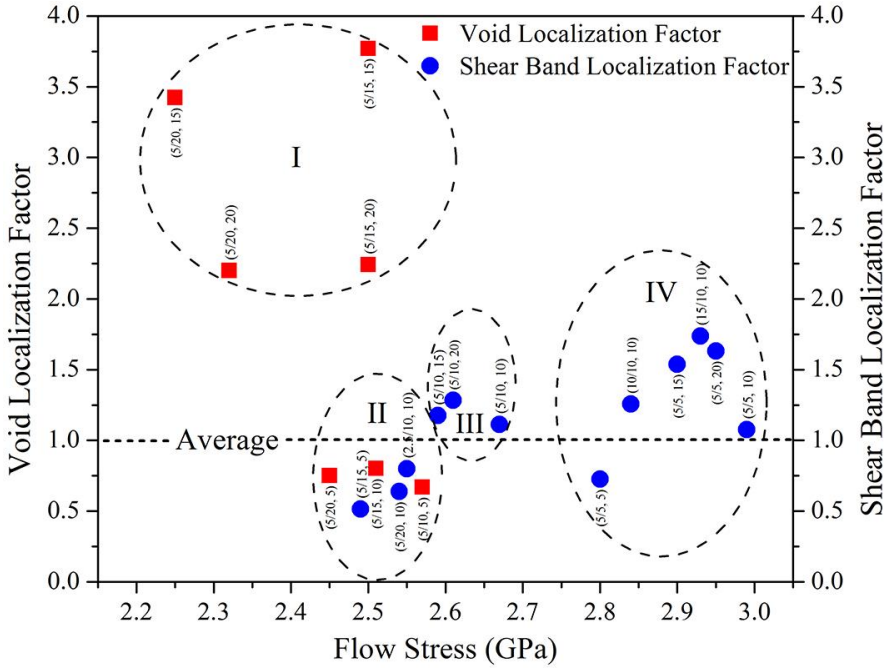

Figure 3.9 Property map for all sets of columnar nanocrystal-amorphous nanolaminates that includes one strength indicator (flow strength) and two plasticity indicators (void localization factor and shear band localization factor). The sample data points are denoted by (t_A/t_C, d), where d (nm) is the grain size of nanocrystalline layer and t_A and t_C (nm) are the layer thickness of amorphous and nanocrystalline layers, respectively. The x position of sample data points is determined by the flow stress whereas the sample's y position, shape, and color are determined by the higher value between the void localization and shear band localization factors. The dashed line is the average line for both void localization and shear band localization factors. Four zones with different properties are outlined and labeled as I, II, III, and IV.

Starting with Zone I, the samples in this zone yield a length scale of $t_A/t_C \leq 0.33$ and $d \geq 15$nm, which are dominated by the crystalline layer with large grain sizes. According to the compound mechanisms map, dislocation and STZ were the operating mechanisms in these samples, which is confirmed by the snapshots that distributed STZs and severe dislocations activities are observed in the amorphous and crystalline layers, respectively. Generally, this group of samples shows flow stress between 2.25 to 2.5 GPa, which is the lowest value among the four zones. The plasticity of this zones was solely determined by the void localization factor as they were labeled as red squares and way above the average line. Huge grain boundary voids are observed in the crystalline layer snapshot of typical zone I

sample agreeing with void localization factor values that this zone is limited by grain boundary voids. Zone II is still dominated by a crystalline phase featuring a layer thickness ratio of $t_A/t_C \leq 0.5$ but a smaller grain size of $d \leq 10$ compared to zone I. Due to the smaller grain size, the grain boundary mechanism was greatly promoted in the sample of this zone in addition to the dislocation and STZ mechanisms forming a triple mechanism mixing zone. The deformation snapshots display a distributed STZ behavior in the amorphous layer and evenly participated dislocation and grain boundary mechanisms in the crystalline layer. The mechanical performance indicates enhanced flow strength between 2.45 to 2.6 GPa and mixed localization factors, which are all below the average value. The excellent plasticity without sacrificing strength was obtained for this zone as the snapshots show no shear band and grain boundary void formation.

The samples with layer thickness ratio $t_A/t_C = 0.5$ and grain size $d \geq 10$nm compose the Zone III in the property map, where either dislocation + STZ + GB or dislocation + STZ combinations were found responsible for the operating mechanism in this zone. Multiple shear bands were observed in the snapshots in the amorphous layer with the dislocation slip bands and grain boundaries activities aligning with shear bands. Undoubtedly, the above-average shear band localization factors accounted for the plasticity limiting in this zone whereas the increasing level of STZs involved in the shear band deformation resulted in higher flow strength spanning 2.6 to 2.7 GPa. Zone III served as a transition zone from crystalline-rich to amorphous-rich zone IV, where the samples show layer thickness ratio $t_A/t_C \geq 1.0$ for any grain size. Zone IV was dominated by the single STZ mechanism, which led to severe shear localization and the tendency of forming a coupled single shear band and dislocation slip band in the CN-NLs. The mechanical properties in Zone IV suggest the highest strength but plasticity is significantly constrained by the shear band localization factor.

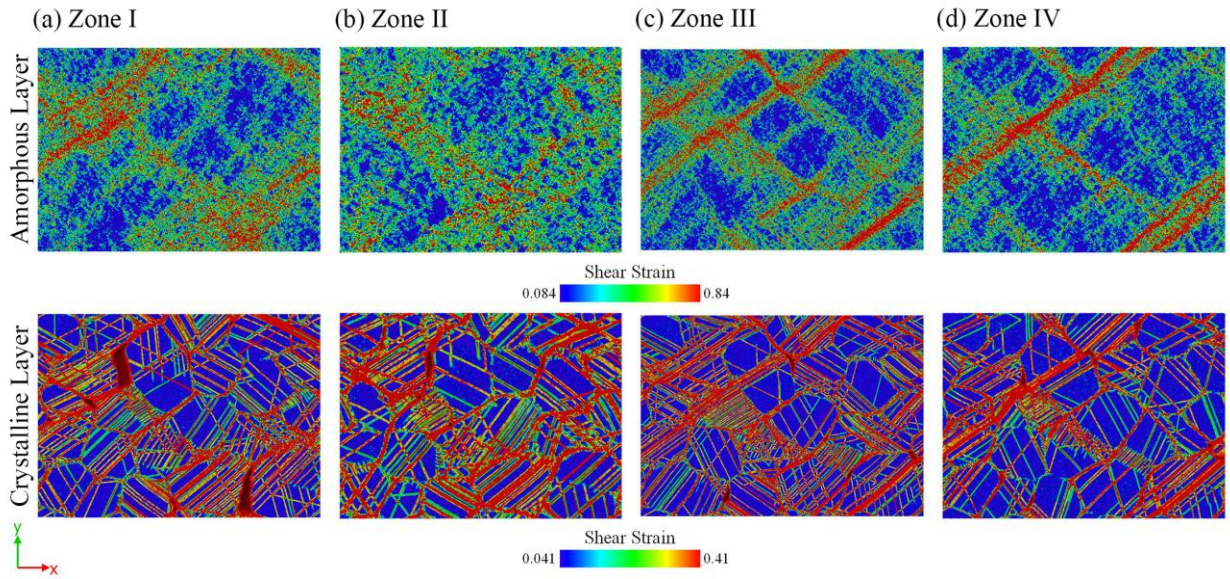

Figure 3.10 Amorphous and crystalline layers' deformation snapshots at the end of deformation (0.2 strain) of typical samples in Zone I (a), Zone II (b), Zone III (c), and Zone IV(d). Atoms are colored by the shear strain.

Table 3.2 Details of length scales, operating mechanisms, and properties of four property zones in Figure 3.10

Region	Length Scales	Mechanisms	Properties
Zone I	$t_A/t_C \leq 0.33$, $d \geq 15$nm	Dislocation + STZ	Lowest strength, severe void formation at GBs
Zone II	$t_A/t_C \leq 0.5$, $d \leq 10$nm	Dislocation + STZ + GB	Good strength, limited GB voids, distribution STZs
Zone III	$t_A/t_C = 0.5$, $d \geq 10$nm	Dislocation + STZ + GB Dislocation + STZ	High strength, full developed multiple shear bands
Zone IV	$t_A/t_C \geq 1.0$, any d	STZ	Highest strength, severe strain localization

The property map generated in this study disclosed the principle of nanolaminate structure design: the low t_A/t_C ratio ($\leq$0.33) with a large grain size length scale combination, such as zone I, biased the mechanical performance of the structure towards a nanocrystalline fashion, which is mainly limited by grain boundaries voids. The addition of amorphous layers to the structure can significantly enhance the strength of nanolaminates compared to monolithic nanocrystalline sample but the extreme increase of t_A/t_C over 0.5, such as Zone III and IV, led to severe shear localization in the deformation mode leaning towards an amorphous solid pattern. It is the crossover length scale combinations with low layer thickness

($t_A/t_C \leq 0.5$) and small grain sizes ($d \leq 10$nm), such as zone II, gave an optimal strength-toughness envelop in crystalline-amorphous nanolaminates by promoting mixed deformation mode to minimize grain boundary void formation and strain localization and achieve the best mechanical performance.

3.5 Concluding Remarks

In this chapter, tensile deformation of columnar nanocrystal-amorphous nanolaminates with varying layer thickness ratio and nanocrystalline grain size were simulated using molecular dynamics simulations. Novel deformation metrics were developed to capture the three major plasticity carriers, whose contributions to the global plasticity were quantitatively measured and incorporated into compound mechanisms maps. The correlation of CN-NLs' mechanical properties with the compound mechanism maps provides an in-depth understanding of nanolaminates' mechanical performance with respect to the characteristic length scales, summarized as follows:

i. The onset of plasticity behaviors of CN-NLs was collectively affected by the grain size and layer thickness ratio during the early stage of deformation. For the CN-NLs with a t_A/t_C ratio less than 1.0, the nanocrystalline layer grain size determined the onset of plasticity because of the grain boundary plasticity domination in the low strain deformation, where the "Hall-Petch Breakdown" was observed. However, as the t_A/t_C ratio increased above 1.0, the initial deformation of CN-NLs was strongly affected by the STZ plasticity, which deviated from the typical nanocrystalline metals' response at the finest grain size.

ii. The strength during the plastic deformation stage was dictated by the layer thickness ratio t_A/t_C of the CN-NLs. The flow stress was found increasing monotonously with the increase of layer thickness ratio t_A/t_C while being insensitive to the grain size variance of the nanocrystalline layer. The augment of STZ plasticity implied by the compound mechanisms maps accounted for this strengthening effect.

iii. The plasticity of CN-NLs was controlled by either the void or shear band localization factors based on the layer thickness ratio. The plasticity of crystalline-rich CN-NLs ($t_A/t_C<0.5$) is limited by the grain boundary voids because of the excess dislocation accommodation at the grain boundaries whereas the amorphous-rich CN-NLs ($t_A/t_C\geq0.5$) was constrained by the severe shear localization in form of single or multiple shear bands caused by STZ dominating plasticity or the continuous STZ and dislocation coupled deformation.

Coupling with the compound mechanisms maps, a property map that includes all the strength and plasticity aspects was generated at the end of this chapter in the context of optimizing the performance of CN-NLs. It is found that the ideal length scale combination of CN-NLs was to promote the mixed-mode deformation where coupling between the disparate mechanisms operating the crystalline and amorphous layers dominated the deformation behavior and prevented strain being localized to any form of single mechanism, which serves as a new mechanics-driven design principles for expanding the strength-ductility envelope for amorphous and nanostructured metals.

Chapter 4 Mechanical Behaviors of Grain Size Modulated Ni-W Nanolaminates Synthesized by Reverse Pulsing Electrodeposition

Most of the existing crystalline-amorphous nanolaminates were synthesized by thin film deposition methods, for example, magnetron sputtering. Even though high-quality nanolaminates with fully amorphous layers can be obtained by the sputtering methods, the relatively low deposition rate and high cost limit the scalable production of this novel metallic nanostructures. The reverse pulsing electrodeposition, developed by Detor and Schuh [34], enables the precise grain size control of nanocrystalline Ni-W alloys from a hundred to a few nanometers, which is approaching the amorphous limit. The finest grain size Ni-W alloys demonstrate glass-like deformation characteristics that are similar to the amorphous solids [35]. In addition, homogenous, high quality, large quantity deposits can be synthesized via electrodeposition within a relative short depositing time and at a low cost, which paves the way for large-scale production of this material and practical engineering applications.

It is in this vein that a grain size modulated Ni-W nanolaminate, which consists of nanoscale glass-like and nanocrystalline layers, is proposed and thus synthesized in this chapter using the reverse pulsing electrodeposition technique via manipulating the current waveform. The as-prepared Ni-W nanolaminates with different glass-like and nanocrystalline layer thickness ratios (t_A/t_C) along with two monolithic glass-like and nanocrystalline samples are characterized by X-ray Diffraction (XRD), scanning electron microscopy (SEM) and transmission electron microscopy (TEM) to confirm the grain structure and size, chemical composition, and layer thickness. Nanoindentation and strain rate sensitivity testing is performed to study the deformation behaviors of electrodeposited Ni-W nanolaminates emphasizing the hardness variation and transition of dominating deformation mechanism with respect to the layer thickness ratio.

4.1 Reverse Pulsing Electrodeposition Procedures

The synthesis of grain size modulated Ni-W nanolaminates starts with the choice of chemicals to be used in the electrodeposition bath. In this study, we adopted the ammoniacal citrate aqueous electrodeposition bath formulated by Yamasaki et al [47] as described in Table 4.1. The nickel and tungsten atoms are provided by metal salt nickel sulfate and sodium tungstate, respectively. However, it is well known that tungsten in pure form is very hard to be deposited from aqueous solutions, which is partly attributed to its low reduction potential [207-210]. Therefore, the sodium citrate and ammonium chloride were introduced to the bath as the complexing agents to facilitate the co-deposition of Ni and W via assimilating the reduction potentials of Ni and W [47, 211]. Finally, to enhance the conductivity and anode reactions, the sodium bromide was added to the electrodeposition bath [212, 213].

Table 4.1 Chemical composition of the ammoniacal citrate aqueous electrodeposition bath [47] for the synthesis of grain size modulated Ni-W nanolaminates.

Chemical Name	Chemical Formula	Concentration (g/L)
Nickel sulfate hexahydrate	$NiSO_4 \cdot 6H_2O$	15.8
Sodium tungstate dihydrate	$Na_2WO_4 \cdot 2H_2O$	46.2
Sodium Citrate dihydrate	$Na_3C_6H_5O_7 \cdot 2H_2O$	147.1
Ammonium Chloride	NH_4Cl	26.7
Sodium Bromide	NaBr	15.4

After mixing the chemicals, the electrodeposition bath was transferred into a Mini Mod 3 electrodeposition station manufactured by Technic Incorporated, which is equipped with a 1000W Teflon coated bottom heater regulated by a digital temperature control. The bath was continuously stirred by a McMaster stand-mount variable-speed electric mixer at a speed of 200 rpm while the bath temperature was maintained at the preset temperature regulated by the thermal control of bottom heater. Commercial 100 pure copper sheet (~12.9 cm^3 area), which came with a mirror finished state from the manufacturer, was used as the cathode or substrate material while inert platinum gauze was applied as the anode material. The cathode and anode submerged in the bath were then connected to an electroplating power supply provided by Digital Matrix Corporation and the current waveform was applied by the plating computer that controls the power supply. During the deposition, a low-flow metering pump was

employed to pump in pristine bath solution for compensating evaporated solution due to the high-temperature plating. A VWR B10P benchtop PH meter calibrated in standard buffer solutions was used to track the PH variance after each deposition and monitor the sudden drop of PH due to bath depletion.

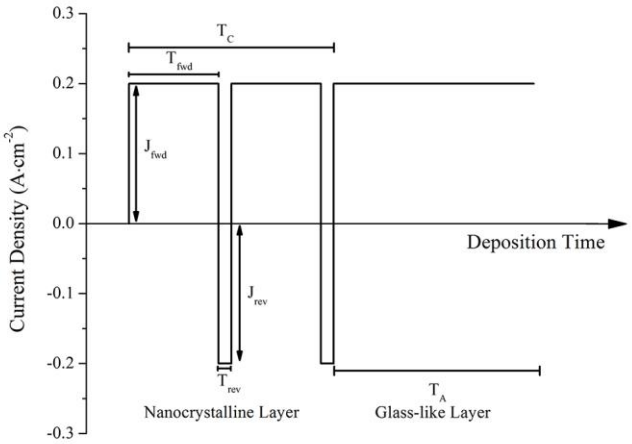

Figure 4.1 Schematic of the current waveform employed in the deposition of grain size modulated Ni-W nanolaminates, where J_{fwd} and J_{rev} are the forward and reverse current density, respectively; T_{fwd} and T_{rev} are the forward and reverse pulse duration, respectively; T_C and T_A are the deposition time of nanocrystalline layer and glass-like layer, respectively. Details are disclosed in Table 4.2 and 4.3.

The patterning of grain size modulated Ni-W nanolaminates is realized via manipulating the current waveform during the electrodeposition process. A typical schematic waveform used in this thesis is illustrated in Fig. 4.1 consisting of two stages. The first stage of the current waveform is the duty cycle for depositing nanocrystalline layers, where reverse pulsing is enforced. As demonstrated in Fig. 4.1, J is the current density and T is the pulsing duration. The subscripts fwd and rev of J and T represent the forward and reverse pulses, respectively. As demonstrated in Section 1.1.3, the precise control of nanocrystalline layer's tungsten composition and in turn grain size is accomplished by modulating the reverse current density J_{rev} or reverse pulse duration T_{rev}. Nevertheless, the composition manipulation is more repeatable by adjusting the magnitude of the reverse current density J_{rev} [34, 213]. Therefore, in this thesis, we only varied the J_{rev} and kept the T_{rev} as a constant during the deposition stage of nanocrystalline layers. The second stage of this waveform is designed for the electroforming of glass-like layers, during which direct current with no reverse pulse is used to deposit layers with the highest tungsten composition

and resulting finest grain size. Finally, the deposition time of nanocrystalline and glass-like stages, which is T_C and T_A, respectively, in Fig. 4.1, determine the corresponding layer thickness. As a result, by modulating the deposition time T_C and T_A, the grain size modulated Ni-W nanolaminates with different layer thickness ratios can be generated.

Table 4.2 Deposition conditions for the glass-like and nanocrystalline layers of grain size modulated Ni-W nanolaminates

Layer Type	Predicted Grain Size (nm)	J_{fwd} (A/cm^2)	T_{fwd} (ms)	J_{rev} (A/cm^2)	T_{rev} (ms)	Bath Temp. (°C)
Glass-like	5	0.2	20	Direct Current Deposition		75
Nanocrystalline	55	0.2	20	0.2	3	75

Choosing the grain sizes of individual layers in the grain size modulated Ni-W nanolaminates is critical in the study of layer thickness ratio's effect on the deformation behavior of nanolaminates. First, the deposition of two composing layers with different grain sizes must have the same bath temperature, which is another factor that controls the tungsten composition and grain size [34, 213]. Second, the strength and deformation behaviors of two composing layers need to be disparate so that the variance of strength and transition of deformation mechanisms can be delineated with respect to the changing of layer thickness ratio. Taking these two factors into consideration, the grain sizes of glass-like and nanocrystalline layers are chosen as 5nm and 55nm, respectively, which indicate hardness difference of ~1GPa and distinct deformation mechanisms reported by Trelewicz et al. [35]. The deposition conditions for these two layers are shown in Table 4.2, which shows they have the same forward current density of 0.2 A/cm^2, forward pulse duration of 20ms, and bath temperature of 75 °C. The difference in deposition conditions lies in the duty cycle of nanocrystalline layer deposition stage, where a 3ms reverse pulsing with a current density J_{rev} of 0.2 A/cm^2 is imposed.

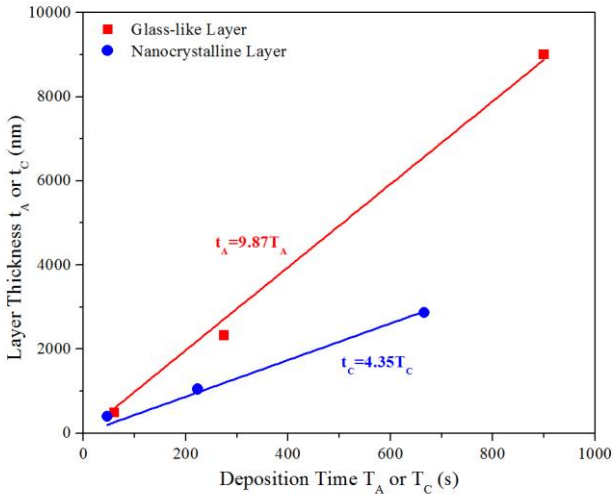

Figure 4.2 Electrodeposition rates of a glass-like layer with a grain size of 5nm and a nanocrystalline layer with a grain size of 55m. The red and blue lines are the linear fits to the data points of glass-like and nanocrystalline layers, respectively, and the fitting equations are displayed close to their corresponding fitting lines. The slope of each equation is the deposition rate with a unit of nm·s^{-1}.

Table 4.3 Target thickness and deposition time of the individual layers and the whole film of 11 samples with different layer thickness ratio. The table is arranged in a descending t_A/ t_C ratio trend, as listed in the last column.

Sample	Glass-like Layer		Nanocrystalline Layer		Total Deposition Time (min)	Predicted Total Thickness (μm)	Target t_A/ t_c Ratio
	Target Thickness t_A (nm)	Deposition T_A Time (s)	Target Thickness t_c (nm)	Deposition T_C Time (s)			
1	50000	6885	-	-	114.75	50	Max t_A
2	100	10	20	5	120	53.76	5
3	50	5	20	5	120	53.94	2.5
4	100	10	50	12	150.6	57.4	2
5	100	10	100	23	150	56.36	1
6	50	5	50	12	150	55.76	1
7	20	2	20	5	150	55.34	1
8	50	5	100	23	192	56.72	0.5
9	20	2	50	12	168	52.94	0.4
10	20	2	100	23	210	55.64	0.2
11	-	-	50000	12500	208.33	50	Min t_A

In the grain size modulated nanolaminates, the individual layer thickness depends on its deposition time, which requires the deposition rate of each type of layer to be determined in advance. As shown in Fig. 4.2, layer thickness values of glass-like and nanocrystalline layers are plotted as a function of deposition time based on the preliminary results. By performing linear regression on the raw data, the deposition rates were thus determined to be 9.87 and 4.35 nm/s for glass-like and nanocrystalline layers, respectively. Then, the grain size modulated nanolaminates with nine different layer thickness ratios together with two monolithic glass-like and nanocrystalline samples are designed. The target individual

layer thickness and deposition time are listed in Table 4.3 in a decreasing t_A/t_C sequence. Both the glass-like and nanocrystalline layer thickness range from 20nm to 100nm but the different layer thickness combinations result in a t_A/t_C ratio spanning from 5 to 0.2. The deposition time for the glass-like layer increases from 2 to 10s while for the nanocrystalline layer, it increases from 5 to 23s because of the disparate deposition rates. For all samples with a total thickness from 50 to 57 μm, a total deposition time of 114~210 minutes is required.

4.2 Characterization of the Grain Size Modulated Ni-W Nanolaminates

The structural characteristics and chemical compositions of as-deposited grain size modulated Ni-W nanolaminates were examined by a number of characterization methods starting with the SEM. The traditional metallographic procedures were employed to prepare the samples for the measurement of total cross-sectional thickness and chemical composition using a JEOL 7600F analytical high-resolution SEM equipped with an Oxford Instruments energy dispersive spectrometer (EDS). To measure the individual glass-like and nanocrystalline layer thickness, the backscattered electron imaging mode, whose brightness scales with the atomic number of element, was used so that these two layers with different tungsten compositions can be visualized because of the brightness contrast. X-ray diffraction (XRD) was carried out using a Rigaku Ultima III diffractometer operating at 40kV and 44mA to first estimate the mean grain sizes of monolithic glass-like and nanocrystalline samples and then confirm the single phase FCC solid solution with a polycrystalline grain structure. The Williamson-Hall method [46] was used to calculate the approximate mean grain size of nanocrystalline sample based on the $\{111\}$ family of peaks in the XRD spectrum whereas for the glass-like sample's spectrum where only the (111) peak was available, the single peak Scherrer analysis [214] was applied. The direct observation of the microstructure of nanolaminates relies on TEM examination. The standard in situ lift-out method was used to prepare TEM samples within a FEI Helios Nanolab 600 DualBeam Focus Ion Beam (FIB)/Scanning Electron Microscope (SEM) system equipped with a gallium ion source. The prepared samples were then

investigated by a JEOL 2100F TEM operating at 200kV, in which normal bright field imaging and selected area diffraction pattern (SADP) characterization were performed.

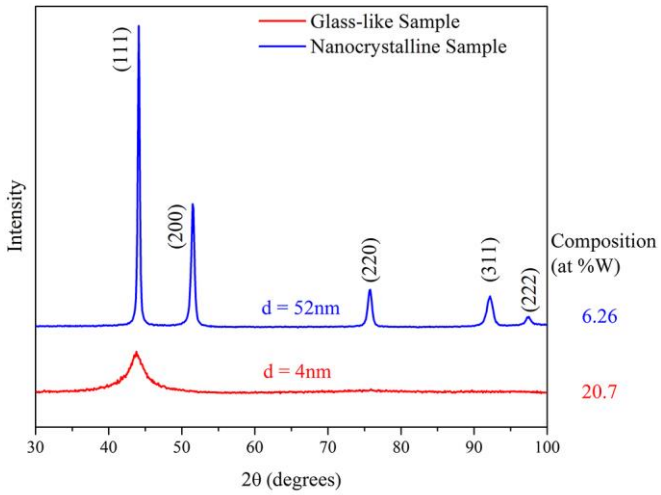

Figure 4.3 X-ray Diffraction (XRD) for the monolithic glass-like and nanocrystalline samples, whose tungsten compositions are measured by energy dispersive spectroscopy (EDS) shown on the right side of the figure. The grain size of the sample displayed near the corresponding spectrum is calculated using the Williamson-Hall method [46].

XRD spectra of monolithic glass-like and nanocrystalline samples are shown in Fig. 4.3, where the estimated grain size and EDS measured tungsten compositions are displayed near their corresponding spectra. The glass-like sample indicates a mean grain size of 4nm with a tungsten composition of 20.7% while the nanocrystalline sample reveals an average grain size of 52nm with only 6.26% tungsten composition in the deposit. These results suggest that by applying the reverse pulses, the tungsten atoms were indeed selectively stripped, resulting in a larger grain size as compared to the direct current deposited sample with a high tungsten composition and small grain size. The increase in the tungsten concentration also leads to a slight shift of peaks towards lower Braggs angles, which can be understood by the nickel lattice swelling because of the high tungsten alloying effect. Using Jade software, the peaks of the nanocrystalline sample were indexed and the crystallographic planes' Miller indexes are labeled near the peaks. The indexing result is similar to the standard single phase nickel FCC reflections confirming that the deposited nanocrystalline sample is indeed a single phase solid solution. However, for the glass-like sample, only the {111} peak was observed and substantially broadened because of the high tungsten composition. Despite a very broad peak in the glass-like sample's X-ray spectrum, the shape of

peak looks like an amorphous hump that is typical in the X-ray diffraction spectrum of the bulk metallic glasses [215] suggesting that there might be a large port of amorphous phase presented in the glass-like sample.

Three representative nanolaminates, which have the same target t_A/t_C ratio of 1.0 but varying individual layer thickness from 20nm to 100nm, were subjected to TEM investigations. The traditional bright field images of the cross-sectional nanolaminate microstructures are shown in Fig. 4.4 (a), (c), and (e) corresponding to the target individual layer thickness of 100, 50, and 20nm, respectively, and the insets are the SADPs of the corresponding images. It is evident that the modulated layer structures were attained by reversing pulsing electrodeposition as the drastic contrast difference between glass-like and nanocrystalline layers are captured. The brighter layers show the typical equiaxed microstructure of nanocrystalline Ni-W grains presented by Trelewicz et al. [35] and Detor et al. [34] while no obvious long-range ordered structure is observed in the glass-like layer suggesting a more disordered state in these layers. In the inset SADP images, the diffraction patterns confirm the equiaxed nanocrystalline grain structure as the diffraction spots are evenly distributed in the continuous rings. The SADPs are also free of partial diffraction rings that are commonly observed in the columnar grain structure with a strong (111) fiber texture in the magnetron sputtered crystalline-amorphous nanolaminates [39, 120, 123, 153, 158, 160]. Even though the typically diffuse rings of amorphous materials were not captured in the SADPs, the less sharp first diffraction rings with amorphous-like halo indicate the presence of the amorphous phase in the nanolaminates and this effect manifests as the individual layer thickness decreases.

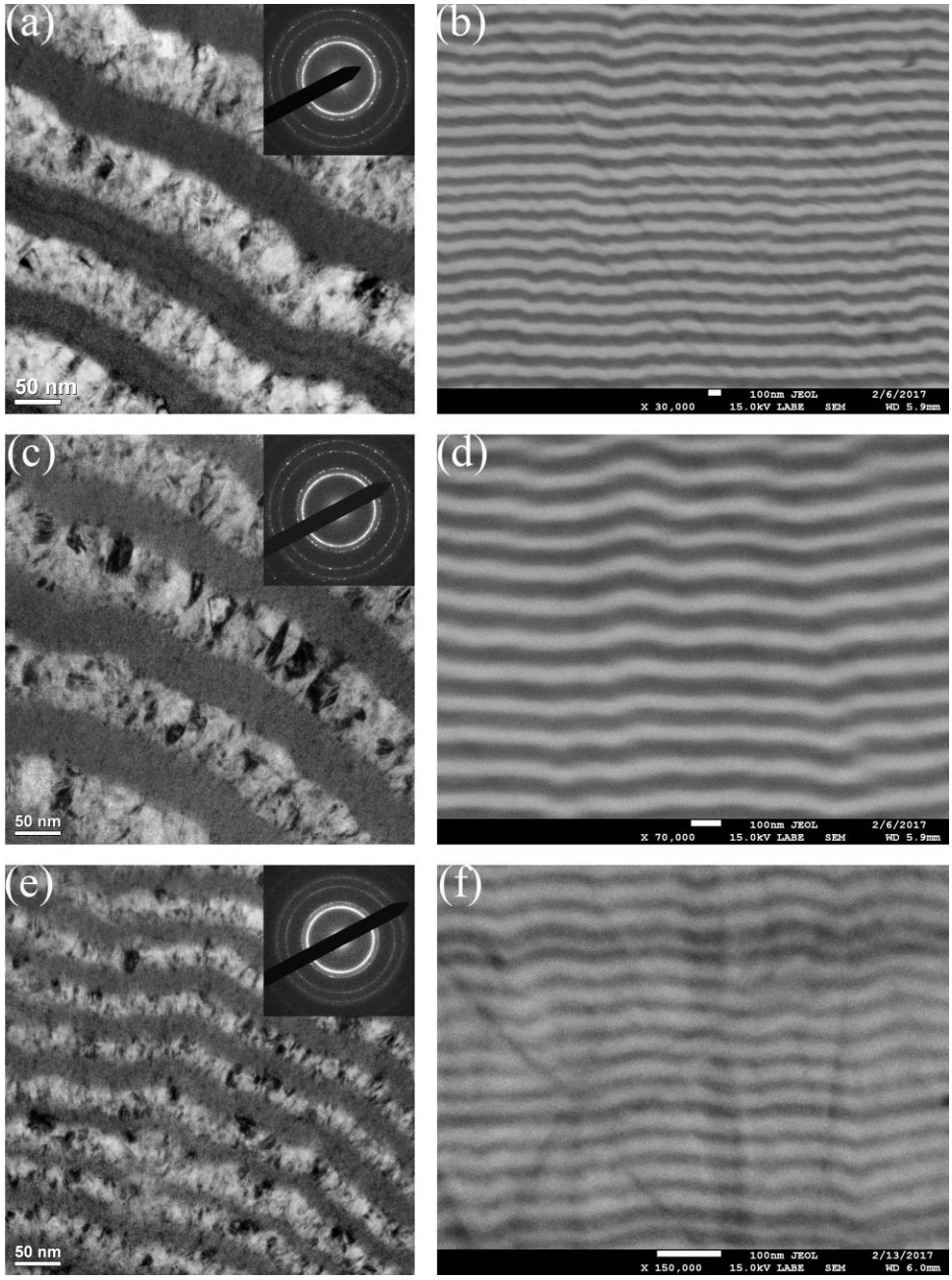

Figure 4.4 Bright-field TEM images and selected area diffraction patterns for the grain size modulated Ni-W nanolaminates with t_A/t_C ratios of (a) 57nm/69nm, (c) 40nm/46nm, and (e) 17nm/17nm and their corresponding SEM images (b), (d) and (f) acquired by backscattered electron signals.

Due to limited TEM and FIB resource time, the layer thickness of all nanolaminates is mainly measured by SEM analysis. The corresponding SEM images of the three representative nanolaminates investigated by TEM are shown in Fig. 4.4 (b), (d), and (f), respectively. Owing to the imaging mechanism of SEM, the detailed microstructural information of nanolaminates are inaccessible but the

layer thickness measurement can be performed by using the backscattered electron imaging mode, which is sensitive to the atomic number of element. Therefore, as shown in Fig. 4.4 (b), (d), and (f), the glass-like layers are much brighter because of the higher tungsten concentration and vice versa. Consequently, different layer length scales become distinguishable. By comparing the scale bar's pixel length to the pixel length of each individual layer, the thickness of nanocrystalline and glass-like layers can be precisely measured. To acquire statistically reliable results, each mean layer's thickness was measured by ten nanocrystalline or glass-like layers and averaged over 30 measurements. The same procedure was applied to three TEM characterized nanolaminates for comparison purpose.

Table 4.4 Actual thickness of the individual layers and the whole film of 11 samples measured by TEM and SEM, collectively. The tungsten composition of each sample is measured by EDS. The table is arranged in a descending t_A/ t_C ratio trend, as listed in the last column.

Sample	Glass-like Layer		Nanocrystalline Layer		Total Thickness (μm)	Composition (at %W)	t_A/ t_c Ratio
	SEM Thickness t_A (nm)	TEM Thickness t_A (nm)	SEM Thickness t_c (nm)	TEM Thickness t_c (nm)			
1	62750 ± 390	-	-	-	62.75 ± 0.39	20.7 ± 0.09	Max t_A
2	80.78 ± 4.4	-	19.69 ± 5.4	-	48.55 ± 0.47	21.11 ± 0.49	4.1 ± 1.15
3	41.17 ± 3.47	-	16.1 ± 2.9	-	38.28 ± 0.21	19.84 ± 0.05	2.56 ± 0.51
4	74.32 ± 4.59	-	40.01 ± 2.44	-	30.15 ± 0.2	20.34 ± 0.27	1.86 ± 0.16
5	16.67 ± 2.32	16.78 ± 2.06	16.78 ± 1.78	16.65 ± 2.85	49.11 ± 0.25	16.32 ± 0.44	0.99 ± 0.17
6	40.61 ± 3.72	40.07 ± 4.35	46.2 ± 4.8	48.17 ± 4.41	54.87 ± 0.14	13.68 ± 0.19	0.88 ± 0.12
7	62.96 ± 4.26	56.52 ± 4.37	74.83 ± 9.39	69.1 ± 9.09	41.2 ± 2.25	13.01 ± 0.13	0.84 ± 0.12
8	41.09 ± 5.44	-	76.65 ± 5.7	-	45.17 ± 0.12	13.92 ± 0.14	0.54 ± 0.08
9	19.94 ± 2.67	-	41.23 ± 1.72	-	51.91 ± 0.2	11.62 ± 0.02	0.48 ± 0.07
10	18.8 ± 2.79	-	76.07 ± 2.78	-	40.26 ± 1.43	12.39 ± 0.23	0.25 ± 0.04
11	-	-	57700 ± 730	-	57.7 ± 0.73	6.26 ± 0.07	Min t_A

The actual layer thickness measurements along with the tungsten composition and total deposit thickness results are disclosed in Table 4.4. Comparing the TEM and SEM layer thickness measurements of sample 5, 6, and 7, the results are fairly close and only show less than 10% error. Therefore, for unity, the SEM layer thickness results are used for representing the layer thickness measurement for all samples. Generally, the actual thickness of both nanocrystalline and glass-like layers are less than the target result, which might result from the different deposition rate of nanoscale layers. As shown in Fig. 4.2, the initial deposition rates were determined by the micron-size deposits, which might not be suitable for extrapolation into the nanoscale layers, especially with the two stages deposition of nanolaminates. As a result, the nanoscale deposition rates of nanocrystalline and glass-like layers are updated to 3.22 and 6.73

nm/s, respectively, for future depositions. The t_A/t_C ratios are also updated to correctly reflect the dominating phases in the nanolaminates. Interestingly, it seems like the tungsten composition measured by EDS is proportional to the t_A/t_C ratio as shown in Table 4.4.

4.3 Nanoindentation Testing of Grain Size Modulated Ni-W Nanolaminates

The mechanical behaviors of as-prepared grain size modulated Ni-W nanolaminates were studied by performing nanoindentation testing. The choice of instrumented indentation technique is attributed to the following reasons: first, the high throughput of nanoindentation testing, which requires only a small volume of testing materials, enables hundreds of indents within a single day of testing that ensures redundancy of testing and statistically reliable results; second, the testing sample preparation is relatively less difficult for nanoindentation comparing to uniaxial tensile testing, whose results are plagued by processing flaws introduced during the "dog bone" preparation of coating samples; Last but not the least, nanoindentation testing allows strain rate varying over three orders of magnitude making it possible for probing the strain rate sensitivity of nanostructured metallic materials.

The preparation of nanoindentation samples followed standard metallographic techniques. The prepared samples were tested by a Hysitron 1575 Triboscope Nanoindenter coupled with a Bruker Dimension ICON scanning probe microscopy (SPM). A diamond Berkovich tip, whose area function was carefully calibrated on fused quartz, was used to measure the hardness of samples. Depending on the specific hardness of samples, the typical indenting depth ranges from 220 to 270 nm corresponding to a constant peak load of 10mN used for all testing. Based on the standard Oliver-Pharr method [216], the hardness was extracted from the unloading part of the load-displacement curves. To ensure the statistical reliability of the testing results, at least 10 load-displacement curves were used to determine the hardness value of each nanolaminate sample. The testing condition for all indentation experiments adopted a constant strain rate $\dot{\varepsilon}$, which is defined by the equation:

$$\dot{\varepsilon} = \frac{1}{h}\frac{\partial h}{\partial t} \quad (4.1)$$

where *h* and *t* stand for indentation depth and time, respectively. As the prerequisite for enforcing constant strain rate, the loading rate normalized by the load ($\dot{P}/P$) must be kept as a constant during the loading section of nanoindentation testing [217]. To characterize the instrumental drift, a 10s holding segment was used during the unloading section at the 10% of the peak load. The load-displacement curves that show more than 5nm drift during the 10s hold were discarded.

Using the constant strain rate of $0.15s^{-1}$, the hardness of grain size modulated Ni-W nanolaminates are plotted in Fig. 4.5(a), together with the hardness levels of monolithic glass-like and nanocrystalline samples represented by the red and blue dash lines, respectively. The hardness value of nanolaminates plotted as a function of t_A/t_C ratio is found as the best way to represent the hardness variation with respect to the changing length scale since t_A/t_C ratio adequately reflects the dominating phases in the nanolaminates. The specific length scales of nanolaminates are listed on the right edge of Fig. 4.5(a) for reference. It is found that all the data points are located between the hardness levels of monolithic glass-like and nanocrystalline samples suggesting a composite-like mechanical response, which scales with the volume fraction of each composing phase. Therefore, by assuming no interaction between glass-like and nanocrystalline layers and an isostrain condition, the rule of mixtures predicted hardness of nanolaminates (H_{NL}) with different layer thickness ratios are calculated by the equation,

$$H_{NL} = H_A \frac{t_A}{t_A+t_C} + H_C \frac{t_C}{t_A+t_C} \quad (4.2)$$

where H_A and H_C are the hardness of glass-like and nanocrystalline layers, respectively. Then the rule of mixtures predicted hardness values are displayed as the green data points in Fig. 4.5(a) linked by a green dash line representing the trend of the rule of mixtures.

All nanolaminates' hardness values are above the rule of mixtures trend indicating the strengthening effect of the modulated layer structure. However, two disparate trends of nanolaminates' hardness are observed. For samples with t_A/t_C greater than 1.0, the hardness value follows the rule of mixtures trend as it increases with the enhancing volume fraction of glass-like phase. Nevertheless, no apparent hardness trend was observed among the samples with t_A/t_C less than 1.0. The hardness values are

fluctuating between 7.4 to 7.8 GPa and insensitive to the length scale variation. To quantitatively measure the strengthening effect, hardness enhancement, which is the difference between the measured hardness and rule of mixtures predicted hardness, are mapped in Fig. 4.5(b) as a function of t_A/t_C. It is evident that the strengthening effect is significant in the nanolaminates with a high fraction of the nanocrystalline phase ($t_A/t_C \leq 1.0$). Particularly, for the nanolaminate with thin glass-like layers ($t_A/t_C \leq 0.5$), the hardness enhancement reached up to 0.5~0.6 GPa relative to the rule of mixtures predicted values. The disparate hardness trend and strength enhancement results with respect to the t_A/t_C suggest that the deformation mechanisms in these two t_A/t_C regions are substantially different, which will be addressed in the latter part of this section.

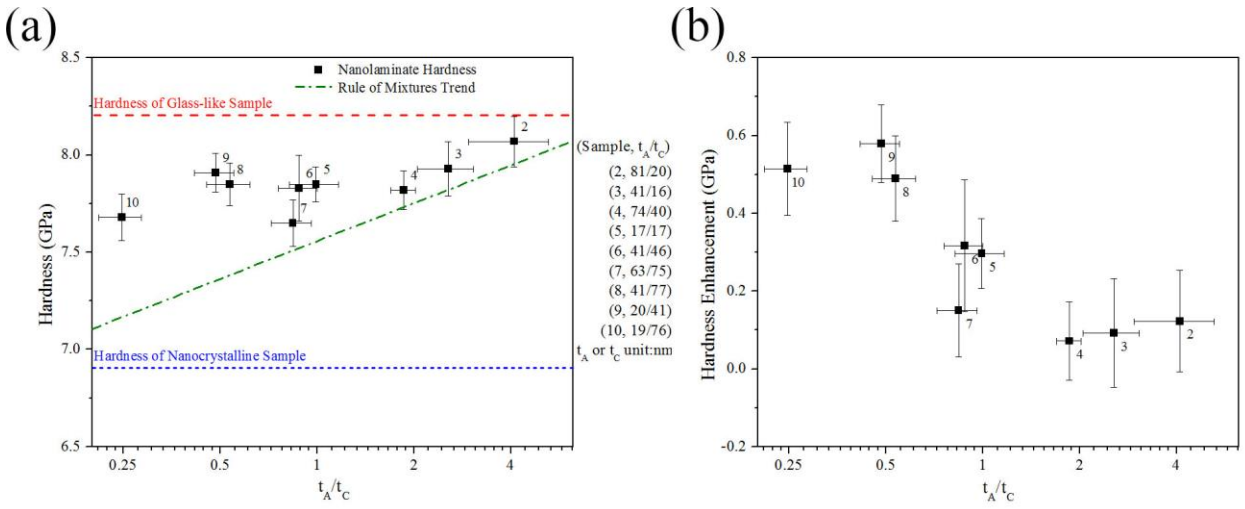

Figure 4.5 (a) Hardness plotted as a function of layer thickness ratio t_A/t_C for the grain size modulated Ni-W nanolaminates. The red and blue dash lines are the hardness values of monolithic glass-like and nanocrystalline samples, respectively, which are also used to calculate the hardness predicted by the rule of mixtures. The predicted hardness trend is displayed as green dash line. Specific t_A/t_C of each sample is listed on the right side of the (a) in the form of (sample, t_A/t_C), where t_A and t_C are in units of nanometer. (b) Hardness enhancement as a function of t_A/t_C, which are calculated based on the difference between the actual hardness of samples and their rule of mixtures predicted hardness. The t_A/t_C axes in (a) and (b) are formatted in a logarithm scale.

The effect of length scales to the nanolaminates' mechanical performance has been investigated by a number of studies using either nanoindentation or micropillar compression testing on the magnetron sputtered crystalline-amorphous nanolaminates [120, 123, 160, 164, 218]. Most suggest an apparent strength scaling with respect to the microstructural length scales, which can be explained by either rule of mixtures [160], Hall-Petch scaling [218], or confined layer slip (CLS) theory [120, 136], especially for the crystalline-rich nanolaminates. However, in our case, the strength scaling trend is found in

nanolaminates with a high glass-like phase fraction (t_A/t_C >1.0), whereas for nanocrystalline-rich (t_A/t_C ≤1.0) nanolaminates almost no length scaling effect has been observed.

From a structural perspective, the difference in strength scaling effect between existing magnetron sputtered nanolaminates and our electrodeposited nanolaminates lies in the grain structure of crystalline layer. In the magnetron sputtered nanolaminates, almost all the crystalline layers show the strong (111) fiber texture while in the electrodeposited nanolaminates, equiaxed grain structure was attained with random orientations. Demonstrated by several experimental works [39, 122, 123, 155, 159, 160] and our simulation work in Chapter 2, the (111) texture results in some close-packed planes perfectly aligning with the 45° max resolved shear stress plane and substantial promotion of the coupled deformation of STZs and dislocations. The dislocation triggered by the shear transformation zone (STZ) at one amorphous-crystalline interface (ACI) can glide through the entire nanograin and be absorbed by the opposite ACI [39, 201]. As a consequence, the thickness of nanocrystalline layer plays a vital role in the nucleation and propagation of dislocations and determining the strength of nanolaminates as described by the Hall-Petch scaling [218] and CSL theory [120, 136]. Due to the equiaxed grain structure in our electrodeposited nanolaminates, this perfect alignment of the close-packed plane and max resolved shear strain plane might not be as prevalent as those in the magnetron sputtered nanolaminates. Even in some cases, dislocations might not be activated due to the extremely unfavorable grain orientation for dislocation nucleation. In addition, the nucleated dislocations might be hindered or deflected by another grain boundary preventing it from reaching the opposite ACIs. The mechanical behaviors of grain size modulated nanolaminates suggest a different deformation mechanism as compared to the magnetron sputtered crystalline-amorphous nanolaminates.

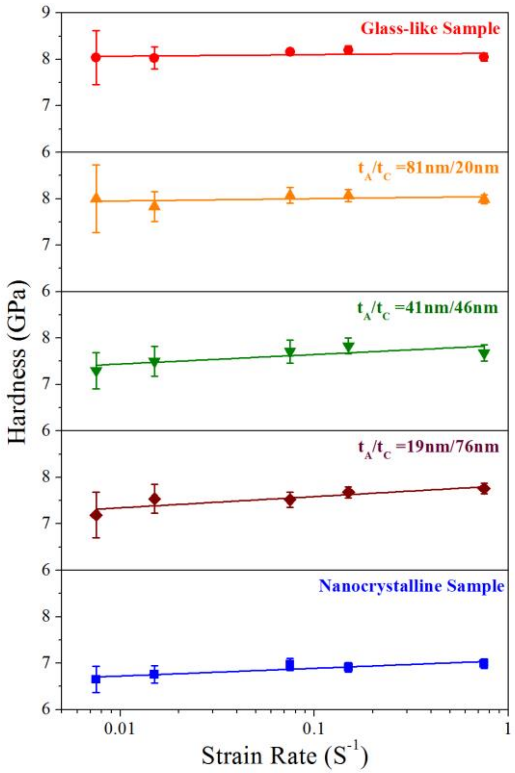

Figure 4.6 Hardness as a function of strain rate for five representative samples, including monolithic glass-like and nanocrystalline samples and grain size modulated Ni-W nanolaminates with t_A/t_C of 81nm/20nm, 41nm/46nm, and 19nm/76nm. The strain rate axis is formatted in a logarithm scale. The error bars of some samples are too small to be visualized in this plot.

Strain rate sensitivity testing was performed to investigate the transition of deformation mechanism regarding the length scale of grain size modulated nanolaminates. Five constant strain rates of 0.0075, 0.015, 0.075, 0.15, and 0.75 s^{-1} were used in the strain rate sensitivity tests covering over 3 orders of magnitude. A minimum of 10 indents were performed to determine the hardness at each strain rate. The hardness of three representative nanolaminate samples along with two monolithic glass-like and nanocrystalline samples are plotted in Fig. 4.6 as a function of strain rate. It is clear that the nanocrystalline sample is strain rate sensitive as its hardness apparently increases with the increasing strain rate indicating a typical nanocrystalline metals' response. However, the hardness increase in the plot of the glass-like sample is almost inconspicuous, suggesting that it is strain rate insensitive similar to the typical response of amorphous solids [35]. For the nanolaminates, the samples with t_A/t_C = 41nm/46nm and 19nm/46nm are clearly strain rate sensitive where for the t_A/t_C = 81nm/20nm sample, no

significant hardness increase was captured, which means the deformation of this sample is more like strain rate insensitive amorphous solids. Therefore, there must exist a transition length scale where the rate-dependent nanocrystalline-like deformation behavior shifts to rate-independent amorphous-like mechanical response.

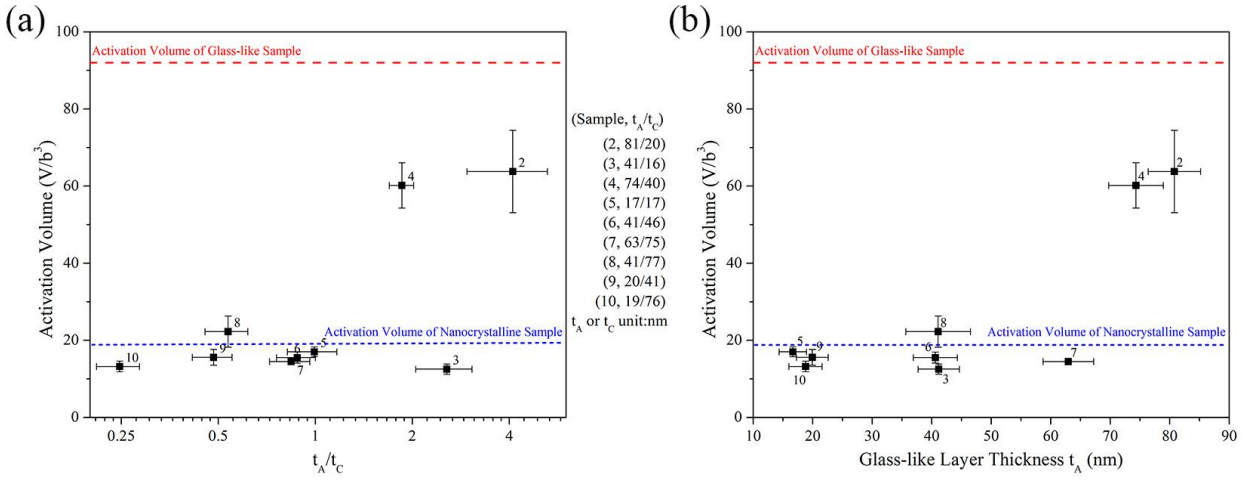

Figure 4.7 Activation volume for the deformation of grain size modulated Ni-W nanolaminates as a function of t_A/t_C ratio (a) or glass-like layer thickness (b). The activation volume is normalized by the cubed Burger vector (b^3) of nickel lattice. The red and blue dash lines are the activation volume values of monolithic glass-like and nanocrystalline samples, respectively. The specific t_A/t_C of each sample is listed on the right side of figure (a) in the form of (sample, t_A/t_C), where t_A and t_C are in units of nanometer. The strain rate axis is formatted in a logarithm scale in figure (a).

To quantify the rate-dependent hardness, a traditional method is adopted by calculating the apparent activation volume (V) for deformation [197], which is defined as,

$$V = 3\sqrt{3}kT\frac{\partial \ln \dot{\varepsilon}}{\partial H} \quad (4.3)$$

where H stands for indentation hardness, $\dot{\varepsilon}$ stands for the strain rate, k is the Boltzmann constant, and T is the temperature. Generally, a high activation volumes is related to a strain rate insensitivity and vice versa. By performing the linear regression of the hardness trends like those shown in Fig. 4.6, the $\partial \ln \dot{\varepsilon}/\partial H$ values of all samples were determined and substituted into Eq. (4.3). The calculated apparent activation volume normalized by the cubed Burgers vector (b^3) of nickel is plotted as a function of t_A/t_C ratio as shown in Fig. 4.7, where the red and blue dash lines exhibit the activation volumes of glass-like and nanocrystalline samples, respectively. Most of the activation volume values of nanolaminates samples with a t_A/t_C ratio less than 1.0 are slightly below nanocrystalline sample's value of ~20 V/b^3 meaning that

they show a deformation behavior close to the nanocrystalline metals, which is rate-dependent. As the t_A/t_C ratio increase above 1.0, the activation volume surges to about 60~65 V/b^3, which is relatively close to the glass-like sample's value of 90 V/b^3. However, there is an exception, which is sample 3 with a t_A/t_C of 2.56. The activation volume of sample 3 is much lower than other nanolaminates with higher glass-like layer fraction and even less than the nanocrystalline samples' value.

Further investigation reveals that the samples with low activation volume have a glass-like layer thickness less than 70nm, which means the activation volume might scale with the thickness of glass-like layer instead of t_A/t_C ratio. Therefore, the activation volume as a function of glass-like layer thickness t_A is plotted in Fig. 4.7. Evidently, the nanolaminates with t_A less than 65nm have low activation volume values, which are close to the monolithic nanocrystalline sample, corresponding to a typical rate-dependent mechanical response of nanocrystalline metals. As the t_A increases above 70nm, the nanolaminate samples' activation volume jumps to 60~65 V/b^3, which is similar to the glass-like sample's value. This suggests these two samples performed more like amorphous solids, whose hardness or strength is rate-independent, and were deforming via a glass-like inhomogeneous flow or, in particular, shear banding. Therefore, the glass layer thickness of 65~70 nm is determined as the critical length scale, where the deformation mechanism transits from rate-dependent nanocrystalline mode to rate-independent amorphous solids fashion. This critical length scale will serve as the design principle for optimizing the mechanical performance of grain size modulated Ni-W nanolaminates.

4.4 Concluding Remarks

In this chapter, the grain size modulated Ni-W nanolaminates were successfully synthesized using reverse pulsing electrodeposition. Using TEM and SEM, the microstructure of as-prepared nanolaminates were confirmed to contain alternatively patterned glass-like and nanocrystalline layers. The equiaxed grain structure was observed in the nanocrystalline layer while no long-range order was captured in the glass-like layer. The layer thickness of glass-like and nanocrystalline layers was precisely measured by examining TEM and SEM images collectively. Then, the nanolaminate samples were subjected to the

instrumented nanoindentation and strain sensitivity testing. The hardness and activation volume were attained and mapped as a function of microstructural length scales. Significant insight was gained into the mechanical behaviors of the grain size modulated nanolaminates, which can be summarized as follow:

i. The hardness of nanolaminates strongly depended on the layer thickness ratio. For the nanolaminates with t_A/t_C greater than 1.0, the hardness value scaled with the increasing t_A/t_C ratio following the trend predicted by the rule of mixtures. However, as the t_A/t_C decreased below 1.0, the hardness of nanolaminates was insensitive to the layer thickness ratio variation, which is attributed to the equiaxed grain structure of nanocrystalline layer hindering the STZ-dislocation coupled deformation. In addition, the substantial strengthening effect of nanolaminates with thin glass-like layers ($t_A/t_C<0.5$) was achieved.

ii. The strain rate sensitivity of nanolaminates was determined by the glass layer thickness t_A. The nanolaminates with a t_A less than 65~70nm indicated a strain rate sensitivity corresponding to a low activation volume. However, as t_A increased above 70nm, the deformation of nanolaminates became strain rate insensitive, which was manifested by a sudden increase of activation volume to a high level. Therefore, the 65~70nm glass-like layer thickness was identified as the critical length scale, where deformation behaviors of nanolaminates transited from the rate-dependent nanocrystalline mode to the rate-independent amorphous fashion.

Based on the above results, the mechanical behaviors of grain size modulated Ni-W nanolaminates can be understood in the context of unique microstructure characteristics and substantial length scale effects. These findings will serve as a new design principle for using structural or length scale characteristics to tune and optimize the mechanical performance of grain size modulated nanolaminates.

Chapter 5 Capturing the Glass-Glass Interfaces in the Computational Nanoglass Model

The interface characterization models discussed in Chapter 1 are derived from the bicrystal-like or planar glassy-glassy interfaces [43, 180], which might not be a good representative for nanoglasses formed by inert gas condensation (IGC) or sputtering processes. The core-shell models [44, 178] generated by consolidating glassy spheres are constrained by its size, which is not suitable for mechanical deformation simulations. Although intriguing interfacial properties have been explored by these models, they are generally limited by their idealized configurations and scalability. In this chapter, we develop a novel method that employs volumetric strain and atomic volume distribution to distinguish the interface and grain regions in a large-scale 3D nanoglass model consolidated from glassy spheres using molecular dynamics simulations. The interface volume fraction and width are adequately estimated accompanied by the disclosure of excess free volume and short-range order characteristics. The result is a scalable nanoglass model with an excellent description of interface and grain regions that permits large-scale deformation and annealing simulations.

5.1 Simulation Procedures

Molecular dynamic simulations were carried out using the LAMMPS package [185] and atomic interactions were simulated using the embedded-atom method (EAM) potential developed by Mendelev et al [200] for a Cu-Zr binary system. A computational $Cu_{64}Zr_{36}$ bulk metallic glass (BMG) sample was first generated by slowly quenching a liquid Cu-Zr alloy equilibrated at 2000K for 2ns to 50K using a cooling rate of $0.01K \cdot ps^{-1}$. The quenched BMG sample indicates a good agreement with literature reported structures in terms of partial radial distribution functions and short-range orders [219, 220]. Glassy spheres with a diameter of 15nm were then cut from the BMG samples and stacked in a FCC configuration resulting in an unconsolidated nanoglass structure with 64 glassy spheres and a total number of atoms of about 7 million. Before the consolidation simulation, an energy minimization procedure was performed for the initial structure to avoid atom overlapping and thus achieve a final

relative energy convergence of 10^{-12}. The consolidation process was realized via loading an external hydrostatic pressure up to 9 GPa and holding for 100 ps at 50K to eliminate voids in the initial structure following by an unloading of pressure to obtain pressure-free conditions in all dimensions. An isobaric-isothermal (NPT) ensemble was employed to control the pressure and temperature and a constant integration time step of 2 fs was used for all simulations.

The characterization of as-prepared nanoglass sample starts with the calculation of volumetric strain, which is the hydrostatic part of the strain tensor, using the unconsolidated structure as the reference. The atoms with significant volume change after consolidation are thus highlighted. In order to perform structural analysis at an atomic resolution, the Voronoi tessellation [188] was applied by taking the positions of atoms as the seeds and dividing the simulation cell into Voronoi polyhedra around the seeds. Then each atom's Voronoi polyhedron was used to precisely calculate atomic volume and Voronoi index, which is crucial for identifying the most prominent short-range order-Cu-centered full icosahedron (FI)-in the Cu-Zr metallic glass system [219, 221]. A surface mesh method [222] was adopted to calculate the void volume fraction during the densification process of nanoglass. The abovementioned characteristics of nanoglass were calculated using the open-source OVTIO software [195], which was also employed for the visualization of structures. A volumetric strain-assorted atomic volume distribution fitting code was developed by the authors to delineate interface and grain regions. For all characterization methods that demand a cutoff distance, a radius of 3.5 Å was used enclosing the first shell of the nearest neighbor atoms. Finally, to ensure the repeatability of the simulations, all reported results were averaged among five independently consolidated and characterized nanoglass samples.

5.2 Generation of Computational Nanoglass Model

The initial FCC stacking of glassy spheres is shown in Fig. 5.1(a), where copper and zirconium atoms are colored red and blue, respectively. Periodic boundary conditions are applied in all three dimensions to ensure the bulk continuity of model. For glassy spheres with equal diameters, FCC stacking

possesses the highest packing density, which reduces the difficulty in eliminating the void regions between spheres shown in the y-z plane cross-sectional view of a 1nm thick nanoglass slice in Fig. 5.1(b). Atomic volume distributions are introduced by calculating the atomic volume of atoms using the Voronoi tessellation method outlined in Section 5.1. Fig. 5.1(c) demonstrates the comparison of atomic volume distributions of initial structure (blue) and BMG sample (black) used for generating glassy spheres. The first distribution peaks centered around 12.5 $Å^3$ correspond to the copper atoms whereas the second peaks centered around 22.5 $Å^3$ link to the zirconium atoms. Despite a little bit of serration, which can be attributed to lack of relaxation process, the initial NG structure's distribution looks very similar to the distribution of BMG expect for the appearance of surface atoms, which usually have an abnormal atomic volume that lies outside of the normal distribution. As depicted in the inset of Fig. 5.1(c), the surface atoms of copper cause the NG's distribution to become higher than the BMG's distribution for the atomic volume above 15 $Å^3$ and the same situation is observed in zirconium atoms.

After the consolidation process, the densified nanoglass was generated and displayed in Fig. 5.1(d), where the structure is free of voids, but the interface is still difficult to be visualized. With the help of volumetric strain, the interfaces emerged and are shown in Fig. 5.1(e) y-z plane cross-sectional view of consolidated nanoglass slice, in which high volumetric strain is observed in the two regions: initial central void and spheres contiguous regions. The high value of volumetric strain in the interfaces signifies the substantial change of atomic volume after consolidation. On the contrary, the initial spheres' central regions show a very low level of volumetric strain that is close to zero indicating almost no volume change during the consolidation. These regions are thought to be grain regions, where the glassy nature is preserved. The atomic volume distribution of consolidated nanoglass (red) is shown in Fig. 5.1(f) with the distribution of BMG. Immediately, it is found that the serration of NG's distribution was removed because the consolidation simulation allowed the local relaxation of atoms, which smoothed the distribution. The densification of initial structure eliminated the surface atoms as evident by the inset of Fig. 5.1(f), in which the copper atoms that have an atomic volume greater than 15 $Å^3$ disappeared.

However, the increase of atom fraction in high atomic volume regions (13~15 $Å^3$ for Cu and 23~25 $Å^3$ for Zr) signals the appearance of atoms with large atomic volume. On the whole, the consolidation of initial structure resulted in the shift of atomic distribution slightly to the right (higher atomic volume) when comparing to the BMG's distribution, suggesting the redistribution of atoms to the interface region with enhanced atomic volume.

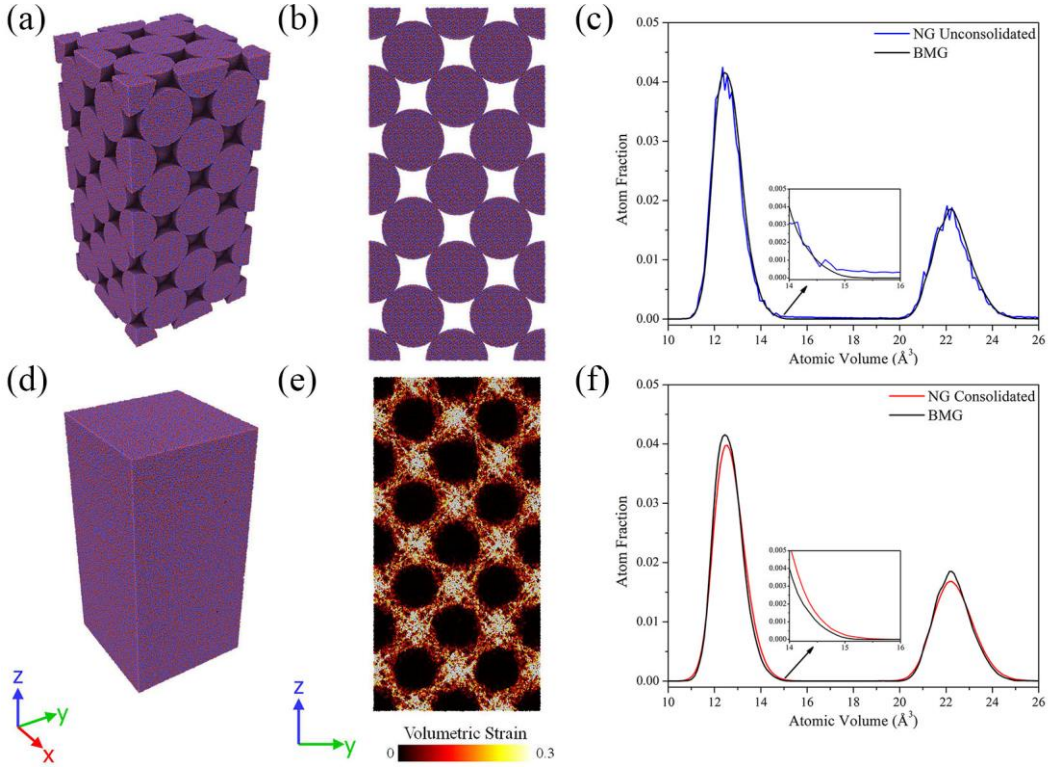

Figure 5.1 (a) Initial FCC stacking of $Cu_{64}Zr_{36}$ glassy spheres. Cu and Zr atoms are colored red and blue, respectively. (b) y-z plane cross-sectional view of 1nm slice cut from initial structure. (c) Atomic volume distribution of bulk metallic glass (BMG) and unconsolidated nanoglass (NG). Inset is the enlarged view of BMG and unconsolidated NG's atomic volume distributions between 14 to 16 $Å^3$. (d) Consolidated nanoglass model. (e) y-z plane cross-sectional view of a 1nm slice cut from consolidated nanoglass colored by volumetric strain. (f) Atomic volume distributions of bulk metallic glass (BMG) and consolidated nanoglass. The inset is the enlarged view of BMG and unconsolidated NG's atomic volume distributions between 14 to 16 $Å^3$.

The consolidation pressure is found to play a critical role in the consolidation process of nanoglass for a high pressure was needed to generate a void-free sample but the loading of pressure must be controlled to avoid detrimental effects to the interfaces. The volume fraction of voids as a function of consolidation pressure was mapped in Fig. 5.2(a). With the increase of pressure, the void volume fraction

decreased and the void-free nanoglass was only obtained at a pressure of 9GPa, which doubles the value of pressure used in the experiment [99]. The reason for this extremely high pressure is that our study aims to use only mechanical force to consolidate the glassy spheres so the temperature was kept at 50K to exclude external thermal effect. The low-temperature consolidation inevitably requires high pressure to densify the nanoglass. The loading scenario of consolidation pressure is another factor that affects the interface properties. As shown in Fig. 5.2(b), there is a system temperature surge at the first 20 ps when loading the pressure. If the pressure is applied instantly without any ramp period, the temperature surge peak could rise to 450K. Because of the shock-like loading of pressure, the overheated region was mainly observed in the interfaces, whose local temperature may rise above the glass transition temperature as illustrated in the inset of Fig. 5.2(b).

Fortunately, a pressure ramp can reduce the peak system temperature spike. As illustrated in Fig. 5.2(b), the peak temperature was progressively reduced with the decreasing pressure ramp rate. Interestingly, small humps at the very beginning of consolidation were observed in the temperature profiles for scenarios with pressure ramps. It is believed that the temperature increase before these humps was caused by the elastic energy storage and after these humps, the interfacial materials started to flow and fill the empty space. Therefore, further temperature increase can be attributed to the friction as the materials flow. After the peak temperature, the void region was filled and the system temperature was equilibrated to the set temperature of 50K. The situation was quite different for the scenario without a pressure ramp. No small hump was observed upon the loading of pressure and the materials were pushed into the voids leading to the extremely high-temperature spike. However, despite the effect of reducing the temperature spike, the voids in the consolidated nanoglasses cannot be eliminated with the decreasing pressure ramp rate as shown in Fig. 5.2(c). The ramp rate of 1.5 GPa/ps was determined to be the ideal scenario that not only guaranteed the full dense sample but also reduced the temperature surge peak by half when compared to the no pressure ramp scenario. In addition, it is found that the densified process happened only in the initial temperature surge period, which is the first half of the total 100ps

consolidation time. The increase of consolidation time after temperature stabilization will not help the densification process.

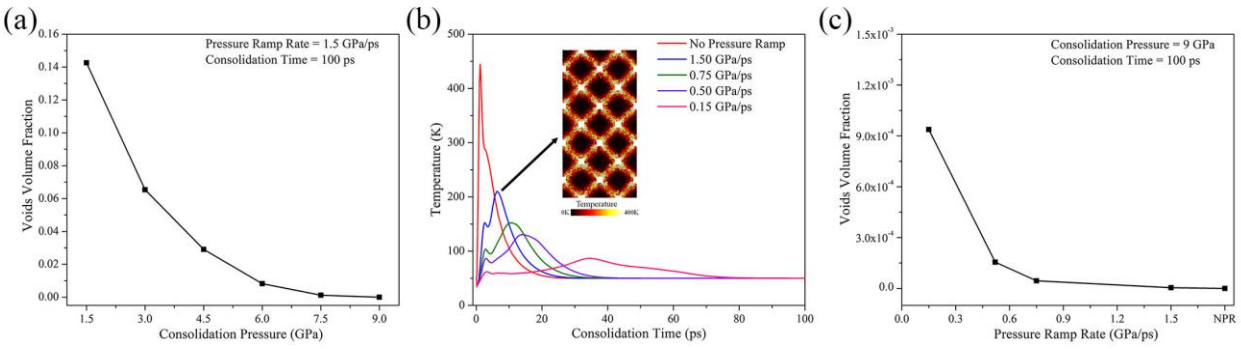

Figure 5.2 (a) Void volume fraction as a function of consolidation pressure. (b) System temperature profiles as a function of consolidation time for five different pressure ramp rates. (c) Void volume fraction as a function of pressure ramp rate. NPR is the abbreviation of no pressure ramp.

5.3 Determining the Interface and Grain Regions in the Consolidated Nanoglass Model

The interface region of consolidated nanoglasses is characterized by high volumetric strain and an enlarged atomic volume but it is still difficult to quantify the volume fraction of the interface region. Coupling the significant volume change and atomic volume enhancement features of interfaces, a volumetric strain assorted atomic volume distribution fitting method that can quantify interface region is hereby presented via setting a volumetric strain threshold for interface atoms. As discussed in Section 5.2, the atomic volume distribution of consolidated nanoglasses contains both interface and grain atoms' contributions. To decompose this distribution, a key value of variance χ^2 is developed and defined as:

$$\chi^2 = \sum_k^N [F_C(k) - F_R(k)]^2 \quad (5.1)$$

where k stands for the k^{th} bin of discretized atomic volume in the distribution function, N is the total number of bins used in the distribution function and $F_C(k)$ and $F_R(k)$ are the atom fraction values for the k^{th} bins of current and reference states, respectively. In this case, the current state is the consolidated nanoglass and the reference state is the BMG sample. The atomic volume distribution of initial nanoglass

would be a better choice for a reference state but the abnormal atomic volume of surface atoms and serration in the distribution make the fitting extremely difficult. Basically, the variance value provides a measurement of atomic volume distributions difference between current and reference states. The larger the variance value is, the more substantial the difference of two structures is.

Based on the spectrum of volumetric strain, a temporary cutoff $\boldsymbol{\varepsilon_v^{cutoff}}$ was set, which was sampled consecutively from 0 to 0.5 with an increment of 0.001. For those atoms that have volumetric strain from 0 to $\boldsymbol{\varepsilon_v^{cutoff}}$, the atomic volume distribution was generated and the variance value was calculated. For instance, Fig. 5.3(a) shows atomic volume distributions of BMG atoms and a subset of consolidated nanoglass atoms with volumetric strain ranging from 0 to 0.01. To clearly demonstrate the difference between these two distributions, only copper peaks are shown in Fig. 5.3(a). For atoms showing a low volumetric strain value (0~0.01), the distribution reveals an obvious shift of copper peak to a lower atomic volume and enhanced peak height indicating this group of atoms has a highly compact atomic packing and strongly resistance to volume change against compression loading. The inset snapshot of consolidated nanoglass slice in Fig. 5.3(a) reveals this subset of atoms colored by green are mainly located in the very center of grain region, which is also the sphere center of the unconsolidated nanoglass as shown in Fig. 1(b). The distribution and snapshot suggest that this central grain region is characterized by low atomic volume and high density, which agree with the Danilov et al. [178] characterization of core region of their core-shell model obtained through consolidation of gas condensed glassy spheres that the central core region has a higher density than both the shell region and BMG sample. Because of the large difference between this subset and BMG distributions, a large variance value of 2.92×10^{-5} was attained.

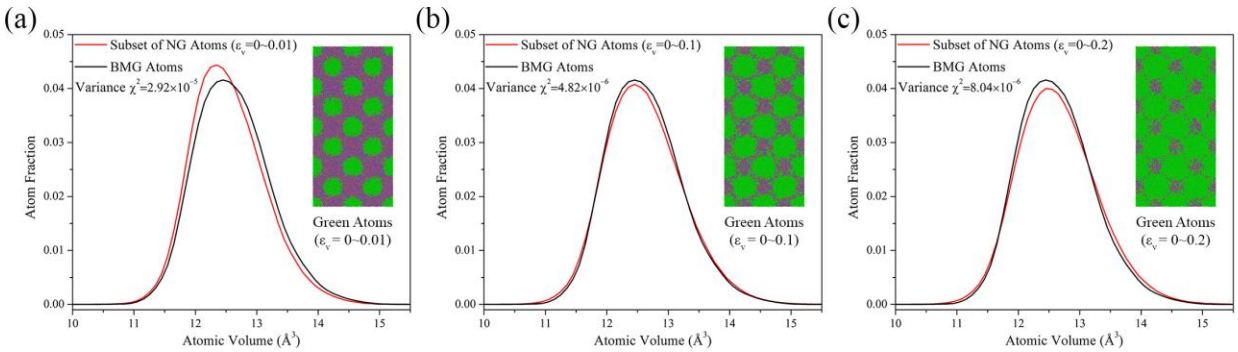

Figure 5.3 Atomic volume distributions of BMG atoms and a subset of consolidated nanoglass atoms with volumetric strain range of (a) 0~0.01, (b) 0~0.1, and (c) 0~0.2. For clarity, only copper peaks are shown in the distributions comparisons. The inset of each figure is the snapshot of nanoglass slice where atoms within certain volumetric strain range are colored green.

Increasing the $\boldsymbol{\varepsilon_v^{cutoff}}$ value to 0.1, the distribution of new subset nanoglass atoms looks closer to the BMG's shown in Fig. 5.3(b) expect for a higher atom fraction in the low atomic volume region between 11 and 12 Å^3 and a lower peak height, which might result from compressive loading and the denser central grain region. The inset snapshot of Fig.5.3(b) shows that the outer shell atoms of the central grain region were included and this group of atoms have higher atomic volume and more likely underwent volume change during the consolidation process. Together with the central grain atoms, this subset of atoms discloses a similar atomic volume packing as the BMG sample and the variance dropped to 4.82×10^{-6}. Based on the first two steps of distribution fitting process, an interesting aspect of nanoglasses is found that the redistribution of atomic volume was obtained even in the unconsolidated glassy spheres, where the core is already denser than the loosely packed shell. The surface effect of the finest size glassy nanoparticle might significantly affect the consolidation process and interface properties of consolidated nanoglass.

Increasing the $\boldsymbol{\varepsilon_v^{cutoff}}$ to 0.2, atoms that are located in or near the interface region as shown in the inset of Fig. 5(c) were included in the NG's distribution leading to an apparent shift of peak to the higher atomic volume and an obvious enhancement of atom fraction in the high atomic volume region between 13.5 and 14.5 Å^3 as illustrated by the distribution in Fig. 5.3(c). The inclusion of interface atoms undoubtedly increased the variance value to 8.04×10^{-6}. Consequently, there must exist a minimum value

of variance between $\boldsymbol{\varepsilon_v^{cutoff}}$ value 0.1 and 0.2, which is able to isolate the grain atoms that highly resemble the glassy BMG atoms from the interface region with enhanced atomic volume.

Variance is then plotted as a function of volumetric strain cutoff as shown in Fig. 5.4(a), where a minimum value is achieved at the volumetric strain of 0.088. The atomic volume distribution of atoms that have volumetric strain value less than 0.088 shows the highest resemblance or best fit to the BMG's distribution. Thus, this group of atoms is thought to be glassy grain atoms that kept most of the features of BMG whereas the atoms that have volumetric strain more than 0.088 are interface atoms. The volumetric strain threshold is therefore set as 0.088. The comparison of interface and grain atoms' distributions to the BMG distribution is shown in Fig. 5.4(b). It is evident that the distribution of interface atoms significantly deviates from the BMG distribution. Not only did peaks shift considerably to the right but also were broadened signifying the conspicuous dilatation of local atomic configuration. On the contrary, the distribution of grain atoms is very close to the BMG distribution except for a very small shift to the left because of the consolidation process.

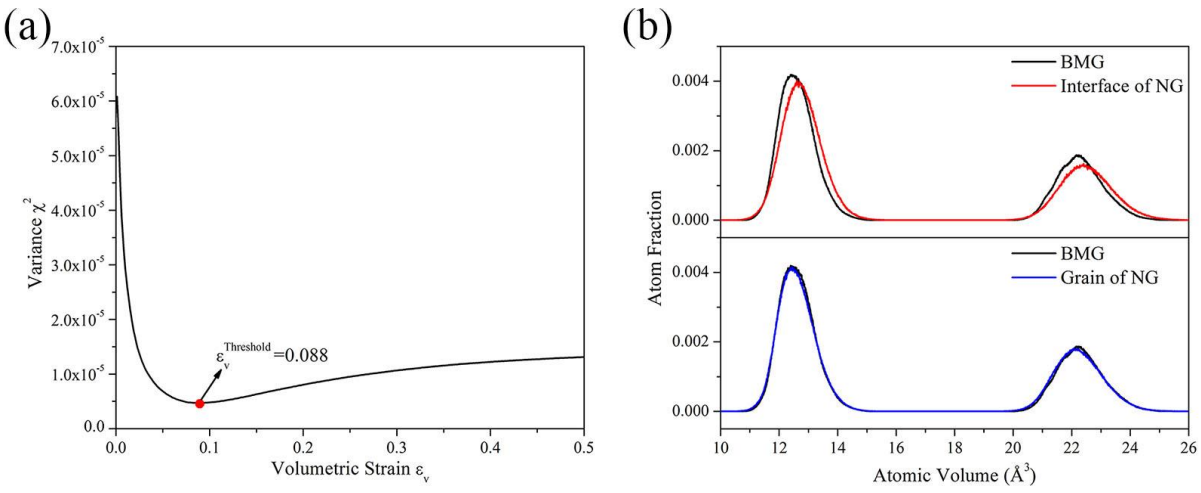

Figure 5.4 (a) Variance χ^2 as a function of volumetric strain cutoff. (b) Comparison of the atomic volume distributions of interface (red) and grain (blue) to the BMG's distribution (black).

5.4 Characterization of Interface and Grain Region in the Consolidated Nanoglass Model

Once the volumetric strain assorted atomic volume distribution fitting method was developed, it was applied to five individually consolidated 15nm grain size nanoglass samples to get statistical results about the structural properties of interface and grain regions, which are tabulated in Table 5.1 with the BMG's value for comparison. The volumetric strain thresholds were determined to be around 0.088 for five samples with a very good consistency. The most important characteristic of nanoglasses is the volume fraction of interface region, which was easily obtained using the abovementioned method by summing the atomic volume of atoms with a volumetric strain greater than the threshold value and normalizing it by the total structure's volume. The calculated result indicates a volume fraction of 0.3591, which is very close to the experimentally determined interface volume fraction of 0.35 [99]. On the other side, the interface region indicates a substantial deviation to the BMG configuration showing a variance value one order of magnitude greater than the grain region, which kept the glassy nature of BMG. Not surprisingly, the average volumetric strain of interface atoms is ten times greater than their grain region counterparts suggesting that during the consolidation process, the volume change of atoms was limited to the interface region.

The atom-based structural properties demonstrate even more differences between the interface and grain regions and can be directly compared to the BMG's properties. As shown in Table 5.1, the average atomic volume of Cu and Zr atoms in the interface region are all greater than the values of grain region, which is just slightly lower than the BMG's value. This approximately 1.3% enlargement of atomic volume can be viewed as the excess free volume of interface with respect to the grain region and agrees with the result reported by Ritter et al [43]. In terms of the short-range order, it is observed that the FI fraction of the interface is only half the value of grain region, which is much closer to the BMG's value. Undoubtedly, the defective short-range order is found in the interface but the grain region also shows a subtle deviation from BMG, which might be attributed to the slight breaking of FIs caused by compressive loading. Compared to the planar glassy-glassy interface models [43], the glass-glass

interfaces generated in this study disclose a higher resemblance to the shear bands as the interfacial FI fraction is almost the same as the literature reported FI fraction of shear bands [223]. The consolidation of glassy spheres resulted in a more disordered interface than joining two planar glassy interfaces. In addition to the structural properties, the segregation phenomenon is also captured in this study. As the chemical compositions of NGs and BMGs are similar shown in Table 5.1, the segregation of Cu atoms to the interface and Zr atoms to the grain are observed, which can be explained by Adjaoud et al.'s [44] finding that due to the larger cohesive energy, Zr atoms with larger atomic radius tend to segregate to the grain to optimize the binding energy and reduce the surface excess energy. Interestingly, in our study, this unnormal segregation behavior is observed even without heat treatment.

Table 5.1 Structural properties of bulk metallic glass (BMG) and nanoglass (NG)

	BMG	NG	Interface of NG	Grain of NG
Volumetric Strain Threshold	-	0.088 ± 0.002	-	-
Volume Fraction	-	-	0.3591 ± 0.0054	0.6409 ± 0.0054
Variance	-	1.52E-5 ± 2.63E-7	9.57E-5 ± 6.33E-7	4.7E-6 ± 4.79E-8
Average Volumetric Strain	-	0.1059 ± 0.0001	0.2541 ± 0.0025	0.0229 ± 0.0004
Cu Atomic Volume ($Å^3$)	12.62	12.67 ± 0.0009	12.78 ± 0.0012	12.61 ± 0.0004
Zr Atomic Volume ($Å^3$)	22.31	22.35 ± 0.0007	22.52 ± 0.0028	22.26 ± 0.0005
FI Fraction	0.2677	0.1861 ± 0.0009	0.1186 ± 0.0002	0.2252 ± 0.0008
Cu Atom Fraction	0.6408	0.6408 ± 0.0002	0.6533 ± 0.0005	0.6338 ± 0.0003
Zr Atom Fraction	0.3592	0.3592 ± 0.0002	0.3467 ± 0.0005	0.3662 ± 0.0003

With the help of volumetric strain threshold, the width of the interface region can be estimated using the following method. As depicted in Fig. 5.5(a), the 5nm thick y-z plane and close-packed plane slices of consolidated nanoglass are shown and colored by the volumetric strain. The scale of volumetric strain's color legend is specially chosen as it starts from the threshold value of this sample and ends at two times the threshold value. Therefore, the interfacial atoms are greatly highlighted. As illustrated in the y-z plane slice, there are two types of interfaces: the normal interfaces where the glassy spheres were initially contiguous and the triple junctions where the initial voids were located. The interfaces are more evident in the close-packed plane slice, where they are displayed in a hexagonal shape and triple junctions are located at the converging points of three normal interfaces.

To obtain the width of normal interfaces, a red dash line that is 45° to the z-axis is drawn crossing four normal interfaces with the volumetric strain profile along the red dash line plotted as a function of distance to the center of the coordination system. The plot is shown in Fig. 5.5(b), where four peaks are observed corresponding to four interfaces as a sign of the severe volume change during the consolidation. Then, a dashed line that has a y value equal to the volumetric strain threshold value is drawn intersecting the four peaks of volumetric strain profile. The distance between the points of intersections for each peak is the estimation of the width for this interface. Using the method developed above, the average width for 20 interfaces of 5 nanoglass samples was determined to be 2.01 ± 0.23 nm. The same technique was applied to the triple junctions intersected by the blue dash line shown in Fig. 5.5(a) and a width of 8.54 ± 0.22 nm was obtained by averaging 10 triple junctions. It is obvious that the triple junctions' volumetric strain is much higher and the width is much thicker than the normal interfaces as illustrated by the peaks' height and width of volumetric strain profile in Fig. 5.5(c). These triple junctions were filled by the surface atoms of glassy spheres and possess an atom packing that is significantly different from grain atoms. The normal interfaces and triple junctions contribute the total interface region volume fraction of 0.36, which is not observed in the former bicrystal-like [43] and Voronoi partitioned nanoglass models [180, 183, 184] and might be a better representative of experimentally accessible nanoglass structures [99].

Aside from the width, the atomic volume and short-range order of the interfaces were examined as well. The second rows of Fig. 5.5(b) and (c) show the normalized atomic volume as a function of distance along the red or blue dash line. The atomic volume was normalized by the slice's average value to sharpen the difference between interface and grain regions. As seen in the normal interface's profile in Fig. 5.5(b), the peaks of normalized atomic volume coincide with the peaks of volumetric strain profile indicating a 1~2% excess free volume above the average value. The circumstance is even more distinct in the triple junctions, where wide regions of excess free volume up to 6% are captured and well correspondent to the volumetric strain peaks. With respect to the short-range order, the calculated FI

fraction along the red and blue dash line is shown in the third rows of Fig. 5.5 (b) and (c), respectively, in which a dashed line indicates the FI fraction of BMG. The low FI fraction regions in both normal interfaces and triple junctions concur with the volumetric strain and excess free volume peaks and can reach down to 0.1, which is significantly lower than the BMG's FI fraction. The rest of region is oscillating around the dashed line of BMG's FI fraction suggesting these regions preserved the initial glassy state. Therefore, the excess free volume and defective short-range order are successfully characterized in the consolidated nanoglass.

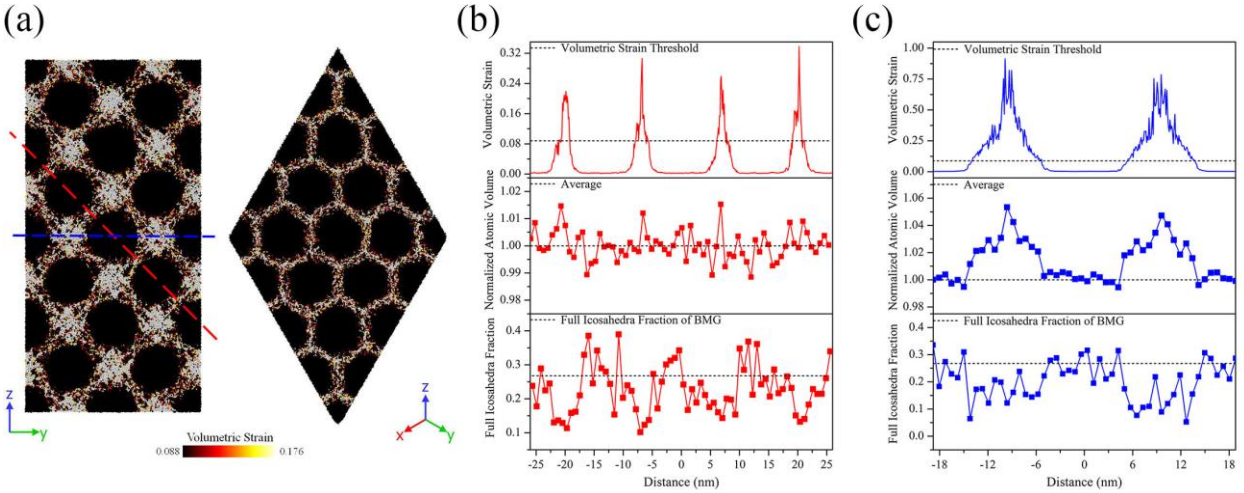

Figure 5.5 (a) 5nm thick y-z and close-packed plane slices of consolidated nanoglass colored by the volumetric strain. The volumetric strain profile, normalized atomic volume and full icosahedra (FI) fraction as a function of distance along the red dash line (b) and blue dash line (c) in the y-z plane slice.

5.5 Concluding Remarks

In this chapter, a large-scale 3D nanoglass model was developed by consolidating FCC stacked 15nm grain size glassy spheres using the hydrostatic pressure and an optimized consolidation scenario was disclosed. Using the volumetric strain coupled with the atomic volume distribution, a novel method that can successfully delineate the interface and grain regions of consolidated nanoglass was established. The characterization of the consolidated nanoglass demonstrated an interface region with a volume fraction of 0.36 that consists of normal interfaces with a width of 2.01 ± 0.23 nm and triple junctions with a width of 8.54 ± 0.22 nm. The interface region was characterized by an enlarged atomic packing in forms of 1.3% excess free volume and a defective short-range order in terms of FI fraction being half the value

of grain region. In addition, the segregation of atoms with large potential energy to the grain region was also captured. The consolidation and characterization methods developed in this chapter pave the way for studying nanoglasses with different grain sizes and annealing states. The correlation of the interface properties to the mechanical performance of nanoglass will provide an excellent explanation for the intriguing deformation behaviors exhibited by glass-glass interfaces, which will be discussed in the next chapter.

Chapter 6 Interfacial Plasticity Governs Strain Delocalization in Nanoglasses

Due to the presence of glass-glass interfaces, nanoglasses indicate an excellent plasticity without catastrophic failure via shear banding, which has been proved by a number of experimental studies. However, controversy remains in the computational studies of nanoglass deformation behaviors with respect to the grain size's effect. The lack of representativeness of existing nanoglass computational models for the experimental nanoglass structure might account for this controversy. On the other hand, despite several sporadic studies, nanoglass mechanical performance after annealing has not been systematically studied. The relationship of interface properties of nanoglasses and their deformation behaviors has not been established yet, which hinders the understanding of nanoglasses' intriguing mechanical behaviors. In this chapter, nanoglasses with different grain sizes are generated by consolidating glassy spheres as extensively described in Chapter 5 and one selected nanoglass is annealed at different temperatures. Simulated uniaxial tensile testing is performed in these nanoglasses with different annealing states and grain sizes and interface properties are correlated to the mechanical behaviors of nanoglasses for an in-depth understanding of the unique deformation mechanisms of nanoglasses.

6.1 Simulation Procedures

The general molecular simulation settings remained the same as described in Chapter 5. Following the same procedure, nanoglasses consolidated from FCC stacked glassy $Cu_{64}Zr_{36}$ spheres with different grain sizes were prepared and the detailed information is disclosed in Table 6.1, where eight sets of nanoglass samples are exhibited. The grain sizes of the sample set 1 to 7 increases from 2.5 to 17.5 nm with a 2.5 nm increment, among which the sets with grain sizes of 2.5, 5, 7.5, 10, and 15 nm have the same simulation domain but changing total spheres number. As shown in Fig. 6.1, because of the same domain size and total number of atoms, four initial structures with different grain sizes have the same length scale and can be compared directly. For the sample sets with grain sizes of 12.5 and 17.5nm, they

were unable to fit into the same simulation domain as other sets while keeping a periodic FCC stacking. Therefore, these two sets of samples have the same total number of spheres (64) with a changing simulation domain. Five individually consolidated nanoglass samples were prepared for each set from 1 to 7 to acquire statistical results of the nanoglass properties. The nanoglass sample set 8 with a grain size of 10nm was intended for the annealing study. Therefore, a total of three smaller samples with 64 glassy spheres and 2 million atoms were prepared so that they were suitable for annealing simulations with an extended timescale. In addition to the nanoglass samples, a bulk metallic glass (BMG) sample that was used to generate the glassy spheres was prepared for the comparison of deformation behaviors of BMG to the nanoglasses.

Table 6.1 Details of initial nanoglass structures for consolidation

Sample Set	Grain Size (nm)	Total Spheres	Total Atoms (million)	Stacking	Number of Samples
1	2.5	55296	7	FCC	5
2	5	6912	7	FCC	5
3	7.5	2048	7	FCC	5
4	10	864	7	FCC	5
5	12.5	64	4	FCC	5
6	15	64	7	FCC	5
7	17.5	64	11	FCC	5
8	10	64	2	FCC	3

The densification process of initial nanoglass structures was accomplished via applying the hydrostatic pressure to the simulation domain. Using a loading rate of 1.5GPa/ps, the consolidation pressure was ramped up to 9GPa and held for 100ps to eliminate voids. To capture the void evolution during the consolidation process, a surface mesh method [222] was employed to calculate the volume fraction of voids as a function of consolidation pressure for different grain sizes, which are shown in Fig. 6.2. It was found out that a consolidation pressure of 9 GPa was necessary to achieving fully dense nanoglass samples for all grain sizes and the difficulty of obtaining void-free samples scaled with the grain size of initial nanoglass structures. To exclude the external thermal effect, all consolidation processes were carried out at 50K and only a mechanical force was used to densify the nanoglass samples,

which inevitably required a high consolidation pressure. The hydrostatic pressure was ramped down and relaxed to attain a pressure-free condition for later deformation simulations. The simulated annealing of nanoglasses was performed on as-prepared 10nm nanoglass samples of set 8, which were heated to 300K, 550K, and 800K using a ramping rate of $1K \cdot ps^{-1}$ and then annealed at these elevated temperatures for 2ns. Then, the annealed samples were cooled down to 50K using the same ramping rate of $1K \cdot ps^{-1}$ for characterization and deformation. For the deformation simulation, uniaxial tensile loading was applied in the z-direction and the samples were deformed at 50K using a strain rate of $10^8 s^{-1}$. During tensile testing, the pressure in the x- and y- directions were relaxed to zero to allow lateral contraction. The NPT ensemble was used to control the pressure and temperature and periodic boundary conditions were applied to ensure the bulk form of nanoglasses.

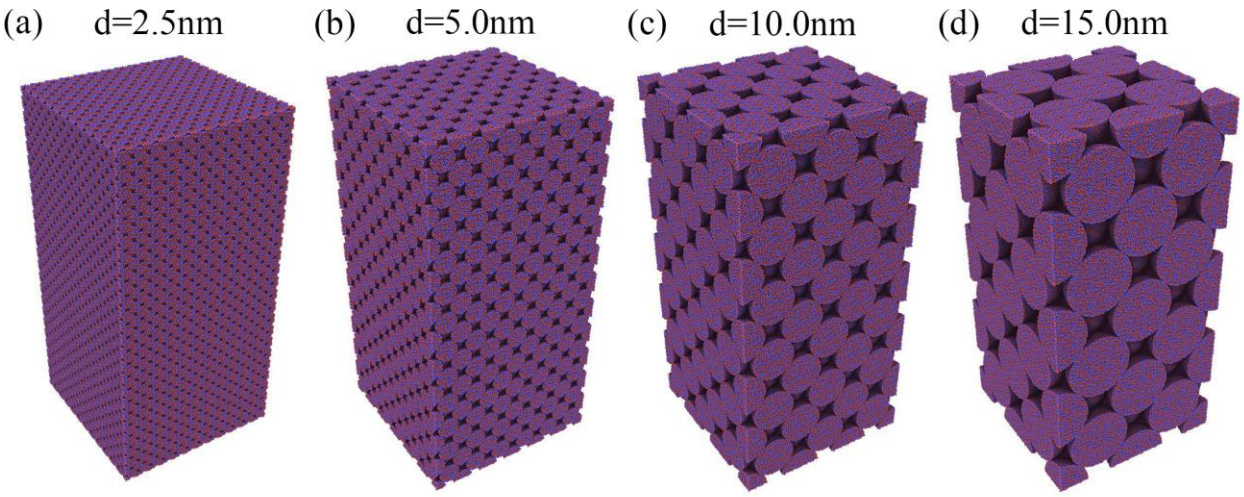

Figure 6.1 FCC stacked initial structures of $Cu_{64}Zr_{36}$ nanoglass with grain size of (a)2.5nm, (b)5.0nm, (c)10nm, and (d) 15nm. Cu and Zr atoms were colored red and blue, respectively.

Characterization of consolidated nanoglasses was focused on the interface properties of nanoglasses with respect to the grain sizes and annealing states. The volumetric strain, which is the hydrostatic part of strain tensor, was used to visualize the interface region, where significant volume change took place. The interface and grain regions were determined using the volumetric strain assorted atomic volume distribution fitting method developed in Chapter 5 and the interface volumetric strain threshold value for each sample was attained. However, the situation was a little different in annealed nanoglass samples, where the annealed state was used as the current state for calculating volumetric strain

and atomic volume distribution fitting. Once the interface region was determined, their properties, including interface volume fraction and width, excess free volume, and short-range order (FI fraction), were obtained following the same method described in Chapter 5. For the characterization of deformed nanoglasses, the Von Mises shear strain [202] was calculated to measure the local inelastic deformation of amorphous atoms. To quantify the shear localization level in the deformed nanoglasses, the shear localization factor ψ developed by Cheng et al. [224] was adopted, which is defined as

$$\psi = \sqrt{\frac{1}{N}\sum_{i=1}^{N}(\eta_i^{Mises} - \eta_{ave}^{Mises})^2} \quad (6.1)$$

where N is the total number of atoms in the simulation domain, η_i^{Mises} is the Von Mises shear strain of atom i, and η_{ave}^{Mises} is the average Von Mises shear strain of all atoms. Generally, a larger shear localization factor suggests a significant fluctuation of atoms' shear strain and a substantially localized deformation mode. At last, the open-source OVITO software [195] was used in the calculation of abovementioned characteristics and visualization of nanoglasses structures.

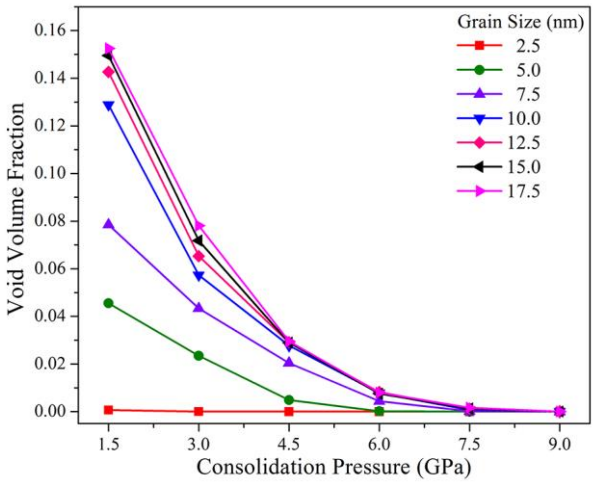

Figure 6.2 Evolution of void volume fraction as a function of consolidation pressure for initial nanoglass structures with grain sizes ranging from 2.5 to 17.5 nm.

6.2 Structural Characterization of Nanoglasses

After the consolidation processes, the voids between amorphous spheres were eliminated and the densified nanoglass structures were generated as shown in Fig.6.3(a) but the interface is still not visible in the consolidated nanoglasses. With the help of volumetric strain, the interface emerged as shown in the small window in the consolidated nanoglass, where atoms were colored by volumetric strain. The volumetric strain also enabled the observation of interface change during the annealing process. The cross-sectional views of 50K as-prepared nanoglass from the sample set 8 together with the 300k, 550K, and 800K annealed states colored by volumetric strain are exhibited in Fig 6.3 (b). It seems like both the interface region and width increased with the increase of annealing temperature while the grain region remained almost unchanged after annealing. No significant structural change was observed for the annealed samples even up to 800K, which is 80 percent of the glass transformation temperature (T_g) of this computational $Cu_{64}Zr_{36}$ amorphous solid, suggesting a good thermal stability. The grain size also affected the interface region of nanoglass as depicted in Fig 6.3(c), where the cross-sectional views of consolidated nanoglasses with grain sizes of 2.5, 5, 10, and 15 nm are shown. Due to the same simulation domain and length scale, these snapshots can be compared directly. Interestingly, the interface width appears to increase with the increasing grain size while the total interface region volume fraction remains the same.

The enlarged views of a single or few interfaces with different annealing states and grain sizes are shown in Fig. 6.4, where atoms are colored by the normalized volumetric strain. The purpose of normalizing the volumetric strain by each sample's interface volumetric strain threshold was first to highlight the interface atoms so that the interface width can be easily visualized and second to bring the color scale of highlighted interface atoms in Fig. 6.4 to the same level since all samples have different threshold values. Therefore, if an atom's normalized volumetric strain is greater than 1, it means that it has a greater volumetric strain than its threshold value and was identified as an interface atom. A single interface of as-prepared and 800K annealed nanoglass are shown in Fig. 6.4 (a) and (b), respectively. It is

apparent that the interface was broadened after the annealing as the width increased from about 1nm in the as-prepared state to almost 2nm in the annealed state while for grain atoms, a small fluctuation was observed in the annealed state near the interface but no fundamental structural change was captured. The enlarged view of interfaces of nanoglasses with grain sizes of 5 and 15 nm are shown in Fig. 6.4 (c) and (d), respectively. The interface width was also found to increase with the grain size augment as it increased from less than 1nm in the grain size 5nm sample to almost 2 nm in the grain size 15nm sample.

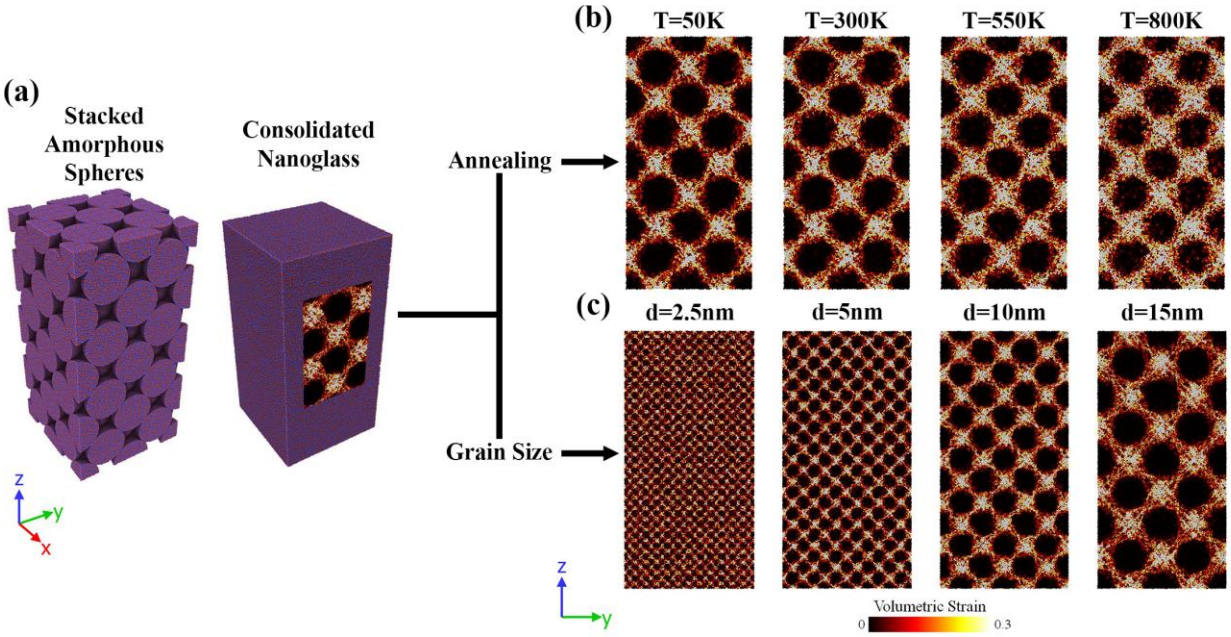

Figure 6.3 (a) Initial FCC stacked $Cu_{64}Zr_{36}$ amorphous spheres and consolidated nanoglass, where the Cu and Zr atoms were colored red and blue, respectively. Atoms in the inset window of consolidated nanoglass were colored by volumetric strain to highlight the significant volume change in the interface region. (b) Volumetric strain colored cross-sectional views of as-prepared nanoglass with a grain size of 10nm at 50K and its annealed states at 300K, 550K, and 800K. (c) Volumetric strain colored cross-sectional views of the nanoglasses with grain sizes of 2.5, 5, 10, and 15nm.

The quantification of interface properties employed the method developed in Chapter 5 for nanoglass samples with different annealing states and grain sizes. Fig. 6.5 (a) shows the interface volume fraction and width as a function of annealing temperature. It is found that the interface volume fraction increased from 0.35 of the 50K as-prepared state to 0.4 at the 300K annealed state and slightly increased to 0.42 in the following annealing temperature while the increasing trend of interface width is more stable and continue to increase from 1.25 to 1.75nm. The comparison of interfaces' atomic volume and full icosahedra (FI) fraction to their grain counterparts is disclosed in Fig. 6.5(b). For clarity, only the Cu

atoms' atomic volume trends are shown here and the Zr atoms trends, which are similar to those of Cu atoms, were omitted. Fig 6.5 (b) clearly shows that the interface atoms' average atomic volume decreased as the annealing temperature increased, whereas the value of grain atoms remained the same. Therefore, the excess free volume, which is the atomic volume difference between interface and grain atoms, decreased from 0.17 to 0.06 $Å^3$ corresponding to a percentage change of 1.3% to 0.5% out of the grain atoms' atomic volume. On the other hand, the FI fraction of interface and grain atoms increased with the increasing annealing temperature but the 0.06 increment of 800K annealed interface with respect to the 50K as-prepared state doubled the value of grain's increment of 0.03. The interface characterization results indicate that the annealing could substantially affect the interface properties of nanoglasses.

The high level of excess free volume and defective short-range order were initially limited to the very center of the interface because of the lack of atomic mobility at the low consolidation temperature of 50K. During the thermal annealing, the atoms in or near the interface gained thermal energy that increased their mobility, which facilitated the transportation of excess free volume to the initial grain region leading to an increase in interface volume fraction and width. However, the redistribution of excess free volume lowered the atomic volume difference between interface and grain but did not completely delocalize the excess free volume. Meanwhile, the thermal energy provided by annealing recovered the short-range order by driving the Cu atoms back to the Cu-centered full icosahedral positions and restored the FI fraction. Due to the highly defective state and excess free volume, the interface Cu atoms with higher mobility showed a higher tendency to restore the FI than the grain atoms so the recovery was more evident in the interface than grain. The annealing results in this study agree with the experimental results reported by Fang et al. [99], where the as-prepared consolidated $Sc_{75}Fe_{25}$ nanoglass showed an increase in interface volume fraction from 0.31 to 0.44 and an increase of interface width from 0.8nm to 1.2nm, which was the result of delocalization of free volume in the interface at elevated temperature. Our results successfully simulated the annealing process and disclosed direct evidence of excess free volume delocalization and recovery of short-range order.

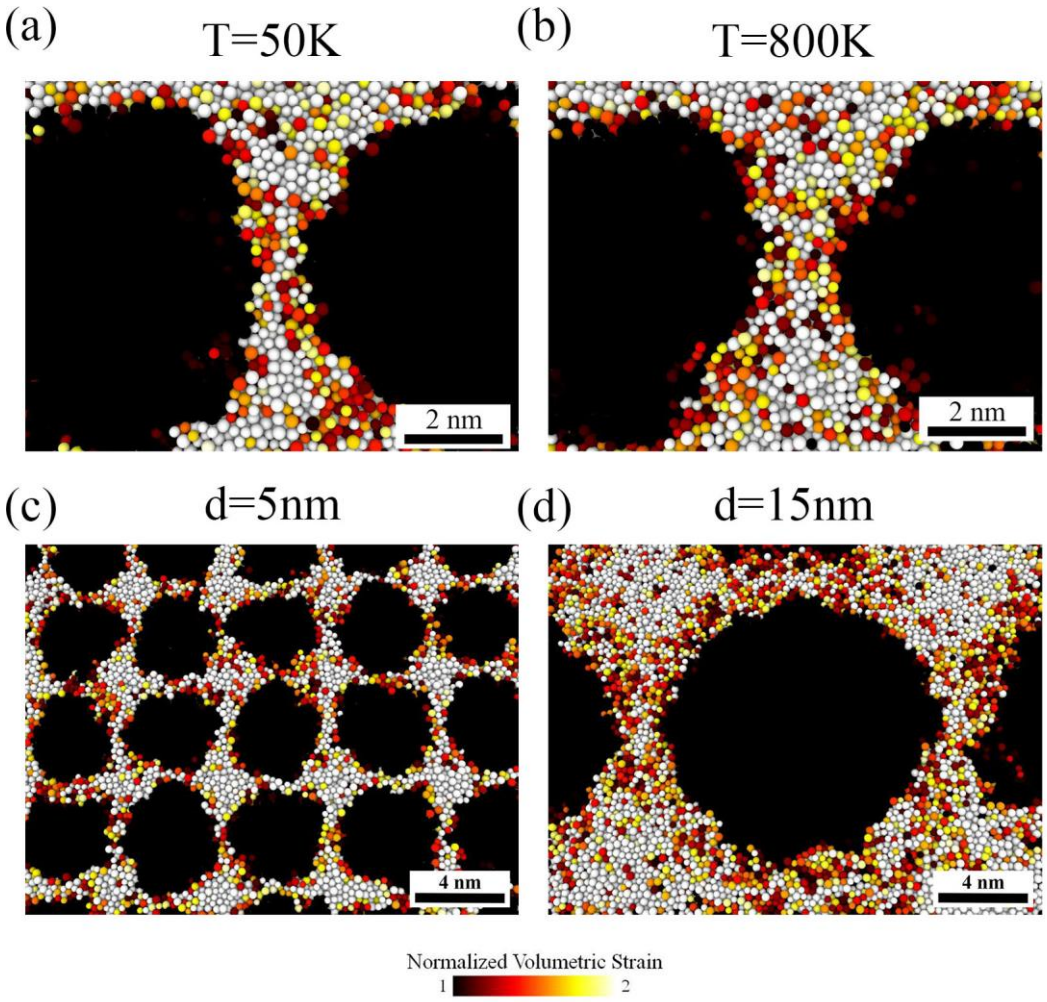

Figure 6.4 A single interface in the as-prepared (a) and 800K annealed (b) nanoglasses with a grain size of 10nm. Few interfaces in the nanoglasses with grains size of 5nm (c) and 15nm (d). Atoms are colored by normalized volumetric strain.

In the case of the grain size's effect on interface properties, astonishing results were observed as shown in Fig. 6.5(c). With the increase of grain size from 2.5 to 17.5nm, the interface volume fraction remained unchanged and only fluctuated around 0.35 whereas the interface width increased from 0.65nm to 2.59nm. For the nanoglass with a grain size of 7.5nm, the results show an interface volume of 0.35 and a width of 0.93nm, which is very close to Fang et al.'s [99] experimental result of the 7nm glassy particles consolidated $Sc_{75}Fe_{25}$ nanoglass with an interface volume fraction of 0.35 and a width of 0.8nm. The atomic volume and FI fraction results for all grain sizes are shown in Fig. 6(d). Interestingly, both the characteristics of interface and grain atoms show an insensitivity to grain size variance by being almost the same value across all 7 grain sizes. All the nanoglass samples show a 1.3% excess free volume with

respect to the grain atoms and the FI fraction is only half of the grain's value suggesting a loose atom packing and a defective short-range order in the interface region.

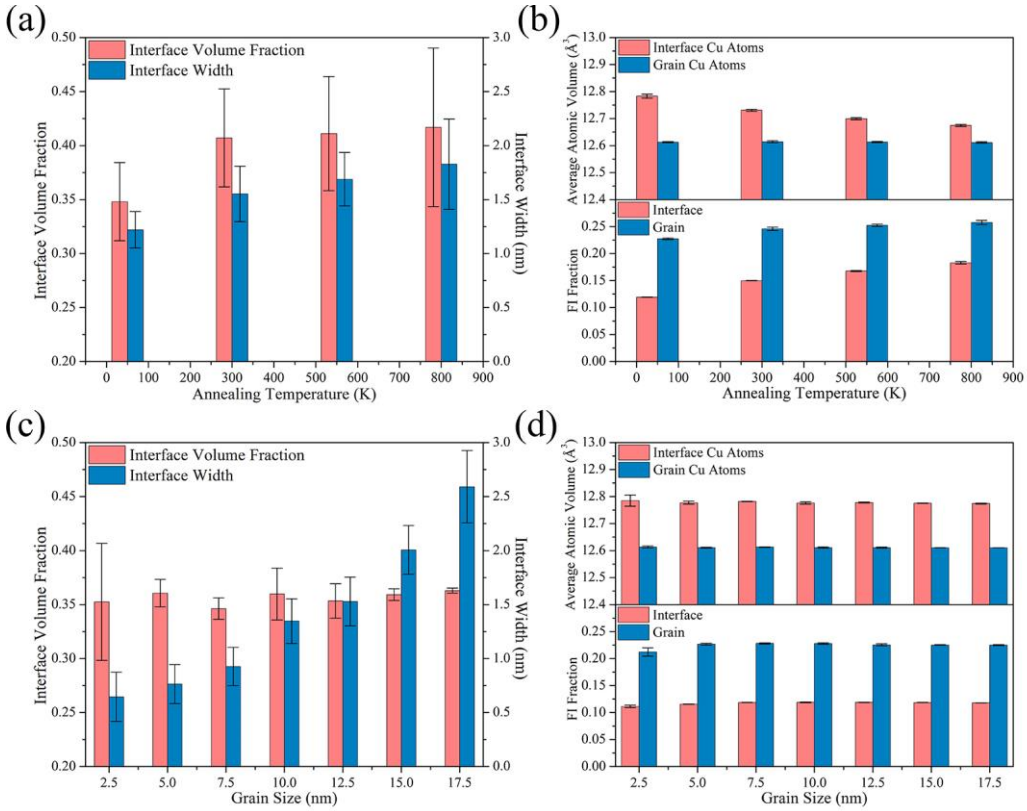

Figure 6.5 (a) Interface volume fraction and width as a function of annealing temperature. (b) Atomic volume and full icosahedra (FI) fraction of interface and grain Cu atoms as a function of annealing temperature. (c) Interface volume fraction and width as a function of grain size. (d) Atomic volume and full icosahedra fraction of interface and grain Cu atoms as a function of grain size.

The reason for the constant interface volume fraction for all grain sizes can be attributed to the increasing interface width as the grain size increases. It is natural to compare the nanoglass structures to polycrystalline structures and build the computational nanoglass structures, like Adibi et al [180, 183, 184] did in their studies. In polycrystalline metals, the formation of grain structure follows the core nucleation and growth model [225] and a grain boundary is formed when one growing grain domain meets another domain. Therefore, the grain boundary thickness usually keeps a constant value. The increase of grain boundary volume fraction at the nanocrystalline grain size region is the result of the decreasing grain interior size and constant grain boundary thickness. However, the nanoglass structure generated through amorphous spheres consolidation is quite different from the core nucleation and growth model in that the

densification process of amorphous sphere involves the use of an external force, which could result in a much wider interface region than the grain boundaries in a polycrystalline structure. As shown in Fig. 6.2, the consolidation pressure required for void-free nanoglass samples increased with an increasing grain size of spheres indicating that it was more difficult to consolidate larger grain size nanoglasses and thus a higher hydrostatic pressure was needed, which inevitably led to a wider interface.

The surface effect of initial nanoscale amorphous spheres might affect the interface properties as well. As demonstrated in Section 5.3, the outer shell of the initial glassy sphere is characterized by a low density and loosely packed configuration, which might result from surface effects of nanometer-scale particles. In the extremely fine spheres, the high-energy state of shell atoms resulted from a high surface to grain ratio, which enabled the easy flow of shell atoms to the voids between spheres. Therefore, the consolidation affected area was confined in the region close to the surface and a smaller interface width was attained. However, with the increase in grain size, the reduced surface to grain ratio lowered the surface energy of shell atoms so that a higher external force was required to activate the flow of shell atoms, which also resulted in a wider interface region. Increasing the grain size above the nanometer region, the external pressure might not able to consolidate the amorphous spheres while keeping the glassy nature of core region. Therefore, thermal energy is needed to facilitate the consolidation process.

6.3 Effect of Annealing State and Grain Size to the Deformation Behaviors of Nanoglasses

The consolidated nanoglass samples were then subjected to uniaxial tensile loading in the z-direction and deformed using a constant strain rate of $10^8 s^{-1}$ at 50K. Even though multiple samples were prepared for each annealing state, only the samples that showed the closest properties to the averaged results were selected for deformation simulation because of limited computational resources. The stress-strain curves and mechanical properties of representative nanoglass samples at as-prepared and annealed states together with a BMG sample are shown in Fig 6.6(a) and Table 6.2, respectively. The deformation

behavior of BMG is typical. After the onset of plasticity, the stress increased to a high level of 5GPa but underwent an abrupt stress drop between 0.1 to 0.12 strain because of catastrophic shear banding.

However, this devastating deformation mode was absent in the nanoglass samples and a more stable deformation behavior was captured. The elastic parts (0~0.02 strain) of stress-strain curves for all nanoglasses deviated from the BMG's curve due to the presence of interfaces. The 300K, 550K, and 800K annealed nanoglasses show almost the same elastic behaviors whereas the 50K as-prepared nanoglass is substantially different from the annealed ones. The Young's modulus results suggest that the annealed nanoglasses show a very small increment from 91.51 to 94.62 GPa, which are much greater than the as-prepared value of 76.85 GPa. The difference in the elastic behavior can be explained by the interface volume fraction of different annealing states. As shown in Fig. 6.5 (a), the annealed samples show a very close interface volume fraction ranging from 0.41~0.42 whereas the as-prepared sample only indicates an interface volume fraction of 0.35. Despite the increased volume fraction of the interface, annealing still significantly strengthened the nanoglass by enhancing elastic modulus.

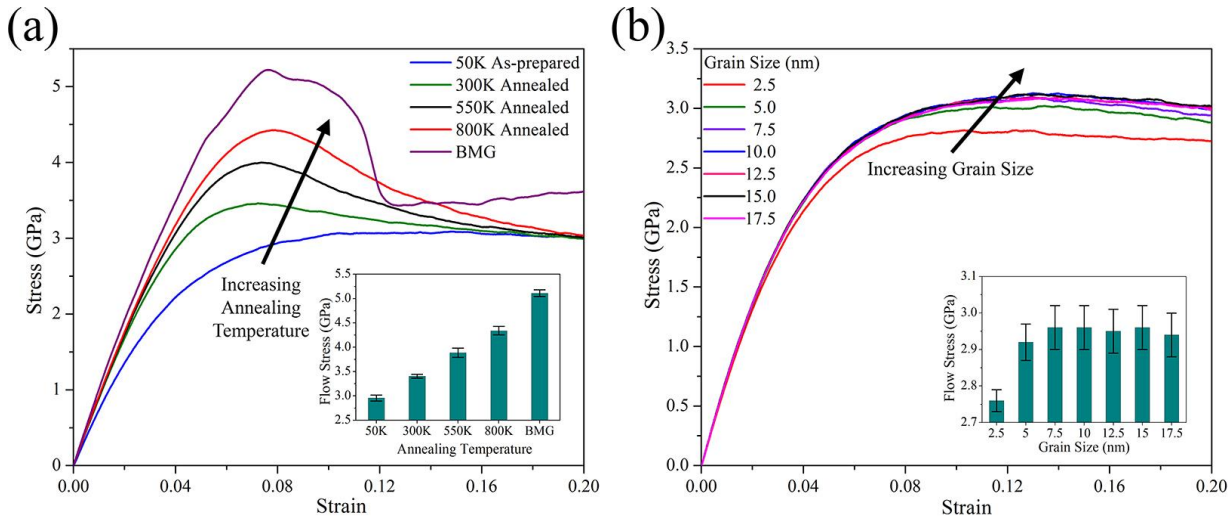

Figure 6.6 (a) Stress-strain curves of 10nm grain size nanoglasses with different annealing states and a bulk metallic glass (BMG) sample. (b) Stress-strain curves of nanoglasses with different grain sizes ranging from 2.5 to 17.5nm. Insets of both figures are the average flow stress of corresponding nanoglasses.

The strengthening effect of annealing was even more evident in the plastic deformation stage of nanoglasses. After the onset of plasticity around 0.018~0.024 strain, the stress of annealed samples kept

increasing, leading to stress overshoots, whose flow stress level scale with the annealing temperature. After the overshoot, the flow stress committed to a smooth strain softening, where no abrupted stress drop was captured. The deformation of as-prepared nanoglass shows a totally different plastic response. After the onset of plasticity at 0.018 strain, the flow stress steadily increased to a plateau level of 3GPa after 0.1 strain and a long strain hardening region between 0.02 to 0.1 strain was observed. Interestingly, all the nanoglasses converged to the same stress level at the end of deformation.

Using the traditional fitting of the linear part of the stress-strain curve and 0.002 strain offset, the stresses at the onset of plasticity were determined and displayed in Table 6.2. It was found that with the increase of annealing temperature, the stress at the onset of plasticity progressively increased. The average flow stress, which is a better representative of strength during the plastic deformation stage, was calculated by averaging flow stress between 0.07 to 0.1 strain [78]. The calculated results are shown in the inset of Fig. 6.6 (a) and tabulated in Table 6.2, where they clearly show that the average flow stress increased with the increasing annealing temperature. The as-prepared sample only has 60% of BMG's strength while the 800K annealed sample reached 90% the strength of BMG. By correlating the interface properties in Fig. 6.5(a), it is evident that the annealing strengthening of nanoglasses is proportional to the degree of interface excess free volume delocalization and recovery of short-range order. However, even though the annealing homogenized the as-prepared nanoglass to some extent, no evidence of severe shear localization was found in the stress-strain curves.

Table 6.2 Mechanical properties of nanoglasses with different annealing states and a bulk metallic glass (BMG)

Sample	Young's Modulus (GPa)	Stress at onset of plasticity (GPa)	Strain at onset of plasticity	Flow Stress (GPa)
50K as-prepared NG	76.85	1.25	0.0182	2.96 ± 0.06
300K annealed NG	91.51	1.79	0.0215	3.4 ± 0.04
550K annealed NG	93.21	1.97	0.0231	3.89 ± 0.1
800K annealed NG	94.62	2.05	0.0237	4.34 ± 0.09
BMG	103.68	2.14	0.023	5.11 ± 0.07

The stress-strain curves of as-prepared nanoglasses with different grain sizes and their mechanical properties are shown in Fig 6.6(b) and Table 6.3, respectively. Generally, the mechanical responses of nanoglasses with different grain sizes are very similar except for the 2.5 and 5nm grain size samples. However, catastrophic shear localization deformation was not observed even up to the 17.5nm grain size samples. The elastic stages of stress-strain curves are almost the same for all grain sizes, which are also proved by the similar Young's moduli in Table 6.3. As shown in Fig. 6.5(b) and (c), the almost constant interface volume fraction and interface properties might account for this similarity in the elastic parts of stress-strain curves. However, plastic deformation behaviors indicate an apparent difference, especially for the 2.5 and 5nm grain size samples. With the similar onset of plasticity, the flow stress diverted after the deformation stabilized. As shown in the inset of Fig. 6.6(b) and Table 6.3, the flow stress increased from 2.76 to 2.96 GPa as the grain size increased from 2.5 to 7.5 nm. When grain size further increased to 10nm, the nanoglasses' stress-strain curves demonstrated very similar behaviors by showing flow stress values oscillating around 2.96 GPa. The strain, where the stress-strain curve entered the stable deformation, is also different for samples with different grain sizes. The nanoglasses with smaller grain sizes of 2 and 5 nm reached the stable plastic flow earlier than the larger grain size samples. Therefore, the strain hardening region between the onset of plasticity and ultimately stable plastic flow is wider in larger grain sizes ($\geq$10nm) than smaller grain sizes (<10nm) nanoglasses, which suggests that there were more obstacles to plastic flow in the large grain size samples than the small grain size ones.

Table 6.3 Mechanical properties of nanoglasses with different grain sizes

Sample Grain Size (nm)	Young's Modulus (GPa)	Stress at onset of plasticity (GPa)	Strain at onset of plasticity	Flow Stress (GPa)
2.5	74.14	1.23	0.0184	2.76 ± 0.03
5	76.45	1.25	0.0184	2.92 ± 0.05
7.5	77.61	1.26	0.0182	2.96 ± 0.06
10	77.22	1.25	0.0183	2.96 ± 0.06
12.5	76.7	1.27	0.0186	2.95 ± 0.06
15	77.58	1.25	0.0181	2.96 ± 0.06
17.5	76.88	1.27	0.0185	2.94 ± 0.06

The deformation snapshots of as-prepared and annealed nanoglasses together with a BMG sample are displayed in Fig. 6.7 (a), where atoms were colored by the Von Mises shear strain. To highlight the deformed atoms in the STZs, the shear strain assorted atomic volume distribution fitting method developed in Chapter 3 was adopted and the shear strain threshold of 0.032 was determined by applying the above-mentioned method to the BMG sample, which was used as the lower limit of color legend in Fig. 6.7(a). The first row of Fig. 6.7 (a) shows snapshots of the nanoglasses and BMG at a strain of 0.06 shortly after the onset of plasticity. The STZs were captured in all nanoglass samples, which were mostly distributed in the interface region whereas the atoms in the grain region remained nearly undeformed. However, as the annealing temperature enhanced, fewer STZs were activated in the interface. For the BMG sample, even fewer STZs were activated and they were homogenously distributed. As the strain increased to 0.18, multiple shear localized paths in all nanoglasses were captured aligning with the interface networks in the consolidated nanoglasses shown in Fig. 6.3(b) and as the annealed temperature increased, the shear localized path became less confined. For BMG at a strain of 0.18, a typical single shear band was observed signifying the catastrophic failure of a homogenous metallic glass without any interface.

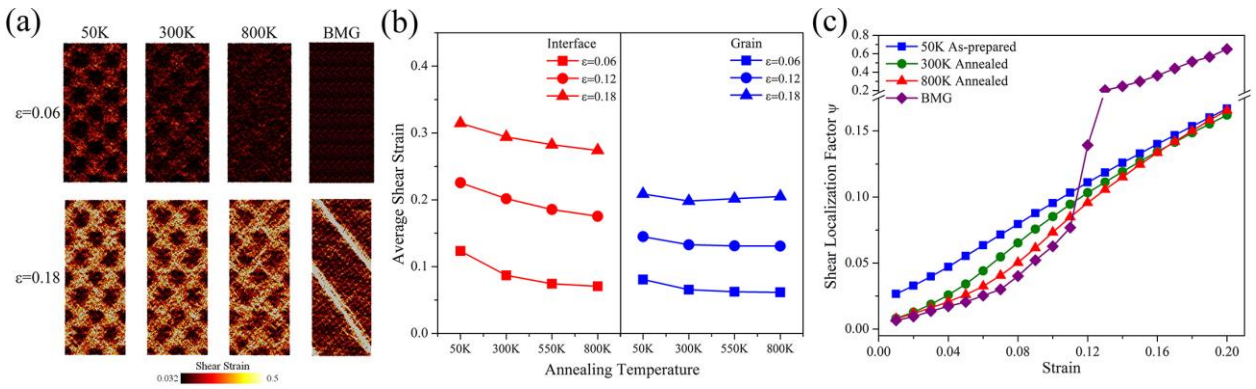

Figure 6.7 (a) Deformation snapshots of nanoglasses with different annealing states and a bulk metallic glass at a strain of 0.06 and 0.18. Atoms are colored by the Von Mises shear strain. (b) Average shear strain of interface and grain atoms for different annealing state nanoglasses at 0.06, 0.12, and 0.18 strain. (c) Shear localization factor as a function of strain for nanoglasses with different annealing states and a bulk metallic glass.

The introduction of interfaces to the glassy matrix created more locations for nucleation of STZs, which also required less stress because of excess free volume and defective short range in the interfaces.

The annealing of nanoglasses delocalized part of the excess free volume and restored the short-range order, which in turn increased the stress level required for activating STZs in the interface resulting in a higher stress at onset of plasticity and flow stress. However, the shear strain was still well distributed to the interface in the annealed sample, preventing it from being localized to a single shear band region. As the deformation carrying on, the plastic strain was further confined to the initial interface networks creating multiple shear paths. If we consider these shear paths as the plane defects in the nanoglasses, the intersection of multiple shear paths could lead to strain hardening as these intersections became the obstacle for shear front propagation and severe shear localization, which led to an improved plasticity. However, annealing homogenized the interface to some extent, which resulted in less confined shear paths, but was still not able to trigger the single shear band failure.

Quantitative results were generated to support the observation based on the snapshots starting with the strain accommodation of different regions in the nanoglass via tracking the average shear strain evolution of interface and grain atoms of different annealing states shown in Fig. 6.7(b). With the increase in strain from 0.06 to 0.18, both interface and grain atoms' shear strain increased for all samples but larger increments were observed in the interface atoms (by 0.1 increments) than grain atoms (by 0.05 increment). This resulted in an apparent shear strain difference indicating that interface atoms accommodated more shear strain than grain atoms. For different annealing states, the interface atoms showed a larger variance such that as the annealing temperature increased, the average shear strain of interface atoms decreased whereas the grain atoms remained almost the same for all samples except for the as-prepared sample, which showed a slightly higher average shear strain of grain atoms. Therefore, as the annealing temperature increased, the difference between the interface and grain's average shear strain shrank suggesting that the deformation of annealed nanoglass indicated a trend toward homogeneity that was still strongly mediated by the interfaces.

To characterize the degree of shear localization, the shear localization factors described in the simulation procedure section were calculated for the different annealing states and BMG and mapped as a

function of strain shown in Fig. 6.7(c). From 0 to 0.11 strain, the BMG sample showed the lowest localization factor, meaning that the deformation during this period was homogenous. However, after the strain reached 0.12 to 0.13, the BMG's localization factor surged, which corresponded to the fast propagation of a single shear band. After the initiation of the shear band, ψ maintained at a very high level (>0.2) and the BMG deformed in a heterogeneous fashion. The as-prepared nanoglass demonstrated a different trend. At the early stage of deformation, the as-prepared nanoglass sample showed higher ψ values than BMG because the softer interface accommodated most of the initial strain instead of homogenously distributing it. However, no ψ surge was observed for the as-prepared sample in the latter strains and the localized factor increased steadily until the end of the simulation, showing a much lower ψ level as compared to the BMG's.

Through distributing the strain to the interface, the severe shear localization that is common in the deformation of BMG was suppressed. Meanwhile, by increasing the annealing temperature, the early stage of nanoglasses (0~0.04 strain) shifted toward a homogeneous deformation (lower ψ value), which can be attributed to the delocalization process of excess free volume and recovery of short-range order. Nevertheless, after a certain stress level, the STZs in the interface were activated and the deformation mode converged to the as-prepared nanoglass fashion presented by the fast increase of ψ value between 0.04 to 0.16 and reached the same ψ value as the as-prepared nanoglass sample at the end of the simulation. Based on the shear localization factor characterization, the annealing didn't fundamentally alter the deformation of nanoglass but increased the difficulty of activating STZs in the interface, which in turn strengthened the nanoglasses while not sacrificing the excellent plasticity.

The snapshots of deformed nanoglasses with grain sizes of 2.5, 5, 10 and 15 nm were displayed in Fig.6.8(a) in order to understand the effect of grain size on the deformation behaviors of nanoglasses. Initially, at strain 0.06, the shear strain was distributed to the interface in all grain sizes proving that the interface was the preferred initiation sites for STZs. However, as the deformation continued, the deformation behaviors diverted. For nanoglasses with smaller grain sizes of 2.5 and 5nm, the grain atoms

started to deform, which led to a smaller shear strain difference between grain and interface atoms. Excellent plasticity was achieved for nanoglasses to deform in this homogenous fashion, which was also termed superplasticity in some studies [180, 183], at the expense of strength weakening as shown in Fig 6.6 (b). As the grain size increased to 7.5nm or above, the interface governed the deformation with most of the shear strain being distributed to the interface region and multiple shear paths intersecting with each other, preventing shear localization in any single path.

The average shear strain results confirmed the observation made from snapshots that a shear strain difference did exist in all grain sizes as the sample deforms but this difference became increasingly narrower as the grain size decreased, shown in Fig. 6.8 (b). The grain atoms average shear strain of the smaller grain size nanoglasses was obviously higher than other grain sizes, whereas the interface atoms show a lower average shear strain value. However, for larger grain size nanoglasses both interface and grain atoms' average shear strain showed an insensitivity to the grain size change, indicating that the strain accommodation was quite similar in large grain size nanoglasses.

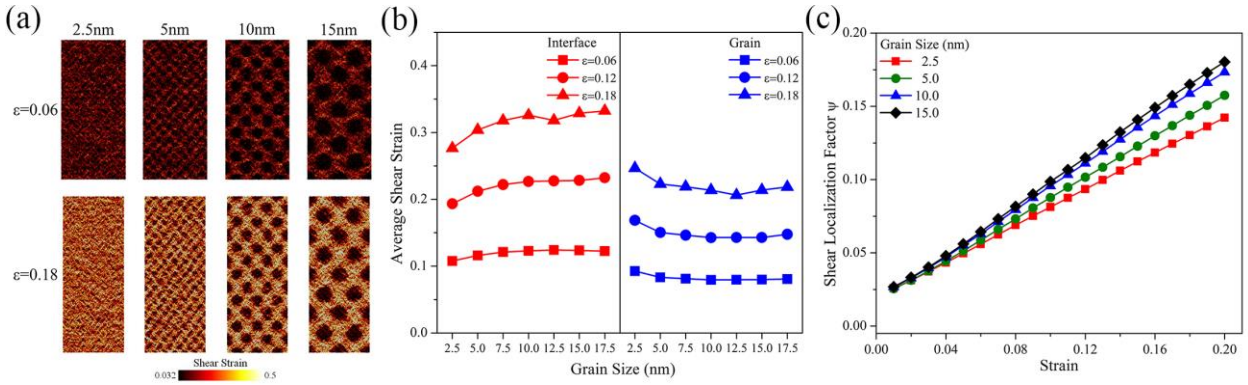

Figure 6.8 (a) Deformation snapshots of nanoglasses with different grain sizes at strains of 0.06 and 0.18. Atoms are colored by the Von Mises shear strain. (b) Average shear strain of interface and grain atoms for different grain size nanoglasses at 0.06, 0.12, and 0.18 strain. (c) Shear localization factor as a function of strain for nanoglasses with grain sizes.

The shear localization factors of 2.5, 5, 10 and 15nm grain size nanoglasses were displayed in Fig. 6.8(c) as a function of strain. The curves show positive linear trends without any suddenly increase, suggesting the steady deformation of nanoglasses free of severe shear localization. The ψ value was very close in the initial stage of deformation (0~0.06 strain), which agrees with the snapshot observation that it

was the interface that accommodated most of the initial strain. However, the higher strain part of curves (>0.06 strain) was differentiated among the nanoglasses with different grain sizes. With the increase in grain size from 2.5 to 15nm, whole trends elevated, which indicates that the smaller grain size showed a more homogenous process as the grain atoms started to deform, whereas, in large grain size samples, most of the strain is accommodated by the wider interface. In addition, the interface governed deformation assimilated the mechanical behaviors of large grain size nanoglasses in that similar average shear strain, shear localization factors, and stress-strain curves were observed as shown in Fig. 6.6 (b) and Fig. 6.8 (b) and (c), respectively.

Interestingly, even with the same interface volume fraction and properties, nanoglasses with different grain sizes show two different deformation behaviors, which can be attributed to the size of grain region. For the small grain size nanoglasses (2.5 and 5 nm), the interface to grain ratio was so high that grain atoms were easily activated during the deformation, which resulted in a poor resistance to shear deformation. When the size of grain region is large enough, like nanoglasses with grain sizes of 7.5 nm or above, the interface to grain ratio dropped substantially and grain atoms were relatively difficult to activate. Therefore, the strong resistance to shear deformation drove the strain to be preferentially accommodated in the softer interface region and thus interface governed deformation behavior was formed. Nevertheless, no matter the homogenous or interfaced governed deformation modes, the strain was well distributed in the nanoglasses, inhibiting severe shear localization behavior and the vastly improved plasticity is accomplished.

6.4 Concluding Remarks

In this chapter, molecular dynamics simulations were performed to study the deformation behaviors of the glassy spheres consolidated nanoglasses with different annealing states and grain sizes. An in-depth understanding of interface mediated deformation mechanisms was gained by using novel characterization methods developed in this thesis, summarized as follows:

i. The annealing of nanoglasses was proved to be a more effective way to tune the interface properties via increasing the volume fraction and width of interfaces, delocalizing excess free volume and recovering of short-range order. Thus, the annealing strengthening of nanoglasses was obtained by elevating the stress required for activating STZs at interfaces. The annealing homogenized the nanoglasses to some extent but did not eliminate the structurally heterogeneous glass-glass interfaces.

ii. The interface properties of nanoglasses indicate an insensitivity to grain size variance whereas the interface width increased with increasing grain size, leading to a constant interface volume fraction of about 0.35 for all grain size nanoglasses. The tensile deformation of nanoglasses with a grain size greater than 7.5nm show a great similarity as the multiple shear paths along the interface network were found to accommodate most of the strain and govern the plastic deformation. However, the extremely fine grain size of nanoglasses (2.5 and 5nm) resulted in a less stiff grain region and a homogeneous deformation, which weakened the strength of nanoglasses.

iii. The excellent plasticity was achieved by distributing the plastic strain to the interface region and a stable plastic flow was obtained with the shear localization factors that are substantially lower than the value of BMG deformed via shear banding. Owing to the interface governed plasticity, no single shear band was observed in any nanoglass with different annealing states and grain sizes.

Based on the above conclusions, the improved plasticity of nanoglasses relative to the monolithic metallic glasses can be understood in the context of the interface mediated deformation mechanisms. The mechanical performance of nanoglasses can be adjusted by manipulating the interface defect state, which provides a novel design strategy for circumventing the catastrophic failure of metallic glasses via shear banding.

Conclusions

Crystalline-amorphous nanolaminates and nanoglasses have exhibited unprecedented opportunities to study interface mediated deformations in heterogeneous metallic nanostructures that contain unique amorphous-crystalline interfaces or glass-glass interfaces. Atomistic simulations play a critical role in understanding the underlying deformation mechanisms of interface governed mechanical behaviors. However, limitations in the current computational models and characterization methods elude the fundamental deformation physics with regard to the disparate mechanisms coupling, microstructural length scales, interface defect state, and thermal annealing effect. On the other hand, the experimental synthesis of crystalline-nanolaminates heavily relies on thin film techniques, which are limited by a relatively low production rate and high cost. A more practical method of preparing crystalline-amorphous nanolaminates is needed for engineering applications of this novel metallic nanostructure. This thesis has successfully addressed these topics using both computational and experimental methods and the conclusions of this thesis are summarized below.

In Chapter 2, the deformation behavior of crystalline-amorphous nanolaminates was explored through molecular dynamics simulations using nanolaminate models that contain columnar nanograins in the crystalline layers to more closely resemble experimentally accessible nanolaminate structures. Quantitative analysis of the plastic strain distribution among competing mechanisms and their coupling at the nanoscale was accomplished through the implementation of continuum deformation metrics. The transfer of plastic strain between STZ and dislocation plasticity initially transpired through the emission of dislocations from STZ activity impinging on the amorphous-crystalline interface (ACI). The addition of grain boundaries biased this process to regions near the boundaries at low strains, which reduced the activation barrier for the onset of dislocation plasticity. With increasing strain, dislocations were absorbed into the amorphous layers via slip transfer across the ACI, in turn triggering the activation of new STZs. Cooperative slip transfer between dislocations and STZs suppressed grain boundary microcracking

collectively with large-scale shear localization and was responsible for the enhanced toughness of crystalline amorphous nanolaminates.

The columnar crystalline-amorphous nanolaminates constructed in Chapter 2 enabled the study of microstructural length scales' effect on the mechanical behaviors of nanolaminates. In Chapter 3, the layer thickness ratio and nanocrystalline grain size were systematically varied, and the mechanical responses of the nanolaminates were characterized under uniaxial tensile loading, employing deformation metrics for atomistic simulations. Illustrative compound mechanisms maps were generated for each length scale combination rooted in the contributions of the three dominant deformation mechanisms: grain boundary, dislocation, and STZ plasticity. Combined with deformation snapshots, the compound mechanism maps provided new insights into the mechanistic transitions in crystalline-amorphous nanolaminates as a function of their microstructural length scales, which have important implications for the resulting mechanical properties. The effective yield strength was collectively determined by the nanocrystalline grain size and layer thickness ratio while the flow stress was dictated by the t_A/t_C ratio. The latter also controlled the transition from shear band-dominated plasticity to the formation of grain boundary voids. From these observations, mixed-mode deformation regions were identified where coupling between the disparate mechanisms operating the crystalline and amorphous layers dominated the deformation behavior. The results were compiled into a property map from which four unique deformation zones were identified to establish new mechanics-driven design principles for optimizing the performance of crystalline-amorphous nanolaminate.

In Chapter 4, the reverse pulsing electrodeposition technique was used to synthesize a grain size modulated NiW nanolaminate that consists of glass-like and nanocrystalline layers. The microstructures and layer thickness of the as-prepared nanolaminates were characterized by transmission electron microscopy (TEM) and scanning electron microscopy (SEM). Using the instrumented nanoindentation and strain rate sensitivity testing, the mechanical behaviors of grain size modulated nanolaminates with varying glass-like/nanocrystalline layer thickness ratio (t_A/t_C) were systematically investigated. It was

found that the hardness of nanolaminates strongly depended on the layer thickness ratio. For nanolaminates with t_A/t_C greater than 1.0, the hardness value scaled with the increasing t_A/t_C ratio, following the trend predicted by the rule of mixtures. However, as t_A/t_C decreased below 1.0, the hardness of nanolaminates was insensitive to the layer thickness ratio variation, which is attributed to the equiaxed grain structure of nanocrystalline layer hindering the STZ-dislocation coupled deformation. In addition, the substantial strengthening effect of nanolaminates with thin glass-like layers ($t_A/t_C<0.5$) was achieved. Strain rate sensitivity testing was performed using different nanoindentation strain rates that cover three orders of magnitude and apparent activation volume of nanolaminate deformation was calculated. The strain rate sensitivity of nanolaminates was determined by glass layer thickness t_A. Nanolaminates with a t_A less than 65~70nm indicated a strain rate sensitivity corresponding to a low activation volume. However, as increased t_A above 70nm, the deformation of nanolaminates became strain rate insensitive, which was manifested by a sudden increase in activation volume to a high level. Therefore, the 65~70nm glass-like layer thickness was identified as the critical length scale, where deformation behaviors of nanolaminates transited from the rate-dependent nanocrystalline mode to the rate-independent amorphous fashion.

In Chapter 5, a large-scale 3D nanoglass model was developed by consolidating FCC stacked 15nm grain size glassy spheres using hydrostatic pressure and an optimized consolidation scenario was disclosed. Using volumetric strain coupled with the atomic volume distribution, a novel method that can successfully delineate the interface and grain regions of consolidated nanoglass was established. The characterization of the consolidated nanoglass demonstrates an interface region with a volume fraction of 0.36 that consists of normal interfaces with a width of 2.01 ± 0.23 nm and triple junctions with a width of 8.54 ± 0.22 nm. The interface region was characterized by an enlarged atomic packing in forms of 1.3% excess free volume and a defective short-range order in terms of FI fraction being half the value of grain region. In addition, the segregation of atoms with large potential energy to the grain region was also observed.

The consolidation and characterization methods developed in Chapter 5 pave the way for studying the deformation behaviors of nanoglasses with different annealing states and grain sizes in Chapter 6. The in-depth understanding of interface mediated deformation mechanism was gained via using novel characterization methods developed in this thesis. It was found that the annealing of nanoglasses was a more effective way to tune the interface properties via increasing the volume fraction and width of interfaces, delocalizing excess free volume and recovering of short-range order. Thus, the annealing strengthening of nanoglasses was obtained by elevating the stress required for activating STZs at interfaces. The annealing homogenized the nanoglasses to some extent but did not eliminate the structurally heterogeneous glass-glass interfaces. The interface properties of nanoglasses indicate an insensitivity to grain size variance whereas the interface width increased with increasing grain sizes, leading to a constant interface volume fraction of about 0.35 for all grain size nanoglasses. The tensile deformation of nanoglasses with a grain size greater than 7.5nm show a great similarity as multiple shear paths along the interface network were found to accommodate most of the strain and govern the plastic deformation. However, the extremely fine grain size of nanoglasses (2.5 and 5nm) resulted in a less stiff grain region and homogeneous deformation, which weakened the strength of nanoglasses. The excellent plasticity was achieved by distributing the plastic strain to the interface region and a stable plastic flow was obtained with the shear localization factors that are substantially lower than the value of BMG deformed via shear banding. Owing to the interface governed plasticity, no single shear band was observed in any nanoglasses with different annealing states and grain sizes.

A comprehensive study of interface mediated deformation behaviors in both crystalline-amorphous nanolaminates and metallic nanoglasses is presented in this thesis work. The insight gained from this work established the correlations between the materials' mechanical behaviors and their microstructures, deformation mechanisms, length scales, interface defect states, and thermal annealing effects, which promote the understanding of metallic nanostructures and lay down design principles for a new generation of metallic nanomaterials that greatly exceed the performance of existing materials.

Future Research Directions

Not only did this thesis work reveal the intriguing interface mediated deformation behaviors presented by crystalline-amorphous nanolaminates and nanoglasses, but it also shed light on future research endeavors, some of which are presented as follows:

i. The mechanistic coupling of dislocation and shear transformation zone (STZ) plasticity has been identified as the underlying deformation mechanism that is responsible for the exceptional mechanical behaviors of crystalline-amorphous nanolaminates in Chapter 2. Even though the strain gradient across the interfaces has been captured during the STZ-dislocation coupling, the driving force for this unique event is still elusive. Two possible scenarios might happen and lead to dislocations emission at the interfaces: the stress concentration resulted from disparate deformation mechanisms operating across the ACIs; the interfacial free volume migration as a result of prevailing STZ plasticity in the amorphous layer. Investigating these two possible causes of dislocation emission will provide a whole picture of STZ-dislocation coupled deformation at interfaces.

ii. In Chapter 3, the strength and plasticity of crystalline-amorphous nanolaminates were comprehensively studied with respect to the variation in length scales. However, more mechanical behaviors of nanolaminates can be explored by varying the testing conditions, such as strain rate, deformation temperature, loading type and annealing state. In particular, the strain rate sensitivity could be illuminating to probe the transition of deformation mechanisms regarding the change in length scales. Since a large fraction of interfaces and the amorphous phase are present in nanolaminates, the thermal annealing might play a vital role in tuning the mechanical behaviors of nanolaminates.

iii. In Chapter 4, the nanoindentation and strain rate sensitivity testing of grain size modulated Ni-W nanolaminates have revealed interesting trends in hardness and activation volume with regard to the length scale variation. However, the underlying deformation mechanism can only be inferred

from ex-situ mechanical testing. To better understand the fascinating deformation physics, in situ TEM or SEM testing, post-mortem High-resolution TEM analysis, and atomistic simulations are recommended, which will provide either a direct observation of operating mechanism or a new understanding from ex-situ testing results. In addition, the pop-in event that is commonly observed in the nanoindentation of metallic glasses [179] was also captured in the load-displacement curves of nanolaminates, providing an opportunity to study the plastic flow of nanolaminates with varying length scales. At last, thermal annealing has been proven to effectively manipulate the interface defect state of nanocrystalline Ni-W alloys [226] and achieve an extraordinary high strength. It is natural to postulate that grain size modulated nanolaminates are also subject to annealing manipulation since a large portion of interfaces is present in the nanolaminates.

iv. In Chapters 5 and 6, a new large-scale 3D nanoglass model was built and used to investigate the effect of grain size and the annealing state to its mechanical behaviors. The novel characterization method developed in this thesis enabled the revelation of correlation between the interface defect state and the mechanical responses of nanoglasses. However, the idealized FCC stacking of equal-size glassy spheres was used in the initial construction of the nanoglass model, which may elude some unique deformation behaviors of nanoglasses. The construction of a more realistic nanoglass model with different grain size glassy spheres being arranged in a Voronoi tessellation-like stacking might be a new direction for nanoglasses simulations. Meanwhile, the segregation of atoms with large cohesive energy to the interface has been observed in this thesis work, which provides another interesting direction for studying segregation phenomenon of nanoglasses with respect to grain size and annealing state.

Reference

[1] Y. Wei, C. Su, L. Anand. A computational study of the mechanical behavior of nanocrystalline fcc metals, Acta Mater. 54 (2006) 3177-3190.
[2] P.G. Sanders, J.A. Eastman, J.R. Weertman. Elastic and tensile behavior of nanocrystalline copper and palladium, Acta Mater. 45 (1997) 4019-4025.
[3] K.M. Youssef, R.O. Scattergood, K.L. Murty, C.C. Koch. Ultratough nanocrystalline copper with a narrow grain size distribution, Applied Physics Letters 85 (2004) 929-931.
[4] R.S. Iyer, C.A. Frey, S.M.L. Sastry, B.E. Waller, W.E. Buhro. Plastic deformation of nanocrystalline Cu and Cu-0.2 wt.% B, Mater. Sci. Eng. A-Struct. Mater. Prop. Microstruct. Process. 264 (1999) 210-214.
[5] H.G. Jiang, Y.T. Zhu, D.P. Butt, I.V. Alexandrov, T.C. Lowe. Microstructural evolution, microhardness and thermal stability of HPT-processed Cu, Materials Science and Engineering a-Structural Materials Properties Microstructure and Processing 290 (2000) 128-138.
[6] G.T. Gray, T.C. Lowe, C.M. Cady, R.Z. Valiev, I.V. Aleksandrov. Influence of strain rate & temperature on the mechanical response of ultrafine-grained Cu, Ni, AND Al-4Cu-0.5Zr, Nanostruct. Mater. 9 (1997) 477-480.
[7] M. Haouaoui, I. Karaman, H.J. Maier, K.T. Hartwig. Microstructure evolution and mechanical behavior of bulk copper obtained by consolidation of micro- and nanopowders using equal-channel angular extrusion, Metallurgical and Materials Transactions a-Physical Metallurgy and Materials Science 35A (2004) 2935-2949.
[8] S.R. Agnew, B.R. Elliott, C.J. Youngdahl, K.J. Hemker, J.R. Weertman. Microstructure and mechanical behavior of nanocrystalline metals, Materials Science and Engineering a-Structural Materials Properties Microstructure and Processing 285 (2000) 391-396.
[9] R.Z. Valiev, E.V. Kozlov, Y.F. Ivanov, J. Lian, A.A. Nazarov, B. Baudelet. DEFORMATION-BEHAVIOR OF ULTRA-FINE-GRAINED COPPER, Acta Metallurgica Et Materialia 42 (1994) 2467-2475.
[10] L. Lu, Y.F. Shen, X.H. Chen, L.H. Qian, K. Lu. Ultrahigh strength and high electrical conductivity in copper, Science 304 (2004) 422-426.
[11] M.A. Meyers, K.K. Chawla. Mechanical Behavior of Materials, 2nd Edition, Mechanical Behavior of Materials, 2nd Edition (2009) 1-856.
[12] Y. Champion, C. Langlois, S. Guerin-Mailly, P. Langlois, J.L. Bonnentien, M.J. Hytch. Near-perfect elastoplasticity in pure nanocrystalline copper, Science 300 (2003) 310-311.
[13] F. Ebrahimi, Q. Zhai, D. Kong. Deformation and fracture of electrodeposited copper, Scr. Mater. 39 (1998) 315-321.
[14] K. Hayashi, H. Etoh. PRESSURE SINTERING OF IRON, COBALT, NICKEL AND COPPER ULTRAFINE POWDERS AND THE CRYSTAL GRAIN-SIZE AND HARDNESS OF THE COMPACTS, Materials Transactions Jim 30 (1989) 925-931.
[15] R.Z. Valiev, I.V. Alexandrov, Y.T. Zhu, T.C. Lowe. Paradox of strength and ductility in metals processed by severe plastic deformation, Journal of Materials Research 17 (2002) 5-8.
[16] J. Chen, L. Lu, K. Lu. Hardness and strain rate sensitivity of nanocrystalline Cu, Scr. Mater. 54 (2006) 1913-1918.
[17] U. Erb. Electrodeposited nanocrystals: Synthesis, properties and industrial applications, Nanostruct. Mater. 6 (1995) 533-538.

[18] G.D. Hughes, S.D. Smith, C.S. Pande, H.R. Johnson, R.W. Armstrong. HALL-PETCH STRENGTHENING FOR THE MICROHARDNESS OF 12 NANOMETER GRAIN DIAMETER ELECTRODEPOSITED NICKEL, Scripta Metallurgica 20 (1986) 93-97.
[19] F. Ebrahimi, G.R. Bourne, M.S. Kelly, T.E. Matthews. Mechanical properties of nanocrystalline nickel produced by electrodeposition, Nanostruct. Mater. 11 (1999) 343-350.
[20] J. Schiotz, K.W. Jacobsen. A maximum in the strength of nanocrystalline copper, Science 301 (2003) 1357-1359.
[21] G.W. Nieman, J.R. Weertman, R.W. Siegel. MECHANICAL-BEHAVIOR OF NANOCRYSTALLINE CU AND PD, Journal of Materials Research 6 (1991) 1012-1027.
[22] M. Legros, B.R. Elliott, M.N. Rittner, J.R. Weertman, K.J. Hemker. Microsample tensile testing of nanocrystalline metals, Philosophical Magazine a-Physics of Condensed Matter Structure Defects and Mechanical Properties 80 (2000) 1017-1026.
[23] X.J. Wu, L.G. Du, H.F. Zhang, J.F. Liu, Y.S. Zhou, Z.Q. Li, L.Y. Xiong, Y.L. Bai. Synthesis and tensile property of nanocrystalline metal copper, Nanostruct. Mater. 12 (1999) 221-224.
[24] S. Cheng, E. Ma, Y.M. Wang, L.J. Kecskes, K.M. Youssef, C.C. Koch, U.P. Trociewitz, K. Han. Tensile properties of in situ consolidated nanocrystalline Cu, Acta Mater. 53 (2005) 1521-1533.
[25] Y.M. Wang, E. Ma. Temperature and strain rate effects on the strength and ductility of nanostructured copper, Applied Physics Letters 83 (2003) 3165-3167.
[26] H. Conrad, D. Yang. Effect of an electric field on the plastic deformation kinetics of electrodeposited Cu at low and intermediate temperatures, Acta Mater. 50 (2002) 2851-2866.
[27] K.M. Youssef, R.O. Scattergood, K.L. Murty, J.A. Horton, C.C. Koch. Ultrahigh strength and high ductility of bulk nanocrystalline copper, Applied Physics Letters 87 (2005).
[28] D.H. Jeong, U. Erb, K.T. Aust, G. Palumbo. The relationship between hardness and abrasive wear resistance of electrodeposited nanocrystalline Ni-P coatings, Scr. Mater. 48 (2003) 1067-1072.
[29] F. Dalla Torre, H. Van Swygenhoven, M. Victoria. Nanocrystalline electrodeposited Ni: microstructure and tensile properties, Acta Mater. 50 (2002) 3957-3970.
[30] A.A. Karimpoor, U. Erb, K.T. Aust, G. Palumbo. High strength nanocrystalline cobalt with high tensile ductility, Scr. Mater. 49 (2003) 651-656.
[31] M. Dao, L. Lu, R.J. Asaro, J.T.M. De Hosson, E. Ma. Toward a quantitative understanding of mechanical behavior of nanocrystalline metals, Acta Mater. 55 (2007) 4041-4065.
[32] K.S. Kumar, H. Van Swygenhoven, S. Suresh. Mechanical behavior of nanocrystalline metals and alloys, Acta Mater. 51 (2003) 5743-5774.
[33] F. Liu, R. Kirchheim. Nano-scale grain growth inhibited by reducing grain boundary energy through solute segregation, Journal of Crystal Growth 264 (2004) 385-391.
[34] A.J. Detor, C.A. Schuh. Tailoring and patterning the grain size of nanocrystalline alloys, Acta Mater. 55 (2007) 371-379.
[35] J.R. Trelewicz, C.A. Schuh. The Hall-Petch breakdown in nanocrystalline metals: A crossover to glass-like deformation, Acta Mater. 55 (2007) 5948-5958.
[36] W.L. Johnson, K. Samwer. A universal criterion for plastic yielding of metallic glasses with a (T/T-g)(2/3) temperature dependence, Physical Review Letters 95 (2005) 4.

[37] E. Pekarskaya, C.P. Kim, W.L. Johnson. In situ transmission electron microscopy studies of shear bands in a bulk metallic glass based composite, Journal of Materials Research 16 (2001) 2513-2518.
[38] A.S. Argon. Plastic deformation in metallic glasses, Acta Metallurgica 27 (1979) 47-58.
[39] Y.M. Wang, J. Li, A.V. Hamza, T.W. Barbee. Ductile crystalline-amorphous nanolaminates, Proceedings of the National Academy of Sciences of the United States of America 104 (2007) 11155-11160.
[40] H. Gleiter. Nanoglasses: a new kind of noncrystalline materials, Beilstein Journal of Nanotechnology 4 (2013) 517-533.
[41] N. Chen, D.V. Louzguine-Luzgin, G.Q. Xie, P. Sharma, J.H. Perepezko, M. Esashi, A.R. Yavari, A. Inoue. Structural investigation and mechanical properties of a representative of a new class of materials: nanograined metallic glasses, Nanotechnology 24 (2013) 045610.
[42] X.L. Wang, F. Jiang, H. Hahn, J. Li, H. Gleiter, J. Sun, J.X. Fang. Plasticity of a scandium-based nanoglass, Scr. Mater. 98 (2015) 40-43.
[43] Y. Ritter, D. Sopu, H. Gleiter, K. Albe. Structure, stability and mechanical properties of internal interfaces in Cu64Zr36 nanoglasses studied by MD simulations, Acta Mater. 59 (2011) 6588-6593.
[44] O. Adjaoud, K. Albe. Interfaces and interphases in nanoglasses: Surface segregation effects and their implications on structural properties, Acta Mater. 113 (2016) 284-292.
[45] D. Şopu, K. Albe. Influence of grain size and composition, topology and excess free volume on the deformation behavior of Cu–Zr nanoglasses, Beilstein Journal of Nanotechnology 6 (2015) 537-545.
[46] G.K. Williamson, W.H. Hall. X-ray line broadening from filed aluminium and wolfram, Acta Metallurgica 1 (1953) 22-31.
[47] T. Yamasaki, R. Tomohira, Y. Ogino, P. Schlossmacher, K. Ehrlich. Formation of ductile amorphous & nanocrystalline Ni-W alloys by electrodeposition, Plat. Surf. Finish. 87 (2000) 148-152.
[48] D. Wolf, V. Yamakov, S.R. Phillpot, A. Mukherjee, H. Gleiter. Deformation of nanocrystalline materials by molecular-dynamics simulation: relationship to experiments?, Acta Mater. 53 (2005) 1-40.
[49] H. Gleiter. NANOCRYSTALLINE MATERIALS, Prog. Mater. Sci. 33 (1989) 223-315.
[50] H. Gleiter. Nanostructured materials: Basic concepts and microstructure, Acta Materialia 48 (2000) 1-29.
[51] J.G. Sevillano, J. Aldazabal. Ductilization of nanocrystalline materials for structural applications, Scr. Mater. 51 (2004) 795-800.
[52] N.J. Petch. THE CLEAVAGE STRENGTH OF POLYCRYSTALS, Journal of the Iron and Steel Institute 174 (1953) 25-28.
[53] E.O. Hall. THE DEFORMATION AND AGEING OF MILD STEEL .3. DISCUSSION OF RESULTS, Proceedings of the Physical Society of London Section B 64 (1951) 747-753.
[54] M.A. Meyers, A. Mishra, D.J. Benson. Mechanical properties of nanocrystalline materials, Prog. Mater. Sci. 51 (2006) 427-556.
[55] C.A. Schuh, T.G. Nieh, H. Iwasaki. The effect of solid solution W additions on the mechanical properties of nanocrystalline Ni, Acta Mater. 51 (2003) 431-443.
[56] J.R. Trelewicz, C.A. Schuh. The Hall-Petch breakdown at high strain rates: Optimizing nanocrystalline grain size for impact applications, Applied Physics Letters 93 (2008).

[57] C.A. Schuh, T.G. Nieh, T. Yamasaki. Hall-Petch breakdown manifested in abrasive wear resistance of nanocrystalline nickel, Scr. Mater. 46 (2002) 735-740.
[58] H. Van Swygenhoven, A. Caro, D. Farkas. Grain boundary structure and its influence on plastic deformation of polycrystalline FCC metals at the nanoscale: A molecular dynamics study, Scr. Mater. 44 (2001) 1513-1516.
[59] J. Schiotz, F.D. Di Tolla, K.W. Jacobsen. Softening of nanocrystalline metals at very small grain sizes, Nature 391 (1998) 561-563.
[60] H. Van Swygenhoven, P.A. Derlet. Grain-boundary sliding in nanocrystalline fcc metals, Physical Review B 64 (2001) 9.
[61] V. Yamakov, D. Wolf, S.R. Phillpot, A.K. Mukherjee, H. Gleiter. Deformation-mechanism map for nanocrystalline metals by molecular-dynamics simulation, Nat. Mater. 3 (2004) 43-47.
[62] V. Yamakov, D. Wolf, S.R. Phillpot, A.K. Mukherjee, H. Gleiter. Dislocation processes in the deformation of nanocrystalline aluminium by molecular-dynamics simulation, Nat. Mater. 1 (2002) 45-48.
[63] V. Yamakov, D. Wolf, M. Salazar, S.R. Phillpot, H. Gleiter. Length-scale effects in the nucleation of extended dislocations in nanocrystalline Al by molecular-dynamics simulation, Acta Mater. 49 (2001) 2713-2722.
[64] J.A. Sharon, H.A. Padilla, B.L. Boyce. Interpreting the ductility of nanocrystalline metals, Journal of Materials Research 28 (2013) 1539-1552.
[65] W.M. Yin, S.H. Whang, R. Mirshams, C.H. Xiao. Creep behavior of nanocrystalline nickel at 290 and 373 K, Materials Science and Engineering a-Structural Materials Properties Microstructure and Processing 301 (2001) 18-22.
[66] A. Hasnaoui, H. Van Swygenhoven, P.M. Derlet. Dimples on nanocrystalline fracture surfaces as evidence for shear plane formation, Science 300 (2003) 1550-1552.
[67] D. Farkas, H. Van Swygenhoven, P.M. Derlet. Intergranular fracture in nanocrystalline metals, Physical Review B 66 (2002) 4.
[68] R.Z. Valiev, R.K. Islamgaliev, I.V. Alexandrov. Bulk nanostructured materials from severe plastic deformation, Prog. Mater. Sci. 45 (2000) 103-189.
[69] C. Suryanarayana. Mechanical alloying and milling, Prog. Mater. Sci. 46 (2001) 1-184.
[70] V.Y. Gertsman, R. Birringer. On the room-temperature grain growth in nanocrystalline copper, Scripta Metallurgica et Materialia 30 (1994) 577-581.
[71] T.R. Malow, C.C. Koch. Grain growth in nanocrystalline iron prepared by mechanical attrition, Acta Mater. 45 (1997) 2177-2186.
[72] M. Ames, J. Markmann, R. Karos, A. Michels, A. Tschöpe, R. Birringer. Unraveling the nature of room temperature grain growth in nanocrystalline materials, Acta Mater. 56 (2008) 4255-4266.
[73] T. Chookajorn, H.A. Murdoch, C.A. Schuh. Design of Stable Nanocrystalline Alloys, Science 337 (2012) 951-954.
[74] H.A. Murdoch, C.A. Schuh. Stability of binary nanocrystalline alloys against grain growth and phase separation, Acta Mater. 61 (2013) 2121-2132.
[75] J.R. Trelewicz, C.A. Schuh. Grain boundary segregation and thermodynamically stable binary nanocrystalline alloys, Physical Review B 79 (2009).
[76] A.J. Detor, C.A. Schuh. Grain boundary segregation, chemical ordering and stability of nanocrystalline alloys: Atomistic computer simulations in the Ni–W system, Acta Mater. 55 (2007) 4221-4232.

[77] A.J. Detor, M.K. Miller, C.A. Schuh. Solute distribution in nanocrystalline Ni–W alloys examined through atom probe tomography, Philos. Mag. 86 (2006) 4459-4475.
[78] J. Schiotz, T. Vegge, F.D. Di Tolla, K.W. Jacobsen. Atomic-scale simulations of the mechanical deformation of nanocrystalline metals, Physical Review B 60 (1999) 11971-11983.
[79] W. Klement, R.H. Willens, P. Duwez. NON-CRYSTALLINE STRUCTURE IN SOLIDIFIED GOLD-SILICON ALLOYS, Nature 187 (1960) 869-870.
[80] M.W. Chen. Mechanical behavior of metallic glasses: Microscopic understanding of strength and ductility. Annual Review of Materials Research, vol. 38. Annual Reviews, Palo Alto, 2008. pp. 445-469.
[81] M.F. Ashby, A.L. Greer. Metallic glasses as structural materials, Scr. Mater. 54 (2006) 321-326.
[82] A.L. Greer, Y.Q. Cheng, E. Ma. Shear bands in metallic glasses, Materials Science & Engineering R-Reports 74 (2013) 71-132.
[83] C.A. Schuh, T.C. Hufnagel, U. Ramamurty. Overview No.144 - Mechanical behavior of amorphous alloys, Acta Mater. 55 (2007) 4067-4109.
[84] H.S. Chen. GLASSY METALS, Reports on Progress in Physics 43 (1980) 353-&.
[85] F. Spaepen. Metallic glasses: Must shear bands be hot?, Nat. Mater. 5 (2006) 7-8.
[86] H. Bei, Z.P. Lu, E.P. George. Theoretical strength and the onset of plasticity in bulk metallic glasses investigated by nanoindentation with a spherical indenter, Physical Review Letters 93 (2004).
[87] J. Frenkel. The theory of the elastic limit and the solidity of crystal bodies, Zeitschrift Fur Physik 37 (1926) 572-609.
[88] J. Schroers, W.L. Johnson. Ductile bulk metallic glass, Physical Review Letters 93 (2004).
[89] M.D. Demetriou, M.E. Launey, G. Garrett, J.P. Schramm, D.C. Hofmann, W.L. Johnson, R.O. Ritchie. A damage-tolerant glass, Nat Mater 10 (2011) 123-128.
[90] J. Das, M.B. Tang, K.B. Kim, R. Theissmann, F. Baier, W.H. Wang, J. Eckert. "Work-hardenable" ductile bulk metallic glass, Physical Review Letters 94 (2005).
[91] A. Inoue, W. Zhang, T. Tsurui, A.R. Yavari, A.L. Greer. Unusual room-temperature compressive plasticity in nanocrystal-toughened bulk copper-zirconium glass, Philosophical Magazine Letters 85 (2005) 221-229.
[92] D.C. Hofmann, J.-Y. Suh, A. Wiest, G. Duan, M.-L. Lind, M.D. Demetriou, W.L. Johnson. Designing metallic glass matrix composites with high toughness and tensile ductility, Nature 451 (2008) 1085-1089.
[93] D.C. Jang, J.R. Greer. Transition from a strong-yet-brittle to a stronger-and-ductile state by size reduction of metallic glasses, Nat. Mater. 9 (2010) 215-219.
[94] C. Fan, R.T. Ott, T.C. Hufnagel. Metallic glass matrix composite with precipitated ductile reinforcement, Applied Physics Letters 81 (2002) 1020-1022.
[95] S. Pauly, S. Gorantla, G. Wang, U. Kühn, J. Eckert. Transformation-mediated ductility in CuZr-based bulk metallic glasses, Nat Mater 9 (2010) 473-477.
[96] C.C. Hays, C.P. Kim, W.L. Johnson. Microstructure Controlled Shear Band Pattern Formation and Enhanced Plasticity of Bulk Metallic Glasses Containing \textit{in situ} Formed Ductile Phase Dendrite Dispersions, Physical Review Letters 84 (2000) 2901-2904.
[97] Q.P. Cao, J.W. Liu, K.J. Yang, F. Xu, Z.Q. Yao, A. Minkow, H.J. Fecht, J. Ivanisenko, L.Y. Chen, X.D. Wang, S.X. Qu, J.Z. Jiang. Effect of pre-existing shear bands on the tensile mechanical properties of a bulk metallic glass, Acta Mater. 58 (2010) 1276-1292.

[98] W.H. Jiang, F.E. Pinkerton, M. Atzmon. Mechanical behavior of shear bands and the effect of their relaxation in a rolled amorphous Al-based alloy, Acta Mater. 53 (2005) 3469-3477.
[99] J.X. Fang, U. Vainio, W. Puff, R. Würschum, X.L. Wang, D. Wang, M. Ghafari, F. Jiang, J. Sun, H. Hahn, H. Gleiter. Atomic Structure and Structural Stability of Sc75Fe25 Nanoglasses, Nano Letters 12 (2012) 458-463.
[100] D. Srolovitz, V. Vitek, T. Egami. An atomistic study of deformation of amorphous metals, Acta Metallurgica 31 (1983) 335-352.
[101] M.L. Falk, J.S. Langer. Dynamics of viscoplastic deformation in amorphous solids, Physical Review E 57 (1998) 7192-7205.
[102] M.L. Falk. Molecular-dynamics study of ductile and brittle fracture in model noncrystalline solids, Physical Review B 60 (1999) 7062-7070.
[103] A.C. Lund, C.A. Schuh. Yield surface of a simulated metallic glass, Acta Mater. 51 (2003) 5399-5411.
[104] W.L. Johnson, K. Samwer. A Universal Criterion for Plastic Yielding of Metallic Glasses with a $(T/{T}_{g}{})}^{2/3}$ Temperature Dependence, Physical Review Letters 95 (2005) 195501.
[105] D. Srolovitz, K. Maeda, V. Vitek, T. Egami. Structural defects in amorphous solids Statistical analysis of a computer model, Philosophical Magazine A 44 (1981) 847-866.
[106] S.G. Mayr. Activation energy of shear transformation zones: A key for understanding rheology of glasses and liquids, Physical Review Letters 97 (2006).
[107] M. Zink, K. Samwer, W.L. Johnson, S.G. Mayr. Plastic deformation of metallic glasses: Size of shear transformation zones from molecular dynamics simulations, Physical Review B 73 (2006).
[108] A.S. Argon, L.T. Shi. Analysis of plastic flow in an amorphous soap bubble raft by the use of an inter-bubble potential, Philosophical Magazine A 46 (1982) 275-294.
[109] F. Spaepen. MICROSCOPIC MECHANISM FOR STEADY-STATE INHOMOGENEOUS FLOW IN METALLIC GLASSES, Acta Metallurgica 25 (1977) 407-415.
[110] G.J. Tucker. Atomistic simulations of defect nucleation and free volume in nanocrystalline materials. Georgia Institute of Technology, 2011.
[111] H. Van Swygenhoven, P.M. Derlet, A. Hasnaoui. Atomic mechanism for dislocation emission from nanosized grain boundaries, Physical Review B 66 (2002) 024101.
[112] H. Van Swygenhoven, P.M. Derlet, A.G. Froseth. Nucleation and propagation of dislocations in nanocrystalline fcc metals, Acta Mater. 54 (2006) 1975-1983.
[113] A. Hasnaoui, H. Van Swygenhoven, P.M. Derlet. On non-equilibrium grain boundaries and their effect on thermal and mechanical behaviour: a molecular dynamics computer simulation, Acta Mater. 50 (2002) 3927-3939.
[114] P.M. Derlet, H. Van Swygenhoven, A. Hasnaoui. Atomistic simulation of dislocation emission in nanosized grain boundaries, Philos. Mag. 83 (2003) 3569-3575.
[115] Y.M. Wang, M.W. Chen, F.H. Zhou, E. Ma. High tensile ductility in a nanostructured metal, Nature 419 (2002) 912-915.
[116] A.S. Argon. Plastic-Deformation in Metallic Glasses, Acta Metallurgica 27 (1979) 47-58.
[117] C.A. Schuh, A.S. Argon, T.G. Nieh, J. Wadsworth. The transition from localized to homogeneous plasticity during nanoindentation of an amorphous metal, Philos Mag 83 (2003) 2585-2597.

[118] Y.F. Shi, M.L. Falk. Structural transformation and localization during simulated nanoindentation of a noncrystalline metal film, Applied Physics Letters 86 (2005) -.
[119] C.A. Schuh, T.C. Hufnagel, U. Ramamurty. Overview No.144 - Mechanical behavior of amorphous alloys, 55 (2007) 4067-4109.
[120] J.Y. Zhang, G. Liu, S.Y. Lei, J.J. Niu, J. Sun. Transition from homogeneous-like to shear-band deformation in nanolayered crystalline Cu/amorphous Cu-Zr micropillars: Intrinsic vs. extrinsic size effect, Acta Mater. 60 (2012) 7183-7196.
[121] J.Y. Zhang, G. Liu, J. Sun. Self-toughening crystalline Cu/amorphous Cu-Zr nanolaminates: Deformation-induced devitrification, Acta Mater. 66 (2014) 22-31.
[122] W. Guo, E.A. Jägle, P.-P. Choi, J. Yao, A. Kostka, J.M. Schneider, D. Raabe. Shear-Induced Mixing Governs Codeformation of Crystalline-Amorphous Nanolaminates, Physical Review Letters 113 (2014) 035501.
[123] W. Guo, E. Jägle, J. Yao, V. Maier, S. Korte-Kerzel, J.M. Schneider, D. Raabe. Intrinsic and extrinsic size effects in the deformation of amorphous CuZr/nanocrystalline Cu nanolaminates, Acta Mater. 80 (2014) 94-106.
[124] J.J. Niu, P. Zhang, R.H. Wang, J.Y. Zhang, G. Liu, G.J. Zhang, J. Sun. Formation of multiple twins and their strengthening effect in nanocrystalline Cu/Zr multilayer films, Materials Science and Engineering: A 539 (2012) 68-73.
[125] Y.M. Wang, A.V. Hamza, T.W. Barbee. Incipient plasticity in metallic glass modulated nanolaminates, Applied Physics Letters 91 (2007).
[126] C. Brandl, T.C. Germann, A. Misra. Structure and shear deformation of metallic crystalline-amorphous interfaces, Acta Mater. 61 (2013) 3600-3611.
[127] M.C. Liu, J.C. Huang, Y.T. Fong, S.P. Ju, X.H. Du, H.J. Pei, T.G. Nieh. Assessing the interfacial strength of an amorphous-crystalline interface, Acta Materialia 61 (2013) 3304-3313.
[128] Y. Wang, J.Q. Zhou, S. Zhang, L. Wang. Mechanical analysis of the crystalline-amorphous laminated composite based on a two-phase model, Mater. Des. 51 (2013) 88-94.
[129] H.J. Pei, S.Y. Kuan, M.C. Liu, J.C. Huang. Tensile behavior of amorphous/nanocrystalline ZrCu/Cu multilayered films with graded interfaces, Intermetallics 31 (2012) 191-195.
[130] J. McKeown, A. Misra, H. Kung, R.G. Hoagland, M. Nastasi. Microstructures and strength of nanoscale Cu–Ag multilayers, Scr. Mater. 46 (2002) 593-598.
[131] H. Huang, F. Spaepen. Tensile testing of free-standing Cu, Ag and Al thin films and Ag/Cu multilayers, Acta Mater 48 (2000) 3261-3269.
[132] Y. Liu, D. Bufford, H. Wang, C. Sun, X. Zhang. Mechanical properties of highly textured Cu/Ni multilayers, Acta Mater. 59 (2011) 1924-1933.
[133] J. Wang, R.G. Hoagland, J.P. Hirth, A. Misra. Atomistic modeling of the interaction of glide dislocations with “weak” interfaces, Acta Mater. 56 (2008) 5685-5693.
[134] R.G. Hoagland, R.J. Kurtz, C.H. Henager Jr. Slip resistance of interfaces and the strength of metallic multilayer composites, Scr. Mater. 50 (2004) 775-779.
[135] J. Wang, A. Misra. An overview of interface-dominated deformation mechanisms in metallic multilayers, Current Opinion in Solid State and Materials Science 15 (2011) 20-28.
[136] A. Misra, J.P. Hirth, R.G. Hoagland. Length-scale-dependent deformation mechanisms in incoherent metallic multilayered composites, Acta Mater. 53 (2005) 4817-4824.
[137] E.G. Fu, N. Li, A. Misra, R.G. Hoagland, H. Wang, X. Zhang. Mechanical properties of sputtered Cu/V and Al/Nb multilayer films, Materials Science and Engineering: A 493 (2008) 283-287.

[138] R.F. Zhang, T.C. Germann, J. Wang, X.Y. Liu, I.J. Beyerlein. Role of interface structure on the plastic response of Cu/Nb nanolaminates under shock compression: Non-equilibrium molecular dynamics simulations, Scr. Mater. 68 (2013) 114-117.
[139] R.G. Hoagland, T.E. Mitchell, J.P. Hirth, H. Kung. On the strengthening effects of interfaces in multilayer fee metallic composites, Philosophical Magazine A 82 (2002) 643-664.
[140] C.H. Henager, R.J. Kurtz, R.G. Hoagland. Interactions of dislocations with disconnections in fcc metallic nanolayered materials, Philos. Mag. 84 (2004) 2277-2303.
[141] J.P. Hirth, X. Feng. Critical layer thickness for misfit dislocation stability in multilayer structures, J. Appl. Phys. 67 (1990) 3343-3349.
[142] A. Misra, J.P. Hirth, R.G. Hoagland, J.D. Embury, H. Kung. Dislocation mechanisms and symmetric slip in rolled nano-scale metallic multilayers, Acta Mater. 52 (2004) 2387-2394.
[143] A. Misra, M. Verdier, Y. Lu, H. Kung, T. Mitchell, M. Nastasi, J. Embury. Structure and mechanical properties of Cu-X (X= Nb, Cr, Ni) nanolayered composites, Scr. Mater. 39 (1998) 555-560.
[144] J. Wang, Q. Zhou, S. Shao, A. Misra. Strength and plasticity of nanolaminated materials, Materials Research Letters 5 (2017) 1-19.
[145] K. Chen, S.-q. Shi, W. Zhu, X. Peng. Plastic deformation due to interfacial sliding in amorphous/crystalline nanolaminates, Comput. Mater. Sci. 109 (2015) 266-276.
[146] T.J. Rupert, J.R. Trelewicz, C.A. Schuh. Grain boundary relaxation strengthening of nanocrystalline Ni-W alloys, Journal of Materials Research 27 (2012) 1285-1294.
[147] C.J. Lee, H.K. Lin, J.C. Huang, S.Y. Kuan. Tension behavior of free-standing amorphous film and amorphous-crystalline nanolaminates in submicron scale, Scr. Mater. 65 (2011) 695-698.
[148] F.F. Wu, K.C. Chan, S.T. Li, G. Wang, P. Lin. Tensile deformation of a Ti-based metallic glass composite lamella confined by commercially pure titanium, Philosophical Magazine Letters 94 (2014) 233-241.
[149] M.C. Liu, J.C. Huang, H.S. Chou, Y.H. Lai, C.J. Lee, T.G. Nieh. A nanoscaled underlayer confinement approach for achieving extraordinarily plastic amorphous thin film, Scr. Mater. 61 (2009) 840-843.
[150] M.C. Liu, X.H. Du, I.C. Lin, H.J. Pei, J.C. Huang. Superplastic-like deformation in metallic amorphous/crystalline nanolayered micropillars, Intermetallics 30 (2012) 30-34.
[151] F. Shimizu, S. Ogata, J. Li. Yield point of metallic glass, Acta Materialia 54 (2006) 4293-4298.
[152] T.G. Nieh, J. Wadsworth. Bypassing shear band nucleation and ductilization of an amorphous-crystalline nanolaminate in tension, Intermetallics 16 (2008) 1156-1159.
[153] A. Donohue, F. Spaepen, R.G. Hoagland, A. Misra. Suppression of the shear band instability during plastic flow of nanometer-scale confined metallic glasses, Applied Physics Letters 91 (2007) 3.
[154] J.Y. Kim, D.C. Jang, J.R. Greer. Nanolaminates Utilizing Size-Dependent Homogeneous Plasticity of Metallic Glasses, Adv. Funct. Mater. 21 (2011) 4550-4554.
[155] W. Guo, J. Yao, E.A. Jägle, P.-P. Choi, M. Herbig, J.M. Schneider, D. Raabe. Deformation induced alloying in crystalline – metallic glass nano-composites, Materials Science and Engineering: A 628 (2015) 269-280.
[156] J.Y. Zhang, G. Liu, J. Sun. Crystallization-aided extraordinary plastic deformation in nanolayered crystalline Cu/amorphous Cu-Zr micropillars, Sci Rep 3 (2013) 6.

[157] W. Guo, B. Gan, J.M. Molina-Aldareguia, J.D. Poplawsky, D. Raabe. Structure and dynamics of shear bands in amorphous–crystalline nanolaminates, Scr. Mater. 110 (2016) 28-32.
[158] I. Knorr, N.M. Cordero, E.T. Lilleodden, C.A. Volkert. Mechanical behavior of nano scale Cu/PdSi multilayers, Acta Mater. 61 (2013) 4984-4995.
[159] Y. Cui, O.T. Abad, F. Wang, P. Huang, T.-J. Lu, K.-W. Xu, J. Wang. Plastic Deformation Modes of CuZr/Cu Multilayers, Sci Rep 6 (2016) 23306.
[160] Y. Cui, P. Huang, F. Wang, T.J. Lu, K.W. Xu. The hardness and related deformation mechanisms in nanoscale crystalline–amorphous multilayers, Thin Solid Films 584 (2015) 270-276.
[161] Y. Cui, Y. Shibutani, S. Li, P. Huang, F. Wang. Plastic deformation behaviors of amorphous-Cu50Zr50/crystalline-Cu nanolaminated structures by molecular dynamics simulations, Journal of Alloys and Compounds 693 (2017) 285-290.
[162] B. Arman, C. Brandl, S.N. Luo, T.C. Germann, A. Misra, T. Cagin. Plasticity in Cu(111)/Cu46Zr54 glass nanolaminates under uniaxial compression, J. Appl. Phys. 110 (2011) 5.
[163] Z. Pan, T.J. Rupert. Amorphous intergranular films as toughening structural features, Acta Mater. 89 (2015) 205-214.
[164] Y.Q. Wang, J.Y. Zhang, X.Q. Liang, K. Wu, G. Liu, J. Sun. Size- and constituent-dependent deformation mechanisms and strain rate sensitivity in nanolaminated crystalline Cu/amorphous Cu–Zr films, Acta Mater. 95 (2015) 132-144.
[165] Y.M. Wang, A.V. Hamza, T.W. Barbee. Incipient plasticity in metallic glass modulated nanolaminates, Applied Physics Letters 91 (2007) 3.
[166] T.G. Nieh, T.W. Barbee, J. Wadsworth. Tensile properties of a free-standing Cu/Zr nanolaminate (or compositionally-modulated thin film), Scr. Mater. 41 (1999) 929-935.
[167] H. Gleiter, T. Schimmel, H. Hahn. Nanostructured solids – From nano-glasses to quantum transistors, Nano Today 9 (2014) 17-68.
[168] X. Wang, F. Jiang, H. Hahn, J. Li, H. Gleiter, J. Sun, J. Fang. Sample size effects on strength and deformation mechanism of Sc75Fe25 nanoglass and metallic glass, Scr. Mater. 116 (2016) 95-99.
[169] R. Witte, T. Feng, J.X. Fang, A. Fischer, M. Ghafari, R. Kruk, R.A. Brand, D. Wang, H. Hahn, H. Gleiter. Evidence for enhanced ferromagnetism in an iron-based nanoglass, Applied Physics Letters 103 (2013) 073106.
[170] N. Chen, D. Wang, T. Feng, R. Kruk, K.-F. Yao, D.V. Louzguine-Luzgin, H. Hahn, H. Gleiter. A nanoglass alloying immiscible Fe and Cu at the nanoscale, Nanoscale 7 (2015) 6607-6611.
[171] J.Q. Wang, N. Chen, P. Liu, Z. Wang, D.V. Louzguine-Luzgin, M.W. Chen, J.H. Perepezko. The ultrastable kinetic behavior of an Au-based nanoglass, Acta Mater. 79 (2014) 30-36.
[172] J. Jing, A. Krämer, R. Birringer, H. Gleiter, U. Gonser. Modified atomic structure in a Pd Fe Si nanoglass, Journal of Non-Crystalline Solids 113 (1989) 167-170.
[173] N. Chen, R. Frank, N. Asao, D.V. Louzguine-Luzgin, P. Sharma, J.Q. Wang, G.Q. Xie, Y. Ishikawa, N. Hatakeyama, Y.C. Lin, M. Esashi, Y. Yamamoto, A. Inoue. Formation and properties of Au-based nanograined metallic glasses, Acta Mater. 59 (2011) 6433-6440.
[174] C. Guo, Y. Fang, B. Wu, S. Lan, G. Peng, X.-l. Wang, H. Hahn, H. Gleiter, T. Feng. Ni-P nanoglass prepared by multi-phase pulsed electrodeposition, Materials Research Letters (2016) 1-7.

[175] H. Shao, Y. Xu, B. Shi, C. Yu, H. Hahn, H. Gleiter, J. Li. High density of shear bands and enhanced free volume induced in Zr70Cu20Ni10 metallic glass by high-energy ball milling, Journal of Alloys and Compounds 548 (2013) 77-81.
[176] M. Ghafari, S. Kohara, H. Hahn, H. Gleiter, T. Feng, R. Witte, S. Kamali. Structural investigations of interfaces in Fe90Sc10 nanoglasses using high-energy x-ray diffraction, Applied Physics Letters 100 (2012) 133111.
[177] O. Franke, D. Leisen, H. Gleiter, H. Hahn. Thermal and plastic behavior of nanoglasses, Journal of Materials Research 29 (2014) 1210-1216.
[178] D. Danilov, H. Hahn, H. Gleiter, W. Wenzel. Mechanisms of Nanoglass Ultrastability, ACS Nano 10 (2016) 3241-3247.
[179] C.A. Schuh, T.G. Nieh. A nanoindentation study of serrated flow in bulk metallic glasses, Acta Mater. 51 (2003) 87-99.
[180] S. Adibi, P.S. Branicio, Y.-W. Zhang, S.P. Joshi. Composition and grain size effects on the structural and mechanical properties of CuZr nanoglasses, J. Appl. Phys. 116 (2014) 043522.
[181] D. Sopu, K. Albe, Y. Ritter, H. Gleiter. From nanoglasses to bulk massive glasses, Applied Physics Letters 94 (2009).
[182] D. Sopu, Y. Ritter, H. Gleiter, K. Albe. Deformation behavior of bulk and nanostructured metallic glasses studied via molecular dynamics simulations, Physical Review B 83 (2011).
[183] S. Adibi, Z.-D. Sha, P.S. Branicio, S.P. Joshi, Z.-S. Liu, Y.-W. Zhang. A transition from localized shear banding to homogeneous superplastic flow in nanoglass, Applied Physics Letters 103 (2013) 211905.
[184] S. Adibi, P.S. Branicio, S.P. Joshi. Suppression of Shear Banding and Transition to Necking and Homogeneous Flow in Nanoglass Nanopillars, Sci Rep 5 (2015) 15611.
[185] S. Plimpton. Fast Parallel Algorithms for Short-Range Molecular Dynamics, Journal of Computational Physics 117 (1995) 1-19.
[186] M.I. Mendelev, D.K. Rehbein, R.T. Ott, M.J. Kramer, D.J. Sordelet. Computer simulation and experimental study of elastic properties of amorphous Cu-Zr alloys, J. Appl. Phys. 102 (2007).
[187] M.I. Mendelev, M.J. Kramer, C.A. Becker, M. Asta. Analysis of semi-empirical interatomic potentials appropriate for simulation of crystalline and liquid Al and Cu, Philos. Mag. 88 (2008) 1723-1750.
[188] G. Voronoi. New applications of continuous parameters to the theory of quadratic forms. - First memoir - Some properties of perfect positive quadratic forms, J. Reine Angew. Math. 133 (1908) 97-178.
[189] A.J. Haslam, S.R. Phillpot, H. Wolf, D. Moldovan, H. Gleiter. Mechanisms of grain growth in nanocrystalline fcc metals by molecular-dynamics simulation, Materials Science and Engineering a-Structural Materials Properties Microstructure and Processing 318 (2001) 293-312.
[190] N. Mattern, A. Schöps, U. Kühn, J. Acker, O. Khvostikova, J. Eckert. Structural behavior of CuxZr100−x metallic glass (x = 35−70), Journal of Non-Crystalline Solids 354 (2008) 1054-1060.
[191] D. Faken, H. Jónsson. Systematic analysis of local atomic structure combined with 3D computer graphics, Comput. Mater. Sci. 2 (1994) 279-286.
[192] H. Tsuzuki, P.S. Branicio, J.P. Rino. Structural characterization of deformed crystals by analysis of common atomic neighborhood, Computer Physics Communications 177 (2007) 518-523.

[193] J.A. Zimmerman, C.L. Kelchner, P.A. Klein, J.C. Hamilton, S.M. Foiles. Surface step effects on nanoindentation, Phys Rev Lett 87 (2001) 165507.
[194] G.J. Tucker, S. Tiwari, J.A. Zimmerman, D.L. McDowell. Investigating the deformation of nanocrystalline copper with microscale kinematic metrics and molecular dynamics, Journal of the Mechanics and Physics of Solids 60 (2012) 471-486.
[195] A. Stukowski. Visualization and analysis of atomistic simulation data with OVITO-the Open Visualization Tool, Model Simul Mater Sc 18 (2010).
[196] A.R. Yavari, A.L. Moulec, A. Inoue, N. Nishiyama, N. Lupu, E. Matsubara, W.J. Botta, G. Vaughan, M.D. Michiel, Å. Kvick. Excess free volume in metallic glasses measured by X-ray diffraction, Acta Mater. 53 (2005) 1611-1619.
[197] R.J. Asaro, S. Suresh. Mechanistic models for the activation volume and rate sensitivity in metals with nanocrystalline grains and nano-scale twins, Acta Mater. 53 (2005) 3369-3382.
[198] B. Arman, C. Brandl, S.N. Luo, T.C. Germann, A. Misra, T. Cagin. Plasticity in Cu(111)/Cu46Zr54 glass nanolaminates under uniaxial compression, Journal of Applied Physics 110 (2011).
[199] K.S. Kumar, S. Suresh, M.F. Chisholm, J.A. Horton, P. Wang. Deformation of electrodeposited nanocrystalline nickel, Acta Mater. 51 (2003) 387-405.
[200] M.I. Mendelev, D.J. Sordelet, M.J. Kramer. Using atomistic computer simulations to analyze x-ray diffraction data from metallic glasses, J. Appl. Phys. 102 (2007).
[201] B. Cheng, J.R. Trelewicz. Mechanistic coupling of dislocation and shear transformation zone plasticity in crystalline-amorphous nanolaminates, Acta Mater. 117 (2016) 293-305.
[202] F. Shimizu, S. Ogata, J. Li. Theory of shear banding in metallic glasses and molecular dynamics calculations, Materials Transactions 48 (2007) 2923-2927.
[203] F. Spaepen. A microscopic mechanism for steady state inhomogeneous flow in metallic glasses, Acta Metallurgica 25 (1977) 407-415.
[204] A. Stukowski. Structure identification methods for atomistic simulations of crystalline materials, Model Simul Mater Sc 20 (2012) 15.
[205] C.H. Rycroft. VORO plus plus : A three-dimensional Voronoi cell library in C plus, Chaos 19 (2009) 1.
[206] H. Van Swygenhoven, M. Spaczer, A. Caro, D. Farkas. Competing plastic deformation mechanisms in nanophase metals, Physical Review B 60 (1999) 22-25.
[207] O. Younes, E. Gileadi. Electroplating of high tungsten content Ni/W alloys, Electrochemical and Solid-State Letters 3 (2000) 543-545.
[208] A.J. Bard, R. Parsons, J. Jordan. Standard potentials in aqueous solution, CRC press, 1985.
[209] S.O. Moussa, M.A.M. Ibrahim, S.S.A.E. Rehim. Induced electrodeposition of tungsten with nickel from acidic citrate electrolyte, Journal of Applied Electrochemistry 36 (2006) 333-338.
[210] A. Brenner. Electrodeposition of alloys: principles and practice, Elsevier, 2013.
[211] O. Younes, E. Gileadi. Electroplating of Ni/W alloys - I. Ammoniacal citrate baths, J. Electrochem. Soc. 149 (2002) C100-C111.
[212] J.R. Trelewicz. Nanostructure stabilization and mechanical behavior of binary nanocrystalline alloys. Massachusetts Institute of Technology, 2008.
[213] A.J. Detor. Grain size control and microstructural evolution in nanocrystalline Ni-W alloys. Massachusetts Institute of Technology, 2007.

[214] B.D. Cullity, J.W. Weymouth. Elements of X-ray Diffraction, American Journal of Physics 25 (1957) 394-395.
[215] D. Xu, G. Duan, W.L. Johnson, C. Garland. Formation and properties of new Ni-based amorphous alloys with critical casting thickness up to 5 mm, Acta Mater. 52 (2004) 3493-3497.
[216] W.C. Oliver, G.M. Pharr. AN IMPROVED TECHNIQUE FOR DETERMINING HARDNESS AND ELASTIC-MODULUS USING LOAD AND DISPLACEMENT SENSING INDENTATION EXPERIMENTS, Journal of Materials Research 7 (1992) 1564-1583.
[217] B.N. Lucas, W.C. Oliver. Indentation power-law creep of high-purity indium, Metall and Mat Trans A 30 (1999) 601-610.
[218] J.Y. Zhang, K. Wu, L.Y. Zhang, Y.Q. Wang, G. Liu, J. Sun. Unraveling the correlation between Hall-Petch slope and peak hardness in metallic nanolaminates, International Journal of Plasticity.
[219] Y.Q. Cheng, H.W. Sheng, E. Ma. Relationship between structure, dynamics, and mechanical properties in metallic glass-forming alloys, Physical Review B 78 (2008).
[220] J.L.Finney. Modelling the structures of amorphous metals and alloys, Nature 266 (1977) 6.
[221] Y.Q. Cheng, A.J. Cao, H.W. Sheng, E. Ma. Local order influences initiation of plastic flow in metallic glass: Effects of alloy composition and sample cooling history, Acta Mater. 56 (2008) 5263-5275.
[222] A. Stukowski. Computational Analysis Methods in Atomistic Modeling of Crystals, JOM 66 (2014) 399-407.
[223] A.J. Cao, Y.Q. Cheng, E. Ma. Structural processes that initiate shear localization in metallic glass, Acta Mater. 57 (2009) 5146-5155.
[224] Y.Q. Cheng, A.J. Cao, E. Ma. Correlation between the elastic modulus and the intrinsic plastic behavior of metallic glasses: The roles of atomic configuration and alloy composition, Acta Mater. 57 (2009) 3253-3267.
[225] D.A. Porter, K.E. Easterling, M. Sherif. Phase Transformations in Metals and Alloys, (Revised Reprint), CRC press, 2009.
[226] T.J. Rupert, J.R. Trelewicz, C.A. Schuh. Grain boundary relaxation strengthening of nanocrystalline Ni–W alloys, Journal of Materials Research 27 (2012) 1285-1294.